THESIS FOR THE DEGREE OF DOCTOR OF PHILOSOPHY

Subsynchronous Resonance in Doubly-Fed Induction Generator Based Wind Farms

SELAM CHERNET

Department of Electrical Engineering
CHALMERS UNIVERSITY OF TECHNOLOGY
Gothenburg, Sweden, 2018

Subsynchronous Resonance in Doubly-Fed Induction Generator Based Wind Farms
SELAM CHERNET
ISBN 978-91-7597-714-0

Doktorsavhandlingar vid Chalmers Tekniska Högskola
Ny serie nr. 4395
ISSN 0346-718X

Division of Electric Power Engineering
Department of Electrical Engineering
Chalmers University of Technology
SE–412 96 Gothenburg
Sweden
Telephone +46 (0)31–772 1000

Printed by Chalmers Reproservice
Gothenburg, Sweden, 2018

To Buta!!!

Subsynchronous Resonance in Doubly-Fed Induction Generator Based Wind Farms
SELAM CHERNET
Department of Electrical Engineering
Chalmers University of Technology

Abstract

The objective of this thesis is to investigate the risk for instabilities due to subsynchronous resonance (SSR) conditions in large wind farms connected to series-compensated transmission lines. In particular, the focus is on doubly-fed induction generator (DFIG) based wind farms. Analytical models of the system under investigation are derived in order to understand the root causes that can lead to instabilities. A frequency-dependent approach based on the generalized Nyquist criterion (GNC) has been applied to investigate the risk for SSR in DFIG based wind turbines. Through this approach, it is shown that the observed phenomenon is mainly due to an energy exchange between the power converter of the turbine and the series compensated grid. This phenomenon, here referred to as subsynchronous controller interaction (SSCI), is driven by the control system of the turbine's converter, which results in a non-dissipative behavior of the DFIG system in the subsynchronous frequency range. The different factors that impact the frequency characteristic of the wind turbine, thereby making the system prone to SSCI interaction, are investigated. Through the analysis, it is shown that in a DFIG wind turbine, the current controller that regulates the rotor current plays a major role in the risk for SSCI, where an increased closed-loop bandwidth negatively impacts the system damping in the subsynchronous frequency range. The level of active power output from the wind farm also has an impact on the overall system stability; in particular, it is shown that the power-dissipation properties of the DFIG improves when the latter is operated in supersynchronous speed range (high-power output).
Methods for proper aggregation of the wind turbines in the farm are investigated. Time-domain studies are performed on the aggregated model connected to a series compensated transmission line to verify the analytical results obtained through the frequency domain analysis. Based on the theoretical analysis, mitigation strategy is proposed in order to shape the frequency behavior of the wind turbine. The effectiveness of the proposed mitigation strategy is evaluated both theoretically through frequency-domain analysis and using detailed time-domain simulations.

Index Terms: Wind power, doubly-fed induction generator (DFIG), subsynchronous resonance (SSR), subsynchronous controller interaction (SSCI), induction generator effect (IGE), Impedance-based analysis, Passivity, generalized Nyquist criterion (GNC).

Acknowledgments

My sincere gratitude goes to my supervisor Prof. Massimo Bongiorno for his technical guidance, immense encouragement, and continuous support during this research work. His patience, positive attitude and exemplary guidance have been my immense inspirations throughout this period. I would also like to extend my thanks to my examiner Prof. Torbjörn Thiringer for the interesting discussion sessions and his invaluable comments. Moreover, I would like to thank both these professors for giving me the opportunity of coming back to Chalmers.

I would also like to express my gratitude to Dr. Mebtu Beza for being my co-supervisor during the past years as well as for the countless fruitful discussions and friendship throughout my time in Chalmers. Moreover, I would also like to thank the late Dr. Hector Zelaya De La Parra, (formerly with ABB corporate research), as well as Dr. Stefan Lundberg for being my co-supervisors during the first half of this work.

The financial support for the project granted by ABB is greatly appreciated. Additionally, I would like to extend my special thanks to Dr. Georgios Demetriades, Dr. Jan Svensson and Dr. Cathy Yao Chen, from ABB corporate research, for their helpful and constructive comments during our meetings. I would also like to thank Prof. Lennart Harnefors for his insightful guidance at the start of this work. My acknowledgment also goes out to the dynamic team at Vestas Wind Systems: Dr. Gert K. Andersen, Dr. Torsten Lund and Prof. Philip Carne Kjaer for their knowledgeable and practical inputs while carrying out part of this work.

Many thanks to the members of the division who have assisted me in several ways and helped to create a good working environment. A special thanks to my former roommate Ehsan Berhrouzian and my current roommates; Kyriaki Antoniadou (Kelly) and Christos Agathokleous, for making our office simply the best.

Finally, I would like to extend my gratefulness to the almighty God for all the blessings in my life. My parents, Tesfaye Chernet and Ghiday G/Egzibher and my siblings, Rahwa Tesfaye and Nebuyou Tesfaye, thank you for your endless love and support throughout my life. Last but not least, I would like to thank my husband Markos Kassa, for his love, support, encouragement and understanding. Thank you for challenging and inspiring me. Yen buta widid aregihalew!!!

Selam Chernet
Gothenburg, Sweden
September, 2018

List of Acronyms

EWEA	European Wind Energy Association
GWEC	Global Wind Energy Council
SWEA	Swedish Energy Association
SSCI	Sub Synchronous Control Interaction
SSR	Sub-synchronous Resonance
IM	Induction Machine
IGE	Induction Generator Effect
TI	Torsional Interaction
TA	Torque Amplification
MMF	Magnetic Motive Force
FSM	Frequency Scanning Method
SISO	Single Input Single Output
IEEE FBM	IEEE First Benchmark Model
IEEE SBM	IEEE Second Benchmark Model
FSIG	Fixed Speed Induction Generator
FPC	Full Power Converter
DFIG	Doubly-Fed Induction Generator
SCIG	Squirrel Cage Induction Generator
BTB	Back To Back
RSC	Rotor Side Converter
GSC	Grid Side Converter
DC	Direct Current
AC	Alternating Current
pu	per unit
LPF	Low Pass Filter
WRIG	Wound Rotor Induction Generator
VSC	Voltage Source Converter
IGBT	Insulated Gate Bipolar Transistor
PLL	Phase Locked Loop
IMC	Internal Mode Control
PCC	Point of Common Coupling
AGO	Advanced Grid Operation
FRT	Fault Ride Through
STATCOM	Static Synchronous Compensator
SVC	Static Var Compensator
GCSC	Gate-Controlled Series Capacitor

TCSC	Thyristor Controlled Series Capacitors
EA	Estimation Algorithm
LPF-EA	Low-Pass Filter based Estimation Algorithm
FLL	Frequency-Locked Loop
PI	Proportional Integral

Contents

Chapter 1

Introduction

1.1 Background and motivation

Renewable energy sources play today and will play even more tomorrow a significant role in the electric power system. In particular, wind and solar installations continue to increase as utilities and power providers are turning towards cleaner, more sustainable and abundant sources of energy. As an example, the capacity of renewable generation in Sweden reached 51% of the total generation capacity in 2017, with a peak of about 11% of energy production from wind and solar in 2015 [1] [2]. It is also reported that by year 2040, the generation capacity in Sweden should reach 100% renewables, with about 45% of the total generation capacity coming from wind and solar [3]. It is therefore not unrealistic to imagine that in the future power system all non-environmental friendly power generation units (such as nuclear or fossil-based units) will be replaced by renewable-based generating plants. Among others, wind power is definitely one of the fastest growing sources of electricity in the world. From the global capacity point-of-view, according to the statistics provided by the Global Wind Energy Council (GWEC) [4], the worldwide cumulative installed wind capacity has reached 540 GW in 2017, with an exponential increase over the last 15 years, as shown in Fig. 1.1. In this scenario, China is definitely the world leader for integration of wind power into the power system, followed by the US, Germany and India. From a national point of view, Sweden is Europe's quickest growing country on wind power generation, where statistics from Wind Europe (formerly known by European Wind Energy Association-EWEA) show that over the last two years, a total of 0.7 GW of new capacity has been developed in the country [5].

However, the future energy mix and the inherited intermittent nature of renewables bring a number of challenges for utilities and grid operators. The electric power grid is a very complex system that continuously requires a balance between energy supply and demand due to its inability to store energy. Adding variable sources of energy may greatly alter this critical balance. Additionally, it is of importance to consider that modern wind turbines are interfaced with the power systems through power-electronic converters due to structural reasons, but also to increase their flexibility, functionalities, allow variable-speed operation and facilitate grid code compliance. In recent years, it has become clear that reaching the targeted levels of renewable power gener-

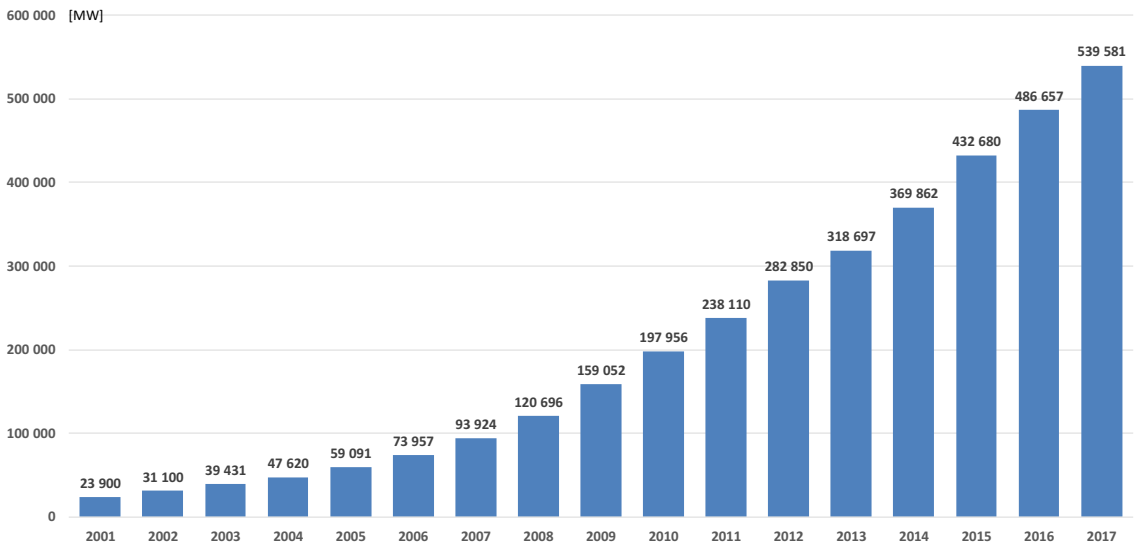

Fig. 1.1 Global cumulative installed wind capacity in 2001-2017. Source: GWEC.

ation poses problems not only from a generation/load balancing point of view, but also in terms of system stability. As an example, in Ireland the contribution from power-electronic interfaced generation is already constrained to 50-55% and recent studies suggest that any penetration of this kind of power sources above 65% would represent an actual risk for the stability of the grid [6–9]. Among others, system stability can be jeopardized due to unwanted interactions between power-electronic converters and interactions between converters and passive components installed in the power systems, such as series-capacitor banks. The latter condition was first experienced in 2009, where low-frequency instability has been experienced in a doubly-fed induction generator (DFIG) based wind farm that became radially connected to a series-compensated transmission line [10] [11]. Initially, the phenomenon has been attributed to self-excitation of a subsynchronous resonance (SSR) condition [12] [13]. However, subsequent analysis has shown that the main cause of the instability had to be attributed to an interaction between the control system of the power-electronic converter and the series-compensated transmission line; this resonant condition has been later addressed to as subsynchronous control interaction (SSCI).

Following the incident, intensive research has been conducted in this field, trying to identify the root causes of the phenomenon and to assess the potential risk for SSR in DFIG-based wind farms when connected to fixed-series compensation. In the majority of the works available in the literature, the stability of the system is analyzed through eigenvalue analysis [14–18], where the complete model of the system (represented by an aggregated model of the wind farm and the series-compensated transmission line) is linearized and expressed in state-space form. However, one disadvantage with this approach is that it can be bulky, as the entire system must be modeled as a single state-space representation. This leads to the difficulty in properly assess and identify the impact of the different parameters when evaluating the system's stability. Furthermore, the entire mathematical model must be rebuild in case of variations in the investigated system, for example in the case of grid reconfiguration. An alternative approach to the investigation of the

stability of a system is based on frequency response of the system's transfer-function through the derivation of the frequency-dependent impedance/admittance of the wind farm and the connecting transmission line [14] [19–21]. Although effective in providing a quick assessment of the potential risk for SSR, often the wind farm representation is largely simplified, for example neglecting the outer control loops that regulates the DFIG's converter and modeling the whole wind farm as a single aggregated wind turbine. These approximations can lead to erroneous conclusions and thereby need to be properly addressed in order to understand the mechanism that can lead to instability and thereby propose effective mitigation methods.

1.2 Purpose of the thesis and main contribution

The aim of this thesis is to provide a deep understanding of the root causes of the interaction due to SSCI in DFIG-based wind farms when connected to a series-compensated transmission line. The final goal is to identify the key parameters that affect the stability of the system and thereby propose effective countermeasures. To the knowledge of the author, the main contribution of this thesis can be summarized as follows:

1. A detailed frequency-domain admittance model of the DFIG wind turbine has been derived. A detailed linearized mathematical model for the DFIG wind turbine has been derived and verified through time-domain simulations. The derived system has been used to perform frequency-domain analysis and characterize the frequency characteristic of the DFIG admittance in the subsynchronous frequency range. The impact of the various control parameters on the power-dissipation properties of the wind turbine have been evaluated. Based on the obtained results, it is shown that the rotor-side current controller of the DFIG plays a major role on the wind turbine's frequency response.

2. An indepth investigation of the risk of SSCI in DFIG-based wind farms has been performed. An impedance based generalized Nyquist criterion (GNC) has been used to evaluate the risk of instabilities in DFIG-based wind farms connected to a series-compensated transmission line. The stability of the system has been evaluated for a variety of operating conditions and control parameters. In particular, the power-dissipation properties of the DFIG wind turbine have been used to identify the control parameters and/or operating conditions that affect the stability of the system.

3. An improved wind farm aggregation model for SSCI investigation has been presented. An improved method for wind farm aggregation suitable for SSCI investigation has been proposed. In particular it has been shown that under specific conditions, the representation of a DFIG-based wind farm through a single aggregate might lead to erroneous conclusions. For this reason, it is recommended to represent the wind farm with at least a two aggregate model representation.

4. A new SSCI mitigation approach has been proposed. The proposed approach involves admittance shaping of the wind turbine for the range of frequencies of interest, aiming at enhancing the power dissipation properties of the turbine through the implementation

of a damping controller that modifies the reference current input to the control system of the rotor-side converter of the DFIG. With the proposed approach, the safe level of series compensation can be drastically increased in case of radial connection of the wind farm to the series-compensated transmission line.

1.3 Structure of the thesis

The thesis is organized into seven chapters. Chapter 1 presents the background, motivation and major contribution of the thesis. Chapter 2 gives an overview of the different types of SSR that can be encountered in the power system, together with an overview of the most commonly used analysis methods employed to evaluate the risk of SSR both in classical and wind generation units. An introduction to the different components of a DFIG wind turbine together with its control system is presented in Chapter 3. In the same chapter, the mathematical representation for the DFIG turbine is derived. The derived mathematical model is then verified against a full-switching DFIG model implemented in PSCAD. The frequency response of the derived frequency-dependent admittance is extended to obtain the power-dissipation properties of the DFIG, used to get insight into possible causes for system interaction. The series-compensated transmission line model is presented together with the combined wind farm model in Chapter 4. In this chapter, an overview of different aggregation methods for wind farm representation is presented. Based on the power-dissipation properties of the wind farm, the impact of different aggregation approaches on the frequency-characteristics of the wind farm response is presented. Frequency-domain stability analysis is performed in Chapter 5. In this chapter, the derived frequency-dependent models are used to identify system parameters and operating conditions that affect the risk for control interaction in the subsynchronous-frequency range. An impedance-based generalized Nyquist criterion that employs the DFIG-based wind farm admittance and the transmission grid impedance is introduced and utilized. Time-domain simulations performed in PSCAD are then used to validate the theoretical analysis. Chapter 6 deals with the derivation of a damping controller to be implemented in the DFIG control scheme, aiming at increasing the power dissipation properties of the wind turbine system at the frequency of interest. Both analytical and time-domain simulation are used to verify the effectiveness of the proposed approach. Finally, Chapter 7 presents the conclusion of the thesis and provides suggestions for future work.

1.4 List of publications

The publications originating from the project are:

I. S. Chernet and M. Bongiorno, ”Input Impedance based Nyquist Stability Criterion for Subsynchronous Resonance Analysis in DFIG based Wind Farms,” in *Proc. of the 7th Energy Conversion Congress and Exposition (ECCE),*, Montreal, QC, Canada, Sept. 2015, pp. 6285–6292.

II. S. Chernet, M. Bongiorno, G.K. Andersen, T. Lund and P.C. Kjaer, ”Online Variation of Wind turbine Controller Parameter for Mitigation of SSR in DFIG based Wind Farms,” in *Proc. of the 8th Annual IEEE Energy Conversion Congress and Exposition, ECCE 2015*, Milwaukee, Wisconsin, USA, Sept. 2016, pp. 1–8.

III. T. Lund, G.K. Andersen, P. Dyrlund, L. Christensen, M. Sogaard, L. Rasmussen, S. Chernet and M. Bongiorno, ”Experimental full scale assessment of SSR behavior of a wind Turbine with Doubly-Fed Induction Generator ,” in *Proc. of the 15th International Workshop on Large-Scale Integration of Wind Power into Power Systems as well as on Transmission Networks for Offshore Wind Power Plants*, Vienna, Austria, Nov. 2016.

IV. S. Chernet and M. Bongiorno, ” Mitigation of SSCI in DFIG based wind farms through modification of Rotor-Side Converter Controller,” in *Proc. of the 3rd Internation Future Energy Electronics conference and ECCE Asia (IFEEC 2017-ECCE Asia)*, Kaohsiung, Taiwan, June. 2017, pp. 603-608.

V. S. Chernet, M. Bongiorno and M. Beza, ” Investigation of Subsynchronous Controller Interaction in DFIG based Wind Farms,” submitted to *Internation Journal of Electrical Power and Energy Systems*

VI. S. Chernet, M. Bongiorno and M. Beza, ” An Adaptive Damping Controller to reduce the risk of Sub-synchronous Controller Interaction in DFIG based Wind Farms,” submitted to *IEEE Transaction Sustainable Energy*

Chapter 2

Subsynchronous Resonance in Power Systems

2.1 Introduction

The first SSR incident was observed in the Mohave generation station, south Nevada, in 1970 [22]. A 750 MVA cross-compound turbine-generator unit experienced shaft damages when a parallel transmission line was switched out due to a ground fault, causing the unit to be radially connected to a series compensated transmission line [23]. Following the first incident in 1970 and a similar occurrence one year later, an IEEE working group was established to investigate the cause of the damage [24]. The Mohave incident was an eye opener to the problem of SSR, but further investigation considering other turbine-generation units gave a reflection on how complex the problem can be [23]. An example is the Navajo project, which consisted of three tandem-compound turbine-generators with a generation capacity of 750 MW and a 2900 km/500 kV transmission line [23] [25]. With the exception of short tie lines, all transmission lines were on series compensation. The initial analysis showed that the Navajo project would have faced a severe SSR problem. After accurate investigation [25], the project continued with the same level of series compensation but with additional countermeasures to reduce the risk of SSR [23].

The likelihood of SSR in renewable generation units, such as large wind farms constituting of variable-speed wind turbines, was not considered up until 2009. In 2009, an incident in southern Texas occurred, where the Zorillo wind farm became radially connected to a series-compensated transmission line due to a fault on a parallel line [26] [10]. This wind farm is mainly based on DFIG wind farm turbines As this wind turbine topology is based on induction generator with power electronic devices, the phenomenon is in general attributed to self-excitation of the system due IGE or control system interaction [27–29].

In this chapter, a general introduction of the problem of SSR in power systems together with the classification of the different types of SSR will be given. The analysis method to asses the risk of SSR will be presented in Section 2.3, with more details to be including in the chapters to follow. In Section 2.4, SSR in classical generator unit is addressed while Section 2.5 will cover

SSR in wind-generation units.

2.2 SSR definition and classification

In accordance with the definition of IEEE, subsynchronous resonance (SSR) is *an electrical power system condition where the electrical network exchanges energy with turbine generator at one or more of the natural frequencies of the combined system below the synchronous frequency of the system following a disturbance from an equilibrium point* [24].

Traditionally, there exist three types of SSR, namely: induction generator effect (IGE), torsional interaction (TI), and torque amplification (TA). Based on the time required for the oscillation to build up, these can be further classified into two groups: steady-state and transient SSR. The steady-state SSR comprises of IGE and TI. Since this kind of SSR typically build up slowly, they might be considered as small signal conditions (at least initially) and can be analyzed using linear model representation. The transient SSR includes TA, which is an SSR that occurs following a large system disturbance, such as system faults. This is therefore a fast phenomenon that can reach dangerous level within a short period of time. This phenomenon, been a large signal disturbance, cannot be analyzed using linear models.

Induction Generator Effect (IGE): IGE is a pure electrical phenomenon caused by self excitation of the electrical system. The subsynchronous current that flows in the armature of the generator creates a magnetic motive force (MMF) that rotates slower than the generator's MMF. This causes the synchronous generator to act as an induction generator in the subsynchronous frequency range. As a result, the resistance of the rotor as viewed from the terminal of the generator, at subsynchronous current, is negative [30] [31]. If the magnitude of the negative rotor resistance of the generator exceeds the sum of the armature and network resistance around the natural frequency of the network, the system presents an overall negative resistance against the subsynchronous current. This results in a self-excitation that leads to a growing subsynchronous current. Being an electrical phenomenon, IGE does not involve the mechanical system of the generator unit.

Torsional Interaction (TI). TI is an electro-mechanical phenomenon that results in an energy exchange between the electrical system and the mechanical shaft of the generator unit. TI occurs when the electrical torque setup by the subsynchronous current component is electrically close to one of the natural frequencies of the generator shaft. When this happens, the rotor starts to oscillate around the rated speed with a frequency equal to the perturbation frequency, f_{per}. Besides its fundamental component, the induced terminal voltage will be constituted by two additional frequency components: a subsynchronous ($f_s - f_{per}$) and a supersynchronous components ($f_s + f_{per}$) [32]. If the generated torque component exceeds the inherent overall damping torque of the system, excitation occurs. During the planning stage for series compensation, the resonance frequency for the system is chosen so that it lies in the subsynchronous frequency range. For a lossless line, this resonance frequency can be calculated as [30]:

$$\omega_n = \sqrt{\frac{1}{LC}} = \omega_B \sqrt{\frac{X_C}{X_L}} \tag{2.1}$$

where ω_B is the base frequency in rad/sec that is equivalent to ($\omega_B = 2\pi f_s$) while X_C and X_L are the equivalent per-unit (pu) inductive and capacitive reactance, respectively. On the other hand, the natural frequencies (normally refereed to as oscillation modes) of the mechanical system always lies in the subsynchronous range. For an SSR to occur, the natural frequency of the generator shaft system must coincide with or be in the vicinity of, the complementary frequency of the electrical system resonance and at the same time the total damping of the system around this frequency is zero or negative. Meaning; if there exist a condition where the mechanical and electrical resonances coincide and the total damping of the system at that frequency is zero or negative, sustained or, in the worst case, growing oscillations will be experienced in the system. TI manifests itself in generator units where the inertia of the turbine is in the same order of magnitude or larger than the inertia of the generator (rotor), for example in thermal power plants or nuclear power plants [33]. However, in a hydro generator station, where the inertia of the generator is much higher than the turbine inertia, any oscillation triggered in the turbine unit will not be reflected on to the rotor, thereby decoupling the mechanical and the electrical system.

Torque Amplification (TA). Torque amplification, also known as transient torque, is a phenomenon that occurs following a system disturbance. Following a disturbance, a high current level that tends to oscillate at the system's natural frequency flows in the network. In a series compensated system, this current charges up the capacitor, which in turn discharges through the network into the generator creating a system that resonates. The resulting high torque due to this current is reflected on the mechanical system. If the complement of this resonance frequency is close to one or more natural torsional frequencies of the mechanical system, it will lead to growing oscillation. Unlike IGE and TI, the growing rate of TA is high and oscillating shaft torque can reach damaging level within a small amount of time [23]. In addition, as the non-linearity of the system comes into play, analysis using conventional linearized model will not be feasible. As a result, analysis for TA must be performed using time-domain simulation program like PSCAD where the system non-linearity is well represented.

2.3 SSR analysis and investigation methods

Through the years, different analytical tools have been developed to identify and analyze the risk for SSR. The most commonly used are the frequency scanning method (FSM), eigenvalue analysis and time-domain simulation. Eigenvalue analysis and FSM are only applicable for assessing the risk for steady-state SSR. On the other hand, time-domain simulation are typically used for assessing the risk for TA.

2.3.1 Frequency-domain methods

Frequency Scanning Method

FSM is a technique widely used to preliminary asses the risk of SSR in a system [30]. The principle is to compute the frequency-dependent equivalent resistance and reactance of the ma-

chine and the network, as seen from the neutral of the generator. If there exists an occurrence where the inductance approaches zero and the resistance is negative for the same frequency, a risk for IGE exists. The advantage with this method is that it gives a quick check for the risk of instability due to SSR [33]. FSM is also a powerful tool to asses the risk of TI [30]. If there exists a series resonance or a reactance minimum close to one or more of the shaft's natural frequencies, it is an indication that there might be a risk for TI; this needs to be verified with other analytical approaches. Damping torque analysis, which is an analytical method involving the computation of the damping torque versus frequency presented by the electrical system (i.e. generator and network) and the mechanical system, is another approach used to analyze TI (see Section 2.4).

Input admittance approach

Various investigation have employed the concept of input admittance to evaluate the stability of a system and the possible interaction that may exist, as in [21] [34–36] to mention a few. Although, the mentioned works differ a bit in their analysis approach, they all share a core theory relating to the behavior of the system for a range of frequencies.

The passivity approach for instance takes into consideration the individual system behavior in the frequency domain to evaluate the stability of the overall system. It is stated in [37] that a single input single output (SISO) system represented as a closed-loop system *F(s)*, expressed in terms of a forward transfer function *G(s)* and a feedback transfer function *H(s)* (see Fig. 2.1), is passive and thereby stable if $G(s)$ and $H(s)$ are both passive and satisfy

- *G(s)* and *H(s)* are stable.
- $\mathrm{Re}\left[G\left(j\omega\right)\right] \geq 0$ and $\mathrm{Re}\left[H\left(j\omega\right)\right] \geq 0, \forall\omega \geq 0$

It should be noted that $F(s)$ is stable does not necessarily imply that the subsystems $H(s)$ and $G(s)$ are passive and stable. Another approach for evaluation of system stability using input admittance is by employing the impedance or admittance transfer function in the same manner as above but instead applying the Nyquist criterion on the open-loop transfer function [21]. These methods are mainly based on the Nyquist criterion. For multiple input multiple output (MIMO), the investigation differs as the classical Nyquist criterion has to be modified. In such systems, the generalized Nyquist criterion (GNC) can be used to evaluate the system stability. This approach is further discussed in detail in Chapter 5.

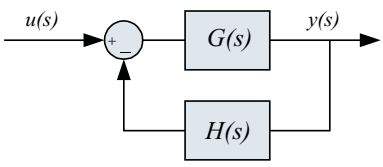

Fig. 2.1 Block diagram of a SISO system with feedback

2.3.2 Eigenvalue analysis

Eigenvalue analysis requires the entire system to be defined in terms of linear differential equation. Based on the equations, the state-space form is obtained for the entire system as:

$$\dot{x} = \mathbf{A}x + \mathbf{B}u \tag{2.2}$$

The eigenvalues can be obtained as a solution of the matrix equation

$$\det\left[\lambda\mathbf{I} - \mathbf{A}\right] = 0 \tag{2.3}$$

Eigenvalue analysis has an advantage over FSM as it provides information about the oscillatory frequencies as well as the corresponding system damping. The downside with eigenvalue analysis is that it can be bulky, especially for large system, as a single state-space model of the entire system is needed to perform the analysis. Furthermore, the state-space model needs to be recalculated for any system modification.

2.3.3 Time-domain simulations

The use of time-domain simulations through dedicated programs (such as SIMULINK, DigSilent or PSCAD, to name a few) becomes necessary in case of SSR investigation in large systems or when small-signal analysis cannot be applied. For the latter, a typical example is the investigation of resonant conditions due to TA. Time-domain simulations allow to implement every component of the system (both active and passive components) with a very high-degree of accuracy. However, this kind of analysis approach is not the most suitable alternative for understanding the root causes of a phenomenon. In this thesis, time-domain simulations are mainly used for verification of the theoretical investigation.

2.4 SSR in classical generation units

In 1970, the Mohave station located in southern Texas, experienced shaft damage when the station became radially connected to a transmission line on series compensation. A similar incident occurred in 1971, which lead to the manual shut down of the station. Fig. 2.2, shows the power system of the station at the time of the incident. Due to a fault, the 500 kV transmission line, connecting Eldorado station to Mohave station, was switched out by opening the circuit breaker at Eldorado substation (shown in Fig. 2.2). This caused the Mohave station to be radially connected to the Lugo bus through a transmission line that was on series compensation. The phenomenon observed included excessive field current, alarm for high vibration, field ground and negative-sequence currents as well as flickering lights in the control room, which continued for two minutes. Post-incident investigations showed that the shaft section in the high pressure turbine experienced extreme heating as a result of cyclic torsional stress [23]. After thorough investigation, it was understood that the incident in Mohave was due to exchange of energy between the mechanical system of the turbine generator and the series capacitor of the transmission line (what we refer today as TI) [23].

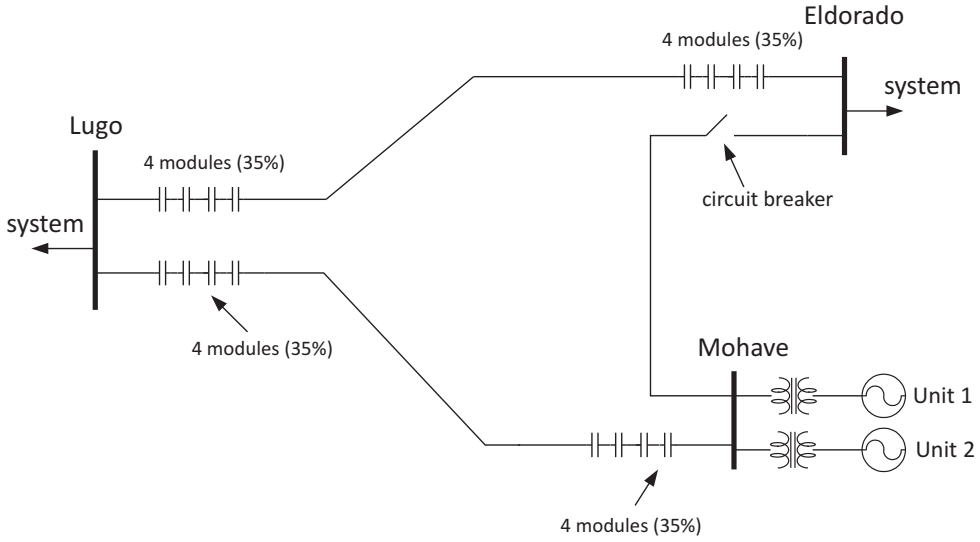

Fig. 2.2 Single-line diagram of the power system around Mohave station.

Following the two incidents that occurred in Mohave, an IEEE working group for subsynchronous resonance has developed the IEEE First Benchmark Model (IEEE FBM) and the IEEE Second Benchmark Model (IEEE SBM) for use in computer program simulation as a base for investigating the risk of SSR. The IEEE FBM system consists of a synchronous generator connected to an infinite bus through a series-compensated transmission line. Figure 2.3 shows the layout of the IEEE FBM, while the detailed modeling and parameters can be found in the Appendix A.

Let us consider a steam turbine generator system with a number of pressure stages as shown in Fig. 2.4. The parameters for the turbine model can be found in the Appendix A. The mechanical system presents five modes with characteristics frequencies 15.71 Hz, 20.205 Hz, 25.547 Hz, 32.28 Hz, and 47.456 Hz. When a mode is excited, the generator rotor will oscillate with a frequency (f_m), which is reflected on the generator voltage having both subsynchronous component ($f_s - f_m$) and supersynchronous component ($f_s + f_m$), where f_s is the system frequency (see Fig. 2.5). The electrical torque in the *dq* frame can be written as [1]

[1] a power-invariant dq transformation is considered.

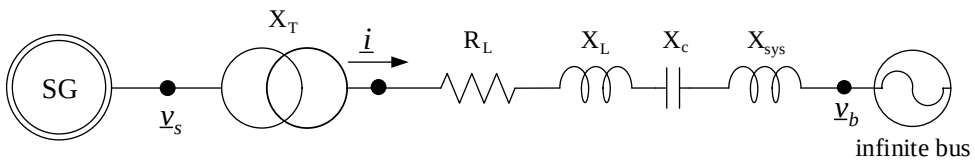

Fig. 2.3 Single-line diagram of a synchronous generator connected to an infinite bus through a series compensated transmission line.

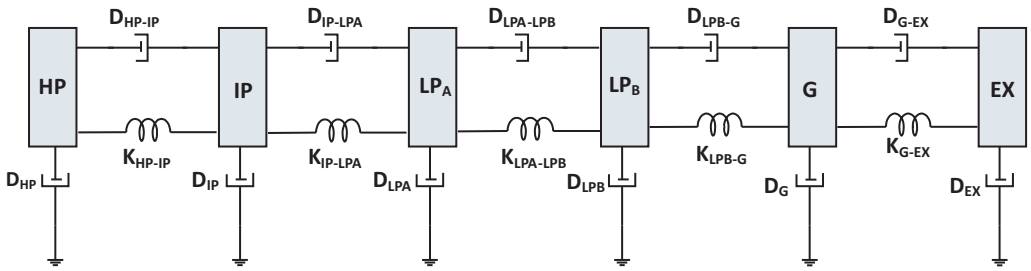

Fig. 2.4 six mass mechanical system representation of a turbine generation unit.

$$T_e = \mathrm{Im}\left[\underline{i}_{dq}\left(\underline{\psi}_{dq}\right)^*\right] = i_q\psi_d - i_d\psi_q \tag{2.4}$$

where $\underline{i}_{dq}$ is the armature current and $\underline{\psi}_{dq}$ is the stator flux. For small variation around an operating point, the linearized equation are

$$\Delta T_e = i_{q0}\Delta\psi_d + \psi_{d0}\Delta i_q - i_{d0}\Delta\psi_q - \psi_{q0}\Delta i_d \tag{2.5}$$

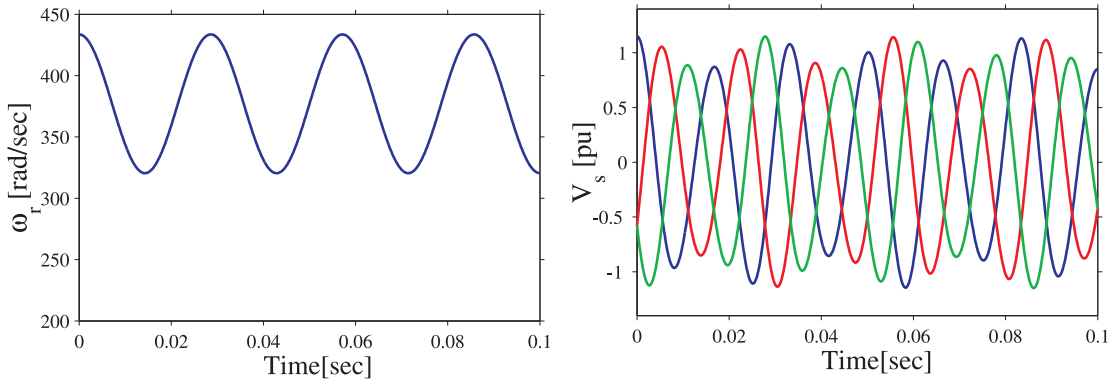

Fig. 2.5 Oscillation on rotor speed (ω_r) (*left plot*). Terminal voltage due to oscillation on rotor speed (*right plot*)

Let us consider the transfer function from $\Delta\omega_r$ to ΔT_e as shown in Fig.2.6

$$G_e(s) = \frac{\Delta T_e}{\Delta\omega_r}(s) \tag{2.6}$$

To get the frequency response of the system, the Laplace variable s in (2.6) is replaced with $j\omega$ where ω is the frequency of interest. The frequency response can be split into its real and imaginary part as

$$G_e(j\omega) = \mathrm{Re}\left[G_e(j\omega)\right] + j\mathrm{Im}\left[G_e(j\omega)\right] = \Delta T_{De}(j\omega) - \frac{\omega_B}{\omega}\Delta T_{Se}(j\omega) \tag{2.7}$$

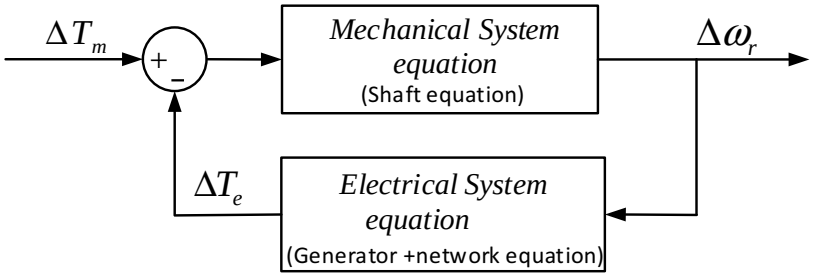

Fig. 2.6 Block diagram showing the interaction between mechanical and electrical system.

where ΔT_{De} and ΔT_{Se} are referred to as electrical damping torque and synchronizing torque respectively [33]. The same definition holds for the mechanical damping torque (ΔT_{Dm}) and synchronizing torque (ΔT_{Sm}). The inherent damping torque of the electrical system under consideration, which includes the generator and the series compensated transmission line, can thus be obtained by taking the real part of the transfer function from rotor speed ($\Delta\omega_G$) to electrical torque (ΔT_e) as

$$T_{De}\left(j\omega_m\right) = \mathrm{Re}\left[\frac{\Delta T_e}{\Delta\omega_r}\left(j\omega_m\right)\right] \tag{2.8}$$

As an example, the electrical damping torque for the IEEE FBM according to (2.8) is depicted in right plot of Fig. 2.7. Similarly the mechanical damping of the system is depicted in the left plot of the same figure. Observing the left and the right plot of Fig. 2.7, the total damping torque calculated based on (2.9) is negative for the second mode (20.205 Hz), which indicates a high risk of TI.

$$\Delta T_D\left(j\omega_m\right) = \Delta T_{De}\left(j\omega_m\right) + \Delta T_{Dm}\left(j\omega_m\right) \leq 0 \tag{2.9}$$

For investigation of SSR due to IGE, it is necessary to evaluate the subsynchronous rotating flux established by the subsynchronous current; in this case the synchronous generator inherits the behavior of an induction generator with a slip described by:

$$s_{ssr} = \frac{f_{sub} - f_r}{f_{sub}} \tag{2.10}$$

where f_{sub} is the frequency of the subsynchronous flux and f_r is the frequency of the rotor flux. Accordingly, the equivalent rotor resistance can be described as:

$$R_{eq}^{sub} = \frac{R_r}{s_{ssr}} \tag{2.11}$$

As the speed of the subsynchronous component of the stator flux is less than the rotor flux vector, which rotates at synchronous speed, the slip (and thus the equivalent resistance, R_{eq}^{sub})

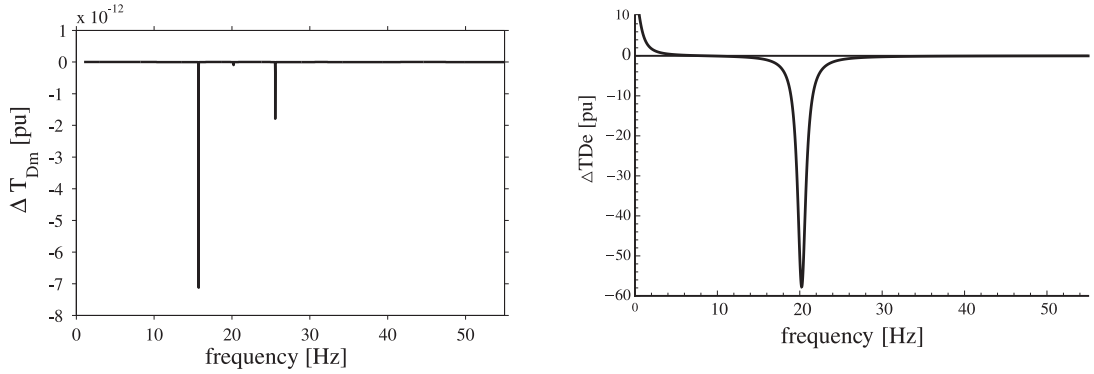

Fig. 2.7 Mechanical damping torque (*left plot*) and Electrical damping torque for 38% series compensation(*right plot*).

becomes negative. To asses the risk of IGE, the impedance of the synchronous generator for subsynchronous frequencies is plotted in Fig. 2.8. As it can be observed from the plot, due to the fictitious slip resulting from the presence of the subsynchronous current, the synchronous generator behaves like an induction generator with a negative rotor resistance. Therefore, the impedance of the synchronous generator for the entire subsynchronous frequency range becomes negative. The problem of IGE prevails if and only if the total resistance of the system, as viewed from the rotor, becomes negative. That is, if the sum of the generator's resistance and network resistance is negative. IGE can occur in all types of generator units, including hydro generator units. However, if we observe Fig. 2.8, the negative resistance of the synchronous generator can possibly exceed the resistance of the network for frequency range close to the system synchronous frequency.

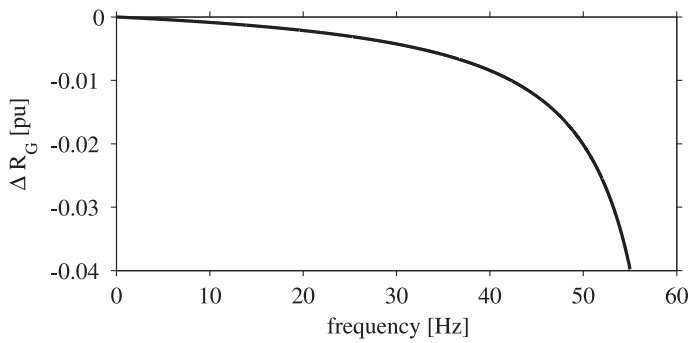

Fig. 2.8 Synchronous generator resistance for subsynchronus frequency range.

For the system resonance to occur within this range, the level of series compensation should be over 80% compensation. This level of compensation is in reality impractical due to thermal issues [23]. As a result, it can be concluded that IGE is not typically encountered in actual system involving synchronous generators.

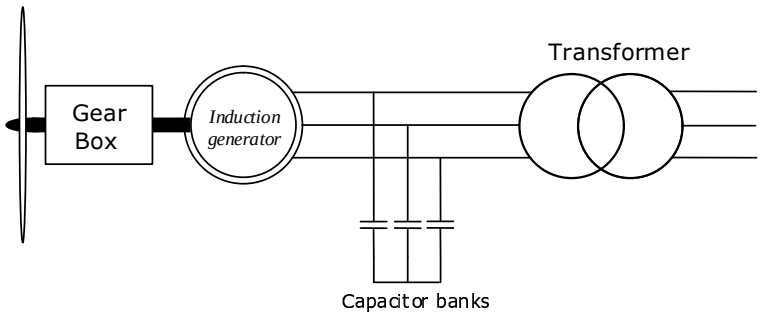

Fig. 2.9 Single-line diagram of a fixed-speed wind turbine.

2.5 SSR in wind generator units

Renewable generator unit is a term given to an energy generation unit where the sources of energy are available abundantly in addition to being re-usable, such as: wind, hydro, tidal and solar energy. To minimize the impact of our energy demand on the environment, actual trends are favoring this kind of energy sources. But the shift is facing various challenges. One of the challenges is to transport the energy produced from the generation sites to the load centers.

The focus of renewable energy source in this thesis is wind. Wind turbines can be typically divided in three types. These are the fixed-speed induction generator (FSIG) wind turbine, the doubly-fed induction generator (DFIG) wind turbine and the full-power converter (FPC) wind turbine. In the sections to follow, the different types of wind turbine together with the associated risk for SSR will be discussed

2.5.1 SSR in fixed speed wind turbines

A FSIG wind turbine mainly consists of a squirrel cage induction generator (SCIG) that is directly connected to the grid through a transformer, as depicted in Fig. 2.9. A SCIG consists of two windings, a stator winding and a rotor winding. The stator winding provides excitation and at the same time carries the generated armature current. The rotor in a SCIG is short circuited and serves the purpose of carrying the induced current. A SCIG presents several advantages over other types of wind turbines, such as robustness, mechanical simplicity and relatively low price [38]. The major downside with this sort of machine, being inductive in nature, is that it requires reactive magnetizing current [39]. As a result, to improve the power factor of the generated power at the connection point, a shunt-connected capacitor bank is added to the system.

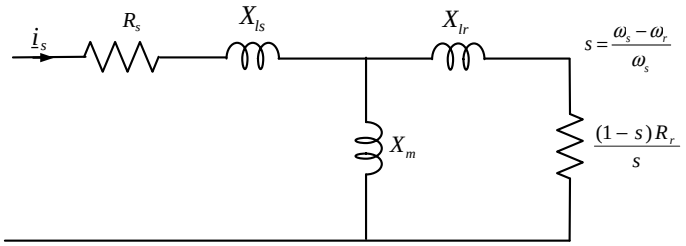

Fig. 2.10 Equivalent circuit of induction machine.

If we observe the equivalent circuit diagram of an induction machine, shown in Fig. 2.10, the rotor resistance is negative when the induction machine is operated as a generator. This is due to the negative slip, as already discussed in the previous section. Expressing the equations governing the IG in the rotating *dq* frame, the stator and rotor voltages in pu are expressed as:

$$\begin{aligned} \underline{v}_s &= R_s \underline{i}_s + j\frac{\omega_s}{\omega_B}\underline{\psi}_s + \frac{1}{\omega_B}\frac{d\underline{\psi}_s}{dt} \\ \underline{v}_r &= R_r \underline{i}_r + j\frac{\omega_2}{\omega_B}\underline{\psi}_r + \frac{1}{\omega_B}\frac{d\underline{\psi}_r}{dt} \end{aligned} \tag{2.12}$$

where R_s and R_r represent the pu stator and rotor resistances, respectively. The term ω_2 is the slip angular frequency, which is equivalent to $\omega_s - \omega_r$ with ω_r representing the rotor angular frequency. The term ω_B is the base angular frequency, which is equivalent to the synchronous angular frequency here expressed as ω_s. $\underline{\psi}_s$ and $\underline{\psi}_r$ are the stator and rotor fluxes, respectively, which are further expressed as:

$$\begin{aligned} \underline{\psi}_s &= \frac{X_{ls}}{\omega_B}\underline{i}_s + \frac{X_m}{\omega_B}\left(\underline{i}_s + \underline{i}_r\right) = \frac{X_{ss}}{\omega_B}\underline{i}_s + \frac{X_m}{\omega_B}\underline{i}_r \\ \underline{\psi}_r &= \frac{X_{lr}}{\omega_B}\underline{i}_r + \frac{X_m}{\omega_B}\left(\underline{i}_s + \underline{i}_r\right) = \frac{X_{rr}}{\omega_B}\underline{i}_r + \frac{X_m}{\omega_B}\underline{i}_s \end{aligned} \tag{2.13}$$

where the different terms in the equation above have the meaning as in Fig.2.10. Breaking (2.12) into components and replacing the currents with the flux expressions in (2.13), the state-space model of the system can be derived as

$$\begin{aligned} \dot{x_G} &= \mathbf{A}_G x_G + \mathbf{B}_G \mathbf{V}_s \\ \boldsymbol{y}_G &= \mathbf{C}_G x_G \end{aligned} \tag{2.14}$$

where

$$\begin{aligned} \mathbf{V}_s &= \begin{bmatrix} v_{sd} \\ v_{sq} \end{bmatrix}, \quad \boldsymbol{y}_G = \begin{bmatrix} i_{sd} \\ i_{sq} \end{bmatrix} \\ x_G &= \begin{bmatrix} \psi_{sd} & \psi_{sq} & \psi_{rd} & \psi_{rq} \end{bmatrix}^T \end{aligned} \tag{2.15}$$

$$\mathbf{A}_G = \begin{bmatrix} \frac{-R_s X_{rr}\omega_B}{D} & \omega_s & \frac{R_s X_m \omega_B}{D} & 0 \\ \omega_s & \frac{-R_s X_{rr}\omega_B}{D} & 0 & \frac{R_s X_m \omega_B}{D} \\ \frac{R_r X_m \omega_B}{D} & 0 & \frac{-R_r X_{ss}\omega_B}{D} & s\omega_s \\ 0 & \frac{R_r X_m \omega_B}{D} & -s\omega_s & \frac{-R_r X_{ss}\omega_B}{D} \end{bmatrix}$$

$$D = \frac{X_{ss}X_{rr} - X_m^2}{\omega_B}$$

$$\mathbf{B}_G = \begin{bmatrix} \omega_B & 0 \\ 0 & \omega_B \\ 0 & 0 \\ 0 & 0 \end{bmatrix}, \quad \mathbf{C}_G = \begin{bmatrix} \frac{X_{rr}}{D} & 0 & \frac{-X_m}{D} & 0 \\ 0 & \frac{X_{rr}}{D} & 0 & \frac{-X_m}{D} \end{bmatrix}$$

Taking the stator voltage as input and stator current as output, the admittance matrix in the *dq* frame can be expressed as

$$\begin{bmatrix} i_{sd}(s) \\ i_{sq}(s) \end{bmatrix} = \begin{bmatrix} Y_{Gdd}(s) & Y_{Gdq}(s) \\ Y_{Gqd}(s) & Y_{Gqq}(s) \end{bmatrix} \begin{bmatrix} v_{sd}(s) \\ v_{sq}(s) \end{bmatrix} \tag{2.16}$$

Note that in a SCIG, the rotor is short circuited, therefore the rotor voltage (v_r) is equal to zero. The admittance matrix being symmetric, the phase admittance can be extracted from the *dq* admittance matrix as [40]:

$$Y_G(s) = Y_{Gdd}(s) + jY_{Gqd}(s) \tag{2.17}$$

The phase impedance for the generator is obtained from the phase admittance as

$$Z_G(s) = \frac{1}{Y_G(s)} = \frac{1}{Y_{Gdd}(s) + jY_{Gqd}(s)} \tag{2.18}$$

Replacing the Laplace variable *s* with $j\omega$ for steady-state representation, the real and imaginary part of $Z_G(j\omega)$ as a function of frequency can be plotted as shown in Fig. 2.11. Parameters used can be found in Appendix A, Table. A.5. The real part of the impedance is negative for the entire subsynchronus range while the imaginary part of the generator impedance is mainly positive, due to the inductive nature of both the stator and rotor circuits. The fact that the resistance is negative in the subsynchronous range only indicates a potential risk for IGE. For IGE to exist, the total resistance of the generator in combination with the network resistance should become zero or negative. Comparing Fig. 2.11 with Fig. 2.8, it can be observed that the induction generator presents a tenth of order higher negative resistance as compared with the synchronous generator. This increases the probability of the grid impedance begin lower than the generators impedance over a wide frequency range, which indirectly increases the risk of IGE.

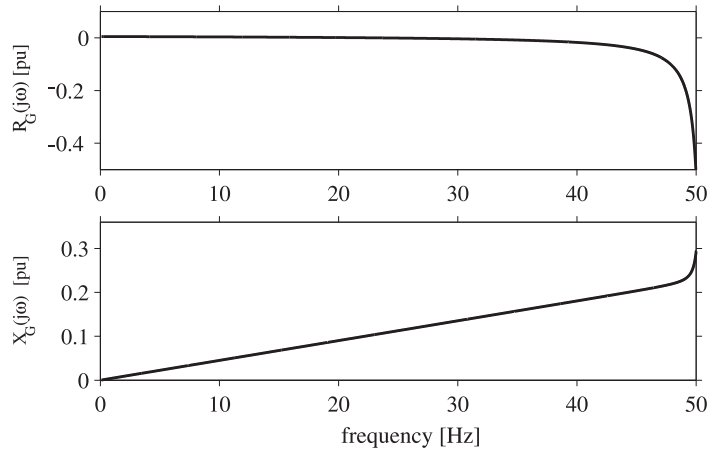

Fig. 2.11 Impedance of an induction generator in the synchronous frequency range.

To evaluate the total resistance of an induction generator in series with a series-compensated transmission line, the transmission line model should be included. For this a rotating reference frame that is aligned to the infinite bus angle is considered (see Fig. 2.3), here represented with the capital letters *DQ*. The terminal voltage $\underline{v}_s$ and $\underline{v}_c$ in the *DQ* frame are expressed as

$$\begin{aligned} \underline{v}_s^{(DQ)} &= (R_L + jX_L)\,\underline{i}_s^{(DQ)} + \tfrac{X_L}{\omega_B}\tfrac{d\underline{i}_s^{(DQ)}}{dt} + \underline{v}_c^{(DQ)} + \underline{v}_b^{(DQ)} \\ \tfrac{d\underline{v}_c^{(DQ)}}{dt} &= -j\omega_s\underline{v}_c^{(DQ)} + \omega_B X_C \underline{i}_s^{(DQ)} \end{aligned} \tag{2.19}$$

Thus, the state-space model for the network can be expressed as

$$\frac{d}{dt}\begin{bmatrix} \mathrm{v}_{c,D} \\ \mathrm{v}_{c,Q} \end{bmatrix} = \mathbf{A}_\mathrm{N}\begin{bmatrix} \mathrm{v}_{c,D} \\ \mathrm{v}_{c,Q} \end{bmatrix} + \mathbf{B}_\mathrm{N}\begin{bmatrix} i_D \\ i_Q \end{bmatrix} \tag{2.20}$$

with

$$\mathbf{A}_\mathrm{N} = \begin{bmatrix} 0 & \omega_s \\ -\omega_s & 0 \end{bmatrix}, \quad \mathbf{B}_\mathrm{N} = \begin{bmatrix} \omega_\mathrm{B}\mathrm{X}_C & 0 \\ 0 & \omega_\mathrm{B}\mathrm{X}_C \end{bmatrix}$$
$$C_N = \begin{bmatrix} 1 & 0 \\ 0 & 1 \end{bmatrix}$$

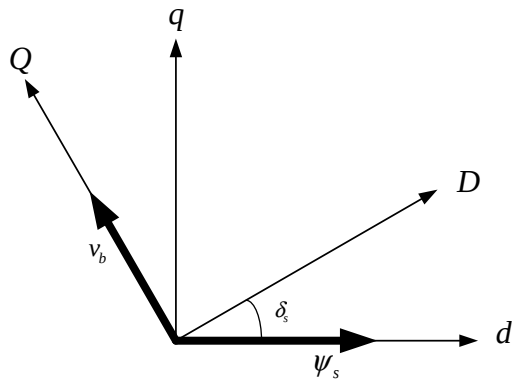

Fig. 2.12 Relation between *dq* and *DQ* frame.

Expressing the terminal voltage ($\underline{v}_s$) in generator *dq*-reference frame

$$\underline{v}_s^{(dq)} = (\mathrm{R_L} + \mathrm{jX_L})\,\underline{i}_s^{(dq)} + \frac{\mathrm{X_L}}{\omega_\mathrm{B}}\frac{\mathrm{d}\underline{i}_s^{(dq)}}{\mathrm{dt}} + \mathrm{e}^{j\delta_s}\left(\underline{v}_C^{(\mathrm{DQ})} + \underline{e}_b^{(\mathrm{DQ})}\right) \tag{2.21}$$

where δ_s is the transformation angle between the two reference frames, as described in Fig.2.12. Since the terms in C_G are all constant and $\begin{bmatrix} i_{sd} \\ i_{sq} \end{bmatrix} = C_G x_G$, the derivative of the current that appears in (2.21) can be expressed as

$$\frac{\mathrm{d}}{\mathrm{dt}}\begin{bmatrix} i_{sd} \\ i_{sq} \end{bmatrix} = \mathbf{C}_G \dot{x}_G \tag{2.22}$$

Substituting (2.22) into (2.21) followed by mathematical manipulation to express the equation in terms of matrices, the terminal voltage can be expressed as

$$\mathbf{V}_s = [\mathbf{F}]_G\,[\mathbf{G}]_\mathrm{G}\,x_\mathrm{G} + [\mathbf{F}]_G\,[\mathbf{P}]_G\left\{\mathbf{Y}_\mathrm{N} + \begin{bmatrix} 0 \\ \mathrm{V}_b \end{bmatrix}\right\} \tag{2.23}$$

with

$$\begin{aligned} [\mathbf{F}]_\mathrm{G} &= \left[\mathbf{I}_2 - \frac{\mathrm{X_L}}{\omega_\mathrm{B}}\,[\mathbf{C}_\mathrm{G}]\,[\mathbf{B}_\mathrm{G}]\right]^{-1} \\ [\mathbf{G}]_\mathrm{G} &= [\mathbf{Z}_\mathrm{L}]\,[\mathbf{C}_G] + \frac{\mathrm{X_L}}{\omega_\mathrm{B}}\,[\mathbf{C}_G]\,[\mathbf{A}_G] \\ \mathbf{V}_s &= \begin{bmatrix} v_{s,d} \\ v_{s,q} \end{bmatrix} \end{aligned} \tag{2.24}$$

where $\mathbf{I}_2$, $[\mathbf{Z}_\mathrm{L}]$ and $[\mathbf{Y}_\mathrm{N}]$ are

$$[\mathbf{Z}_\mathrm{L}] = \begin{bmatrix} \mathrm{R_L} & -\omega_s \mathrm{X_L} \\ \omega_s \mathrm{X_L} & \mathrm{R_L} \end{bmatrix}, \mathbf{I}_2 = \begin{bmatrix} 1 & 0 \\ 0 & 1 \end{bmatrix}$$
$$[\mathbf{Y}_\mathrm{N}] = \begin{bmatrix} \mathrm{v}_{c,D} \\ \mathrm{v}_{c,Q} \end{bmatrix} = [\mathbf{C}_\mathrm{N}]\begin{bmatrix} \mathrm{v}_{c,D} \\ \mathrm{v}_{c,Q} \end{bmatrix}$$

Matrix $[\mathbf{P}]_G$ accounts for the transformation matrix between the network reference frame and the generator reference frame and is expressed as

$$[\mathbf{P}]_{\mathrm{G}} = \begin{bmatrix} \cos\delta_s & -\sin\delta_s \\ \sin\delta_s & \cos\delta_s \end{bmatrix}, \tag{2.25}$$

Now taking the terminal voltage expression in (2.23) and substituting it in the generator state-space model in (2.14) together with the network equation in (2.20), the combined state-space for the generator and the transmission line can be expressed as [31]:

$$\dot{X}_G^{'} = \mathbf{A}_{\mathrm{G}}^{'} X_G^{'} + \mathbf{B}_G^{'} \mathrm{E}_b \tag{2.26}$$

where

$$\begin{aligned} \mathbf{A}_G^{'} &= \begin{bmatrix} \mathbf{A}_G + \mathbf{B}_G [\mathbf{F}]_G [\mathbf{G}] & \mathbf{B}_G [\mathbf{F}]_G [\mathbf{P}]_G [\mathbf{C}_N] \\ \mathbf{B}_N [\mathbf{P}]_G^{\mathrm{T}} \mathbf{C}_G & \mathbf{A}_N \end{bmatrix} \\ \mathbf{B}_G^{'} &= \mathbf{B}_G [\mathbf{F}]_G [\mathbf{P}]_G \begin{bmatrix} 0 \\ 1 \end{bmatrix} \end{aligned} \tag{2.27}$$

The new state variables $X_G^{'}$ are

$$X_{\mathrm{G}} = \begin{bmatrix} \psi_{sd} & \psi_{sq} & \psi_{rd} & \psi_{rq} & \mathrm{e}_{c,D} & \mathrm{e}_{c,Q} \end{bmatrix}^{\mathrm{T}} \tag{2.28}$$

The induction generator's rotor speed (ω_r) expressed in terms of the slip is considered as input during linearization. Extracting the phase impedance from (2.16) to (2.18), the total impedance for the generator in series with the transmission line can be obtained. Fig. 2.13 shows the total impedance of a radial connection between an induction generator and a transmission line with 35% series compensation. From the figure, we can observe that the total resistance of the system is negative at the resonance frequency, which is a clear indication of the risk for IGE. To summarize, fixed speed induction generator present a risk for IGE at a realistic level of compensation. This is attributed to the negative resistance that the generator presents towards the transmission network.

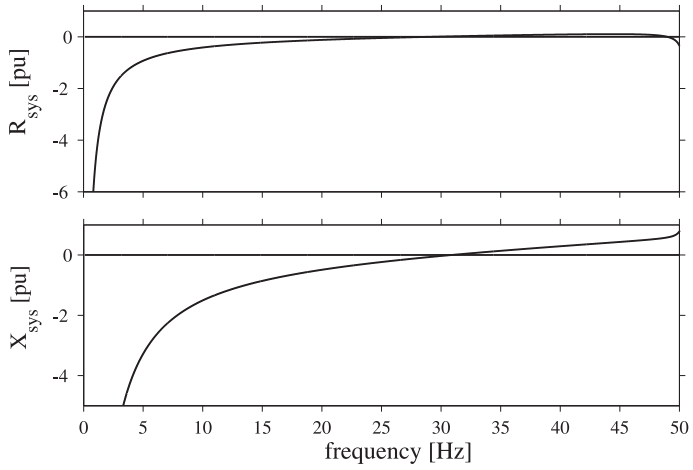

Fig. 2.13 Impedance of Induction generator radially connected to a series compensated network. Resistance in pu (*upper plot*), Reactance in pu (*lower plot*), $X_C = 0.35pu$

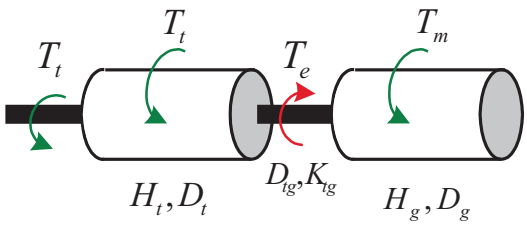

Fig. 2.14 Two mass representation for the mechanical system of an induction generation unit.

To evaluate the risk of torsional interaction, the electrical damping torque for the electrical system and the mechanical damping torque of the mechanical system is compared. The drive train for the fixed-speed wind turbine is modeled using the two-mass system shown in Fig. 2.14. The set of equation that define the dynamics of the mechanical drive train is expressed as:

$$\begin{aligned}
\frac{1}{\omega_B}\frac{d\delta_t}{dt} &= \omega_t \\
2H_t\frac{d\omega_t}{dt} &= T_m - D_t\omega_t - D_{tg}\left(\omega_t - \omega_g\right) - K_{tg}\left(\delta_t - \delta_g\right) \\
\frac{1}{\omega_B}\frac{d\delta_g}{dt} &= \omega_g \\
2H_g\frac{d\omega_g}{dt} &= T_e - D_g\omega_g - D_{tg}\left(\omega_g - \omega_t\right) - K_{tg}\left(\delta_g - \delta_t\right)
\end{aligned} \tag{2.29}$$

The mechanical damping torque is then calculated using the transfer function from the rotor speed to mechanical torque as:

$$T_{Dm}(s) = \mathrm{Re}\left[\frac{\Delta T_m}{\Delta\omega_g}(s)\right] \tag{2.30}$$

Plotting the electrical damping torque against the mechanical damping torque as in Fig. 2.15 shows that the mechanical mode for a wind turbine occurs at a very low frequency, i.e. in the range 2-9 Hz. It is also known that when the various rotating components, like the gear box and the blades for instance, are lumped into a two-mass model, our view is limited when it comes to the different mechanical modes that might exists. In [41], where a five-mass model for the drive train is considered, the dominant frequency appeared at 2.5 Hz, i.e. still occurs at very low frequencies. As a result, for an interaction between the mechanical and electrical system to occur, the negative electrical damping torque needs to occur at the complementary frequency of $f_o - f_m$, i.e. comes close to the synchronous frequency. The network resonance frequency occurs very close to the synchronous frequency if the level of series compensation is very high (about 90% compensation), which is not realistic in actual installation. In conclusion, the likelihood of SSR due to TI in wind farm is very low and as a result will not be further discussed in this work.

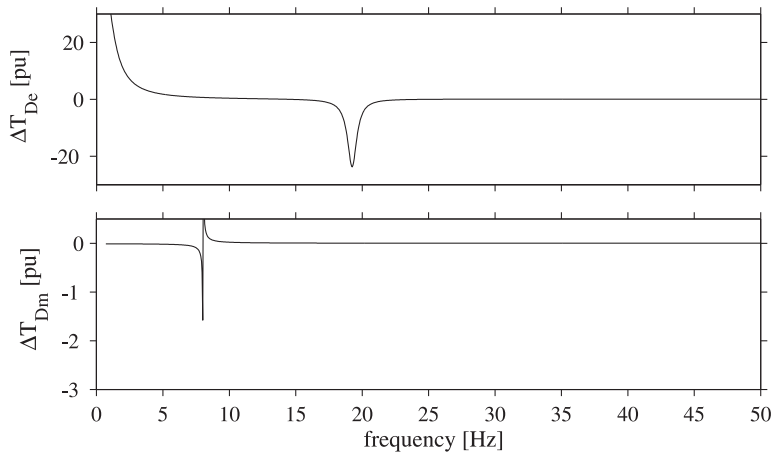

Fig. 2.15 Electrical damping torque (*upper plot*) and mechanical damping torque (*lower plot*) for induction generator connected to IEEE FBM network, $X_c = 0.35pu$

2.5.2 SSR in doubly-fed induction generator (DFIG) wind turbines

Attention concerning SSR in variable-speed wind turbines came into focus following the incident in south Texas in 2009. Figure 2.16, shows the single-line diagram of the transmission network topology around the Zorillo Gulf wind farm in south Texas. Two wind farms with installed capacity of 93.6 MW and 96 MW, respectively, were connected to the Ajo station [10].

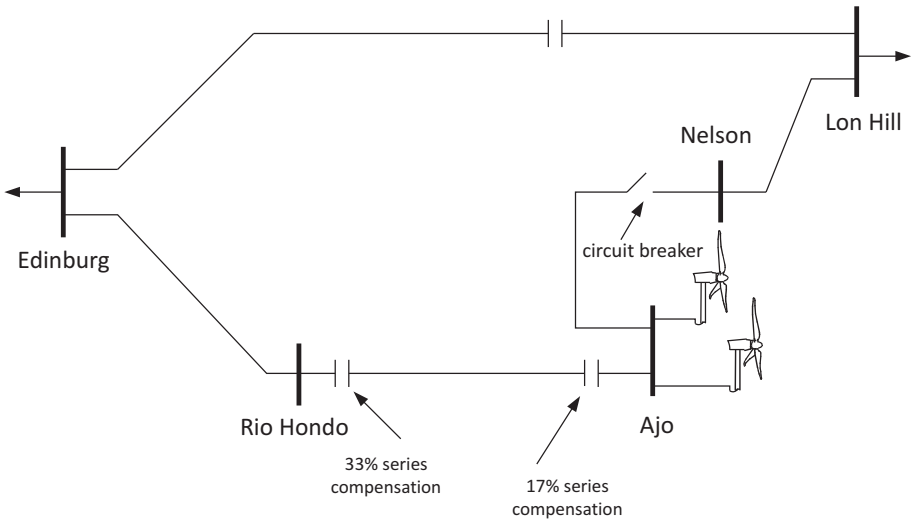

Fig. 2.16 Single-line diagram of the power system around Zorillo Gulf wind farm

The 345 kV transmission from Ajo to Rio Hondo has two stages of series compensation (17% and 33%) located at the Rio Hondo station, with both stages typically in service. During the incident, a single-line to ground fault occurred in the transmission line that goes from Nelson to Ajo. To clear the fault, the circuit breaker indicated in the figure was opened, which caused the Zorillo Gulf wind farm to be radially connected to the series-compensated line between Ajo

and Rio Hondo. As a consequence, system voltage oscillation started to build up with a peak voltage reaching up to 2 pu. This caused the shunt reactor at Ajo and the transmission line from Ajo to Rio Hondo to trip. The series capacitors was bypassed in approximately 1.5 sec into the event. Measurements on the series capacitors indicated the presence of subsynchronous current. Within the wind farms, a large number of crowbars were activated [10].

The Zorillo Gulf wind farm was the first recorded incident of SSR in variable speed wind turbine. In 2012, another incident was reported in northern China involving a wind farm connected to series compensated transmission lines [18]. Most of the installed wind turbines were of DFIG type. A typical DFIG wind turbine consists of an induction generator, whose stator is directly connected to the grid while a four quadrant Back-to-Back (BTB) converter connects the rotor to the grid. A three winding transformer connects the stator, the BTB converter and the grid, as shown in Fig 2.17. Typically, the rotor-side converter (RSC) controls the torque and the reactive power of the generator, while the grid side converter (GSC) controls the dc-link voltage and in some cases might be utilized to control the terminal voltage [14] [10] [42] [43].

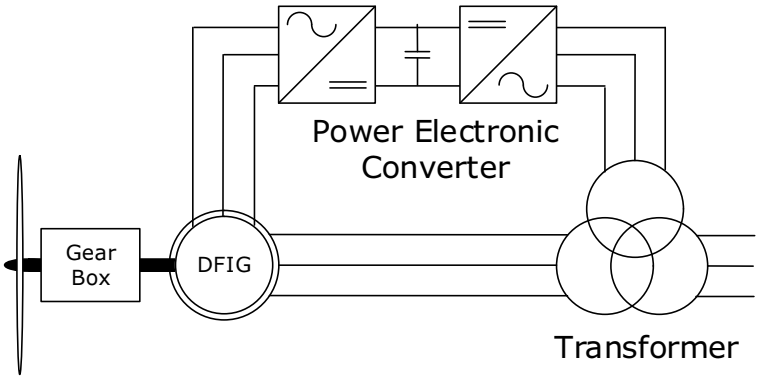

Fig. 2.17 Single-line diagram of a DFIG wind turbine

Following the incident, enormous efforts from the research community and turbine manufacturers has been put forward to explain the phenomenon, while developing different mitigation techniques. The incident has been identified to have been caused by subsynchronous controller interaction (SSCI) [10]. SSCI is a type of interaction that involves energy exchange between the control system of a power electronic device and a series-compensated electrical network [28]. SSCI, like IGE, is a purely electrical phenomenon that does not involve the mechanical system. The focus of this thesis is to analyze the SSCI phenomenon in DFIG based wind farms, hence further details will be presented in the chapters that follow.

2.5.3 SSR in full-power converter wind turbines

Another variable speed wind turbine solution is the full-power converter wind turbine. This wind turbine consists of a multiple-pole synchronous generator in series with a BTB converter as shown in Fig. 2.18. Due to variation in wind speed, the generated voltage at the generator terminal has a variable frequency. The BTB converter, among other function, acts as a frequency converter to adopt the variable frequency voltage to the grid frequency.

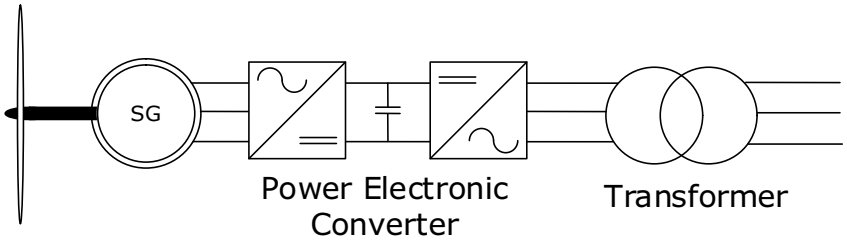

Fig. 2.18 Single-line diagram of a full-power converter wind turbine

The advantage of a full-power converter wind turbine over the DFIG is that the presence of the BTB converter creates a decoupling between the grid and the turbine. As a result, any oscillation that is triggered on the grid does not propagate towards the turbine. Hence SSR due to TI is very unlikely in this types of wind turbines. However, the risk of controller interaction in this type of wind turbines still needs attention.

2.6 Conclusion

In this chapter, an overview of the various types of SSR in power system with fixed series compensation has been covered. Various generator units and the associated types of SSR that can exist have been addressed. An introduction to different types of analysis approaches that can be used for SSR analysis has also been presented. In addition, some of the analysis methods that involve the use of linearized model, presented at the beginning of the chapter, have been employed to investigate SSR in classical generator units (involving synchronous generator based steam turbine) and fixed-speed wind turbines (involving induction generator). In the following chapters, the focus of the work will be on the analysis of the risk of SSCI in DFIG based wind turbines.

Chapter 3

DFIG Wind Turbine Model and Control

3.1 Introduction

The previous chapter has been dedicated to review the principle for SSR both in classical and in wind-based generator units. Different analysis methods used for assessing the risk of SSR have been addressed. As the focus of this thesis is on the investigation of SSCI in DFIG-based wind farms connected to series-compensated transmission lines, a proper model representation of the wind turbine becomes crucial. This chapter focuses on the description and model development of the DFIG wind turbine used in this thesis. The purpose of the different components that build up a DFIG wind turbine is discussed at the beginning of the chapter. This is followed by a description of the control structure, thereby establishing the basis for the electrical dynamic behavior of the DFIG wind turbine. A mathematical derivation to develop a linearized wind turbine model is presented at a later stage of the chapter. Frequency response obtained using the developed linearized model is used to get insight into the electrical behavior of a DFIG wind turbine.

3.2 DFIG wind turbine model

A typical configuration of a DFIG wind turbine is illustrated in Fig.3.1. It consists of a wound rotor induction generator (WRIG) whose stator is directly connected to the grid through a three winding transformer. A back-to-back voltage source converter (VSC) connects its rotor to the grid. In the DFIG model that is considered for this work, the GSC controller controls the dc-link capacitor voltage while the RSC controller controls the point of common coupling (PCC) active and reactive power exchange of the DFIG. It is important to observe that only the slip power is handled by the converters. Therefore, the power rating for these converters are in the range of 15-30% of the turbine's rated power. This means that the losses in the converter and the cost of the converter are reduced in comparison to other topologies where the converter has to handle the total power.

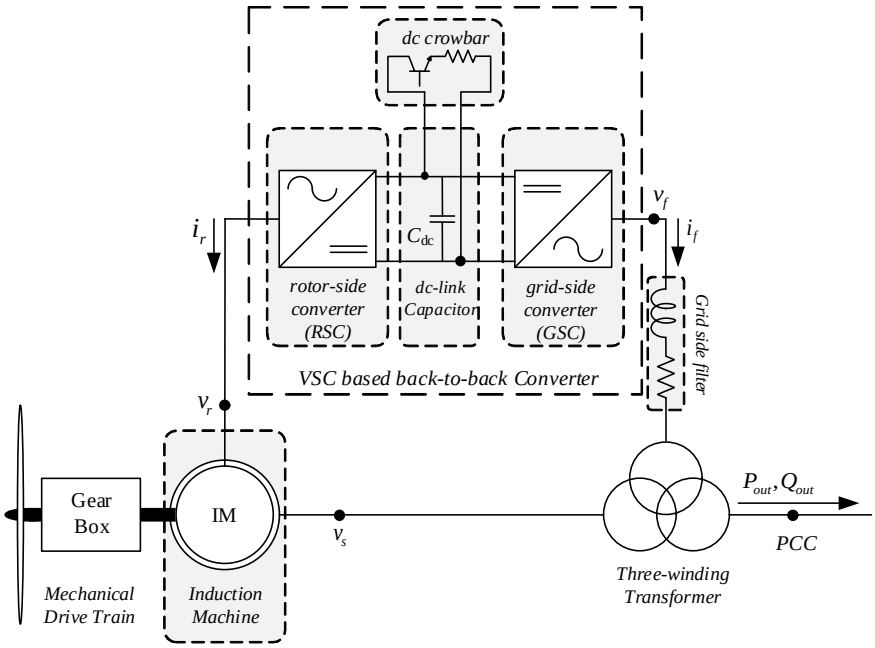

Fig. 3.1 Components of a DFIG turbine unit.

In the subsections to follow, the model description of the induction generator followed by the model description for the dc-link capacitor are presented. In the next section, the model description for the RSC controller and GSC controller are covered. To avoid redundancy, the grid-side filter model description is presented along side the GSC controller.

3.2.1 Induction generator

When modeling analytically an induction machine, a T-representation of the system can be adopted (see Fig.3.2(a)), where R_s and L_{ls} represent the stator winding losses and leakage inductance, respectively, while R_r and L_{lr} are the rotor winding losses and leakage inductance, respectively. The inductance L_m represents the magnetizing inductance of the machine, while the back-EMF of the machine is represented as $j\omega_r \underline{\Psi}_r^{(s)}$ with ω_r representing the rotor angular frequency. Although this is an accurate way of modeling an induction machine, often when dealing with control systems, it is preferred to use a Γ-representation (Fig. 3.2(b)), due to its simplicity for deriving the control law. The main difference between these two models lies in where the leakage inductances are placed [42]. According to [44], it is possible to represent the machine with no loss of information by placing all the leakage inductances in the rotor circuit (see Fig. 3.2(b)). When moving from the T- to the Γ-representation, the relation between the different parameters [45] is

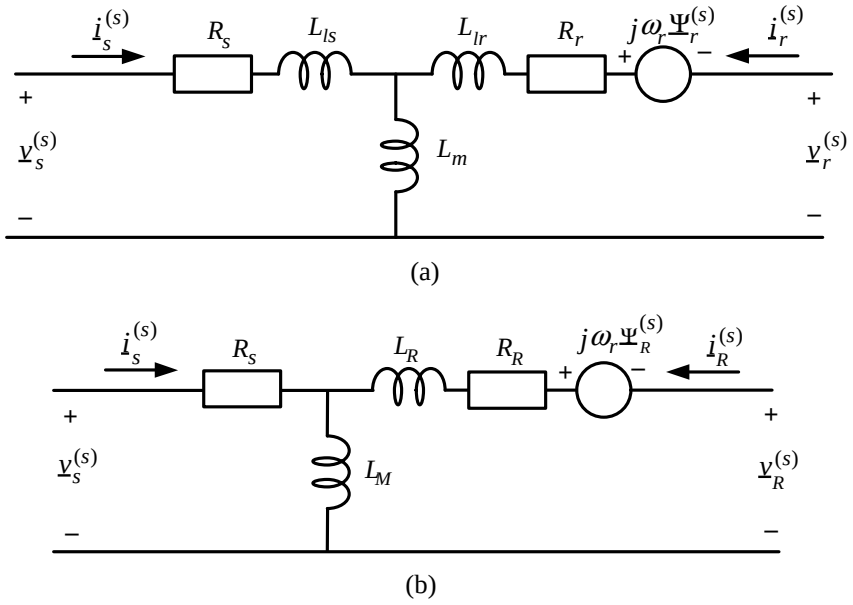

Fig. 3.2 Representation of an induction generator in the stationary-stator coordinate frame: (a) T-model representation and (b) Γ-model representation.

$$\gamma = \frac{L_s}{L_m}, \qquad \underline{v}_R = \gamma \underline{v}_r, \qquad \underline{i}_R = \frac{\underline{i}_r}{\gamma}, \qquad L_M = \gamma L_m$$
$$\underline{\Psi}_R = \gamma \underline{\Psi}_r, \qquad R_R = \gamma^2 R_r, \qquad L_R = \gamma L_{ls} + \gamma^2 L_{lr} \tag{3.1}$$

with $L_s = L_{ls} + L_m$. In this chapter and in the chapters that follow, expressions and parameters with the subscript "R" indicate that the Γ-representation of the machine is considered, whereas subscript "r " indicates T-model representation.

With reference to the symbols introduced in Fig. 3.2(b), the equations governing the electrical dynamics of the machine in the stationary-stator coordinate frame are:

$$\underline{v}_s^{(s)} = R_s \underline{i}_s^{(s)} + \frac{d\underline{\Psi}_s^{(s)}}{dt}$$
$$\underline{v}_R^{(s)} = R_R \underline{i}_R^{(s)} + \frac{d\underline{\Psi}_R^{(s)}}{dt} - j\omega_r \underline{\Psi}_R^{(s)} \tag{3.2}$$

Using Park's transformation described in Appendix B, (3.2) can be transformed into the rotating dq-coordinate systems. Here, a flux-oriented dq frame, where the d-axis is aligned with the stator flux of the machine, has been selected [1]. The resulting equations are given by

[1] Unless stated differently, rms-invariant dq transformation is considered for the DFIG model

$$\begin{aligned} \underline{v}_s^{(dq)} &= R_s \underline{i}_s^{(dq)} + \frac{d\underline{\Psi}_s^{(dq)}}{dt} + j\omega_s \underline{\Psi}_s^{(dq)} \\ \underline{v}_R^{(dq)} &= R_R \underline{i}_R^{(dq)} + \frac{d\underline{\Psi}_R^{(dq)}}{dt} + j\omega_2 \underline{\Psi}_R^{(dq)} \end{aligned} \tag{3.3}$$

ω_s corresponds to the synchronous angular frequency whereas $\omega_2 = \omega_s - \omega_r$ is the slip angular frequency. The stator and rotor fluxes expressed in (3.3) are given by

$$\begin{aligned} \underline{\Psi}_s^{(dq)} &= L_M \left(\underline{i}_s^{(dq)} + \underline{i}_R^{(dq)} \right) \\ \underline{\Psi}_R^{(dq)} &= L_M \underline{i}_s^{(dq)} + \underline{i}_R^{(dq)} \left(L_M + L_R \right) = L_R \underline{i}_R^{(dq)} + \underline{\Psi}_s^{(dq)} \end{aligned} \tag{3.4}$$

Finally, the IG model must be completed by considering the mechanical dynamics of the machine. Here, it is important to stress that the aim of this work is on the investigation of resonance conditions due to control interaction (SSCI, as discussed in Section 2.5.2); in this case, the mechanical system will not have a major impact on the system dynamics. For this reason, it is possible to model the mechanical side of the machine by simply using a single-mass representation, as

$$2H_g \frac{d\omega_g}{dt} = T_m - T_e - D_g \omega_g \tag{3.5}$$

where H_g is the inertia time-constant for the single mass. T_e and T_m are the electrical and mechanical torque, respectively. D_g is the damping coefficient while ω_g is the mechanical rotor speed. If a more detailed representation of the mechanical system is needed, a two-mass model as in the one presented in [15] and as shown in Fig. 2.14 can be adopted.

3.2.2 DC-link model

The dc-link of the BTB converter is modeled as a pure capacitor (i.e., losses are neglected). The aim of the dc-link for the BTB converter is to provide a temporary storage for the system to allow proper operation of the RSC and GSC. The capacitor is charged and discharged based on the power balance between the GSC and the RSC converter as indicated in Fig. 3.3.

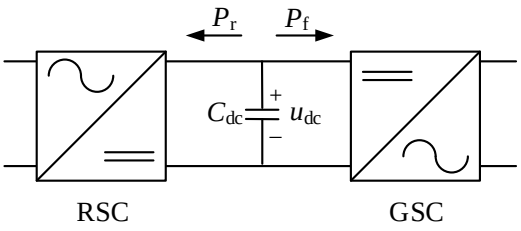

Fig. 3.3 dc-link model

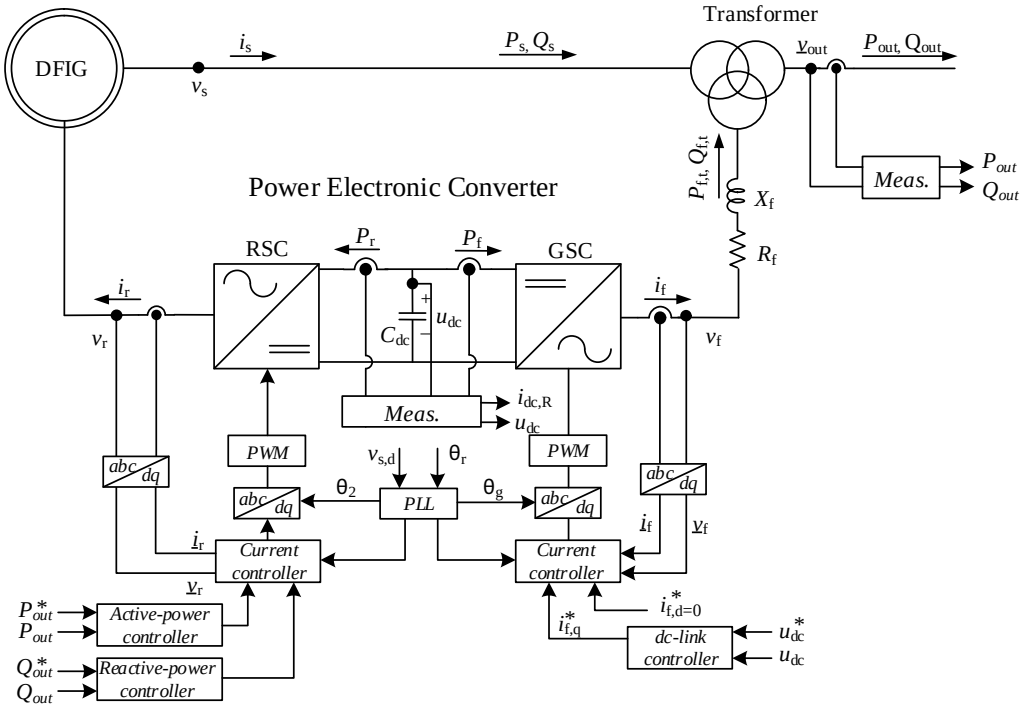

Fig. 3.4 Detailed controller structure for DFIG

With the signal convention given in Fig.3.3, the rate of change of the stored energy in the dc-link capacitor can be expressed as

$$\frac{dW_{dc}}{dt} = \frac{1}{2}C_{dc}\frac{du_{dc}^2}{dt} = -P_r - P_f \tag{3.6}$$

where W_{dc} is the energy stored in the dc-link, while u_{dc} represents the dc-link capacitor voltage. Under the assumption that the dc-link capacitor C_{dc} is constant and the converters are lossless, the time derivative of the stored energy in the dc-link can be expressed in terms of the power balance between the RSC and GSC as in (3.6).

3.3 DFIG control

The principle of using space vectors to represent three phase ac quantities as vectors having dc characteristics, gives the freedom of using conventional proportional integral (PI) regulators in the control loops. A typical control structure for a DFIG turbine is shown in Fig. 3.4. The RSC and GSC are controlled independently from each other. A phase-locked loop (PLL) is used for synchronization purpose. The details of the different control loops are discussed in the upcoming subsections.

3.3.1 Rotor-side converter controller

The aim of the RSC is to control the terminal active and reactive power of the DFIG system. The control for this converter has a cascade structure, with an inner current controller and an outer power controller. The outer controller generates the reference rotor current ($i^*_{R,d}$ and $i^*_{R,q}$), which serves as an input to the inner current controller. The controller is derived based on the Γ-representation of the induction generator. As a result, measured quantities and generator parameters are transformed to the Γ-representation using the expression given in (3.1).

Active and reactive power controller

The terminal power, P_{out}, of the wind turbine is composed by the power through the stator, P_s, and the power through the grid side filter, $P_{f,t}$ as

$$P_{out} = P_s + P_{f,t} \tag{3.7}$$

The power through the stator has a proportional relation to the electrical torque and speed as

$$P_s \quad \alpha \quad T_e \omega_r \tag{3.8}$$

where T_e is expressed as $T_e = 3n_p \mathrm{Im}\left[\underline{\Psi}_s^{(dq)} \left(\underline{i}_R^{(dq)}\right)^*\right]$ and n_p represents the number of poles. Considering a stator-flux oriented dq-frame, the electrical torque expression reduces to

$$T_e = 3\left(n_p \Psi_{s,d} i_{R,q}\right) \tag{3.9}$$

From (3.8) and (3.9), it can be deduced that the q-component of the rotor current can be used to control the stator active power (P_s). However, the aim of the power controller is not to control the stator power (P_s) but the terminal power (P_{out}) of the wind turbine. In order to control the terminal power in a closed-loop manner, the power $P_{f,t}$ in (3.7) is considered as a disturbance as depicted in Fig. 3.5. The error introduced as a result of $P_{f,t}$ is instead taken care of by the integrator term of the power controller (see Fig. 3.5).

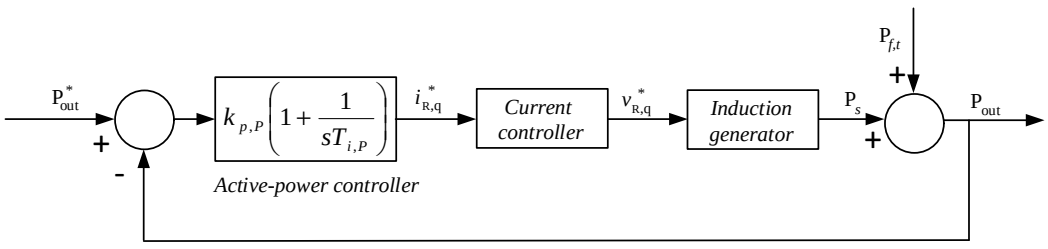

Fig. 3.5 Main structure for active power controller for DFIG

Similar to the active power, the terminal reactive power, Q_{out}, is composed of stator reactive power (Q_s) and reactive power through the grid-side filter ($Q_{f,t}$). According to [45], the reactive

power through the stator (again, considering a flux oriented dq-frame and a Γ-representation of the machine) can be expressed as

$$Q_s = 3\left[\omega_1 \Psi_{s,d}\left(\frac{\Psi_{s,d}}{L_M} - i_{R,d}\right)\right] \tag{3.10}$$

From (3.10), it can be seen that the stator reactive power (Q_s) can be controlled by controlling the d-component of the rotor current ($i_{R,d}$) where as the reactive power contribution from the grid-side filter ($Q_{f,t}$) is effectively controlled to zero in steady-state by the GSC controller. The block diagram of the implemented reactive-power controller is depicted in Fig. 3.6.

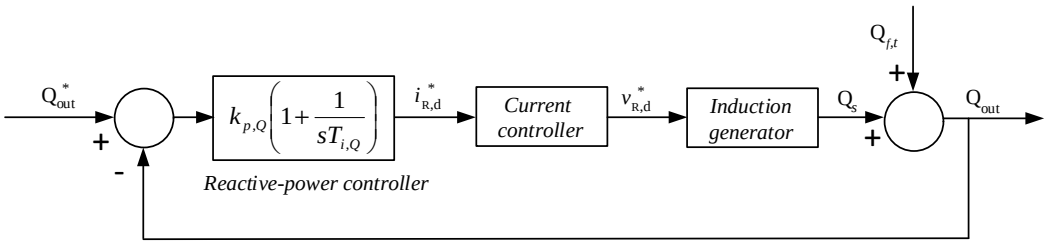

Fig. 3.6 Main structure for reactive power controller for DFIG

The pu control law governing the active and reactive power controller in the frequency-domain are then given as

$$\begin{aligned} i^*_{R,q}(s) &= k_{p,P}\left(1 + \frac{1}{sT_{i,P}}\right)\left(P^*_{out}(s) - P_{out}(s)\right) \\ i^*_{R,d}(s) &= k_{p,Q}\left(1 + \frac{1}{sT_{i,Q}}\right)\left(Q^*_{out}(s) - Q_{out}(s)\right) \end{aligned} \tag{3.11}$$

The terms k_p and T_i are the proportional gain and integrator time-constant, respectively. The outputs from these controllers serve as reference current input for the rotor current control loop.

Rotor-side current controller

Let us now observe the equivalent circuit of the induction generator in series with the RSC shown in Fig. 3.7. The voltage ($\underline{v}_R$) at the rotor terminal in the dq frame can be expressed as:

$$\underline{v}_R^{(dq)} = R_R \underline{i}_R^{(dq)} + \frac{d\underline{\Psi}_R^{(dq)}}{dt} + j\omega_2 \underline{\Psi}_R^{(dq)} \tag{3.12}$$

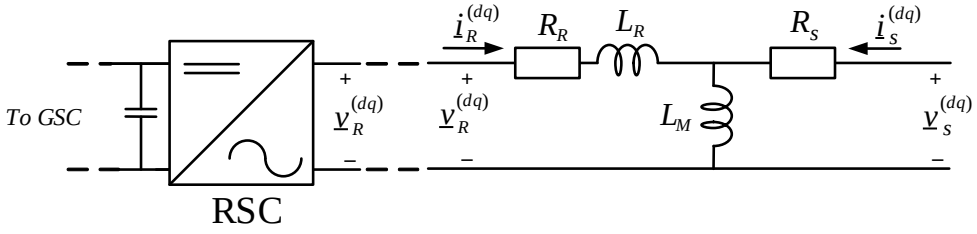

Fig. 3.7 RSC in series with Γ-model representation of an induction generator

Taking the rotor flux equation in (3.4) with $\underline{\Psi}_R^{(dq)} = L_R \underline{i}_R^{(dq)} + \underline{\Psi}_s^{(dq)}$ and substituting it into (3.12), the expression for the rotor voltage can be rewritten as

$$\underline{v}_R^{(dq)} = (R_R + j\omega_2 L_R)\,\underline{i}_R^{(dq)} + L_R \frac{d\underline{i}_R^{(dq)}}{dt} + \underbrace{\frac{d\underline{\Psi}_s^{(dq)}}{dt} + j\omega_2 \underline{\Psi}_s^{(dq)}}_{\underline{e}_{emf}^{(dq)}} \tag{3.13}$$

where $\underline{e}_{emf}^{(dq)}$ represents the back EMF of the machine. The above equation can be rearranged to describe the dynamics of the rotor current as

$$L_R \frac{d\underline{i}_R^{(dq)}}{dt} = \underline{v}_R^{(dq)} - R_R \underline{i}_R^{(dq)} - j\omega_2 L_R \underline{i}_R^{(dq)} - \underline{e}_{emf}^{(dq)} \tag{3.14}$$

Further, (3.14) can be expressed explicitly in terms of its d and q components as

$$\begin{aligned} L_R \frac{di_{R,d}}{dt} &= v_{R,d} - R_R i_{R,d} + \omega_2 L_R i_{R,q} - e_{emf,d} \\ L_R \frac{di_{R,q}}{dt} &= v_{R,q} - R_R i_{R,q} - \omega_2 L_R i_{R,d} - e_{emf,q} \end{aligned} \tag{3.15}$$

From (3.15), it can be observed that there exists a cross-coupling between the $i_{R,d}$ and $i_{R,q}$ currents. In the control law described in [45] [46], it is possible to decouple the cross-coupling between the $i_{R,d}$ and $i_{R,q}$ and compensate for the back EMF of the machine in order to achieve an independent control of the *d*-and *q*-current and, thereby, of the reactive and active power. This is accomplished by introducing a decoupling term $j\omega_2 L_R \underline{i}_R^{(dq)}$ and a feed-forward term for the estimated back EMF as

$$\underline{v}_R^{*(dq)} = \underline{v}_R^{(dq)'} + j\omega_2 L_R \underline{i}_R^{(dq)} + \hat{\underline{e}}_{emf}^{(dq)} \tag{3.16}$$

where $\underline{v}_R^{(dq)'}$ is the output from the PI controller. In this analysis, the converters are treated as lossless linear amplifiers. In addition they are assumed to be ideal, meaning that they are able to generate the reference voltage with no delay as

$$\underline{v}_R^{*(dq)} = \underline{v}_R^{(dq)} \tag{3.17}$$

Now moving the analysis to the frequency-domain, the dynamics of the rotor current expressed in (3.14) can be rewritten as

$$sL_R\underline{i}_R^{(dq)}(s) = \underline{v}_R^{(dq)}(s) - R_R\underline{i}_R^{(dq)}(s) - j\omega_2 L_R\underline{i}_R^{(dq)}(s) - \underline{\hat{e}}_{emf}^{(dq)}(s) \tag{3.18}$$

Similarly, the reference voltage expression in (3.16) along side the structure for controller in frequency-domain can be expressed as

$$\begin{aligned}\underline{v}_R^{(dq)*}(s) &= \underline{v}_R^{(dq)'}(s) + j\omega_2 L_R\underline{i}_R^{(dq)}(s) + \underline{\hat{e}}_{emf}^{(dq)}(s) \\ &= F_{cc,R}(s)\left(\underline{i}_R^{(dq)*}(s) - \underline{i}_R^{(dq)}(s)\right) + j\omega_2 L_R\underline{i}_R^{(dq)}(s) + \underline{\hat{e}}_{emf}^{(dq)}(s)\end{aligned} \tag{3.19}$$

where $F_{cc,R}(s)$ is the transfer function of the controller applied to the current error. Under the previous assumption that $\underline{v}_R^{(dq)*} = \underline{v}_R^{(dq)}$ and assuming a perfect estimation of the back EMF, (3.18) and (3.19) can be combined as

$$\begin{aligned}sL_R\underline{i}_R^{(dq)}(s) &= -R_R\underline{i}_R^{(dq)}(s) + F_{cc,R}(s)\left(\underline{i}_R^{(dq)*}(s) - \underline{i}_R^{(dq)}(s)\right) \Rightarrow \\ \underline{i}_R^{(dq)}(s) &= \underbrace{\frac{1}{sL_R + R_R}}_{G_{cc,R}(s)} F_{cc,R}(s)\left(\underline{i}_R^{(dq)*}(s) - \underline{i}_R^{(dq)}(s)\right)\end{aligned} \tag{3.20}$$

Rearranging (3.20), the closed-loop expression from $\underline{i}_R^{(dq)*}(s)$ to $\underline{i}_R^{(dq)}(s)$ can be obtained as

$$\underline{i}_R^{(dq)}(s) = \underbrace{\frac{G_{cc,R}(s)F_{cc,R}(s)}{1 + G_{cc,R}(s)F_{cc,R}(s)}}_{G_{cc,cl}(s)}\underline{i}_R^{(dq)*}(s) \tag{3.21}$$

Using internal model control (IMC) [47] [48], the closed-loop transfer function can be shaped as a first order low-pass filter having a closed-loop bandwidth $\alpha_{cc,R}$ as

$$G_{cc,cl}(s) = \frac{\alpha_{cc,R}}{s + \alpha_{cc,R}} = \frac{\frac{\alpha_{cc,R}}{s}}{1 + \frac{\alpha_{cc,R}}{s}} \tag{3.22}$$

From (3.21) and (3.22), the transfer function of the controller $F_{cc,R}(s)$ can be obtained as

$$F_{cc,R}(s) = \frac{\alpha_{cc,R}}{s}G_{cc,R}^{-1}(s) = \frac{\alpha_{cc,R}}{s}(sL_R + R_R) = \alpha_{cc,R}L_R + \frac{\alpha_{cc,R}R_R}{s} \tag{3.23}$$

which indicates that $F_{cc,R}(s)$ is a PI controller with a proportional $k_{p,cc}$ equal to $\alpha_{cc,R}L_R$ and integral gain $k_{i,cc}$ equal to $\alpha_{cc,R}R_R$. Here it is worth noting that the aim of the RSC is to control the active and reactive powers. As a result, the integral part of the inner current controller can be omitted as any steady-state error that could arise is taken care of by the integral action of

the outer-loop controller. Under this assumption, the control law for the RSC current controller considered for this work is given by

$$\underline{v}_R^{*(dq)} = k_{p,cc}\left(\underline{i}_R^{(dq)*}(s) - \underline{i}_R^{(dq)}(s)\right) + j\omega_2 L_R \underline{i}_R^{(dq)}(s) + \underbrace{\frac{1}{sT_{LP}+1}}_{H_{LP}(s)}\underline{\hat{e}}_{emf}^{(dq)}(s) \tag{3.24}$$

where $k_{p,cc}$ is as defined in (3.23). Note that a low-pass filter term $H_{LP}(s)$ with a time constant T_{LP} is introduced to reduce the dynamics in the estimated back EMF.

3.3.2 Grid-side converter controller

The purpose of the GSC converter is to maintain the dc-link capacitor voltage to its reference value by controlling the active power flow through the grid-side filter. Similar to the RSC, it has a cascade structure with an outer dc-link voltage controller and an inner current controller (see Fig.3.4). The inner current controller receives the reference current ($\underline{i}_f^{(dq)*}$) from the outer controller and outputs the reference voltage ($\underline{v}_f^{(dq)*}$) for the GSC. The controller for the GSC is aligned with the grid flux, meaning that the voltage vector $\underline{v}_g^{(dq)}$ in Fig.3.8 is aligned with the q-axis. The apparent power at the terminal of the grid-side filter can be expressed as

$$S_{f,t} = P_{f,t} + jQ_{f,t} \xrightarrow{\text{for } v_{g,d}=0} 3\left\{jv_{g,q}\text{conj}\left[\underline{i}_f^{(dq)}\right]\right\} \tag{3.25}$$

Thus, the active and reactive power through the grid-side filter can be expressed as

$$\begin{aligned} P_{f,t} &= 3v_{g,q}i_{f,q} \\ Q_{f,t} &= 3v_{g,q}i_{f,d} \end{aligned} \tag{3.26}$$

Grid-side current controller

Figure 3.8 shows the equivalent circuit for the grid side filter along side the GSC. The grid-side filter consists of a inductance L_f and a resistance R_f. The voltage equation at the terminal of the GSC can be written as

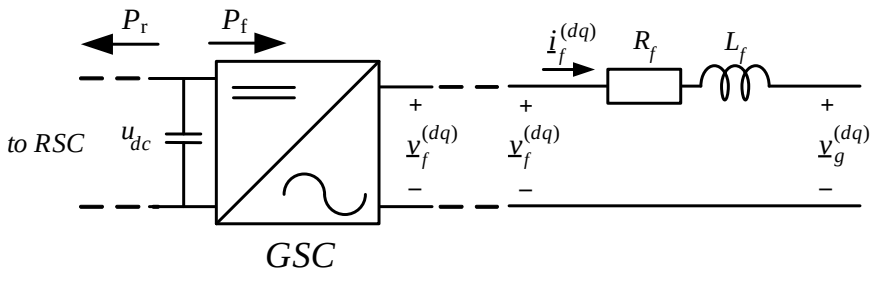

Fig. 3.8 GSC converter with grid-side filter

$$\underline{v}_f^{(dq)} = R_f \underline{i}_f^{(dq)} + L_f \frac{d\underline{i}_f^{(dq)}}{dt} + j\omega_s L_f \underline{i}_f^{(dq)} + \underline{v}_g^{(dq)} \tag{3.27}$$

Following the same procedure described for the derivation of the RSC current controller, the control law for the GSC current controller in the frequency domain can be expressed as

$$\underline{v}_f^{*(dq)}(s) = \left(k_{pf,cc} + \frac{k_{if,cc}}{s}\right)\left(\underline{i}_f^{*(dq)}(s) - \underline{i}_f^{(dq)}(s)\right) + j\omega_s L_f \underline{i}_f^{(dq)}(s) + \underbrace{\frac{1}{sT_{LP}+1}}_{H_{LP}(s)} \underline{v}_g^{(dq)}(s) \tag{3.28}$$

where, calling $\alpha_{cc,f}$ the closed-loop current controller bandwidth, the parameters for the PI regulator are given by $k_{pf,cc} = \alpha_{cc,f} L_f$ and $k_{if,cc} = \alpha_{cc,f} R_f$. Again, the measured grid voltage is filtered to reduce its dynamics. The block diagram describing the GSC current controller is depicted in Fig. 3.9. The reference q component of the filter current is used to control the dc-link voltage where as the reference d component is directly controlled to zero. For this purpose, unlike the RSC current controller, the GSC current controller current controller is equipped with an integrator term as in (3.28).

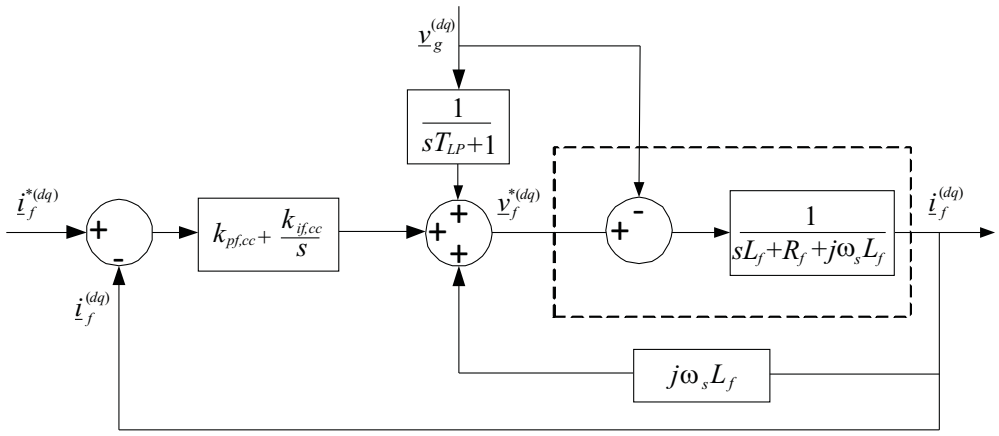

Fig. 3.9 Block diagram of the GSC current controller

DC-link voltage controller

The dc-link capacitor voltage can be controlled in two ways: in terms of the dc-link voltage (u_{dc}) involving the flow of current in and out of the dc-link or in terms of the energy stored in the dc-link capacitor involving the power exchange. The latter is adopted in this thesis. For the sake of clarity, the dynamics of the dc-link described in (3.6) is repeated here

$$\frac{dW_{dc}}{dt} = \frac{1}{2} C_{dc} \frac{du_{dc}^2}{dt} = -P_f - P_R \tag{3.29}$$

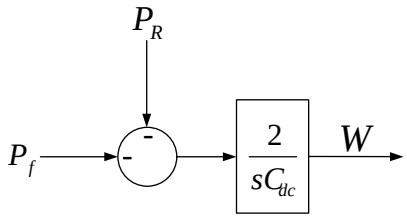

Fig. 3.10 Block diagram of dc-link capacitor dynamics

where P_R is the power flowing from the capacitor into the RSC, while P_f is the power flowing into the GSC, as indicated in Fig. 3.3. It should be noted that (3.29) is non-linear in nature due to the u_{dc}^2 term. With the aim of extracting the control law, the above expression can be linearized, resulting in

$$\frac{1}{2}C_{dc}u_{dc,0}\frac{d\Delta u_{dc}}{dt} = -\Delta P_f - \Delta P_R \tag{3.30}$$

where $u_{dc,0}$ is the dc-link voltage at the operating point. Equation (3.30) hints that, the relation is operating point dependent. To avoid this, a technique called feedback linearization [47] can be employed, in which a non-linear equation can be replaced with an equivalent linear equation where traditional control techniques can be employed. Here the square of the voltage, u_{dc}^2, is replaced with a new variable, W, which in physical sense is proportional to the energy stored in the capacitor as in [49] [47]. The dc-link dynamics can now be rewritten as

$$\frac{1}{2}C_{dc}\frac{dW}{dt} = -P_f - P_R \tag{3.31}$$

Figure 3.10 shows the open-loop dynamics for the dc-link capacitor. From the controller point of view, P_R can be viewed as a disturbance. Using IMC, as in previous sections, the dc-link controller can be shaped as a first order low-pass filter having a closed-loop bandwidth α_{dc}, resulting in a proportional controller with a gain $k_{p,dc} = -\alpha_{dc}C_{dc}$. As the dc-link voltage controller is an outer-control loop, any steady-state error that could arise due to parameters mismatch or disturbances can not be removed through a proportional controller. To alleviate this, a small integral term is introduced during the controller design. Active damping is adopted for controller tunning as in [47] [50].

Considering the GSC to be lossless and the losses in the grid-side filter to be negligible, the power P_f at the terminal of GSC converter can be approximated as

$$P_f \approx P_{f,t} = 3v_{g,q}i_{f,q} \tag{3.32}$$

Inserting (3.32) into (3.31), under the assumption that the voltage vector is perfectly aligned with the q-axis as $\underline{v}_g = jv_{g,q} = |v_g|$, the dc-link expression from (3.31) reduces to

$$\frac{1}{2}C_{dc}\frac{dW}{dt} = -3\,|v_g|\,i_{f,q} - P_R \tag{3.33}$$

The control law governing the q-component of the filter current ($i_{f,q}^*$) with active damping term as implemented in [47] is expressed below

$$i_{f,q}^* = i_{f,q}^{'} + G_a W \tag{3.34}$$

where $i_{f,q}^{'}$ is the controller output and G_a is the gain of the active damping term. Considering that the inner current controller is much faster than the outer loop for stability reasons ($i_{f,q}^{*} = i_{f,q}$), the above expression can be inserted in (3.33) to obtain

$$\frac{1}{2}C_{dc}\frac{dW}{dt} = -3\left|v_g\right|\left(i_{f,q}^{'} + G_a W\right) - P_R \tag{3.35}$$

Treating P_R as a disturbance, the transfer function from $i_{f,q}^{'}$ to W can be written as

$$W\left(s\right) = \underbrace{\frac{-6\left|v_g\right|}{sC_{dc} + 6\left|v_g\right|G_a}}_{G_{dc}(s)} i_{f,q}^{'}\left(s\right) \tag{3.36}$$

with

$$i_{f,q}^{'}\left(s\right) = F_{dc}\left(s\right)\left(W\left(s\right)^{*} - W\left(s\right)\right)$$

where F_{dc} represents the transfer function of the controller. With the aim of shaping the closed-loop system step response as the one of a first order low-pass filter that has a desired bandwidth of α_{dc}, $F_{dc}\left(s\right)$ can be obtained using IMC as

$$F_{dc}\left(s\right) = k_{p,dc} + \frac{k_{i,dc}}{s} = \frac{\alpha_{dc}}{s}G_{dc}^{-1}\left(s\right) = -\frac{\alpha_{dc}C_{dc}}{6\left|v_g\right|} - \frac{\alpha_{dc}G_a}{s} \tag{3.37}$$

As done in [47], by placing the poles of $G_{dc}\left(s\right)$ at α_{dc}, the closed-loop system can retain a closed-loop bandwidth corresponding to α_{dc} as

$$G_{dc}\left(s\right) = \frac{-6\left|v_g\right|}{sC_{dc} + 6\left|v_g\right|G_a} \Rightarrow \frac{6\left|v_g\right|G_a}{C_{dc}} = \alpha_{dc} \tag{3.38}$$

resulting in $G_a = \frac{\alpha_{dc}C_{dc}}{6|v_g|}$. Combining (3.37) with the Laplace transform of (3.34), an expression for the dc-link voltage controller is obtained as (3.39). A block-diagram description for the dc-link voltage controller is also shown in Fig. 3.11

$$i_{f,q}^{*}\left(s\right) = \left(k_{p,dc} + \frac{k_{i,dc}}{s}\right)\left(W\left(s\right)^{*} - W\left(s\right)\right) + G_a W\left(s\right) \tag{3.39}$$

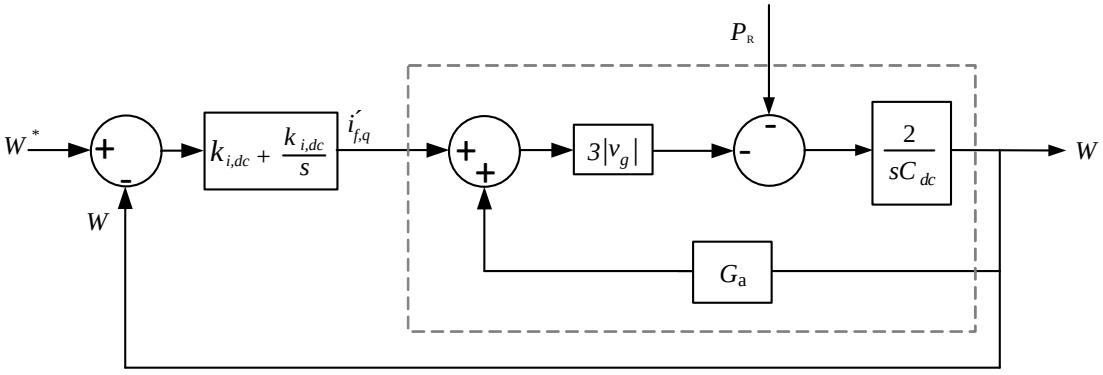

Fig. 3.11 Block diagram of the closed-loop controller for the dc-link voltage

As briefly mentioned earlier, the d-component of the filter current can be used to control the reactive power output from the GSC. In this thesis, the reactive current component, $i_{f,d}$, is controlled to zero by setting $i^*_{f,d} = 0$. This is to indicate that in steady-state, the reactive power ($Q_{f,t}$) output from the grid-filter is effectively controlled to zero.

3.3.3 Phase-locked loop (PLL)

In sections leading up to this, it has been mentioned that a stator flux oriented dq-coordinate frame has been used, where the voltage vector ($\underline{v}_s^{(s)}$) is aligned with the q-axis. The alignment of the voltage vector with the q-axis is achieved through the knowledge of the phase angle (θ_s) for $\underline{v}_s^{(s)}$. As the angle of the voltage vector is not known, a PLL is used for estimation purpose. The control law of the PLL is as below

$$\begin{aligned} \dot{\hat{\omega}}_s &= k_{i,PLL}\varepsilon_{PLL} \\ \dot{\hat{\theta}}_s &= \hat{\omega}_s + k_{p,PLL}\varepsilon_{PLL} \end{aligned} \tag{3.40}$$

where $\hat{\omega}_s$ and $\hat{\theta}_s$ are the estimated grid frequency and voltage angle, respectively. The gains $k_{p,PLL} = 2\alpha_{PLL}$ and $k_{i,PLL} = \alpha^2_{PLL}$ are selected in accordance to [51]. ε_{PLL} is the error signal for the PLL. In order to determine the error signal for the PLL, the focus is directed to Fig. 3.12 where a voltage vector ($\underline{v}_s^{(s)}$) together with the stationary $\alpha\beta$-frame and a non-aligned dq-frame is shown. As can be seen, the dq decomposition of the voltage vector ($\underline{v}_s^{(s)}$) results in a non-zero d-component. It can be easily seen that the *d*-component of voltage is given by

$$v_{s,d} = -\left|v_s^{(s)}\right| \sin\left(\theta_s - \hat{\theta}_s\right) \tag{3.41}$$

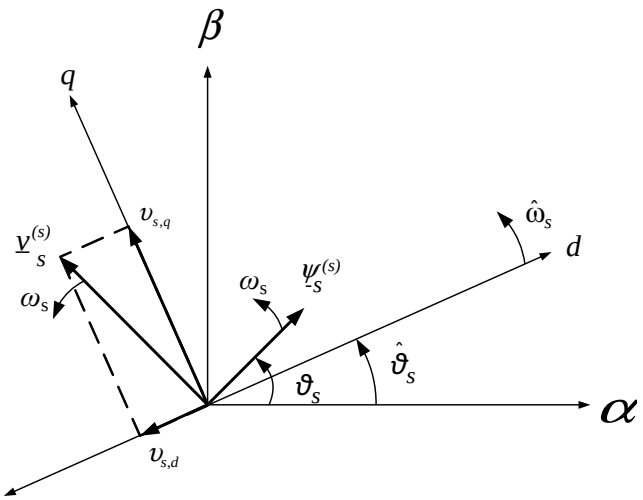

Fig. 3.12 Decomposition of voltage vector($\underline{v}_s^{(s)}$) into a non-aligned dq frame

Taking $\theta_s - \hat{\theta}_s$ to be very small ($\sin\left(\theta_s - \hat{\theta}_s\right) \approx \left(\theta_s - \hat{\theta}_s\right)$), the error signal ε_{PLL} is then given by

$$\varepsilon_{PLL} = -\frac{v_{s,d}}{\left|\underline{v}_s^{(s)}\right|} \tag{3.42}$$

Therefore, using (3.42), the PLL can be made to adjust $\hat{\omega}_s$ thereby changing $\hat{\theta}_s$ until the error ($-\frac{v_{s,d}}{\left|\underline{v}_s^{(s)}\right|}$) is set to zero.

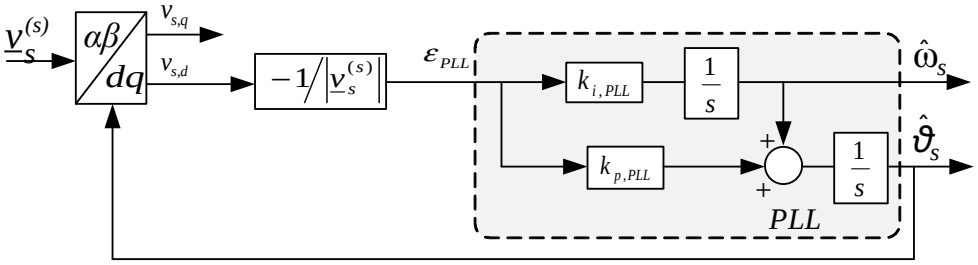

Fig. 3.13 Block diagram of PLL

Figure 3.13 shows the block diagram of the adopted PLL structure. The voltage vector ($\underline{v}_s^{(s)}$) is transformed to the dq-frame using the estimated $\hat{\theta}_s$. From the decomposed dq components of the voltage vector, the d-component is normalized with the magnitude of the voltage vector which is fed into the PLL structure described by (3.40) (shown highlighted in Fig. 3.13). The updated estimated phase is fed back to the stationary to dq transformation block to produce the updated dq decomposition of the voltage vector. In this way, the PLL works to set the error to zero. Here it is important to stress that if the investigation is related to the GSC, then the voltage vector ($\underline{v}_s^{(s)}$) in the above analysis should be replaced with filter voltage vector ($\underline{v}_g^{(s)}$). In a similar manner, transformations dealing with quantities on the rotor-side should take into account both the rotor speed (ω_r) and position angle (θ_r).

3.4 DFIG admittance

The modeling approach consists of developing small subsystems that are connected to build the total system. The advantage with this approach is that, a complex system can be built through a step-by-step interconnection of smaller subsystems. Moreover, the system is verified for each subsystem added, making the debugging process less complicated. Another added advantage with this approach is the possibility of removing subsystems and analyzing their impact on the overall system. The DFIG is considered as an entire system built from smaller subsystems like the induction generator model, the RSC model, the GSC model and the dc-link dynamics model.

Figure. 3.14 shows the DFIG system to be modeled. In this section, the DFIG is considered to be connected to an infinite bus. The WRIG is represented in terms of resistances (R_s and R_R) and

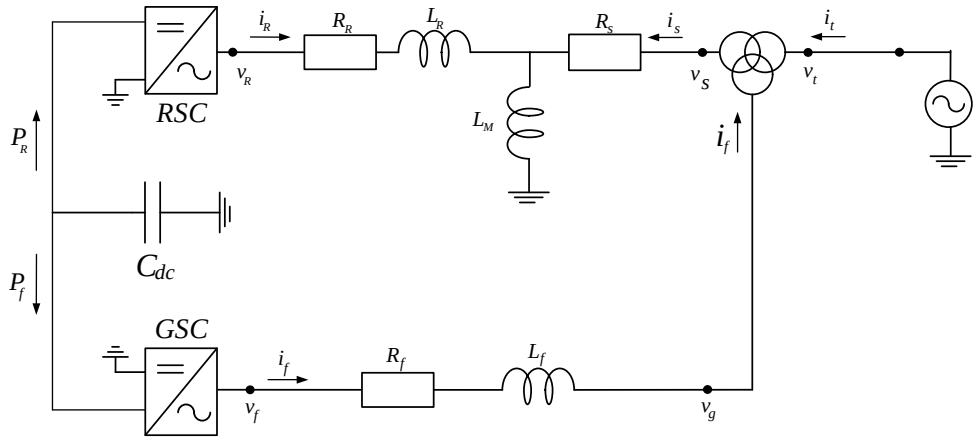

Fig. 3.14 Model of a DFIG turbine

inductances (L_M and L_R). The ac-side of the RSC is connected directly to the rotor of WRIG whereas the dc-side is coupled to the dc-side of the GSC through the dc-link with a capacitance (C_{dc}). The ac-side of the GSC is coupled to the grid-side filter represented by a resistance (R_f) and an inductance (L_f).

First, the WRIG with the RSC current controller excluding the dc-link dynamics and the outer-loop controllers is derived. Next the subsystem consisting of the grid-side filter and the GSC current controller is developed. The two subsystems are cascaded to create a simplified model, not including outer-loop controllers for the RSC and the GSC. Following this, a subsystem comprising the outer power control loop for the RSC is developed. A final subsystem for the outer-loop controller for the GSC and the dc-link dynamics is derived. In the end, the two subsystems for the outer-loop controllers are cascaded with the simplified model to create the electrical model for the DFIG.

3.4.1 WRIG with rotor-side current controller

In this section, the WRIG together with the RSC current controller excluding outer-loop controllers and dc-link dynamics is derived. For the purpose of clarity, the stator and rotor voltage equations for the WRIG considering the Γ-representation in the dq-frame as described in (3.3) are repeated here:

$$\begin{aligned} \underline{v}_s^{(dq)} &= R_s \underline{i}_s^{(dq)} + \frac{d\underline{\Psi}_s^{(dq)}}{dt} + j\omega_s \underline{\Psi}_s^{(dq)} \\ \underline{v}_R^{(dq)} &= R_R \underline{i}_R^{(dq)} + \frac{d\underline{\Psi}_R^{(dq)}}{dt} + j\omega_2 \underline{\Psi}_R^{(dq)} \end{aligned} \tag{3.43}$$

Expressing the stator and rotor flux expressions using $\underline{i}_s$ and $\underline{i}_R$, (3.43) is expressed as

$$\begin{aligned}\underline{v}_s^{(dq)} &= R_s\underline{i}_s^{(dq)} + L_M\frac{d\underline{i}_s^{(dq)}}{dt} + L_M\frac{d\underline{i}_R^{(dq)}}{dt} + j\omega_s L_M\underline{i}_s^{(dq)} + j\omega_s L_M\underline{i}_R^{(dq)} \\ \underline{v}_R^{(dq)} &= R_R\underline{i}_R^{(dq)} + L_M\frac{d\underline{i}_s^{(dq)}}{dt} + (L_M+L_R)\frac{d\underline{i}_R^{(dq)}}{dt} + j\omega_2 L_M\underline{i}_s^{(dq)} + j\omega_2(L_M+L_R)\underline{i}_R^{(dq)}\end{aligned} \tag{3.44}$$

The above expression governing the WRIG can be expressed in the frequency-domain as

$$\begin{aligned}\underline{v}_s^{(dq)}(s) &= (R_s + sL_M + j\omega_s L_M)\underline{i}_s^{(dq)}(s) + (sL_M + j\omega_s L_M)\underline{i}_R^{(dq)}(s) \\ \underline{v}_R^{(dq)}(s) &= (sL_M + j\omega_2 L_M)\underline{i}_s^{(dq)}(s) + (R_R + s(L_M+L_R) + j\omega_2(L_M+L_R))\underline{i}_R^{(dq)}(s)\end{aligned} \tag{3.45}$$

Using (3.45), the WRIG can be expressed in a matrix form in terms of stator and rotor currents, input rotor voltage and input stator voltage as

$$\mathbf{M}_g\mathbf{i}_g = \mathbf{M}_R\mathbf{v}_R + \mathbf{M}_s\mathbf{v}_s \tag{3.46}$$

where

$$\mathbf{i}_g = \begin{bmatrix}\mathbf{i}_s \\ \mathbf{i}_R\end{bmatrix},\ \mathbf{i}_s = \begin{bmatrix}i_{s,d}(s) \\ i_{s,q}(s)\end{bmatrix},\ \mathbf{i}_R = \begin{bmatrix}i_{R,d}(s) \\ i_{R,q}(s)\end{bmatrix}, \mathbf{v}_R = \begin{bmatrix}v_{R,d}(s) \\ v_{R,q}(s)\end{bmatrix}, \mathbf{v}_s = \begin{bmatrix}v_{s,d}(s) \\ v_{s,q}(s)\end{bmatrix}$$

$$\mathbf{M}_g = \begin{bmatrix} R_s+sL_M & -\omega_s L_M & sL_M & -\omega_s L_M \\ \omega_s L_M & R_s+sL_M & \omega_s L_M & sL_M \\ sL_M & -\omega_2 L_M & R_R+s(L_M+L_R) & -\omega_2(L_M+L_R) \\ \omega_2 L_M & sL_M & \omega_2(L_M+L_R) & R_R+s(L_M+L_R)\end{bmatrix}$$

$$\mathbf{M}_R = \begin{bmatrix}0&0\\0&0\\1&0\\0&1\end{bmatrix},\quad \mathbf{M}_s = \begin{bmatrix}1&0\\0&1\\0&0\\0&0\end{bmatrix}$$

In this chapter, variables with bold letter are used to represent both matrices and vectors. In Section 3.3.1, the derivation of the RSC current controller was presented. The reference rotor voltage generated by the RSC current controller shown in (3.24) is repeated here:

$$\underline{v}_R^{*(dq)}(s) = F_{cc,R}(s)\left(\underline{i}_R^{*(dq)}(s) - \underline{i}_R^{(dq)}(s)\right) + j\omega_2 L_R\underline{i}_R^{(dq)}(s) + H_{LP}(s)\,\underline{\hat{e}}_{emf}^{(dq)}(s) \tag{3.47}$$

where the estimated back EMF term is $\underline{\hat{e}}_{emf}^{(dq)}(s) = v_s(s) - \left(\frac{R_s}{L_M} + j\omega_r\right)\underline{\hat{\Psi}}_s^{(dq)}$ and the low-pass filter term is $H_{LP}(s) = \frac{\alpha_{LP}}{s+\alpha_{LP}}$. The transfer function $F_{cc,R}(s)$ is a proportional controller

with the term $k_{p,cc} = \alpha_{cc,R} L_R$. Under the assumption that the RSC converter is ideal, the rotor voltage vector $\mathbf{v}_R$ can be expressed as

$$\mathbf{v}_R^* = \begin{bmatrix} v_{R,d}^*(s) \\ v_{R,q}^*(s) \end{bmatrix} = \mathbf{F}_{cc,R}\mathbf{i}_R^* + \mathbf{M}_{cc,R}\mathbf{i}_g + \mathbf{M}_{cc,v}\mathbf{v}_s \tag{3.48}$$

where

$$\mathbf{F}_{cc,R} = \begin{bmatrix} F_{cc,R}(s) & 0 \\ 0 & F_{cc,R(s)} \end{bmatrix}, \quad \mathbf{M}_{cc,v} = \begin{bmatrix} H_{LP}(s) & 0 \\ 0 & H_{LP}(s) \end{bmatrix}, \quad \mathbf{i}_R^* = \begin{bmatrix} i_{R,d}^*(s) \\ i_{R,q}^*(s) \end{bmatrix}$$

$$\mathbf{M}_{cc,R} = \begin{bmatrix} -R_s H_{LP}(s) & \omega_r L_M H_{LP}(s) & -F_{cc,R}(s) & -(\omega_2 L_R - \omega_r L_M H_{LP}(s)) \\ -\omega_r L_M H_{LP}(s) & -R_s H_{LP}(s) & (\omega_2 L_R - \omega_r L_M H_{LP}(s)) & -F_{cc,R}(s) \end{bmatrix}$$

As the output voltage from the rotor-side converter serves as an input to the WRIG rotor, combining (3.46) and (3.48) results in a system representation in terms of currents, reference values and input voltages as

$$\mathbf{M}_{gcc,i}\mathbf{i}_g = \mathbf{M}_{gcc,ref}\mathbf{i}_R^* + \mathbf{M}_{gcc,vs}\mathbf{v}_s \tag{3.49}$$

with matrices $\mathbf{M}_{gcc,i}$, $\mathbf{M}_{gcc,ref}$ and $\mathbf{M}_{gcc,vs}$ expressed as

$$\mathbf{M}_{gcc,i} = \mathbf{M}_g - \mathbf{M}_R\mathbf{M}_{cc,R}$$

$$\mathbf{M}_{gcc,ref} = \mathbf{M}_R\mathbf{F}_{cc,R}$$

$$\mathbf{M}_{gcc,vs} = \mathbf{M}_R\mathbf{M}_{cc,v} + \mathbf{M}_s$$

The losses and phase shift due to the three-winding transformer (see Fig. 3.14) are here neglected. However, the transformation ratio between the different sides of the transformer is accounted for. Considering the transformer's ratio (k_{tr1}) between the stator side and the generator terminal side, the stator voltage vector ($\mathbf{v}_s$) can be replaced by DFIG terminal voltage ($\mathbf{v}_t$) resulting in

$$\mathbf{M}_{gcc,i}\mathbf{i}_g = \mathbf{M}_{gcc,ref}\mathbf{i}_R^* + k_{tr1}\mathbf{M}_{gcc,vs}\mathbf{v}_t \tag{3.50}$$

At an early stage, the admittance of WRIG with the rotor current controller can be obtained by rearranging (3.50) into a form corresponding to

$$\mathbf{i}_g = \begin{bmatrix} \mathbf{i}_s \\ \mathbf{i}_R \end{bmatrix} = \begin{bmatrix} \mathbf{G}_{gccs,ref} \\ \mathbf{G}_{gccR,ref} \end{bmatrix}\mathbf{i}_R^* + \begin{bmatrix} \mathbf{Y}_{gcc} \\ \mathbf{Y}_{gccR} \end{bmatrix}\mathbf{v}_t \tag{3.51}$$

with

$$\begin{bmatrix} \mathbf{G}_{gccs,ref} \\ \mathbf{G}_{gccR,ref} \end{bmatrix} = [\mathbf{M}_{gcc,i}]^{-1}\,\mathbf{M}_{gcc,ref} \quad \text{and} \quad \begin{bmatrix} \mathbf{Y}_{gcc} \\ \mathbf{Y}_{gccR} \end{bmatrix} = [\mathbf{M}_{gcc,i}]^{-1}\,\mathbf{M}_{gcc,v}$$

$\mathbf{G}_{gccs,ref}$, $\mathbf{G}_{gccR,ref}$, $\mathbf{Y}_{gcc}$ and $\mathbf{Y}_{gccR}$ are 2×2 transfer function matrices. $\mathbf{Y}_{gcc}$ expressing the relation from terminal voltage vector ($\underline{v}_t$) to stator current vector ($\underline{i}_s$) is considered as the admittance matrix, which is expressed explicitly as

$$\begin{bmatrix} i_{s,d}(s) \\ i_{s,q}(s) \end{bmatrix} = \begin{bmatrix} \mathbf{Y}_{gcc}(1,1) & \mathbf{Y}_{gcc}(1,2) \\ \mathbf{Y}_{gcc}(2,1) & \mathbf{Y}_{gcc}(2,2) \end{bmatrix} \begin{bmatrix} v_{t,d}(s) \\ v_{t,q}(s) \end{bmatrix} \tag{3.52}$$

The combined system constituting the WRIG and the rotor-side current controller is symmetric in nature as the system is identical along the d and q axis. Hence the admittance can equivalently be expressed using a complex transfer function as [40]

$$\underline{Y}_{gcc}(s) = \mathbf{Y}_{gcc}(1,1) + j\mathbf{Y}_{gcc}(2,1) \tag{3.53}$$

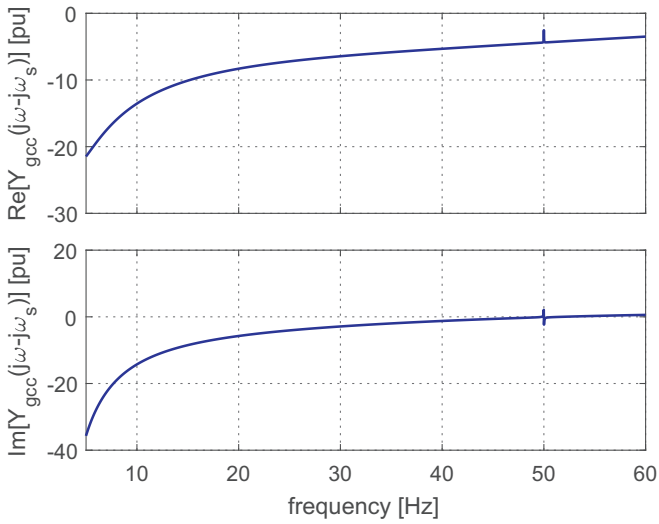

Fig. 3.15 Admittance of WRIG in series with the RSC connected to the rotor terminal only considering the inner-current controller for a closed-loop current controller bandwidth of 1 pu

The admittance of a WRIG with current controller in the subsynchronous frequency range obtained by evaluating the frequency response of (3.53) is depicted in Fig. 3.15. The admittance is normalized by the DFIG ratings. The admittance of a WRIG with the rotor circuit connected to a rotor-side current controller by itself does not give a direct insight into the total behavior of the DFIG turbine, but can be used to create an understanding. Up to this point, the obtained admittance matrix is symmetric, hence the real part of the phase admittance begin negative can be used to interpret this setup's ability to dissipate power by directly looking at Fig. 3.15. When outer-loop controller are added to the system, the symmetry in the admittance is lost. As a result, methods that can interpret MIMO system behavior should be considered. However the model result obtained using (3.52) will serve as a building block for total DFIG admittance.

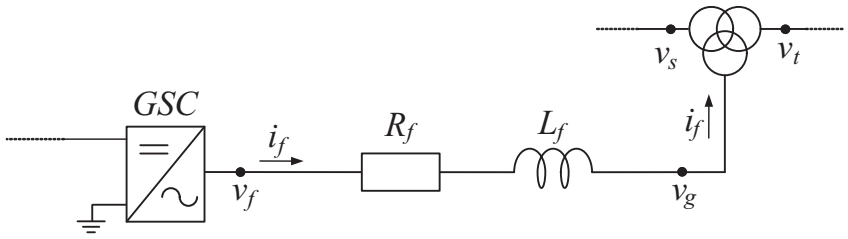

Fig. 3.16 Grid-side filter connected to GSC

3.4.2 Grid-side filter with GSC current controller

In this section, the grid-side filter together with the GSC current controller as a stand-along shunt device is considered. Figure 3.16 shows a portion of Fig. 3.14 with the grid-side filter connected to the GSC. The outer dc-link controller for the GSC is neglected in this subsection and will be connected as an added subsystem in the coming subsection. With reference to Fig. 3.16, the voltage v_f at the terminal of the GSC in the frequency domain can be expressed as

$$\underline{v}_f^{(dq)}(s) = (R_f + sL_f)\,\underline{i}_f^{(dq)}(s) + j\omega_s L_f \underline{i}_f^{(dq)}(s) + \underline{v}_g^{(dq)}(s) \tag{3.54}$$

The expression for the GSC current controller as described in (3.28) is repeated here

$$\underline{v}_f^{*(dq)}(s) = F_{cc,f}(s)\left(\underline{i}_f^{*(dq)}(s) - \underline{i}_f^{(dq)}(s)\right) + j\omega_s L_f \underline{i}_f^{(dq)}(s) + H_{LP}(s)\,\underline{v}_g^{(dq)}(s) \tag{3.55}$$

where $F_{cc,f}(s) = k_{pf,cc} + \frac{k_{if,cc}}{s}$ is a PI controller with $k_{pf,cc} = \alpha_{cc,f} L_f$ and $k_{if,cc} = \alpha_{cc,f} R_f$. Again assuming $\underline{v}_f^{(dq)} = \underline{v}_f^{*(dq)}$, (3.54) and (3.55) can be be expressed as

$$\mathbf{M}_{fcc,i}\mathbf{i}_f = \mathbf{M}_{fcc,ref}\mathbf{i}_f^* + \mathbf{M}_{fcc,vg}\mathbf{v}_g \tag{3.56}$$

where

$$\mathbf{i}_f = \begin{bmatrix} i_{f,d}(s) \\ i_{f,q}(s) \end{bmatrix}, \mathbf{i}_f^* = \begin{bmatrix} i_{f,d}^*(s) \\ i_{f,q}^*(s) \end{bmatrix}, \mathbf{v}_g = \begin{bmatrix} v_{g,d}(s) \\ v_{g,q}(s) \end{bmatrix}$$

$$\mathbf{M}_{fcc,i} = \begin{bmatrix} R_f + sL_f + F_{cc,f}(s) & 0 \\ 0 & R_f + sL_f + F_{cc,f}(s) \end{bmatrix}$$

$$\mathbf{M}_{fcc,ref} = \begin{bmatrix} F_{cc,f}(s) & 0 \\ 0 & F_{cc,f}(s) \end{bmatrix}, \mathbf{M}_{fcc,vg} = \begin{bmatrix} H_{LP}(s) - 1 & 0 \\ 0 & H_{LP}(s) - 1 \end{bmatrix}$$

In the same manner as in the previous subsection, the losses and phase-shift due to the three-winding transformer are neglected. However, considering the transformer's ratio (k_{tr2}) between the grid-filter side and the generator terminal side (see Fig. 3.16), the voltage vector $\mathbf{v}_g$ can be expressed as

$$\mathbf{v}_g = k_{tr2}\mathbf{v}_t \tag{3.57}$$

Inserting (3.57) into (3.56), the model of the grid-side filter connected to the GSC with a current controller in terms of the terminal input voltage, the actual and reference filter currents is given by

$$\mathbf{M}_{fcc,i}\mathbf{i}_f = \mathbf{M}_{fcc,ref}\mathbf{i}_f^* + \mathbf{M}_{fcc,v}\mathbf{v}_t \tag{3.58}$$

with

$$\mathbf{M}_{fcc,v} = k_{tr2}\mathbf{M}_{fcc,vg}$$

3.4.3 Combined WRIG, RSC and GSC current controllers

In Subsections 3.4.1, the WRIG together with rotor-side current controller has been expressed as a single subsystem having terminal voltage ($\mathbf{v}_t$) and rotor current reference ($\mathbf{i}_R^*$) as input and currents as outputs (refer to equation (3.50)). Similarly, in Subsection 3.4.2, the grid-side filter along with the GSC current controller has been described using transfer function matrices having terminal voltage ($\mathbf{v}_t$) and filter current reference ($\mathbf{i}_f^*$) as input is shown in (3.58). Combining the two subsystems, a simplified DFIG model neglecting the outer-loop controllers both for the RSC and GSC can be obtained. Using (3.50) and (3.58), the cascaded system is expressed as

$$\mathbf{M}_{grcc,i}\mathbf{i} = \mathbf{M}_{grcc,ref}\mathbf{i}_{ref}^* + \mathbf{M}_{grcc,v}\mathbf{v}_t \tag{3.59}$$

with

$$\mathbf{M}_{grcc,i} = \begin{bmatrix} \mathbf{M}_{gcc,i} & \mathbf{P}_1 \\ \mathbf{P}_1^T & \mathbf{M}_{fcc,i} \end{bmatrix}, \qquad \mathbf{M}_{grcc,ref} = \begin{bmatrix} \mathbf{M}_{gcc,ref} & \mathbf{P}_1 \\ \mathbf{P}_2 & \mathbf{M}_{fcc,ref} \end{bmatrix}$$

$$\mathbf{M}_{grcc,v} = \begin{bmatrix} \mathbf{M}_{gcc,v} \\ \mathbf{M}_{fcc,v} \end{bmatrix}, \qquad \mathbf{i} = \begin{bmatrix} \mathbf{i}_g \\ \mathbf{i}_f \end{bmatrix} = \begin{bmatrix} \mathbf{i}_s \\ \mathbf{i}_R \\ \mathbf{i}_f \end{bmatrix}, \qquad \mathbf{i}_{ref}^* = \begin{bmatrix} \mathbf{i}_R^* \\ \mathbf{i}_f^* \end{bmatrix}$$

$$\mathbf{P}_1 = zeros\,[4{\times}2]\,, \qquad \mathbf{P}_2 = zeros\,[2{\times}2]$$

In a similar manner, the expression in (3.59) can be rearranged to generate the admittance and reference matrices as

$$\mathbf{i} = \mathbf{G}_{grcc}\mathbf{i}_{ref}^* + \mathbf{Y}_{grcc}\mathbf{v}_t \tag{3.60}$$

with matrices $\mathbf{G}_{grcc}$ and $\mathbf{Y}_{grcc}$ expressed as

$$\begin{aligned} \mathbf{G}_{grcc} &= \mathbf{M}_{grcc,i}^{-1}\mathbf{M}_{grcc,ref} = \begin{bmatrix} \mathbf{G}_{grcc,is}^{iRref} & \mathbf{P}_2 \\ \mathbf{G}_{grcc,iR}^{iRref} & \mathbf{P}_2 \\ \mathbf{P}_2 & \mathbf{G}_{grcc,if}^{ifref} \end{bmatrix} \\ \mathbf{Y}_{grcc} &= \mathbf{M}_{grcc,i}^{-1}\mathbf{M}_{grcc,v} = \begin{bmatrix} \mathbf{Y}_{grcc,is} \\ \mathbf{Y}_{grcc,iR} \\ \mathbf{Y}_{grcc,if} \end{bmatrix} \end{aligned} \tag{3.61}$$

where

- $\mathbf{G}_{grcc,is}^{iRref}$ is a 2×2 transfer function matrix expressing the relation from $\underline{i}_R^{*(dq)}$ to $\underline{i}_s^{(dq)}$.
- $\mathbf{G}_{grcc,iR}^{iRref}$ is a transfer function matrix of size 2×2 expressing the relation from $\underline{i}_R^{*(dq)}$ to $\underline{i}_R^{(dq)}$.
- $\mathbf{G}_{grcc,if}^{ifref}$ represents the transfer function relation from $\underline{i}_f^{*(dq)}$ to $\underline{i}_f^{(dq)}$.
- $\mathbf{Y}_{grcc,is}$ represents the transfer function matrix from terminal voltage ($\underline{v}_t^{(dq)}$) to stator current ($\underline{i}_s^{(dq)}$).
- $\mathbf{Y}_{grcc,if}$ is the transfer function matrix from terminal voltage ($\underline{v}_t^{(dq)}$) to filter current ($\underline{i}_f^{(dq)}$).

Observing (3.60), the system with WRIG, RSC current controller and the GSC current controller is represented in a transfer function matrix form explicitly defined as matrices affecting the reference term and matrices affecting the admittance term.

3.4.4 Active and reactive power controllers

The outer control-loops are based on a PI controllers that control the terminal active and reactive power of the DFIG. For the convenience of the reader, the expression for the controller are repeated

$$\begin{aligned} i_{R,d}^{*}(s) &= F_{Qc}\left(Q_{out}^{*} - H_{LP,Q}Q_{out}\right) \\ i_{R,q}^{*}(s) &= F_{Pc}\left(P_{out}^{*} - H_{LP,p}P_{out}\right) \end{aligned} \tag{3.62}$$

where

$$F_{Pc} = k_{p,p}\left(1 + \frac{1}{sT_{i,p}}\right), \quad F_{Qc} = k_{p,Q}\left(1 + \frac{1}{sT_{i,Q}}\right), \quad H_{LP,p} = H_{LP,Q} = \frac{\alpha_{LP,p}}{s + \alpha_{LP,p}}$$

The expression for the terminal powers, P_{out} and Q_{out} are

$$\begin{aligned} P_{out} &= 3\left(-v_{s,d}i_{s,d} - v_{s,q}i_{s,q} + v_{g,d}i_{f,d} + v_{g,q}i_{f,q}\right) \\ Q_{out} &= 3\left(v_{s,d}i_{s,q} - v_{s,q}i_{s,d} - v_{g,d}i_{f,q} + v_{g,q}i_{f,d}\right) \end{aligned} \tag{3.63}$$

It should be noted that the inclusion of the power controllers introduces non-linearities in the system. Hence, (3.62) can be linearized as

$$\begin{aligned} \Delta i_{R,d}^{*} &= F_{Qc}\left(\Delta Q_{out}^{*} - H_{LP,Q}\Delta Q_{out}\right) \\ \Delta i_{R,q}^{*} &= F_{Pc}\left(\Delta P_{out}^{*} - H_{LP,p}\Delta P_{out}\right) \end{aligned} \tag{3.64}$$

here represented using transfer function matrices as

$$\begin{bmatrix} \Delta i_{R,d}^{*} \\ \Delta i_{R,d}^{*} \end{bmatrix} = \mathbf{F}_{PQc}\begin{bmatrix} \Delta P_{out}^{*} \\ \Delta Q_{out}^{*} \end{bmatrix} - \mathbf{F}_{PQc}H_{LP,p}\begin{bmatrix} \Delta P_{out} \\ \Delta Q_{out} \end{bmatrix} \tag{3.65}$$

with

$$\mathbf{F}_{PQc} = \begin{bmatrix} 0 & F_{Qc} \\ F_{Pc} & 0 \end{bmatrix}$$

Linearization of the power expression in (3.63) results in

$$\begin{aligned} \begin{bmatrix} \Delta P_{out} \\ \Delta Q_{out} \end{bmatrix} &= \underbrace{\begin{bmatrix} -3v_{s,d0} & -3v_{s,q0} \\ -3v_{s,q0} & 3v_{s,d0} \end{bmatrix}}_{\mathbf{M}_{PQ,is}} \begin{bmatrix} \Delta i_{s,d} \\ \Delta i_{s,q} \end{bmatrix} + \underbrace{\begin{bmatrix} 3v_{g,d0} & 3v_{g,q0} \\ 3v_{g,q0} & -3v_{g,d0} \end{bmatrix}}_{\mathbf{M}_{PQ,if}} \begin{bmatrix} \Delta i_{f,d} \\ \Delta i_{f,q} \end{bmatrix} \\ &+ \underbrace{\begin{bmatrix} -3i_{s,d0} & -3i_{s,q0} \\ 3i_{s,q0} & -3i_{s,d0} \end{bmatrix}}_{\mathbf{M}_{PQ,vs}} \begin{bmatrix} \Delta v_{s,d} \\ \Delta v_{s,q} \end{bmatrix} + \underbrace{\begin{bmatrix} 3i_{f,d0} & 3i_{f,q0} \\ -3i_{f,q0} & 3i_{f,d0} \end{bmatrix}}_{\mathbf{M}_{PQ,vg}} \begin{bmatrix} \Delta v_{g,d} \\ \Delta v_{g,q} \end{bmatrix} \\ \begin{bmatrix} \Delta P_{out} \\ \Delta Q_{out} \end{bmatrix} &= \mathbf{M}_{PQ,is} \begin{bmatrix} \Delta i_{s,d} \\ \Delta i_{s,q} \end{bmatrix} + \mathbf{M}_{PQ,if} \begin{bmatrix} \Delta i_{f,d} \\ \Delta i_{f,q} \end{bmatrix} + \mathbf{M}_{PQ,v} \begin{bmatrix} \Delta v_{t,d} \\ \Delta v_{t,q} \end{bmatrix} \end{aligned} \tag{3.66}$$

where

$$\mathbf{M}_{PQ,v} = \mathbf{M}_{PQ,vs} + k_{tr2}\mathbf{M}_{PQ,vg}$$

The "0" in the subscript indicates initial conditions. Expression (3.66) can be conveniently expressed as

$$\begin{bmatrix} \Delta P_{out} \\ \Delta Q_{out} \end{bmatrix} = \underbrace{\begin{bmatrix} \mathbf{M}_{PQ,is} & \mathbf{P}_2 & \mathbf{M}_{PQ,if} \end{bmatrix}}_{\mathbf{M}_{PQ,i}} \Delta\mathbf{i} + \mathbf{M}_{PQ,v} \begin{bmatrix} \Delta v_{t,d} \\ \Delta v_{t,q} \end{bmatrix} \tag{3.67}$$

with

$$\Delta\mathbf{i} = \begin{bmatrix} \Delta i_{s,d} & \Delta i_{s,q} & \Delta i_{R,d} & \Delta i_{R,q} & \Delta i_{f,d} & \Delta i_{f,q} \end{bmatrix}^T$$

Equations (3.65) and (3.67) can be combined to generate the expression for the reference rotor currents $\begin{bmatrix} \Delta i^*_{R,d} \\ \Delta i^*_{R,d} \end{bmatrix}$ as

$$\begin{bmatrix} \Delta i^*_{R,d} \\ \Delta i^*_{R,d} \end{bmatrix} = \mathbf{F}_{PQc} \begin{bmatrix} \Delta P^*_{out} \\ \Delta Q^*_{out} \end{bmatrix} - \mathbf{F}_{PQc} H_{LP,p} \mathbf{M}_{PQ,i} \Delta\mathbf{i} - \mathbf{F}_{PQc} H_{LP,p} \mathbf{M}_{PQ,v} \begin{bmatrix} \Delta v_{t,d} \\ \Delta v_{t,q} \end{bmatrix} \tag{3.68}$$

Even with the numerous expression derived so far, the coupling between the subsystem constituting the WRIG and RSC, and the subsystem constituting the grid-side filter and GSC has not been accomplished yet. The RSC and GSC are electrically coupled through the dc-link capacitor. Hence the incorporation of the dc-link dynamics together with the implemented dc-link voltage controller is a crucial step.

3.4.5 DC-link voltage controller

Recalling the dc-link voltage controller that acts on q-component of the filter current, (3.39) can be rewritten as

$$i^*_{f,q} = F_{dc}\left(U^{*2}_{dc} - U^2_{dc}\right) + G_a U^2_{dc} \tag{3.69}$$

with

$$F_{dc} = k_{p,dc} + \frac{k_{i,dc}}{s}$$

with $k_{p,dc}$ and $k_{i,dc}$ as described in (3.37). Linearization around a steady-state operating point leads to

$$\Delta i^*_{f,q} = 2U^*_{dc0} F_{dc} \Delta U^*_{dc} + 2U_{dc0}\left(G_a - F_{dc}\right)\Delta U_{dc} \tag{3.70}$$

To obtain the expression for ΔU_{dc}, the dynamics of the dc-link capacitor are considered. The dc-link capacitor dynamics as described in Section 3.3.2 can be expressed in terms of the active power exchange between the RSC and the GSC. Under the assumption that both the RSC and GSC converter are ideal, meaning that the power on the dc-side is considered equivalent to the power on the ac-side, the expression for the dc-link capacitor can be written as

$$\frac{1}{2} C_{dc} \frac{dU^2_{dc}}{dt} = -P_f - P_R \tag{3.71}$$

Linearization of the above expression and transformation to the frequency domain results in

$$\Delta U_{dc} = \frac{-\Delta P_f - \Delta P_R}{C_{dc} U_{dc0} s} \tag{3.72}$$

The expression for $\Delta i^*_{f,q}$ in (3.70) can now be combined with (3.72) to obtain

$$\Delta i^*_{f,q} = m_{dcref} \Delta U^*_{dc} + m_p\left(\Delta P_f + \Delta P_R\right) \tag{3.73}$$

where

$$m_{dcref} = 2U^*_{dc0} F_{dc}, \qquad m_p = \frac{2\left(F_{dc} - G_a\right)}{C_{dc} s}$$

To further expand (3.73), linearized expression for power flowing into RSC and GSC are required. The active power flow from the GSC, using small signal, can be expressed as

$$\Delta P_f = \begin{bmatrix} 3v_{f,d0} & 3v_{f,q0} \end{bmatrix} \begin{bmatrix} \Delta i_{f,d} \\ \Delta i_{f,q} \end{bmatrix} + \begin{bmatrix} 3i_{f,d0} & 3i_{f,q0} \end{bmatrix} \begin{bmatrix} \Delta v_{f,d} \\ \Delta v_{f,q} \end{bmatrix} \tag{3.74}$$

The expression for the voltage ($\underline{v}_f$) at the terminal of the GSC (under the considered assumptions) can be extracted from (3.55) as

$$\begin{bmatrix} \Delta v_{f,d} \\ \Delta v_{f,q} \end{bmatrix} = \mathbf{M}_{fcc,ref} \begin{bmatrix} \Delta i^*_{f,d} \\ \Delta i^*_{f,q} \end{bmatrix} + \begin{bmatrix} -F_{cc,f} & -\omega_s L_f \\ \omega_s L_f & -F_{cc,f} \end{bmatrix} \Delta \mathbf{i}_f + \begin{bmatrix} k_{tr2} H_{LP} & 0 \\ 0 & k_{tr2} H_{LP} \end{bmatrix} \Delta \mathbf{v}_t \tag{3.75}$$

Combining (3.74) and (3.75), the linearized expression for ΔP_f can be rewritten as

$$\Delta P_f = \mathbf{M}_{Pfref} \begin{bmatrix} \Delta i^*_{f,d} \\ \Delta i^*_{f,q} \end{bmatrix} + \mathbf{M}_{Pfif} \Delta \mathbf{i}_f + \mathbf{M}_{Pfv} \Delta \mathbf{v}_t \tag{3.76}$$

where

$$\begin{aligned} \mathbf{M}_{Pfref} &= \begin{bmatrix} 3i_{f,d0} & 3i_{f,q0} \end{bmatrix} \mathbf{M}_{fcc,ref} \\ \mathbf{M}_{Pfif} &= \begin{bmatrix} 3v_{f,d0} & 3v_{f,q0} \end{bmatrix} + \begin{bmatrix} 3i_{f,d0} & 3i_{f,q0} \end{bmatrix} \begin{bmatrix} -F_{cc,f} & -\omega_s L_f \\ \omega_s L_f & -F_{cc,f} \end{bmatrix} \\ \mathbf{M}_{Pfv} &= \begin{bmatrix} 3i_{f,d0} & 3i_{f,q0} \end{bmatrix} \begin{bmatrix} k_{tr2} H_{LP} & 0 \\ 0 & k_{tr2} H_{LP} \end{bmatrix} \end{aligned}$$

The linearized expression for the power flowing out of the RSC can be expressed as

$$\Delta P_R = \begin{bmatrix} 3v_{R,d0} & 3v_{R,q0} \end{bmatrix} \begin{bmatrix} \Delta i_{R,d} \\ \Delta i_{R,q} \end{bmatrix} + \begin{bmatrix} 3i_{R,d0} & 3i_{R,q0} \end{bmatrix} \begin{bmatrix} \Delta v_{R,d} \\ \Delta v_{R,q} \end{bmatrix} \tag{3.77}$$

Since the expression for $\mathbf{v}_R$ in (3.48) is linear, $\begin{bmatrix} \Delta v_{R,d} \\ \Delta v_{R,q} \end{bmatrix}$ can be obtained from the same expression as

$$\begin{bmatrix} \Delta v_{R,d} \\ \Delta v_{R,q} \end{bmatrix} = \mathbf{F}_{cc,R} \begin{bmatrix} \Delta i^*_{R,d} \\ \Delta i^*_{R,d} \end{bmatrix} + \mathbf{M}_{cc,R} \Delta \mathbf{i}_g + \mathbf{M}_{cc,v} \Delta \mathbf{v}_t \tag{3.78}$$

The combination of (3.77) and (3.78) results in

$$\Delta P_R = \mathbf{M}_{PRref} \begin{bmatrix} \Delta i^*_{R,d} \\ \Delta i^*_{R,d} \end{bmatrix} + \mathbf{M}_{PRig} \Delta \mathbf{i}_g + \mathbf{M}_{PRv} \Delta \mathbf{v}_t \tag{3.79}$$

where

$$\begin{aligned} \mathbf{M}_{PRref} &= \begin{bmatrix} 3i_{R,d0} & 3i_{R,q0} \end{bmatrix} \mathbf{F}_{cc,R} \\ \mathbf{M}_{PRig} &= \begin{bmatrix} 3i_{R,d0} & 3i_{R,q0} \end{bmatrix} \mathbf{M}_{cc,R} + \begin{bmatrix} 0 & 0 & 3v_{R,d0} & 3v_{R,q0} \end{bmatrix} \\ \mathbf{M}_{PRv} &= \begin{bmatrix} 3i_{R,d0} & 3i_{R,q0} \end{bmatrix} \mathbf{M}_{cc,v} \end{aligned}$$

The expression for ΔP_R in (3.79) in combination with the expression for $\begin{bmatrix} \Delta i^*_{R,d} \\ \Delta i^*_{R,d} \end{bmatrix}$ in (3.68) and ΔP_f in (3.76) can be manipulated to obtain

$$\Delta P_f + \Delta P_R = \mathbf{M}_{Pfref} \begin{bmatrix} \Delta i^*_{f,d} \\ \Delta i^*_{f,q} \end{bmatrix} + \mathbf{M}_{PRref} \mathbf{F}_{PQc} \begin{bmatrix} \Delta P^*_{out} \\ \Delta Q^*_{out} \end{bmatrix} + \mathbf{M}_{ifrefi} \Delta \mathbf{i} + \mathbf{M}_{ifrefv} \Delta \mathbf{v}_t \tag{3.80}$$

where

$$\mathbf{M}_{ifrefi} = \left[\begin{array}{cc} \mathbf{M}_{PRig} & \mathbf{M}_{Pfif} \end{array} \right] - \mathbf{M}_{PRref}\mathbf{F}_{PQc}\mathbf{H}_{LP,p}\mathbf{M}_{PQ,i}$$
$$\mathbf{M}_{ifrefv} = \mathbf{M}_{PRv} + \mathbf{M}_{Pfv} - \mathbf{M}_{PRref}\mathbf{F}_{PQc}\mathbf{H}_{LP,p}\mathbf{M}_{PQ,v}$$

Inserting (3.80) into (3.73) results in

$$\begin{aligned} \Delta i^*_{f,q} = m_{dcref}\Delta U^*_{dc} + m_p\mathbf{M}_{Pfref}\left[\begin{array}{c} \Delta i^*_{f,d} \\ \Delta i^*_{f,q} \end{array} \right] + m_p\mathbf{M}_{PRref}\mathbf{F}_{PQc}\left[\begin{array}{c} \Delta P^*_{out} \\ \Delta Q^*_{out} \end{array} \right] \\ + \quad m_p\mathbf{M}_{ifrefi}\Delta\mathbf{i} \quad + \quad m_p\mathbf{M}_{ifrefv}\Delta\mathbf{v}_t \end{aligned} \tag{3.81}$$

As it was presented in Section 3.3.2, the d-component of the filter current is controlled to zero by setting the reference value to zero. However for the ease of matrix manipulation, the expression for the reference d-component is here described as

$$\Delta i^*_{f,d} = \Delta i'^*_{f,d} \tag{3.82}$$

Combining (3.81) and (3.82) results in

$$\begin{aligned} \left[\begin{array}{c} \Delta i^*_{f,d} \\ \Delta i^*_{f,q} \end{array} \right] = \underbrace{\left[\begin{array}{cc} 1 & 0 \\ 0 & m_{dcref} \end{array} \right]}_{\mathbf{M}_{dcref}} \left[\begin{array}{c} \Delta i'^*_{f,d} \\ \Delta U^*_{dc} \end{array} \right] + \underbrace{\left[\begin{array}{c} \mathbf{P}_3 \\ m_p\mathbf{M}_{Pfref} \end{array} \right]}_{\mathbf{M}_{dcif}} \left[\begin{array}{c} \Delta i^*_{f,d} \\ \Delta i^*_{f,q} \end{array} \right] \\ + \underbrace{\left[\begin{array}{c} \mathbf{P}_3 \\ m_p\mathbf{M}_{PRref}\mathbf{F}_{PQc} \end{array} \right]}_{\mathbf{M}_{pdcref}} \left[\begin{array}{c} \Delta P^*_{out} \\ \Delta Q^*_{out} \end{array} \right] + \underbrace{\left[\begin{array}{c} \mathbf{P}_4 \\ m_p\mathbf{M}_{ifrefi} \end{array} \right]}_{\mathbf{M}_{dci}} \Delta\mathbf{i} + \underbrace{\left[\begin{array}{c} \mathbf{P}_3 \\ m_p\mathbf{M}_{ifrefv} \end{array} \right]}_{\mathbf{M}_{dcv}} \Delta\mathbf{v}_t \end{aligned} \tag{3.83}$$

where $\mathbf{P}_3$ and $\mathbf{P}_4$ are vectors of zero with size corresponding to

$$\mathbf{P}_3 = \text{zeros}\left[1\times 2\right], \qquad \mathbf{P}_4 = \text{zeros}\left[1\times 6\right]$$

Following some matrix manipulation, the reference filter current expression can be obtained as

$$\begin{aligned} \left[\begin{array}{c} \Delta i^*_{f,d} \\ \Delta i^*_{f,q} \end{array} \right] = \mathbf{M}_{dc}\mathbf{M}_{dcref}\left[\begin{array}{c} \Delta i'^*_{f,d} \\ \Delta U^*_{dc} \end{array} \right] + \mathbf{M}_{dc}\mathbf{M}_{pdcref}\left[\begin{array}{c} \Delta P^*_{out} \\ \Delta Q^*_{out} \end{array} \right] \\ + \quad \mathbf{M}_{dc}\mathbf{M}_{dci}\Delta\mathbf{i} + \mathbf{M}_{dc}\mathbf{M}_{dcv}\Delta\mathbf{v}_t \end{aligned} \tag{3.84}$$

where, denoting with $\mathbf{I}$ a 2×2 identity matrix, the matrix $\mathbf{M}_{dc}$ is defined as

$$\mathbf{M}_{dc} = \left[\mathbf{I} - \mathbf{M}_{dcif}\right]^{-1}$$

Equation (3.84) gives the representation of the reference filter current ($\Delta\underline{i}^*_f$) in terms of input references (ΔP^*_{out}, ΔQ^*_{out}, $\Delta i'^*_{f,d}$ and ΔU^*_{dc}), input terminal voltage ($\Delta\underline{v}_t$) and currents ($\Delta\underline{i}_s$, $\Delta\underline{i}_R$ and $\Delta\underline{i}_f$). This expression is used in the next section, where the various subsystems are combined to obtain the overall system model.

3.4.6 Combined subsystems

In Section (3.4.3), a combined subsystem consisting of the WRIG, the RSC and GSC current controller has been generated leading to a structure defined in (3.60) that can be expressed in small-signal as

$$\Delta \mathbf{i} = \mathbf{G}_{grcc} \Delta \mathbf{i}^*_{ref} + \mathbf{Y}_{grcc} \Delta \mathbf{v}_t \tag{3.85}$$

where

$$\Delta \mathbf{i}^*_{ref} = \begin{bmatrix} \Delta i^*_{R,d} & \Delta i^*_{R,q} & \Delta i^*_{f,d} & \Delta i^*_{f,q} \end{bmatrix}^T$$

To incorporate the outer-controller loops using the expressions derived in Sections 3.4.4 and 3.4.5, (3.68) and (3.84) are combined as

$$\begin{aligned} \Delta \mathbf{i}^*_{ref} = & \begin{bmatrix} \mathbf{F}_{PQc} & \mathbf{P}_2 \\ \mathbf{M}_{dc}\mathbf{M}_{pdcref} & \mathbf{M}_{dc}\mathbf{M}_{dcref} \end{bmatrix} \begin{bmatrix} \Delta P^*_{out} \\ \Delta Q^*_{out} \\ \Delta i'^*_{f,d} \\ \Delta U^*_{dc} \end{bmatrix} \\ & + \begin{bmatrix} -\mathbf{F}_{PQc}\mathbf{H}_{LP,p}\mathbf{M}_{PQ,i} \\ \mathbf{M}_{dc}\mathbf{M}_{dci} \end{bmatrix} \Delta \mathbf{i} + \begin{bmatrix} -\mathbf{F}_{PQc}\mathbf{H}_{LP,p}\mathbf{M}_{PQ,v} \\ \mathbf{M}_{dc}\mathbf{M}_{dcv} \end{bmatrix} \Delta \mathbf{v}_t \end{aligned} \tag{3.86}$$

Inserting (3.86) into (3.85) and following some matrix manipulation

$$\Delta \mathbf{i} = \mathbf{G}_{\text{tot}} \begin{bmatrix} \Delta P^*_{out} \\ \Delta Q^*_{out} \\ \Delta i'^*_{f,d} \\ \Delta U^*_{dc} \end{bmatrix} + \mathbf{Y}_{\text{tot}} \Delta \mathbf{v}_t \tag{3.87}$$

with

$$\begin{aligned} \mathbf{G}_{\text{tot}} &= \mathbf{G}_{\text{I}} \left\{ \mathbf{G}_{grcc} \begin{bmatrix} \mathbf{F}_{PQc}\mathbf{H}_{LP,p} & \mathbf{P}_2 \\ \mathbf{M}_{dc}\mathbf{M}_{pdcref} & \mathbf{M}_{dc}\mathbf{M}_{dcref} \end{bmatrix} \right\} \\ \mathbf{Y}_{\text{tot}} &= \mathbf{G}_{\text{I}} \left\{ \mathbf{G}_{grcc} \begin{bmatrix} -\mathbf{F}_{PQc}\mathbf{H}_{LP,p}\mathbf{M}_{PQ,v} \\ \mathbf{M}_{dc}\mathbf{M}_{dcv} \end{bmatrix} + \mathbf{Y}_{grcc} \right\} \\ \mathbf{G}_{\text{I}} &= \left\{ \mathbf{I}_{6\text{x}6} - \mathbf{G}_{grcc} \begin{bmatrix} -\mathbf{F}_{PQc}\mathbf{H}_{LP,p}\mathbf{M}_{PQ,i} \\ \mathbf{M}_{dc}\mathbf{M}_{dci} \end{bmatrix} \right\}^{-1} \end{aligned}$$

The admittance transfer function matrix ($\mathbf{Y}_{\text{tot}}$) is a 6×2 transfer function matrix constituting the relation from terminal voltage $\underline{v}_t$ to $\underline{i}_s$, $\underline{i}_R$ and $\underline{i}_f$. The matrix $\mathbf{G}_{\text{tot}}$ is a 6×4 transfer function matrix showing the relation from reference input to currents $\underline{i}_s$, $\underline{i}_R$ and $\underline{i}_f$. The various transfer functions from matrices $\mathbf{G}_{\text{tot}}$ and $\mathbf{Y}_{\text{tot}}$ can be used to define new transfer functions matrices for the individual currents as

$$\begin{bmatrix} \Delta i_{s,d} \\ \Delta i_{s,q} \end{bmatrix} = \mathbf{G}_{\text{tot,is}} \begin{bmatrix} \Delta P^*_{out} \\ \Delta Q^*_{out} \\ \Delta i'^*_{f,d} \\ \Delta U^*_{dc} \end{bmatrix} + \mathbf{Y}_{\text{tot,is}} \begin{bmatrix} \Delta v_{t,d} \\ \Delta v_{t,q} \end{bmatrix} \tag{3.88}$$

$$\begin{bmatrix} \Delta i_{R,d} \\ \Delta i_{R,q} \end{bmatrix} = \mathbf{G}_{\text{tot,iR}} \begin{bmatrix} \Delta P^*_{out} \\ \Delta Q^*_{out} \\ \Delta i'^*_{f,d} \\ \Delta U^*_{dc} \end{bmatrix} + \mathbf{Y}_{\text{tot,iR}} \begin{bmatrix} \Delta v_{t,d} \\ \Delta v_{t,q} \end{bmatrix} \tag{3.89}$$

$$\begin{bmatrix} \Delta i_{f,d} \\ \Delta i_{f,q} \end{bmatrix} = \mathbf{G}_{\text{tot,if}} \begin{bmatrix} \Delta P^*_{out} \\ \Delta Q^*_{out} \\ \Delta i'^*_{f,d} \\ \Delta U^*_{dc} \end{bmatrix} + \mathbf{Y}_{\text{tot,if}} \begin{bmatrix} \Delta v_{t,d} \\ \Delta v_{t,q} \end{bmatrix} \tag{3.90}$$

with

$$\mathbf{G}_{\text{tot}} = \begin{bmatrix} \mathbf{G}_{\text{tot,is}} \\ \mathbf{G}_{\text{tot,iR}} \\ \mathbf{G}_{\text{tot,if}} \end{bmatrix}, \qquad \mathbf{Y}_{\text{tot}} = \begin{bmatrix} \mathbf{Y}_{\text{tot,is}} \\ \mathbf{Y}_{\text{tot,iR}} \\ \mathbf{Y}_{\text{tot,if}} \end{bmatrix}$$

Observing (3.88), the transfer function matrix ($\mathbf{Y}_{\text{tot,is}}$) represents the admittance viewed from the DFIG terminal into the generator stator where as the transfer function matrix ($\mathbf{Y}_{\text{tot,if}}$) in (3.90) represents the admittance matrix as viewed from the terminal into the grid-side filter. From the terminal of the DFIG, these two admittances appear to be connected in parallel. Hence the total terminal current expression can be expressed as

$$\begin{bmatrix} \Delta i_{t,d} \\ \Delta i_{t,q} \end{bmatrix} = \mathbf{G}_{\text{DFIG}} \begin{bmatrix} \Delta P^*_{out} \\ \Delta Q^*_{out} \\ \Delta i'^*_{f,d} \\ \Delta U^*_{dc} \end{bmatrix} + \mathbf{Y}_{\text{DFIG}} \begin{bmatrix} \Delta v_{t,d} \\ \Delta v_{t,q} \end{bmatrix} \tag{3.91}$$

where $\mathbf{G}_{\text{DFIG}} = \mathbf{G}_{\text{tot,is}} - \mathbf{G}'_{\text{tot,if}}$. The admittance transfer function matrix for the DFIG as viewed from the terminal into the generator can be obtained as

$$\mathbf{Y}_{\text{DFIG}} = \mathbf{Y}_{\text{tot,is}} - \mathbf{Y}'_{\text{tot,if}} = \begin{bmatrix} \text{Y}_{\text{DFIG,dd}} & \text{Y}_{\text{DFIG,dq}} \\ \text{Y}_{\text{DFIG,qd}} & \text{Y}_{\text{DFIG,qq}} \end{bmatrix} \tag{3.92}$$

where $\mathbf{Y}'_{\text{tot,if}}$ and $\mathbf{G}'_{\text{tot,if}}$ are the transfer function $\mathbf{Y}_{\text{tot,if}}$ and $\mathbf{G}_{\text{tot,if}}$ transformed to the high voltage-side of the three-winding transformer.

3.4.7 Phase-locked-loop

The phase-locked loop acting in a closed-loop manner aims to drive the d component of the PCC voltage in the DFIG dq frame to zero. The expression that is derived in (3.91) is expressed in

terms of currents and voltages that use the PLL angle for transformation for the input admittance model. To incorporate the PLL model dynamics, the dq frame model derived based on the angle extracted from the PLL, $\hat{\theta}_s$ (mostly referred to as DFIG reference frame), should be expressed in terms of the true grid angle θ_s where $d\theta_s/dt = \omega_s$. As a result, $\underline{v}_t$ that is a signal in the DFIG reference frame can be expressed in terms of a signal in the grid reference frame ,$\underline{v}_{t,g}$, as:

$$\underline{v}_t = \underline{v}_{t,g} e^{-j\left(\hat{\theta}_s - \theta_s\right)} = \underline{v}_{t,g} e^{-j\Delta\theta} \tag{3.93}$$

As described in Section 3.3.3, the PLL is a second-order system that drives the real part of the terminal voltage vector $\underline{v}_t$ to zero. Therefore, the frequency deviation within the PLL can be obtained as

$$\Delta\omega_s = \underbrace{\left(K_{p,PLL} + \frac{K_{i,PLL}}{s}\right)}_{F_{PLL}(s)} \left[\frac{-\mathrm{Re}\left\{\underline{v}_t\right\}}{|\underline{v}_t|}\right] \tag{3.94}$$

where the nominal angular synchronous frequency ω_s^0 is added. The transformation angle is obtained by integrating this expression as

$$\frac{d\hat{\theta}_s}{dt} = \omega_s^0 + \Delta\omega_s = \omega_s^0 + F_{PLL}(s) \left[\frac{-\mathrm{Re}\left\{\underline{v}_t\right\}}{|\underline{v}_t|}\right] \tag{3.95}$$

Linearization of the expression in (3.93) results in

$$\Delta\underline{v}_t = \Delta\underline{v}_{t,g} - j\underline{v}_{t,g0}\Delta\theta \tag{3.96}$$

where the real part can be expressed as

$$\mathrm{Re}\left\{\Delta\underline{v}_t\right\} = v_{tq,g0}\Delta\theta + \mathrm{Re}\left\{\Delta\underline{v}_{t,g}\right\} \tag{3.97}$$

The expression for $\frac{d\Delta\theta}{dt}$ can be described using $\frac{d\hat{\theta}_s}{dt} - \frac{d\theta_s}{dt}$ as

$$\frac{d\Delta\theta}{dt} = \omega_s^0 + \Delta\omega_s - \omega_s = F_{PLL}(s) \left[\frac{-\mathrm{Re}\left\{\underline{v}_t\right\}}{|\underline{v}_t|}\right] \tag{3.98}$$

since $\omega_s^0 = \omega_s$. Inserting the linearized d-component voltage given in (3.97) in (3.98) and rearranging, the angle deviation is

$$\Delta\theta = \frac{-F'_{PLL}(s)}{s + v_{tq,g0}F'_{PLL}(s)} \mathrm{Re}\left\{\Delta\underline{v}_t\right\} = G_{PLL}(s)\,\Delta v_{td,g} \tag{3.99}$$

where $F'_{PLL}(s) = F_{PLL}(s)/|\underline{v}_t|$. Using the expression in (3.96), the voltage in the DFIG rotating reference frame can be expressed in the grid rotating reference frame as

$$\begin{bmatrix} \Delta v_{t,d} \\ \Delta v_{t,q} \end{bmatrix} = \begin{bmatrix} 1 + v_{t,gq0}G_{PLL}(s) & 0 \\ 0 & 1 \end{bmatrix} \begin{bmatrix} \Delta v_{t,gd} \\ \Delta v_{t,gq} \end{bmatrix} = G_{\mathrm{V},PLL}(s) \begin{bmatrix} \Delta v_{t,gd} \\ \Delta v_{t,gq} \end{bmatrix} \tag{3.100}$$

In a similar manner, the terminal current in the grid rotating reference can be obtained as $\underline{i}_{t,g} = \underline{i}_t e^{j\Delta\theta}$. Linearizing this expression results in

$$\Delta\underline{i}_{t,g} = \Delta\underline{i}_t + j\underline{i}_{t,0}\Delta\theta \tag{3.101}$$

Inserting (3.99) in (3.101) and rearranging, the expression for current in the grid reference frame can be described as

$$\Delta\underline{i}_{t,g} = \Delta\underline{i}_t + j\underline{i}_{t,0}G_{PLL}\left(s\right)\Delta v_{t,gd}$$

$$\left[\begin{array}{c}\Delta i_{t,gd}\\ \Delta i_{t,gq}\end{array}\right] = \left[\begin{array}{c}\Delta i_{t,d}\\ \Delta i_{t,q}\end{array}\right] + \left[\begin{array}{cc}-i_{t,q0}G_{PLL}\left(s\right) & 0\\ i_{t,d0}G_{PLL}\left(s\right) & 0\end{array}\right]\left[\begin{array}{c}\Delta v_{t,gd}\\ \Delta v_{t,gq}\end{array}\right] = \left[\begin{array}{c}\Delta i_{t,d}\\ \Delta i_{t,q}\end{array}\right] + G_{\mathrm{C},PLL}\left(s\right)\left[\begin{array}{c}\Delta v_{t,gd}\\ \Delta v_{t,gq}\end{array}\right] \tag{3.102}$$

Substituting (3.100) and (3.102) into (3.91), the model in terms of current and voltages in the grid reference frame becomes

$$\left[\begin{array}{c}\Delta i_{t,gd}\\ \Delta i_{t,gq}\end{array}\right] = \mathbf{G}_{\mathrm{DFIG}}\left[\begin{array}{c}\Delta P^*_{out}\\ \Delta Q^*_{out}\\ \Delta i'^*_{f,d}\\ \Delta U^*_{dc}\end{array}\right] + \underbrace{\left\{\mathbf{Y}_{\mathrm{DFIG}}G_{\mathrm{V},PLL}\left(s\right) + G_{\mathrm{C},PLL}\left(s\right)\right\}}_{\mathrm{Y}'_{\mathrm{DFIG}}}\left[\begin{array}{c}\Delta v_{t,gd}\\ \Delta v_{t,gq}\end{array}\right] \tag{3.103}$$

where $\mathrm{Y}'_{\mathrm{DFIG}}$ is the DFIG admittance. Figure. 3.17, shows the admittance response of a DFIG turbine for the subsynchronous frequency range. The DFIG admittance matrix frequency response is observed to have negative value for the dd and qq components. Note that, being an unsymmetrical system, the fact that the real part of one or more components of the admittance matrix presents a negative real part does not directly imply that the DFIG negatively contributes to the system stability. In order to assess the ability of the DFIG to dissipate power in a specific frequency range, a different approach (as described in Section 3.5.2) must be used. In the sections to follow, the various components of the DFIG derived earlier are evaluated in the frequency domain to gain a better understanding of the DFIG behavior in the subsynchronous frequency range.

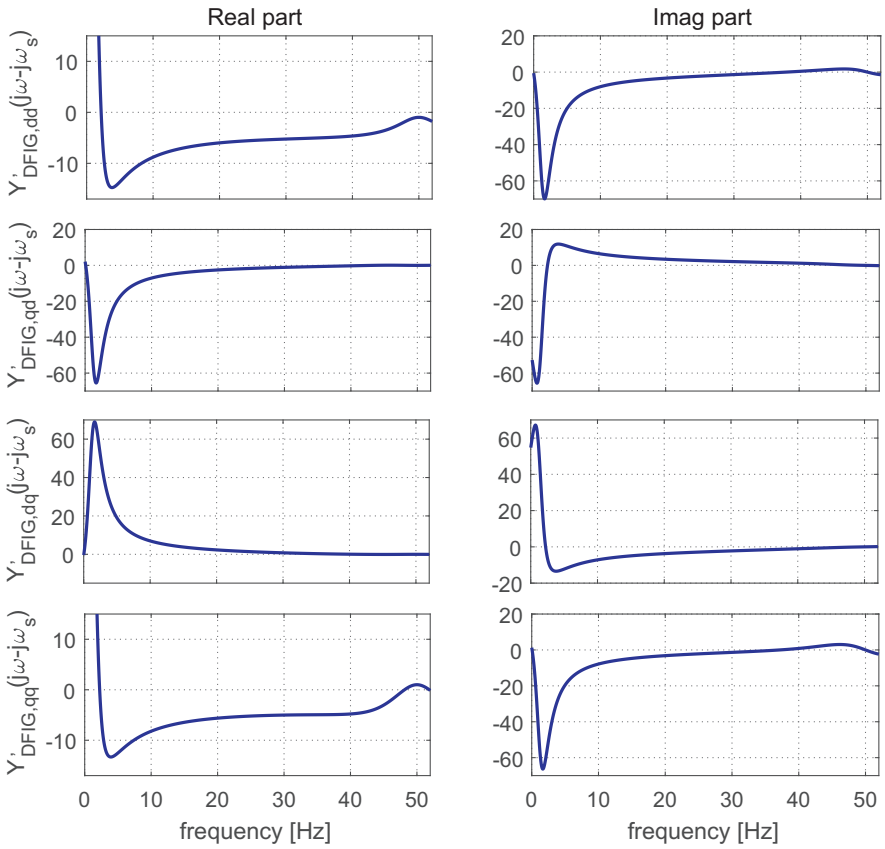

Fig. 3.17 Admittance matrix of a single DFIG wind turbine in the subsynchronous frequency range. Pout=1 pu, Qout=0 pu, $\alpha_{cc,R}$ = $\alpha_{cc,f}$ = 1 pu, α_{dc} = 0.1 pu

3.4.8 Model verification

To validate the derived linearized model of the DFIG, a full switching model implemented in PSCAD having the same parameters and control structure has been utilized. The DFIG model in PSCAD is a generic model developed for voltage-dip analysis, which has been verified against an actual wind turbine installed in Tvååker, Sweden [49]. Here, all control features related to low-voltage ride through (LVRT) have been disabled.

A frequency sweep is performed by imposing a balanced three phase voltage at the terminal having a fundamental frequency component and a harmonic frequency component with a pre-determined amplitude (5% of the fundamental). For every frequency sweep, the superimposed harmonic frequency is varied between 1 Hz and 48 Hz in steps of 1 Hz. When steady-state is reached, the current response is measured. From the measurements, the harmonic voltage and current components are extracted to obtain an average phase impedance/ admittance.

In order to easily compare the two models, a per-phase transfer function of the DFIG in the fixed $\alpha\beta$ frame has been considered. According to [31], the phase transfer function in $\alpha\beta$ can

be obtained from the dq model through averaging, as

$$\begin{aligned} \mathrm{Y}_{\mathrm{DFIG,avg}}(s) = \frac{1}{2}\left[\mathrm{Y}'_{\mathrm{DFIG},dd}(s-j\omega_s) + \mathrm{Y}'_{\mathrm{DFIG},qq}(s-j\omega_s)\right] + \\ j\frac{1}{2}\left[\mathrm{Y}'_{\mathrm{DFIG},qd}(s-j\omega_s) - \mathrm{Y}'_{\mathrm{DFIG},dq}(s-j\omega_s)\right] \end{aligned} \tag{3.104}$$

where $\mathrm{Y}'_{\mathrm{DFIG},dd}$, $\mathrm{Y}'_{\mathrm{DFIG},dq}$, $\mathrm{Y}'_{\mathrm{DFIG},qd}$ and $\mathrm{Y}'_{\mathrm{DFIG},qq}$ are the components of the derived input admittance $\mathrm{Y}'_{\mathrm{DFIG}}$. The validation has been performed for various operating points and controller parameters. For demonstration, two output power levels are presented: P_{out} = 0.72 pu and P_{out} = 0.25 pu. Depending on the selected reference power, the operating speed both for the mathematical model and the PSCAD simulation is determined using a look-up table and is assumed to be constant during the perturbation. The power level P_{out} = 0.72 pu corresponds to super-synchronous speed operation, where power flows out both from the stator and from the rotor of the machine. In this range of operation, the GSC operates as an inverter feeding power into the grid. Fig. 3.18 shows a comparison for the real and imaginary part of the admittance obtained using the linearized model and the PSCAD model.

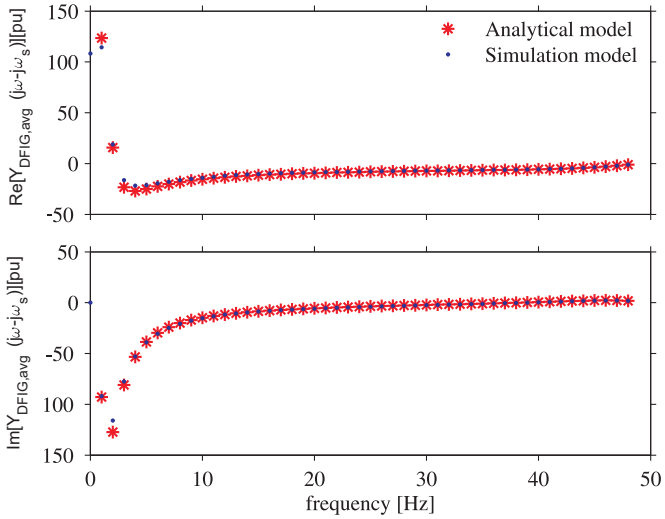

Fig. 3.18 DFIG mathematical model validation. Pout=0.72 pu, Qout=0 pu, $\alpha_{cc,R}$ = $\alpha_{cc,f}$ = 1 pu and α_{dc}=0.1 pu

The power level P_{out} = 0.25 pu corresponds to subsynchronous speed operations, where power is fed into the rotor from the grid via the BTB converter. Here the GSC operates as a rectifier. The model verification for this power range showing the real and imaginary part of the admittance is depicted in Fig. 3.19

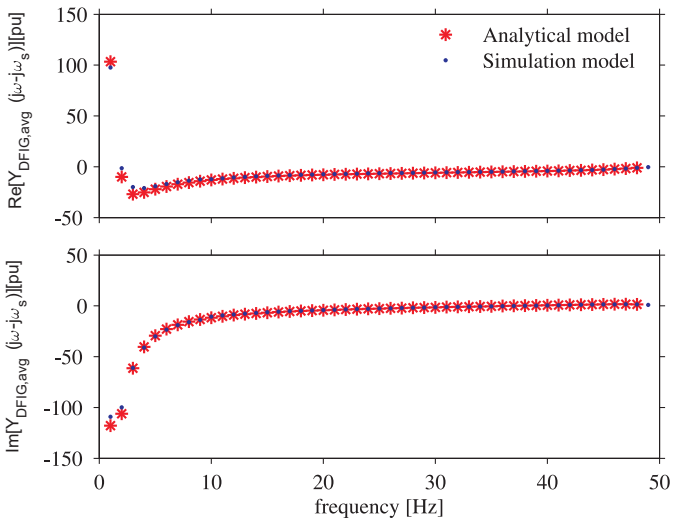

Fig. 3.19 DFIG mathematical model validation. Pout=0.25 pu, Qout=0 pu, $\alpha_{cc,R}$ = $\alpha_{cc,f}$ = 1 pu and α_{dc}=0.1 pu

The frequency sweeps performed in PSCAD show a very good agreement with the curve obtained using the linearized model. For the considered parameters, the DFIG is shown to exhibits a zero-crossing on the imaginary part of its admittance in the frequency range (36 Hz - 38 Hz), meaning that the DFIG exhibits a resonance that falls in the subsynchronous frequency. In addition, the real part of the input admittance has a negative value for most of the subsynchronous frequency. This indicates a potential risk of undamped oscillation in these range of frequencies.

3.5 Frequency-domain analysis for DFIG admittance

In Section 3.4, the admittance modeling for the overall DFIG turbine has been presented. The method has been proven to be an efficient approach for obtaining the frequency-domain based admittance model.

The DFIG mainly comprises of an induction generator with converters. Its behavior is therefore influenced by the behaviors of the induction generator and converters collectively. To just evaluate individually the various subsystems and arrive to a viable conclusion is not feasible. However the same approach can be used to identify system parameters and conditions that affect the various subsystem frequency response. Initially, the influence due to the induction generator is evaluated from an input admittance point of view.

3.5.1 Influence of induction generator

To evaluate the influence of the induction generator only, for the analysis carried out in this section, the converters are not considered and the rotor is short-circuited. Thus, the WRIG acts as a squirrel cage induction generator. This is a justified simplification as the aim is to alienate the effect of the induction generator from the one of the converter.

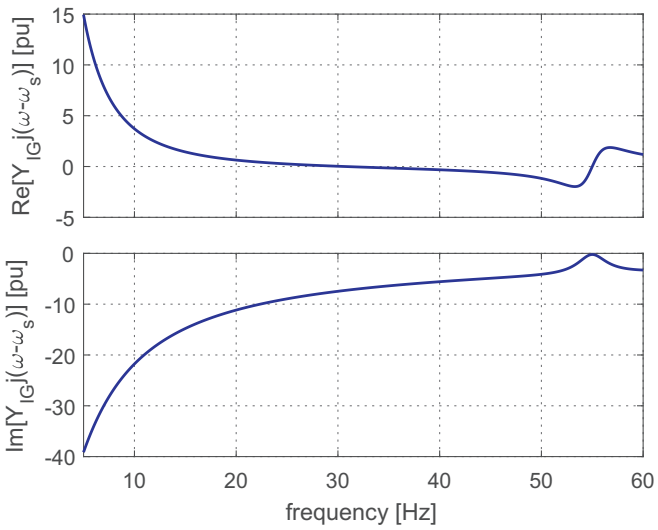

Fig. 3.20 Frequency domain input admittance of induction generator. $\omega_r = 1.1$ pu

From the transfer function matrix description for the WRIG given in (3.45), the admittance for the WRIG looking into the stator can be expressed as

$$\mathbf{i}_s = \mathbf{Y}_{IG}\mathbf{v}_s \tag{3.105}$$

where $\mathbf{Y}_{IG} = \mathbf{M}_g^{-1}\mathbf{M}_s\,[1:2,:]$. As the induction generator is symmetric in nature, the admittance can be extracted using a similar approach as in (3.53). Figure 3.20 shows the admittance plot for the induction generator that has a rotor electrical speed corresponding to $\omega_r = 1.1\omega_s$. The induction generator input admittance presents a negative real part for a range of frequencies below the synchronous frequency. This indicates that the induction generator is non-passive.

To analytically elaborate this, the steady-state equivalent circuit for the induction generator using the Γ- representation depicted in Fig. 3.21 is considered. The term s' indicates the slip term due to the slip associated with the rotor speed of rotation. Here, the input impedance is used to draw conclusions as the slip term can be interpreted in a simplified manner. In frequency domain, the slip term can be expressed as

$$s' = \frac{s - j\omega_r}{s} \tag{3.106}$$

where ω_r is the rotor electrical angular frequency. From the equivalent circuit (see Fig. 3.21), the impedance for the induction generator can be written (in the s-domain) as

$$Z_G(s) = R_s + \left(\frac{R_R}{s'} + sL_R\right)//sL_M \tag{3.107}$$

As the magnetizing inductance of the machine is much larger than the rotor inductance ($L_M >> L_R$), the parallel branch can be neglected and the above expression can be further simplified as

$$Z_G(s) = R_s + sL_R + \frac{R_R}{s'} \tag{3.108}$$

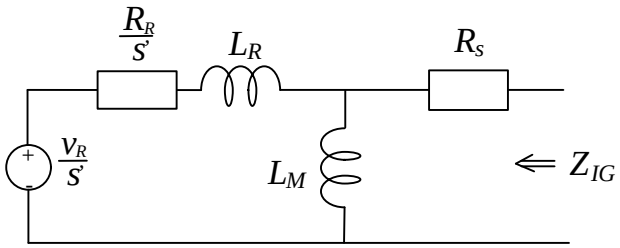

Fig. 3.21 Steady-state Γ- model equivalent circuit of an induction generator

Evaluating the relation in (3.108), there exists a term R_s that under the given assumptions, is frequency independent. The second term sL_R results in a positive-complex impedance that contributes to the imaginary part of the induction generator impedance. The third term, constituting of the ratio of the rotor resistance R_R and s' is the one attributing to the observed negative real part of the input admittance. For a fixed rotor speed, the negative value increases as the frequency approaches the synchronous frequency ω_s.

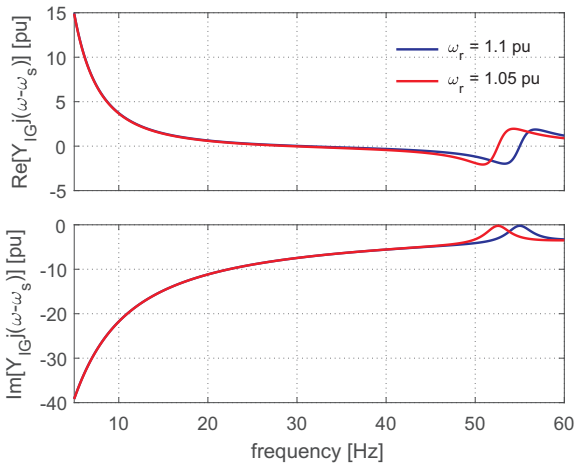

Fig. 3.22 Frequency domain input admittance of an induction generator for varied rotor speed. ω_r=1.05 pu (blue curve) and ω_r=1.1 pu (red curve)

To observe the influence of the rotor speed, the impedance of the generator for two different rotor speeds is plotted in Fig. 3.22. It can be observed that the curve with a higher rotor speed exhibits a lower negative resistance. This is associated with the fact that as the rotor speed increases, the term $|s'|$ get larger resulting in lower values of $\frac{R_R}{s'}$.

3.5.2 Influence of rotor-side converter

The impact of the rotor-side converter on the risk of SSCI has been reported in a number of works available in the literature, such as [52–54] to name a few. The admittance plot of the WRIG together with the RSC is shown in Fig. 3.23. For this analysis, the outer-loops have been neglected, meaning that the admittance is as the one derived in (3.53). Note that the obtained

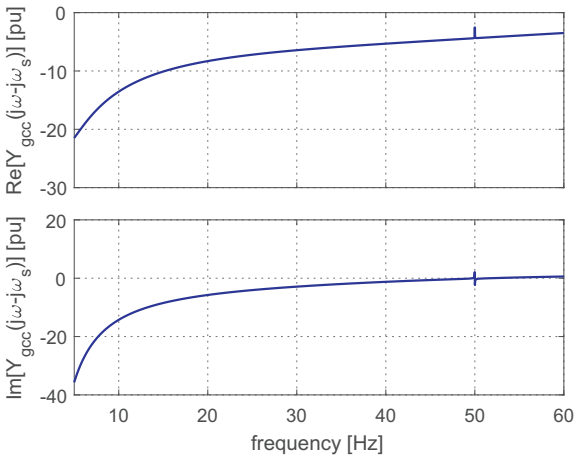

Fig. 3.23 Frequency domain input admittance of an induction generator with a current controller based voltage source attached to the rotor. Closed-loop bandwidth for the current controller, α_{cc}=1.0 pu.ω_r=1.1 pu

transfer function is still symmetrical. The system shows a negative real part throughout the entire subsynchronous frequency range. Comparing the result with the plots in Fig. 3.20, it can be observed that a higher negative real part occurs with the inclusion of the RSC current controller.

Consider the rotor voltage equation generated by the current controller presented in (3.47)

$$\underline{v}_R^{*(dq)}(s) = F_{cc,R}(s)\left(\underline{i}_R^{*(dq)}(s) - \underline{i}_R^{(dq)}(s)\right) + j\omega_2 L_R \underline{i}_R^{(dq)}(s) + H_{LP}(s)\,\underline{\hat{e}}_{emf}^{(dq)}(s) \tag{3.109}$$

For ease of analysis, the feed-forward term involving the back-EMF is neglected. Assuming $\underline{v}_R^{(dq)} = \underline{v}_R^{*(dq)}$, (3.109) results in

$$\underline{v}_R^{(dq)}(s) = F_{cc,R}(s)\,\underline{i}_R^{*(dq)}(s) - \left[F_{cc,R}(s) - jM_{dq}\right]\underline{i}_R^{(dq)}(s) \tag{3.110}$$

where jM_{dq} is the controller decoupling term. Moving the analysis to the stationary reference frame, the above expression can be rewritten as

$$\underline{v}_R(s) = F_{cc,R}(s - j\omega_s)\,\underline{i}_R^{*}(s) - \left[F_{cc,R}(s - j\omega_s) - jM_{dq}\right]\underline{i}_R(s) \tag{3.111}$$

From (3.111), the current controller can be expressed by a voltage source $v_{cc,R} = F_{cc,R}(s - j\omega_s)\,\underline{i}_R^*$ behind an impedance $Z_{cc,R}(s) = [F_{cc,R}(s - j\omega_s) - jM_{dq}]$. Fig. 3.24 shows the steady-state equivalent circuit representation of an induction generator with a rotor-side current controller. From an equivalent circuit point of view, the inclusion of the rotor-side current controller results in a frequency dependent complex impedance in series with a voltage source. Therefore, comparing the result for an induction generator (shown in Fig. 3.20) and an induction generator with a current controller (shown in Fig. 3.23), the consequences of having a current controller leads to a more negative for the latter. In addition, according to (3.111), the complex impedance ($Z_{cc,R}$) is influenced by parameter selection for the controller.

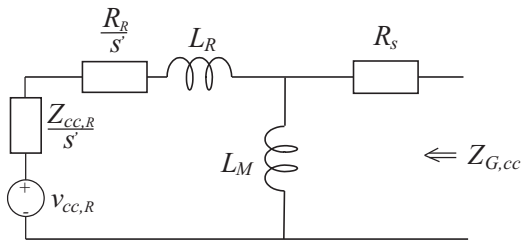

Fig. 3.24 Equivalent circuit diagram of an induction generator with current controller based voltage source connected to the rotor

Variation in rotor-side current controller bandwidth

Recalling that the RSC current controller is a proportional controller with gain, $k_{p,cc} = \alpha_{cc,R} L_R$, its impact can be evaluated by considering the closed-loop current controller bandwidth $\alpha_{cc,R}$. As the aim is to evaluate the weight of this parameter on the input admittance behavior for the DFIG subsystem, the overall input admittance model of the DFIG (i.e., including all control loops) derived in Section 3.4, is considered for the analysis. Figure 3.25 shows the DFIG input admittance for different values of $\alpha_{cc,R}$.

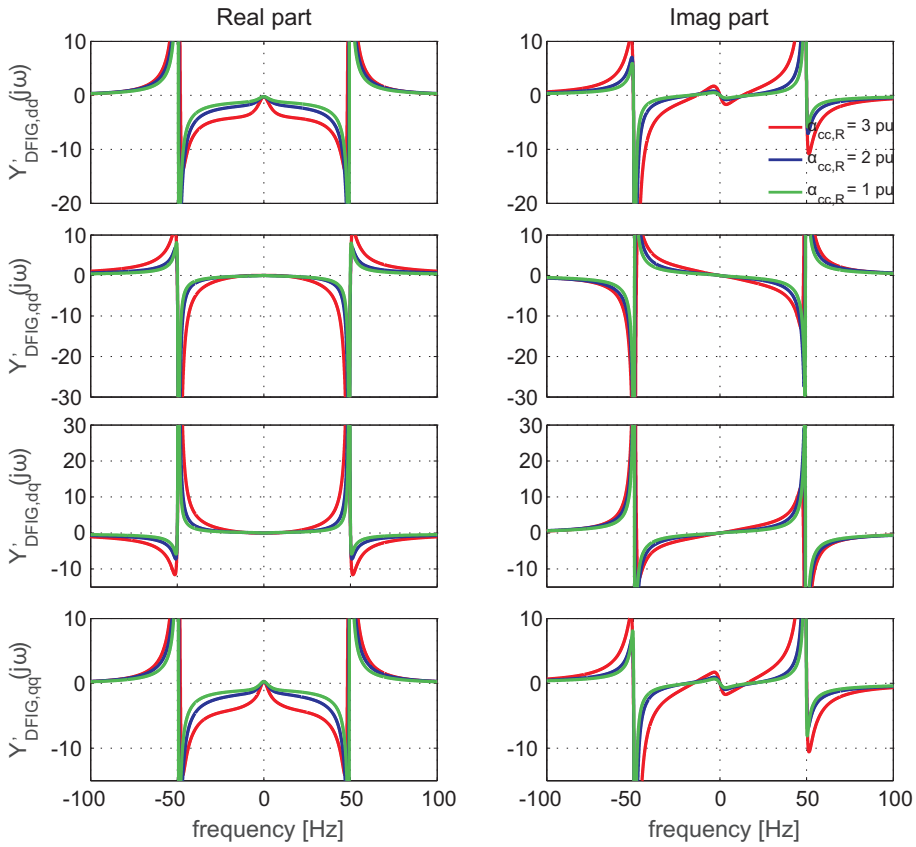

Fig. 3.25 DFIG input admittance for varied RSC current controller bandwidth. α_{CC} varied from 1 pu to 3 pu

Here, a constant output power corresponding to P_{out} = 1 pu and Q_{out} = 0 pu is assumed. The closed-loop current controller bandwidth for the GSC is set to $\alpha_{cc,f} = \alpha_{cc,R}$. The outer power controller gain is held at $k_{p,P}$ = 5 pu with an integrator time constant corresponding to $T_{i,P}$ = 0.2 sec. The loop bandwidth for the dc-link voltage controller is $\alpha_{dc} = 0.1\alpha_{cc,f}$ pu.

The presence of the outer control leads to the fact that the admittance matrix Y'_{DFIG} is asymmetrical. Assessing the impact of a control parameter on the input admittance behavior is not straightforward. For this reason, a difference compared with the analysis carried out in the previous section, it is needed to investigate all components of the matrix. For this purpose, the criterion based on power dissipation of asymmetrical system presented in [34] is adopted. Consider a generic system where the complex current and voltage phasors are related through complex admittance $\mathbf{Y}(j\omega)$. The input active power can be expressed as[2]

$$\begin{aligned} P &= \mathrm{Re}\left[\underline{vi}^*\right] = \frac{1}{3}\left[\mathbf{v}^H\mathbf{i} + \mathbf{i}^H\mathbf{v}\right] \\ &= \mathbf{v}^H\left[\mathbf{Y}(j\omega) + \mathbf{Y}^H(j\omega)\right]\mathbf{v} \end{aligned} \tag{3.112}$$

For the sake of simplicity, the matrix expression can be rewritten as

$$\mathbf{Y}(j\omega) + \mathbf{Y}^H(j\omega) = \begin{bmatrix} a_{11} & a_{12} \\ a_{21} & a_{22} \end{bmatrix} \tag{3.113}$$

$$\begin{aligned} a_{11} &= Y_{dd}(j\omega) + Y^*_{dd}(j\omega) = 2\mathrm{Re}\left\{Y_{dd}(j\omega)\right\} \\ a_{22} &= Y_{qq}(j\omega) + Y^*_{qq}(j\omega) = 2\mathrm{Re}\left\{Y_{qq}(j\omega)\right\} \\ a_{21} &= Y_{qd}(j\omega) + Y^*_{dq}(j\omega) = a^*_{12} \end{aligned}$$

According to [34] [55], the matrix $\mathbf{Y}(j\omega)$ is positive definite if $\mathbf{Y}(j\omega) + \mathbf{Y}^H(j\omega) > 0$, the system is dissipative. The above holds if the eigenvalues for $\mathbf{Y}(j\omega) + \mathbf{Y}^H(j\omega)$ are both positive for $\forall\omega$. Taking the determinant of the characteristics polynomial and equating to zero, the corresponding eigenvalues can be expressed as

$$\det\left[\lambda\mathbf{I} - \mathbf{Y}(j\omega) - \mathbf{Y}^H(j\omega)\right] = \lambda^2 - \lambda\left(a_{11} + a_{22}\right) + a_{11}a_{22} - |a_{21}|^2 = 0 \tag{3.114}$$

solving for λ in the above expression yields to

$$\lambda_{1,2} = \frac{1}{2}\left(\left(a_{11} + a_{22}\right) \pm \sqrt{\left(a_{11} - a_{22}\right)^2 + 4\left|a_{21}\right|^2}\right) \tag{3.115}$$

[2] the superscript H indicates the hermitian conjugate for the matrix

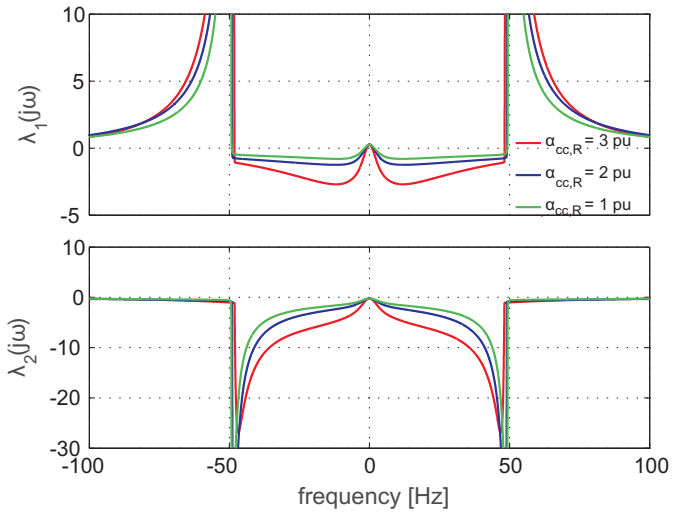

Fig. 3.26 Impact of RSC current controller bandwidth, $\alpha_{cc,R}$. $\alpha_{cc,R} = 1$ pu (*green*), $\alpha_{cc,R} = 2$ pu (*blue*) and $\alpha_{cc,R} = 3$ pu (*red*). λ_1 (*upper plot*), λ_2 (*lower plot*)

Using equation from (3.113)-(3.115), and replacing the Y with $\mathrm{Y}'_{\mathrm{DFIG}}$, the $\lambda_{1,2}$, for three different value of the RSC current controller bandwidth ($\alpha_{cc,R}$), is depicted in Fig. 3.26. From the figure, it can be observed that the frequency range where the DFIG exhibits a non-dissipative behavior increase with $\alpha_{cc,R}$ value. From the plots, it is evident that the system presents risk for poorly damped oscillation for frequencies below nominal frequency (50 Hz).

Variation in rotor-side converter outer-loop controller parameter

In general, the impact of the outer-loop power controller can be considered to be a critical issue during modeling. The outer-loop RSC controller introduces non-linearities in the DFIG system derivation (as can be observed from Section 3.4). As the power expression is known to affect the dc-link controller, this propagates to create an unsymmetrical input admittance matrix. The asymmetry plays a major role in the selection of analysis method to assess the system stability.

In [20] [21], the outer-loop controllers for the RSC and GSC have been neglected. As a result, the DFIG model could be drastically simplified and the analysis could be based on the classical Nyquist criterion. In this part, the impact of the outer-loop power controller parameters for the RSC is evaluated and the obtained frequency response is shown in Fig. 3.27. For this case study, the integrator time constant, $T_{i,p}$ = $T_{i,Q}$, has been varied from the orignal value of 0.2 sec. From the result, it is evident that the impact of the speed of response of the outer-loop power controller on the DFIG admittance is negligible.

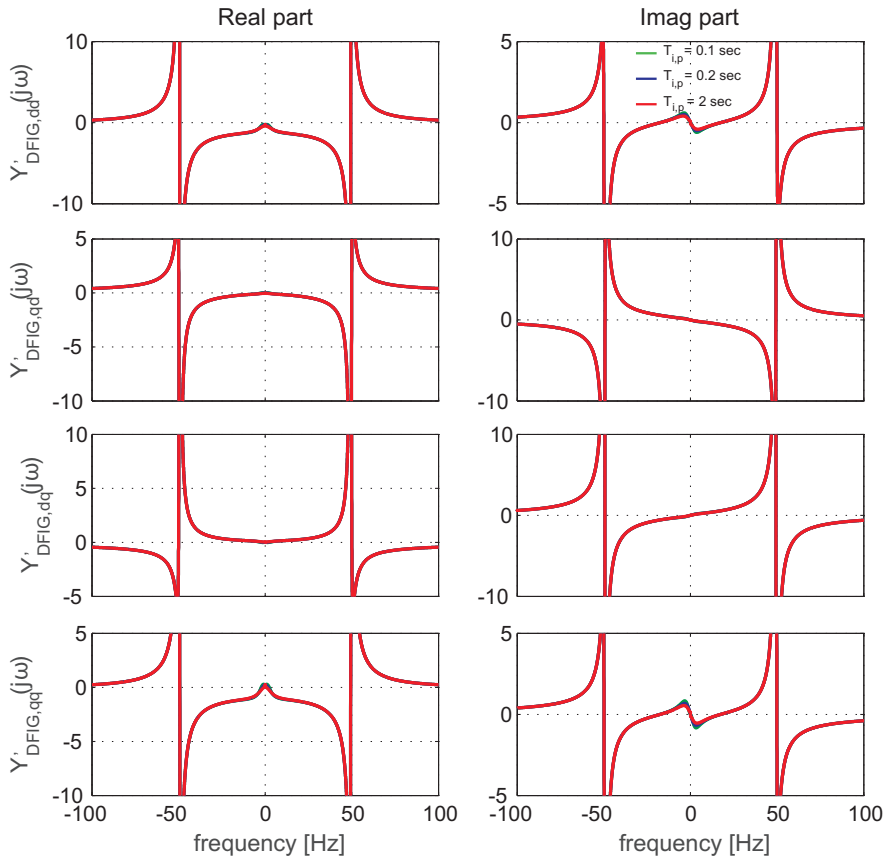

Fig. 3.27 DFIG input admittance for varied RSC outer power loop controller time constant $T_{i,p}$. $T_{i,p}$ = 0.1 sec (*green curve*), $T_{i,p}$ = 0.2 sec (*blue curve*) and $T_{i,p}$ = 2 sec (*red curve*)

Similar conclusions can be drawn when investigating the impact of the integrator time constant on the power dissipation properties of the system. Figure 3.28 shows the trend of the frequency response of λ_1 and λ_2 for the three time constants considered in Fig. 3.27. These results can be used to support the assumption of ignoring the impact of the outer-loop power controllers when assessing the system stability.

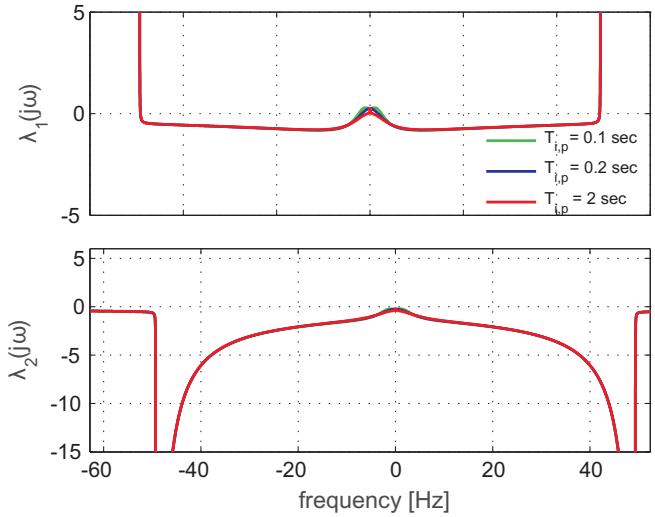

Fig. 3.28 Impact of RSC outer power loop controller time constant $T_{i,p}$. $T_{i,p}$ = 0.1 sec (*green curve*), $T_{i,p}$ = 0.2 sec (*blue curve*) and $T_{i,p}$ = 2 sec (*red curve*). λ_1 (*upper plot*), λ_2 (*lower plot*)

3.5.3 Influence of grid-side converter

In this Section, the influence of the different control loops that govern the GSC on the input admittance of the DFIG is investigated.

Variation in grid-side current controller bandwidth

Similar to the RSC, in this section the GSC closed-loop current controller bandwidth is selected as a variable. Fig. 3.29 shows the frequency sweep of the total DFIG input admittance considering three different values of $\alpha_{cc,f}$. A constant output power of P_{out} = 1 pu and Q_{out} = 0 pu are assumed. The closed-loop current controller bandwidth for the RSC is held constant at $\alpha_{cc,R}$ = 1 pu whereas the closed-loop bandwidth of the GSC is varied between 1 pu and 3 pu. The RSC outer power controller gain is held at $k_{p,P}$ = 5 pu with the integrator $T_{i,P}$ = 0.2 sec. The closed-loop bandwidth of the dc-link voltage controller is set to α_{dc} = 0.1 pu. The frequency sweep of Fig. 3.29 shows minimal influence, both on the real and imaginary components of DFIG input admittance characteristics, in the subsynchronous frequency range. The same conclusion can be reached from evaluating of the wind turbine's power dissipation capabilities, as shown in Fig.3.30

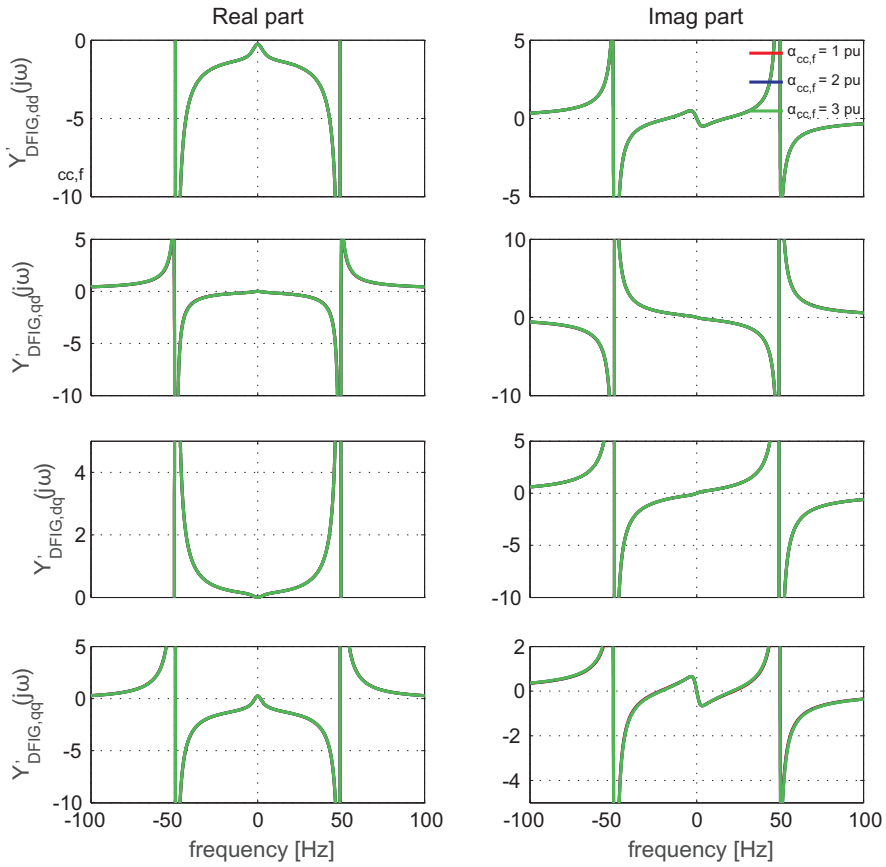

Fig. 3.29 DFIG input admittance for varied grid-side current controller bandwidth. Real component (*left plot*), imaginary components (*left plot*). $\alpha_{cc,f}$ varied between 1 pu to 3 pu.

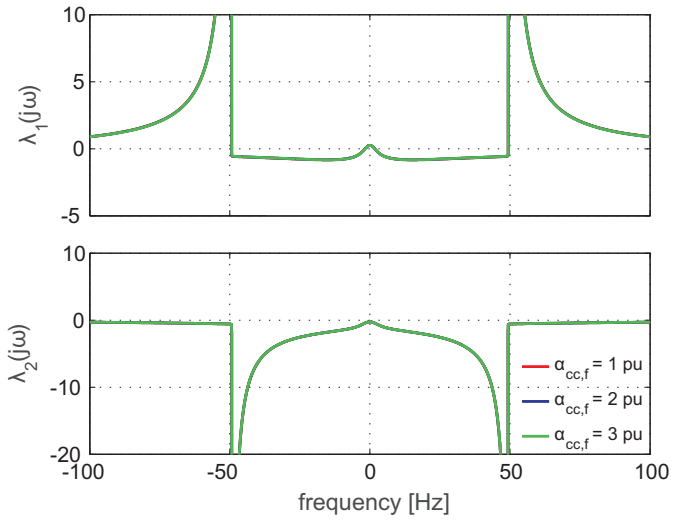

Fig. 3.30 Impact of grid-side current controller bandwidth. $\lambda_1\,(j\omega)$ (*left plot*), $\lambda_1\,(j\omega)$ (*left plot*). $\alpha_{cc,f}$ = 1 pu (*red*), $\alpha_{cc,f}$ = 2 pu (*blue*) and $\alpha_{cc,f}$ = 3 pu (*green*).

Variation in dc-link voltage controller parameters

The final step in evaluating the effects of the controller parameters on the DFIG impedance is to investigate the impact of the dc-link voltage controller. For this purpose, a frequency sweep of the DFIG input admittance with varied α_{dc} is depicted in Fig. 3.31. The RSC and GSC current controller bandwidth are held constant at $\alpha_{cc,R}$ = $\alpha_{cc,f}$ = 1 pu. According to Fig. 3.31, a very small variation is observed, in the $Y_{DFIG,qd}$ and $Y_{DFIG,qq}$ of the DFIG admittance (in the frequency range, 10-40 Hz) as the dc-link controller affects the q- component. A higher α_{dc} value results in a less negative real part for the $Y_{DFIG,qq}$ component. However it should be noted that as compared to the impact of the RSC current controller bandwidth, the impact of the dc-link voltage controller can be considered to be insignificant.

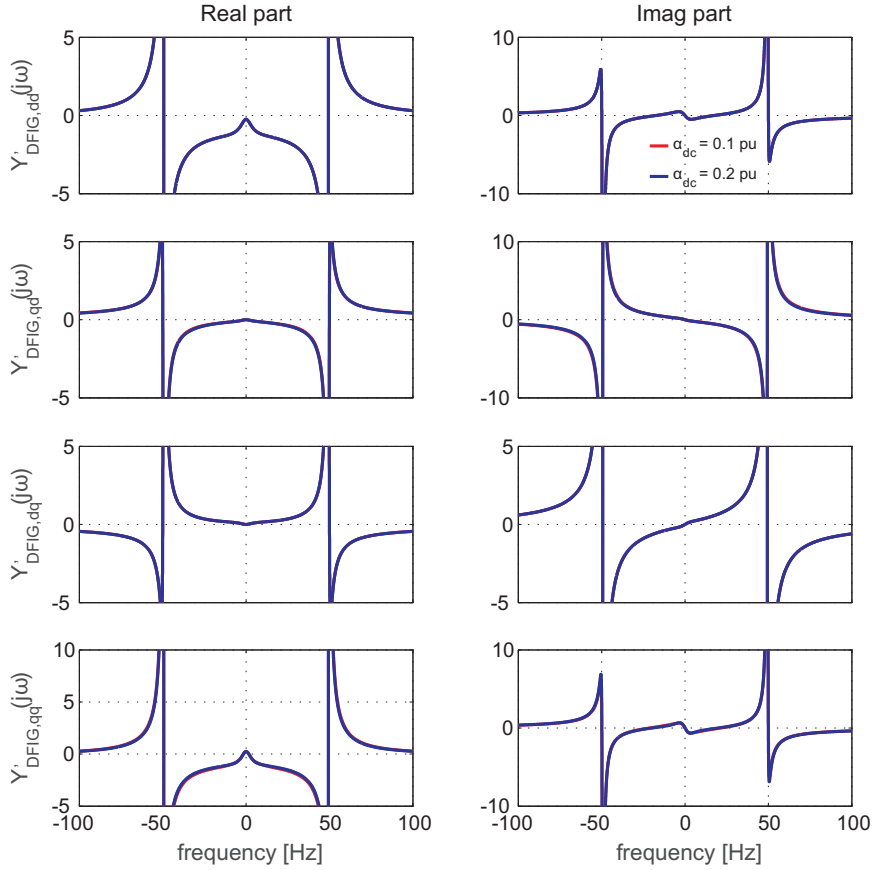

Fig. 3.31 DFIG impedance for varied dc-link controller bandwidth. $\alpha_{dc} = 0.1$ pu (blue) and $\alpha_{dc} = 0.2$ pu (red)

The system is evaluated from a power dissipation point of view in Fig. 3.32. From the obtained results, it is possible to conclude that the loop bandwidth of the direct voltage controller has a negligible impact on the stability. However, as shown in [34], the direct voltage controller directly impacts the system behavior depending on the direction of the active power flow. Based on this fact, the impact of the dc-link controller when the DFIG is operated in the subsynchronous speed operation i.e. the GSC operates as a rectifier, will be evaluated in the next section

dealing with the influence of operating condition.

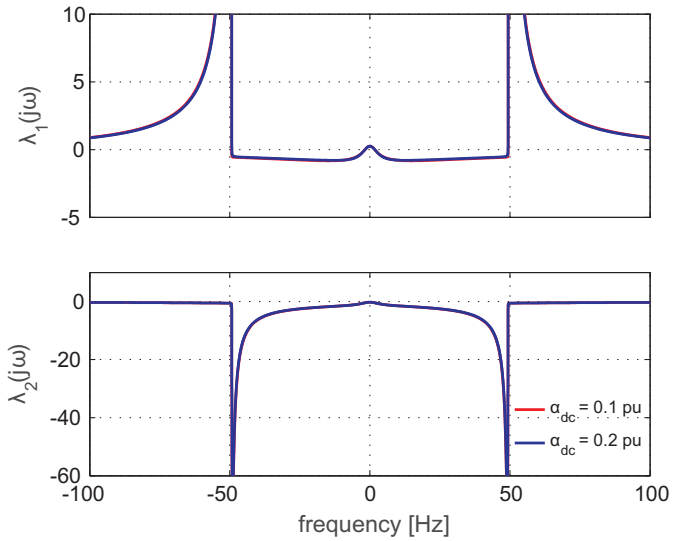

Fig. 3.32 Impact of dc-link voltage controller bandwidth. $\alpha_{dc} = 0.1$ pu (blue) and $\alpha_{dc} = 0.2$ pu (red)

3.5.4 Influence of operating condition

Energy harnessed from wind generation units varies through time due to the variable nature of the available wind speed. Therefore the power generated from wind also varies in a somewhat proportional manner with the available wind speed. The advantage of employing a variable speed wind turbine is mainly for the purpose of capturing this energy over a wider range of wind-speed. In case of a DFIG based wind turbine, this is accomplished by proper control of the BTB converter. At a low wind speeds, when the turbine rotational speed (electrical speed) is below ω_s (here referred to as subsynchronous speed range), the GSC operates as a rectifier supplying power from the grid into the rotor. On the other hand, at high wind speeds, when the turbine electrical rotational speed is above ω_s (supersynchronous speed range), the GSC operates as an inverter pushing power into the grid. In the results presented in the previous sections, the analysis has been carried out under the assumption that the turbine is operated in the supersynchronous speed range. In this section, results dealing with subsynchronous speed range are presented.

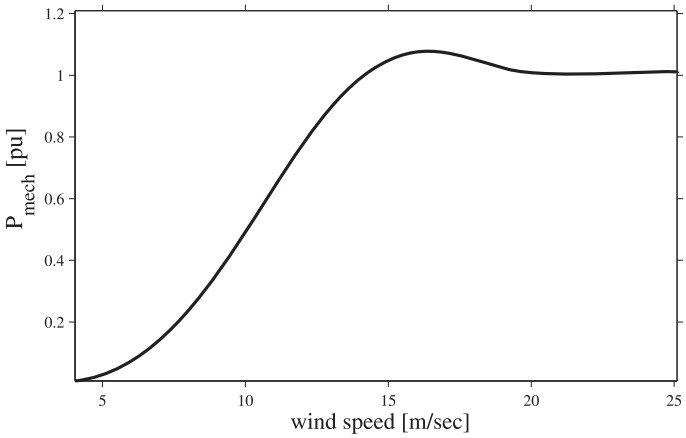

Fig. 3.33 Mechanical power verse wind speed at rated rotor speed

According to [45], the impact of the wind speed can be directly related to the input mechanical power as

$$\begin{aligned} P_{mech} &= \frac{1}{2}\rho A_r C_p\left(\lambda,\beta\right) w^3 \\ \lambda &= \frac{\omega_r r_r}{w} \end{aligned} \tag{3.116}$$

where C_p is the coefficient of performance, β is the pitch angle, λ is the tip-speed ratio and w is the wind speed. ω_r represents the rotor speed on the low-speed side and r_r is the plane rotor radius. ρ is the density of the air and A_r represents the area swept by the rotor. Detailed description of (3.116), is beyond the scope of this work. However, as shown in [45] a typical trend is used to illustrate the relationship between the input mechanical power and the wind speed (shown in Fig. 3.33). As it can be observed, the input to the wind turbine has a fairly linear relation up to a certain wind speed limit; beyond this limit the pitch of the blades are controlled to limit the input power to the rated value.

Returning to the analysis at hand, the impact of the variation of the wind speed (here represented through the variation of output power, P_{out}), on the input admittance of the DFIG is shown in Fig. 3.34. The reactive power Q_{out} is controlled to 0 pu. Both the RSC and GSC current controller loop bandwidth are set to $\alpha_{cc,R}$ = $\alpha_{cc,f}$ = 1 pu. The outer power controller parameters $k_{p,P}$ = 5 pu and $T_{i,P}$ = 0.2 sec are considered. The dc-link voltage controller closed-loop bandwidth is set to α_{dc} = 0.1 pu.

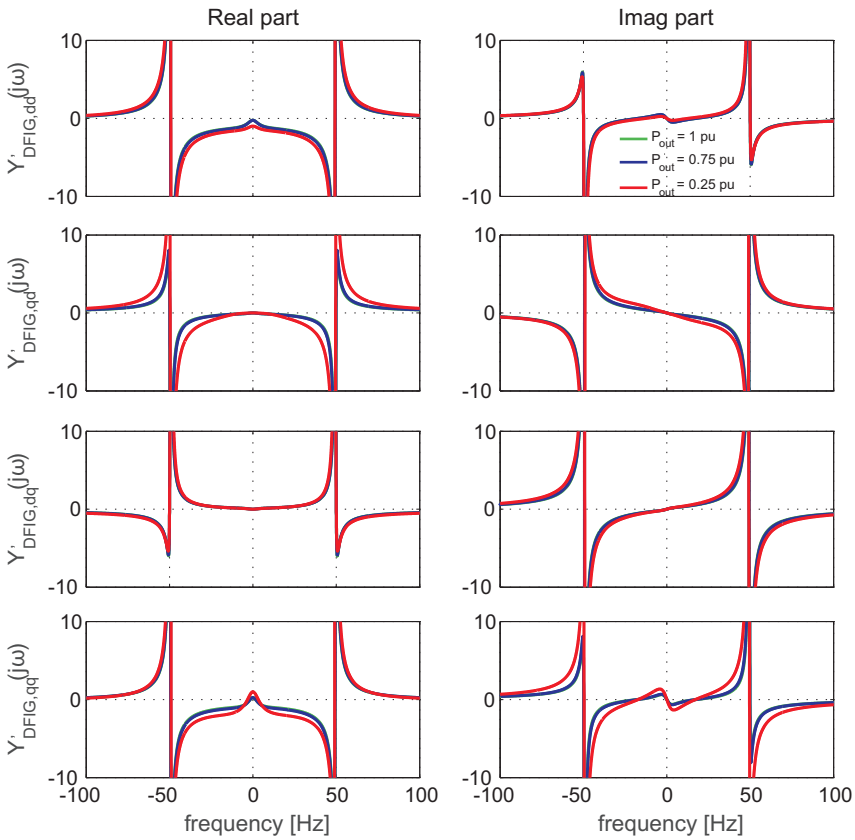

Fig. 3.34 DFIG impedance for different output power. $P_{out} = 0.25$ pu (red), $P_{out} = 0.75$ pu (blue), and $P_{out} = 1.0$ pu (green)

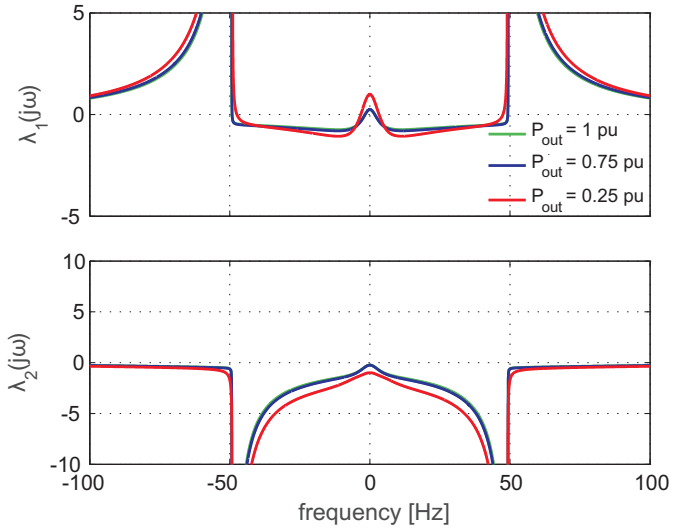

Fig. 3.35 Impact of output power. $P_{out} = 0.25$ pu (red), $P_{out} = 0.75$ pu (blue), and $P_{out} = 1.0$ pu (green)

The real and imaginary parts for the frequency response corresponding to P_{out} = 1 pu and P_{out}

= 0.75 pu, show minimal variation for all the four components of the DFIG admittance matrix. It can be noted that P_{out} = 1 pu and P_{out} = 0.75 pu correspond to operation at supersynchronous speed, where the variation in the rotor speed ω_r between the two output power is 0.01 pu. The result is justifiable, as this variation (although insignificant) can be associated to the frequency dependent slip term. For P_{out} = 0.25 pu, corresponding to operation in the subsyncronous speed range, the input admittance presents a more negative real part in the frequency range from 5-45 Hz. This can be attributed to the operation in subsynchronous speed range associated with a lower value of ω_r that affects the slip term. In addition to the slip term, operation in the subsynchronous speed range (as mentioned in the previous subsection) corresponds to the operation of the GSC as a rectifier. Figure 3.35 shows the impact of operating point on the ability of the DFIG to dissipate the power. From the results it is possible to conclude that for decreased output power from the DFIG, the risk for poorly damped region increases.

As the direct-voltage controller differently impacts the frequency response of the turbine depending on the direction of the active power, it is of interest to understand how α_{dc} affects the $Y_{DFIG,qd}(s)$ when the DFIG is operated in the subsynchronous speed range. From Fig. 3.36 it can be observed that the impact of α_{dc} on the $Y_{DFIG,qd}(s)$ component of the input admittance is more pronounced as compared with the result in Fig. 3.31. The impact of this parameter using $\lambda_{1,2}$ for the rectifier operation of the GSC is depicted in Fig. 3.37 showing that a reduction of α_{dc} slightly improves the power dissipation capabilities of the turbine.

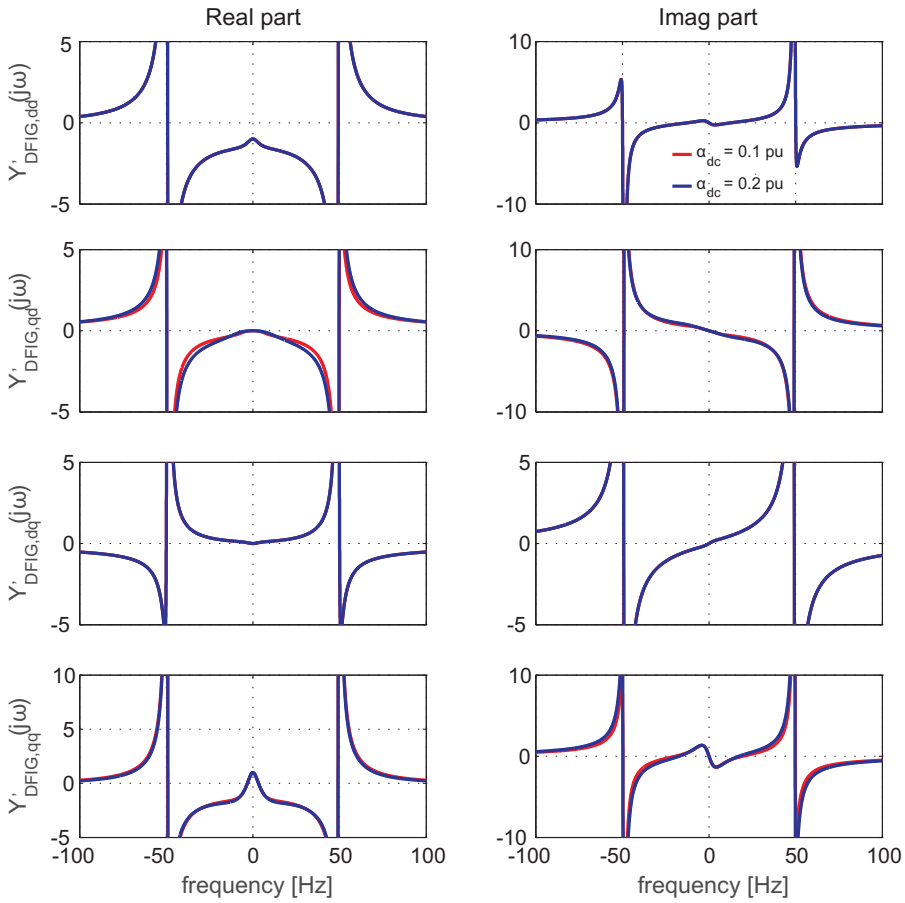

Fig. 3.36 DFIG input admittance for varied dc-link voltage controller bandwidth in the subsynchronous speed range. ω_r = 0.9 pu. $\alpha_{dc} = 0.1$ pu (blue) and $\alpha_{dc} = 0.2$ pu (red)

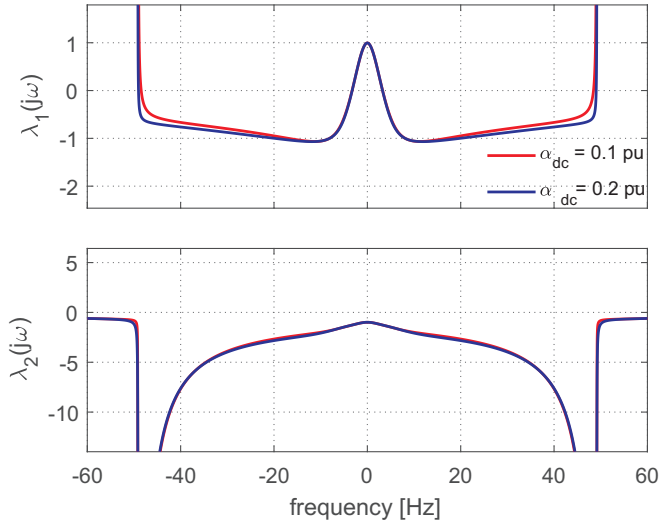

Fig. 3.37 Impact of dc-link closed loop controller bandwidth, α_{dc}, at P_{out} = 0.25 pu. α_{dc} = 0.1 pu (red), α_{dc}= 0.2 pu (blue)

3.6 Conclusion

This chapter focused on establishing an understanding on the modeling and behavior of the DFIG wind turbine system used in this thesis. The different components building up the wind turbine have been explained. A section aiming to create the basis of the control system used for the DFIG wind turbine has been presented. On the basis of the description provided, derivation involved for admittance model development has been covered. The developed admittance model adopted a modular approach that breaks the DFIG turbine into smaller subsystems, which can later be interfaced with each other to build the complete generator system.

Further, the developed admittance model has been used to get insights into the behavior of the DFIG wind turbine generator unit. Frequency response of the obtained admittance for various controller parameters and operating conditions has been presented. As the obtained admittance model involved MIMO transfer function matrix, the frequency response of the admittance matrix cannot provide conclusive result regarding DFIG behavior. For this reason, an approach that evaluates the system behavior based on its ability to dissipate power has been adopted during the analysis. From the analysis, it has been concluded that the following conditions influence the impedance behavior of the DFIG subsystem

1. The closed-loop bandwidth of RSC current controller. The higher the RSC closed-loop current controller bandwidth, the lower the power dissipative behavior for the DFIG turbine.

2. The amount of active power generated by the DFIG. The more power is produced by the DFIG, the less negative the power dissipative capabilities from the DFIG turbine.

3. The closed-loop bandwidth of dc-link voltage controller. The impact varies whether the GSC converter is operated as a rectifier or as an inverter. It is shown that for the GSC operated as rectifier a small variation has been observed in the power dissipation behavior, where a lower controller bandwidth improves the DFIG behavior.

Chapter 4

System Representation

4.1 Introduction

In Chapter 3, the DFIG turbine admittance and its frequency domain behavior have been evaluated. It has been shown that the DFIG has a non-dissipative behavior, which depends on different control parameters and the operating condition. In this chapter, the modeling and analysis is extended to include the DFIG farm with the collection system and the transmission grid.

4.2 Investigated system overview

A single-line diagram of the investigated power system is shown in Fig. 4.1(a). The system is developed from the IEEE FBM, where the synchronous generator is replace with a 100 MW DFIG based wind farm. The wind farm is represented as an aggregate model of 50 wind turbines, where each wind turbine is rated 2 MW. The 2 MW DFIG model used in this work is based on a generic model that was verified against a 2 MW wind turbine installed at Tvååker, Sweden [49]. It is based on the parameters of this 2 MW wind turbine that the aggregate model is developed. The wind farm is then connected to an infinite bus via a 161 kV series compensated transmission line. In this thesis, the point where the feeder bus (PCC bus in Fig. 4.1(a)) meets the low voltage side of the grid transformer is referred to as the PCC. The values of the parameters for the aggregated model are presented in Table. 4.1

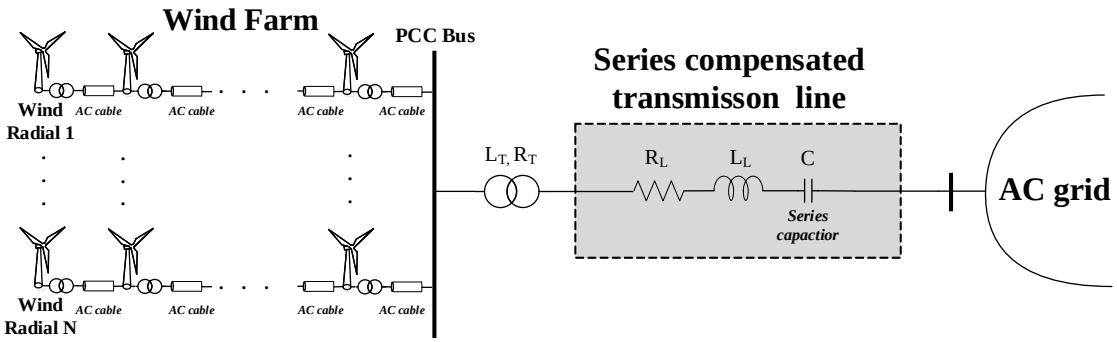

(a)

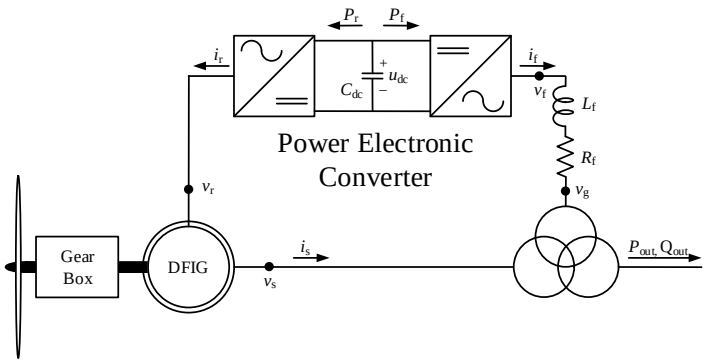

(b)

Fig. 4.1 (a) Single-line diagram of wind farm connected to a series-compensated transmission line, (b) single line diagram of a wind turbine unit.

TABLE 4.1. PARAMETERS OF THE 100 MW AGGREGATE MODEL

Rated power	100 MW
Rated voltage	33 kV
X_{ls}	0.158367 pu
X_m	3.8271871 pu
X_{lr}	0.065986 pu
R_s	0.0092417 pu
R_r	0.0075614 pu
X_f	1.055 pu
R_f	0.1055 pu
C_{dc}	2.45 pu

4.3 Wind farm representation

Through the years, various methods for wind farm representation have been proposed, which are valid for various types of application. To study the overall impact of the wind farm on the

power system, it is common practice to use aggregate models [56] [57] [58]. Different methods for aggregation have been proposed through the years. In this section, the different aggregation methods are summarized.

4.3.1 Detailed model

This method involves detailed models of all wind turbines and collection system, which include internal cables, within the wind farm. Wind speed driving the different wind turbines within the wind farm varies. As a result, the response of the individual wind turbines is different. In addition, the wind turbines are geographical located at different location. This affects the impedance of the cable connecting the wind turbine to its respective feeder. The detailed model takes into account these factors. Another factor might be that the wind farm consists of wind turbines from different manufacturers that differ in parameters and control structure. This method presents a very accurate representation for the system under investigation. However, in case of large wind farms, involving numerous wind turbines, the detailed model presents a high order model that is computational cumbersome.

4.3.2 Full aggregated model

In this modeling approach, all wind turbines in the farm are aggregated into a single equivalent wind turbine model. The aggregated model is assumed to represent the response of the entire wind farm at the PCC. In this approach, all wind turbines within the wind farm are assumed to receive identical wind speed and hence operate at the same operating conditions. The losses are also aggregated. The equivalent generator rating is equal to the sum of the rating for the individual wind turbines in the wind farm as expressed in (4.1). The advantage with this approach is that a simple mathematical representation of the system can be obtained. This method gives an effective representation if a regular wind speed distribution is assumed during modeling. For irregular wind speed distribution, the disadvantage lies in estimating the equivalent wind speed so that the collective response of the wind turbines from the farm matches the equivalent response of the aggregated single turbine model.

$$S_{tot} = \sum_{j=1}^{n} S_j, \qquad P_{tot} = \sum_{j=1}^{n} P_j \tag{4.1}$$

4.3.3 Multiple wind turbine aggregated model

In the multiple wind turbine (MWT) aggregation approach, the assumption is that all wind turbines facing the same wind speed and/or operating at the same operating condition are aggregated together using an equivalent aggregated model. A collection of this aggregates are then used to replicate the behavior of the wind farm. This method is advantageous in modeling wind farms in a multi-vendor system, where there exist differences in system parameters and control

structure or more general, dynamic behavior. Even in a single vendor system, with identical wind turbines installed, this method offers a good balance between a full aggregate model and the detailed model. This approach will further be used to evaluate the aggregation method used in the investigated system.

4.4 DFIG and collection system admittance

In Chapter 3, the input admittance of the aggregated DFIG wind generator has been presented. To generate an equivalent model of the wind farm as shown in Fig. 4.1 (a), a representation for the collector system has to be incorporated. In the subsection that follows, a representation for the collector system is first presented. The obtained collection system representation is integrated with the DFIG model (from Chapter 3), to obtain a generic radial model that serves as a building block for the wind farm model in Fig. 4.1 (a).

4.4.1 Collection system representation

The collector system, in the context here, is the internal cable from the individual wind turbine to the feeder bus (PCC bus). In the configuration shown in Fig. 4.1, there exists N number of radials consisting of m wind turbines. Considering a schematic for one radial (shown in Fig. 4.2), there exists two types of cables: a cable connecting the wind turbine to the radial point and a cable connecting the radial point to the feeder bus (or the PCC point) at the low-voltage side of the grid transformer. Table 4.2 presents the parameters for the collection system with ac cable 1 referring to the cable connecting the wind turbine to the radial.

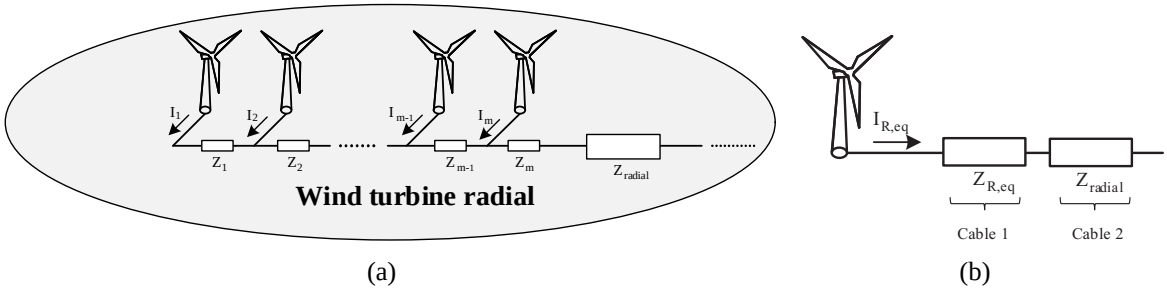

Fig. 4.2 (a) Single-line diagram of for one radial , (b) single line equivalent representation for the circuit in (a).

TABLE 4.2. PARAMETERS OF THE COLLECTION SYSTEM

Nominal power	100 MW
Nominal voltage	33 kV
ac cable 1	
$R_{c,1}$	0.193 Ω/km
$L_{c,1}$	0.475 mH/km
$C_{c,1}$	0.132 μF/km
ac cable 2	
$R_{c,2}$	0.037 Ω/km
$L_{c,2}$	0.341 mH/km
$C_{c,2}$	0.252 μF/km

Under the assumption that the currents from the individual wind turbines are identical, the total current from the radial can be expressed as

$$I_{R,eq} = I_1 + I_2 + ... + \mathrm{I}_{m-1} + \mathrm{I}_m = mI \tag{4.2}$$

Considering the voltage drop across each cable impedance as

$$\begin{aligned}
&\Delta v_{Z_1} = I_1 Z_1 = I Z_1 \\
&\Delta v_{Z_2} = (I_1 + I_2)\, Z_2 = 2 I Z_2 \\
&\qquad\qquad\vdots \\
&\Delta v_{Z_{m-1}} = (I_1 + I_2 + ... + \mathrm{I}_{m-1})\, Z_{m-1} = (m-1) I Z_{m-1} \\
&\Delta v_{Z_m} = (I_1 + I_2 + ... + \mathrm{I}_m)\, Z_m = m I Z_m
\end{aligned} \tag{4.3}$$

the power loss across each impedance can be approximated as

$$\begin{aligned}
\Delta S_{L,Z_1} =& \Delta v_{Z_1} I_1^* = I_1 I_1^* Z_1 = I_1^2 Z_1 = I^2 Z_1 \\
\Delta S_{L,Z_2} =& \Delta v_{Z_2} \left(I_1^* + I_2^*\right) = (I_1 + I_2)\left(I_1^* + I_2^*\right) Z_2 = 2^2 I^2 Z_2 \\
\Delta S_{L,Z_{m-1}} =& \Delta v_{Z_{m-1}} \left(I_1^* + I_2^* + ... I_{m-1}^*\right) = (I_1 + I_2 + ... + \mathrm{I}_{m-1})\left(I_1^* + I_2^* + ... I_{m-1}^*\right) Z_{m-1} \\
=& (m-1)^2 I^2 Z_{m-1} \\
\Delta S_{L,Z_m} =& \Delta v_{Z_m} \left(I_1^* + I_2^* + ... I_m^*\right) = (I_1 + I_2 + ... + \mathrm{I}_m)\left(I_1^* + I_2^* + ... I_m^*\right) Z_m = m^2 I^2 Z_m
\end{aligned} \tag{4.4}$$

Under the assumption $I_{R,eq} = mI$, the equivalent power loss can be further simplified as

$$\begin{aligned}
&\Delta S_{L,eq} = I^2 \left(Z_1 + 2^2 Z_2 + ... + (m-1)^2 Z_{m-1} + m^2 Z_m\right) \\
&\Delta S_{L,eq} = I^2 \sum_{p=1}^{m} p^2 Z_p = I_{R,eq}^2 Z_{R,eq}
\end{aligned} \tag{4.5}$$

From (4.5), the equivalent cable impedance can be approximated as

$$Z_{c,1eq} = \frac{\sum_{p=1}^{m} p^2 Z_p}{m^2} \tag{4.6}$$

In terms of passive components, the equivalent parameter for the cable between the wind turbines within a radial can be expressed as [56]

$$R_{c,1eq} + jX_{c,1eq} = \frac{\sum_{p=1}^{m} p^2 \left(R_p + jX_p\right)}{m^2}, \quad B_{c,1eq} = \sum_{p=1}^{m} B_p \tag{4.7}$$

where $R_{c,1eq}$ and $X_{c,1eq}$ are obtained using the parameters given in Table 4.2. From Fig. 4.2(b), the equivalent model of a collection system (for a radial) would require two Π representation that are series connected. This would increase the order of each radial in the system by five. However, since the contribution of the collection system admittance in relation to the DFIG turbine is comparatively small, further simplification to the collection system equivalent model as in (4.8) is considered [1]

$$Z_{col,eq} = Z_{c,1eq} + Z_{c,2eq} \quad B_{col,eq} = B_{c,1eq} + B_{c,2eq} \tag{4.8}$$

where $Z_{c,2eq}$ and $B_{c,2eq}$ are equivalent parameters for Z_{radial} in Fig. 4.2(b). As radials combine to build the wind farm model, the assumption in (4.8), reduces the order of the system by two for each radial. The obtained collection system model using an equivalent Π representation, with $Z_{col,eq} = R_{col,eq} + jX_{col,eq}$, is shown in Fig. 4.3.

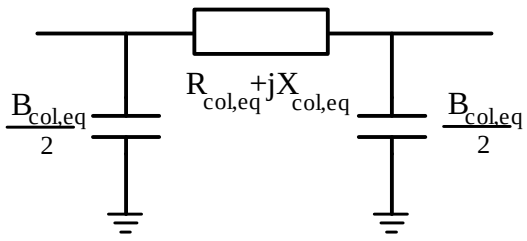

Fig. 4.3 Equivalent circuit for one collection system within a wind farm.

4.4.2 Combined DFIG and collection system

In this section, the DFIG model with terminal voltages ($v_{t,gd}$,$v_{t,gq}$) as input and currents ($i_{t,gd}$,$i_{t,gq}$) as output has to be combined to obtain the radial representation. The current from the DFIG model serves as input to the collection system equivalent model. One problem in the system modeling is that when later in this chapter the wind farm system will be integrated with the

[1] For a single radial, $Z_{c,2eq} = R_{c,2} + X_{c,2}$ and $B_{c,2eq} = B_{c,2}$ using parameters from Table. 4.2 scaled to the rating of the radial.

model of the series compensated transmission line, the latter will be characterized by an improper transfer function matrix. As a workaround, one of the shunt elements of the Π model of the equivalent collection system model is considered as a part of the grid impedance model. As a result, the schematic depicted in Fig. 4.4 is considered for the wind farm side. The combined system therefore has voltage at the shunt branch as input and the current flowing through $Z_{col,eq}$ as output (shown in Fig. 4.4)

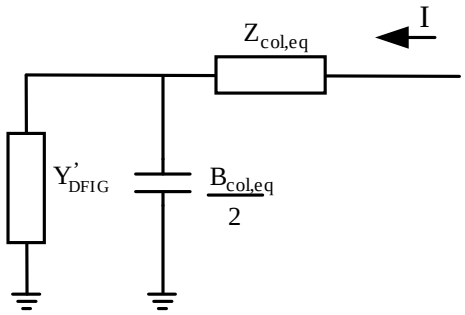

Fig. 4.4 Equivalent schematic for one radial with collection system model representation.

Based on Fig. 4.4, the collection system impedance model can be integrated with the input admittance model for the DFIG and represented in state space as

$$A_{radial} = \begin{bmatrix} A'_{DFIG} & B'_{DFIG}\,C_{cR,eq} & \mathbf{0} \\ B_{cR,eq}\,C'_{DFIG} & A_{cR,eq} & -B_{cR,eq}\,C_{R,eq} \\ \mathbf{0} & B_{R,eq}\,C_{cR,eq} & A_{R,eq} \end{bmatrix}, \quad B_{radial} = \begin{bmatrix} \mathbf{0} \\ \mathbf{0} \\ B_{R,eq} \end{bmatrix} \tag{4.9}$$

$$C_{radial} = \begin{bmatrix} \mathbf{0} & \mathbf{0} & C_{R,eq} \end{bmatrix}, \quad D_{radial} = \mathbf{0}$$

with

$$A_{R,eq} = \begin{bmatrix} -R_{col,eq}\omega_B & \omega_s \\ -\omega_s & -R_{col,eq}\omega_B \end{bmatrix}, B_{R,eq} = \begin{bmatrix} \frac{\omega_B}{X_{col,eq}} & 0 \\ 0 & \frac{\omega_B}{X_{col,eq}} \end{bmatrix},$$

$$C_{R,eq} = \begin{bmatrix} 1 & 0 \\ 0 & 1 \end{bmatrix}, D_{R,eq} = \begin{bmatrix} 0 & 0 \\ 0 & 0 \end{bmatrix}$$

$$A_{cR,eq} = \begin{bmatrix} 0 & \omega_s \\ -\omega_s & 0 \end{bmatrix}, \; B_{cR,eq} = \begin{bmatrix} \frac{2\omega_B}{B_{col,eq}} & 0 \\ 0 & \frac{2\omega_B}{B_{col,eq}} \end{bmatrix}, \; C_{cR,eq} = \begin{bmatrix} 1 & 0 \\ 0 & 1 \end{bmatrix}, \; D_{cR,eq} = \begin{bmatrix} 0 & 0 \\ 0 & 0 \end{bmatrix}$$

where A'_{DFIG}, B'_{DFIG}, C'_{DFIG} and D'_{DFIG} are the state space representation for $\mathbf{Y}'_{DFIG}$. The combined model of the DFIG and the collection system here represented using state-space matrices A_{radial} ,B_{radial} , C_{radial} and D_{radial} serves as building blocks for the wind farm model.

4.4.3 Multiple wind turbine aggregate model of wind farm

Prior to this sections, the wind farm has been modeled using a single-aggregate wind turbine model connected to an equivalent collection system model. This assumption has been commonly used in the analysis of SSCI in most of the works available in the literature, such as [15], [59] [60].

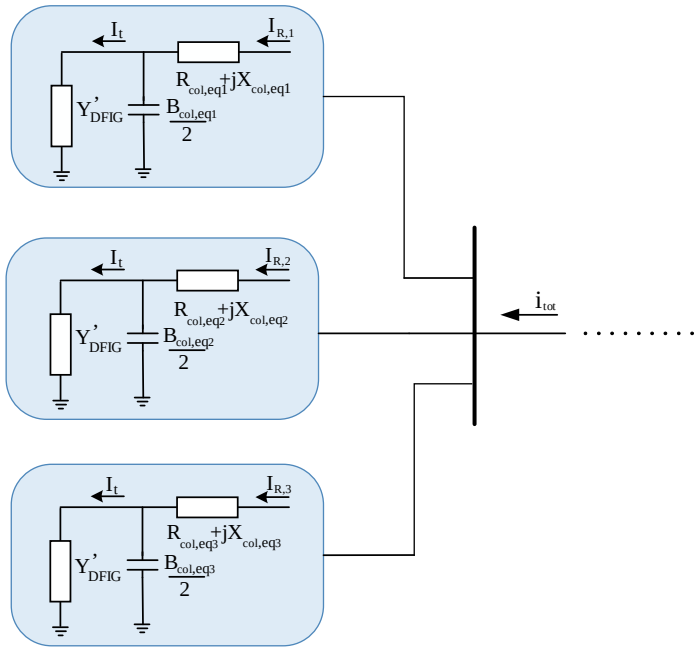

Fig. 4.5 Schematics of wind farm model with multiple aggregate model

However the full aggregated model, as mentioned earlier, has its limitation in representing the wind farm, for example when turbines within the wind farm are subjected to different operating conditions. From Section 3.5.4, the operating point plays a major role both on the input admittance and the power dissipative behavior of the DFIG turbine model. Based on this, the MWT modeling approach, where wind turbines facing similar operating condition can be aggregated together, appear to be a better modeling alternative, allowing the representation of the impact of wind turbines with different operating conditions on the system dynamics.

For the purpose of explaining the MWT model development, the wind farm has been divided into three sections (each represented by a single aggregate) as shown in Fig. 4.5. The equivalent collection system is divided in a similar manner among the three aggregates. Each subsystem has input and output that are interconnected to generate the collective input and output variables. As the sum of the current from the different radials gives the total current from the wind farm, the wind farm model can be derived as

$$A_{farm} = \begin{bmatrix} A_{radial,1} & \mathbf{0} & \mathbf{0} \\ \mathbf{0} & A_{radial,2} & \mathbf{0} \\ \mathbf{0} & \mathbf{0} & A_{radial,3} \end{bmatrix}, \quad B_{farm} = \begin{bmatrix} B_{radial,1} \\ B_{radial,2} \\ B_{radial,3} \end{bmatrix} \tag{4.10}$$

$$C_{farm} = \begin{bmatrix} C_{radial,1} & C_{radial,2} & C_{radial,3} \end{bmatrix} \quad , D_{farm} = \mathbf{0}$$

where the $\mathbf{0}$ represent matrices of zeros with their respective sizes. It should be noted that with this approach, the modeling becomes very modular, as different types of DFIG wind turbine can be inserted to diversify the wind farm model. This is of great advantage when employing such an approach. For the sake of clarity, a model consisting of three radials has been used in this section. However, the approach can be extended to system with higher number of radials. It should be kept in mind that the order of the model would increase with increased number of radials.

4.5 Frequency-domain analysis for multiple wind turbine aggregated model

In previous sections, model representation using aggregated DFIG turbine and corresponding equivalent collection system has been combined to generate a radial equivalent model representation. As a demonstration, an example case (using three radial), has been used to illustrate the process of obtaining an equivalent multiple-radial wind farm representation using the equivalent radial representation. In this section, frequency domain based evaluation has been used to investigate the impact of using a single aggregate turbine model (equivalent to a single aggregate radial rated to the wind turbine capacity) versus a multiple wind turbine aggregate model (MWT, having a multiple number of radial aggregates).

4.5.1 Influence of operating condition on MWT aggregated model

In this section the influence of operating point on MWT aggregated model is discussed. Initially, a single aggregated wind turbine model including its equivalent collection system generating output power, P_{out} = 0.395 pu is depicted in Fig. 4.6. In the same figure, plotted using a blue dashed curve, result obtained using the MWT approach with three radials each producing P_{out} = 0.23 pu, P_{out} = 0.3 pu and P_{out} = 0.65 pu is shown. The reactive output Q_{out} = 0 and parameter for the DFIG aggregate turbine are maintained as in the input admittance plot presented in Fig. 3.17[2].

[2]Note that, in Fig. 4.6, the collection system impedance is included in the admittance model

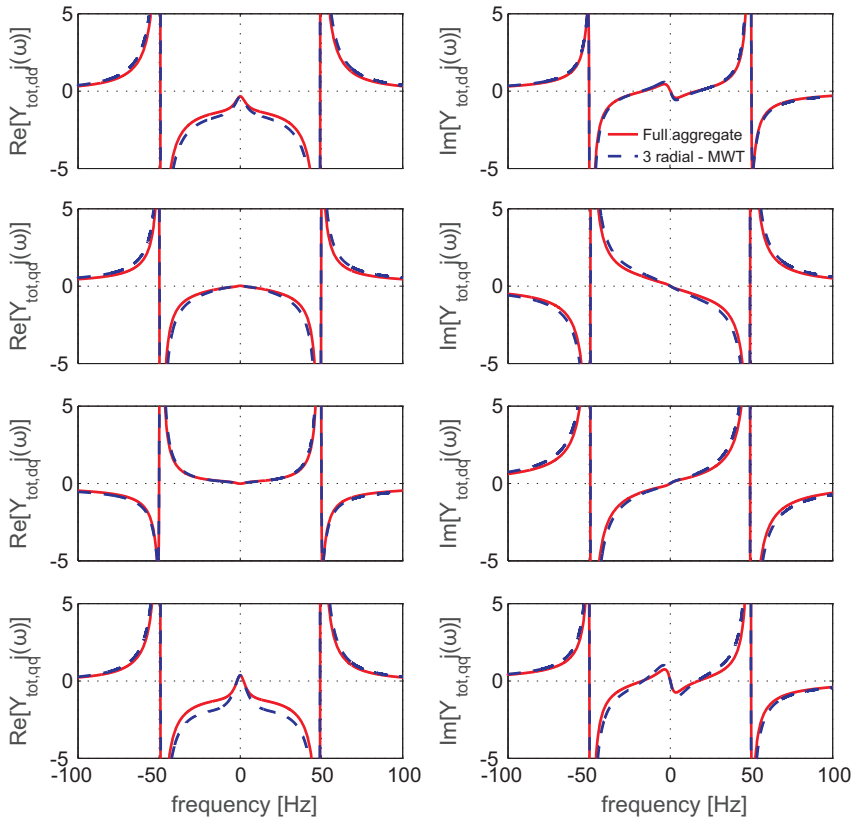

Fig. 4.6 Input admittance to a single aggregate (full aggregate) wind farm model vs three radial MWT aggregate model. P_{out} = 0.395 pu (*blue dashed*) for the full aggregate model. $P_{radial,1}$ = 0.23 pu, $P_{radial,2}$ = 0.3 pu and $P_{radial,3}$ = 0.65 pu of the rated radial power of their corresponding radial for MWT model (*red curve*). $\alpha_{cc,R}$ = 1 pu

The impact of the aggregation is visible both in the $Y'_{tot,dd}$ and $Y'_{tot,qq}$ terms, where the three radials model (*dashed blue curve*), as compared to a single aggregated model (*red curve*), shows a more negative real part. To evaluate the effect of aggregation on the behavior of the wind farm, the frequency response of $\lambda_{1,2}$ for Y_{tot} described in Section 3.5.2 is plotted in Fig. 4.7. The negative real part for the model with three radials MWT is increased compared with the full aggregated model. The reason can be associated with the choice of output power for the respective radials set at 0.23 pu, 0.3 pu and 0.65 pu. The fact that a majority of the radials is operated at subsynchronous speed affects the overall input admittance for the wind farm, which in the case of a single aggregated model can be represented using the average power from the wind farm.

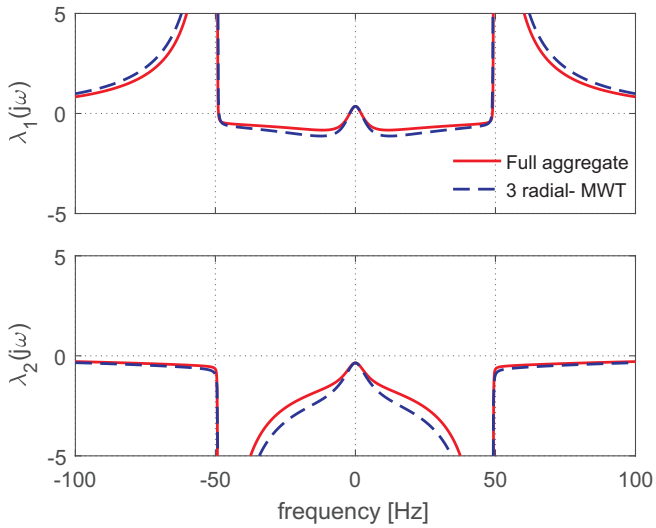

Fig. 4.7 Impact of aggregation. P_{out} = 0.395 pu (*blue dashed*) for the full aggregate model. $P_{radial,1}$ = 0.23 pu, $P_{radial,2}$ = 0.3 pu and $P_{radial,3}$ = 0.65 pu of the rated radial power of their corresponding radial for MWT model (*red curve*). $\alpha_{cc,R}$ = 1 pu

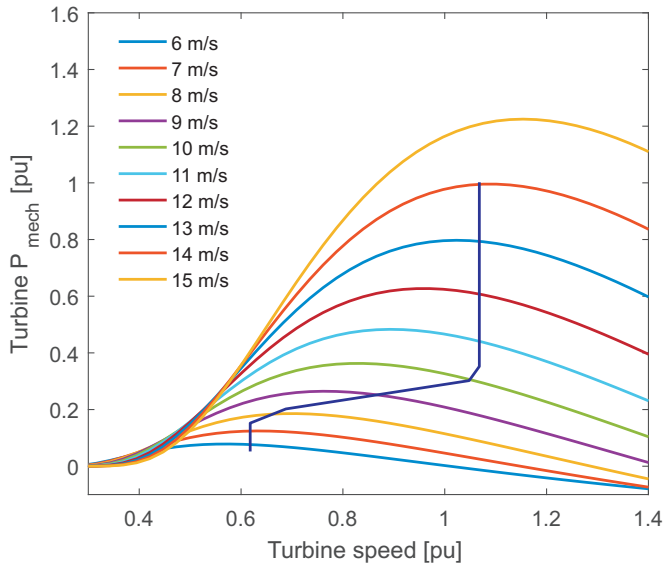

Fig. 4.8 Power curve for DFIG wind turbine considered.

In general case, based on the available wind speed, the DFIG wind turbine uses the optimal tracking strategy to extract the maximum wind energy, which would follow the blue curve in Fig. 4.8. This curve has different section from low-wind speed to high wind speed. In the subsynchronous speed range, there exist a part where a slight change in speed results in a jump of output power. After a point, there exists a section where a variation in the wind speed (ω_r) has little effect on the output power. A third section exists where there is a sudden jump of output power. Finally there exists wind speed beyond which the output power is fixed to rated value

(referred to as stall condition). In the example considered in Fig. 4.6 and Fig. 4.7, the use of a full-aggregated model leads to a single wind turbine model operating in the supersynchronous-speed range; this regardless of the fact that a majority of the wind turbines in the farm (66% for the considered case), operate in subsynchronous speed.

As a result, the relation between wind speed and total output power can be used as a simple guideline for aggregation in a MWT model representation. Based on the result in Fig. 4.8, wind turbines falling in the region where the power variation is small, the average power for this group of wind turbines are suitable in the aggregation process whereas for wind turbines falling in the region where wind speed variation is small, averaging the speed becomes advantageous.

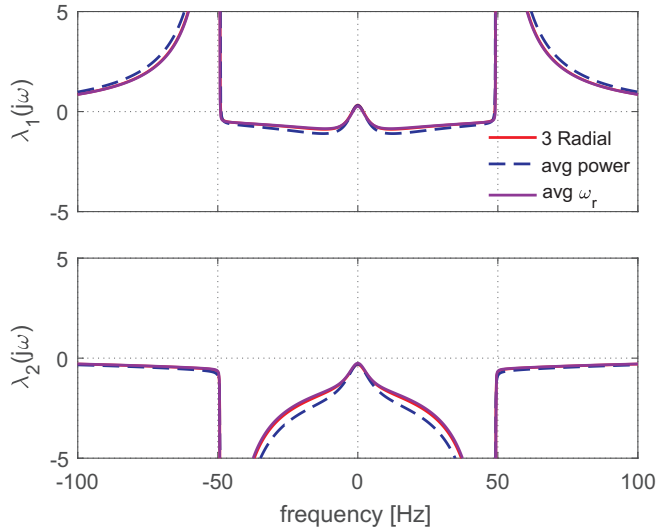

Fig. 4.9 Impact of aggregation using uniform average power vs average wind speed. A single aggregate model using average ω_r (*purple curve*). Aggregation using three radials operated at P_{out} = 0.22 pu, 0.25 pu and 0.45 pu(*red curve*) and a single aggregate model using average output power (*dashed blue curve*)

From this, it is apparent that the choice between averaging the power and averaging the wind speed is mainly dependent on the region of operation. A collection of wind turbines in the sub-syncronous speed range together with supersynchronous speed is used to illustrate its impact. A three radial wind farm model is compared with a single aggregate using average power and a second aggregate model using average wind speed. The results are depicted in Fig 4.9, where averaging the wind speed gives a very accurate representation as compared to averaging the power output because of the operating range.

So far, the dissipative behavior for the wind farm has been used to directly compare aggregation based on average output power or average wind speed. This has been observed to depend on the area of operation for the individual radial operation. Fig. 4.9, assumes wind turbine operating point that favors averaging speed over averaging output power. To evaluate the advantage of using multiple aggregate model, power dissipative behavior for a three radial model aggregated based on combined average speed (ω_r) and average output power vs a detailed model having five radials (with distributed output power) are plotted in Fig. 4.10. As it can be observed, the

three radial model (*violet curve*) and the detailed five radial model (*red curve*) show properties that are very similar to each other.

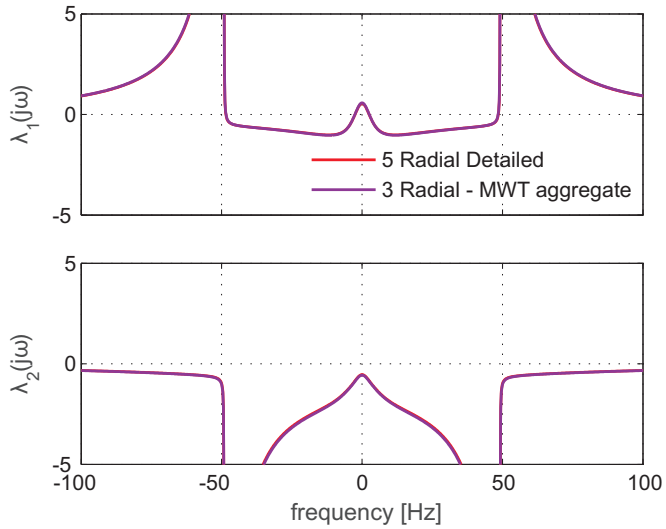

Fig. 4.10 Impact of aggregation using operating condition. Detail model with five radials operated at P_{out} = 0.23 pu, 0.3 pu, 0.6 pu, 0.7 pu and 0.9 pu.(*red curve*) verses Multiple aggregate model with 3 radials operated at P_{out} = 0.265 pu, P_{out} = 0.6 pu and P_{out} = 0.8 pu

From the results presented, it is then possible to deduce that the operating point for the radial can be used to aggregate based on average power, average speed or a combination of the two. Based on the preliminary assessment on the behavior of a wind turbine performed in Section 3.5.4, a significant difference is observed whether the wind turbines are operated in the supsynchronous speed range or supersynchronous speed range. As a result, it can be interesting to evaluate the performance of a modeling approach where turbines facing low wind speed can be aggregated into one equivalent radial aggregate and turbines receiving high wind speed are aggregated into a second equivalent radial. Evaluating aggregation through collection of wind turbine operated in subsynchronous speed and at the same time collecting wind turbines with supersynchronous speed is compared against the detailed five radial model shown in Fig. 4.11.

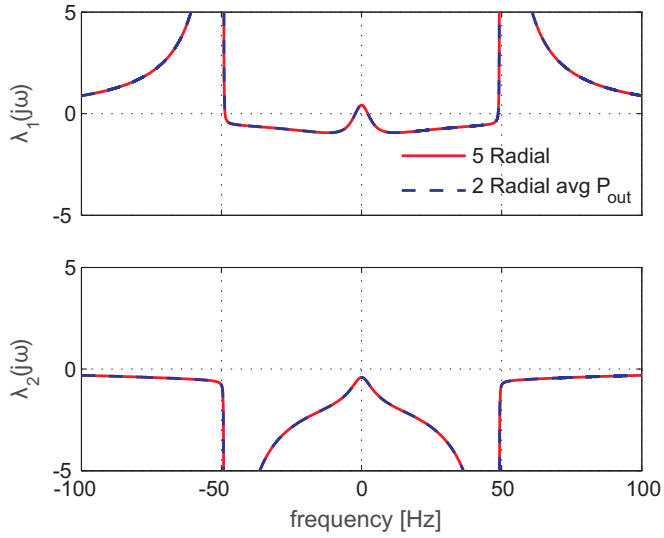

Fig. 4.11 Impact of aggregation based on subsynchrous and supersynchronous speed. A two radial aggregate model using average P_{out} (*blue curve*). Detail model with five radials operated at P_{out} = 0.2 pu, 0.25 pu, 0.45 pu, 0.55 pu and 0.65 pu.(*red curve*) verses Multiple aggregate model having two radials operated at P_{out} = 0.225 pu and P_{out} = 0.55 pu

The power output for the five radials is choosen to be 0.23 pu, 0.3 pu, 0.45 pu, 0.55 pu and 0.65 pu. Radials operated at subsynchronous speed are modeled using a single radial having an average output power of P_{out} = 0.225 pu and radials operated in the supersynchronous speed are represented using a single radial having an average output P_{out} = 0.55 pu. From the result, it can be seen that the two radial model gives a good match to the detailed radial model.

4.6 Grid impedance model

The transmission line in Fig. 4.1(a) is derived based on IEEE FBM for SSR analysis (see Appendix A), with the parameters adopted to accommodate the aggregated wind farm model. The term v_{pcc} is the voltage at the connection point to the wind farm. R_T and R_L are the resistive losses of the grid transformer and the transmission line, respectively. L_T and L_L are the inductive components of the grid transformer and the transmission line, respectively. C represents the capacitance of the fixed-series compensation whereas v_B represents the infinite bus voltage. In reference with the symbols shown in Fig. 4.1(a), the voltage at the connection point can be expressed as

$$v_t^{(dq)} = R_{tot} i_t^{(dq)} + L_{tot} \frac{di_t^{(dq)}}{dt} + j\omega_s L_{tot} i_t^{(dq)} + v_c^{(dq)} + v_b^{(dq)} \tag{4.11}$$

with $R_{tot} = R_L + R_T$ and $L_{tot} = L_L + L_T$. The dynamics of the fixed-series capacitor can be

written as

$$\frac{dv_c^{(dq)}}{dt} = \frac{1}{C} i_l^{(dq)} - j\omega_s v_c^{(dq)} \tag{4.12}$$

By explicitly extracting the d and q component of (4.11) and (4.12), the dynamic equations for the grid impedance expressed in terms of the grid resistive, inductive and capacitive components can be rearranged into state-space matrices as

$$A_L = \begin{bmatrix} -R_{tot}\omega_B & \omega_s \\ -\omega_s & -R_{tot}\omega_B \end{bmatrix}, \quad B_L = \begin{bmatrix} \frac{\omega_B}{X_{tot}} & 0 \\ 0 & \frac{\omega_B}{X_{tot}} \end{bmatrix}, \; C_L = \begin{bmatrix} 1 & 0 \\ 0 & 1 \end{bmatrix}, \; D_L = \begin{bmatrix} 0 & 0 \\ 0 & 0 \end{bmatrix} \tag{4.13}$$

The dynamics in the series compensation capacitor using state-space can be expressed as

$$A_c = \begin{bmatrix} 0 & \omega_s \\ -\omega_s & 0 \end{bmatrix}, \quad B_c = \begin{bmatrix} \omega_B X_c & 0 \\ 0 & \omega_B X_c \end{bmatrix}, \quad C_c = \begin{bmatrix} 1 & 0 \\ 0 & 1 \end{bmatrix}, \quad D_c = \begin{bmatrix} 0 & 0 \\ 0 & 0 \end{bmatrix} \tag{4.14}$$

As mentioned earlier, in order to generate a proper transfer function for the input impedance matrices of the transmission grid system, the equivalent capacitance branch for the collection system is included in the grid impedance model. Looking into the grid, the dynamics for the equivalent capacitor branch, $B_{col,eq}$, can be described as

$$\frac{dv_{pcc}}{dt} = \frac{2\omega_B}{B_{col,eq}} i_{c,eq} - j\omega_s v_{pcc} = \frac{2\omega_B}{B_{col,eq}} i_{c,eq} - j\omega_s v_{pcc} = \frac{2\omega_B}{B_{col,eq}} (i_{in} - i_l) - j\omega_s v_{pcc} \tag{4.15}$$

Combining (4.11) - (4.15), the state-space expression of the grid can be derived as

$$A_{grid} = \begin{bmatrix} A_{cR,eq} & -B_{cR,eq} & \mathbf{0} \\ B_L C_{cR,eq} & A_L & -B_L C_c \\ \mathbf{0} & BcC_L & A_c \end{bmatrix}, \quad B_{grid} = \begin{bmatrix} B_{cR,eq} \\ \mathbf{0} \\ \mathbf{0} \end{bmatrix} \tag{4.16}$$

$$C_{grid} = \begin{bmatrix} \mathbf{0} & \mathbf{0} & C_{cR,eq} \end{bmatrix}, \quad D_{grid} = zeros\,[2\times 2]$$

where $A_{cR,eq}$, $B_{cR,eq}$ and $C_{cR,eq}$ are as described for (4.9). The transfer function of a linear time-invariant system expressed in a state-space form having matrices $\begin{bmatrix} \mathbf{A} & \mathbf{B} & \mathbf{C} & \mathbf{D} \end{bmatrix}$ can be obtained using the equation $H(s) = \mathbf{C}(s\mathbf{I} - \mathbf{A})^{-1}\mathbf{B} + \mathbf{D}$. Taking into account that the series-compensated transmission line is a linear time-invariant system, its transfer function can be expressed as

$$\mathbf{v}_{pcc}(s) = \mathbf{Z}_{TL}(s)\,\mathbf{i}_{in}(s) \tag{4.17}$$

where

$$Z_{TL}(s) = \begin{bmatrix} Z_{TL,dd}(s) & Z_{TL,dq}(s) \\ Z_{TL,qd}(s) & Z_{TL,qq}(s) \end{bmatrix} = \mathbf{C}_{grid}(s\mathbf{I} - \mathbf{A}_{grid})^{-1}\mathbf{B}_{grid}$$

The series-compensated transmission line is symmetric, i.e. $Z_{TL,dd}(s) = Z_{TL,qq}(s)$ and $-Z_{TL,dq}(s) = Z_{TL,qd}(s)$. Thus, it can be expressed using complex transfer functions as [40]

$$\mathbf{Z}_{TL}(s) = Z_{TL,dd}(s) + jZ_{TL,qd}(s) \tag{4.18}$$

To obtain the frequency response of the transfer function in (4.17), the variable "s" is replaced with $j\omega$ with ω representing the angular frequency range of interest. In the stationary frame ($\alpha\beta$ frame), the resonance frequency for the transmission line is $f_{res} = \sqrt{\frac{X_c}{X_{tot}}} f_s$. The impact of increasing the series compensation level (SCL), expressed as a $\%$ of X_L, on the input impedance of the grid is shown in Fig. 4.12 for two values of SCL (in the rotating dq frame). The resonance point where the reactance crosses zero tends to shift with the variation of the SCL.

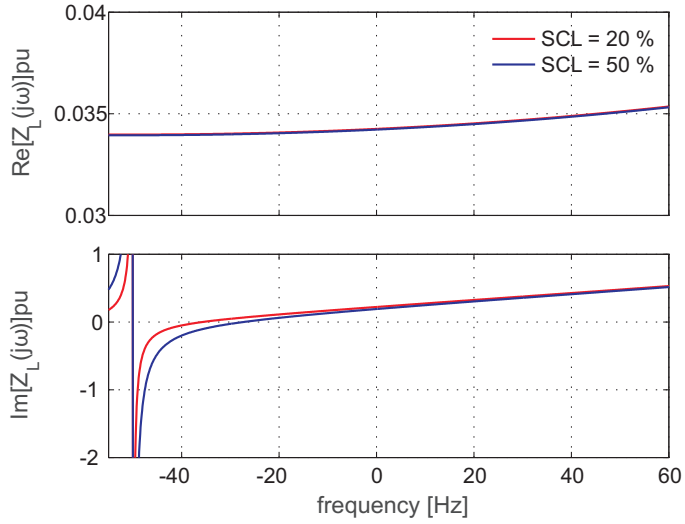

Fig. 4.12 Frequency domain input impedance of a series compensation transmission line in dq frame with SCL of 20% and 50%

4.7 Conclusion

In this chapter the DFIG admittance has been combined with the collection system, aiming at providing a mathematical representation of the entire wind farm. The system has been further developed to evaluate the impact of using a single aggregate model versus multiple aggregate model. It has been shown that the use of multiple aggregate model gives a more accurate representation of the system. The results have been also extended to model the system using two aggregate MWT model representation. Finally, a model for the grid representation has been derived, thus providing all building blocks needed for the overall system representation.

Chapter 5

Frequency-domain stability analysis and verification

The system investigated in this thesis has been presented in Chapter 4, respectively. In the same chapter, the system has been divided into two subsystems, comprising of the wind farm and the transmission subsystems. A model representation for a single wind turbine has been derived, which scaled will be utilized to represent the aggregate wind farm model. The wind farm is rated at 100 MW with a 33 kV collection system. In this chapter, frequency domain analysis will be used to assess the stability of the interconnected system.

5.1 Frequency-domain analysis

Consider the system shown in Fig. 5.1, where the aggregated wind farm is connected to a series compensated transmission line through a collection system.

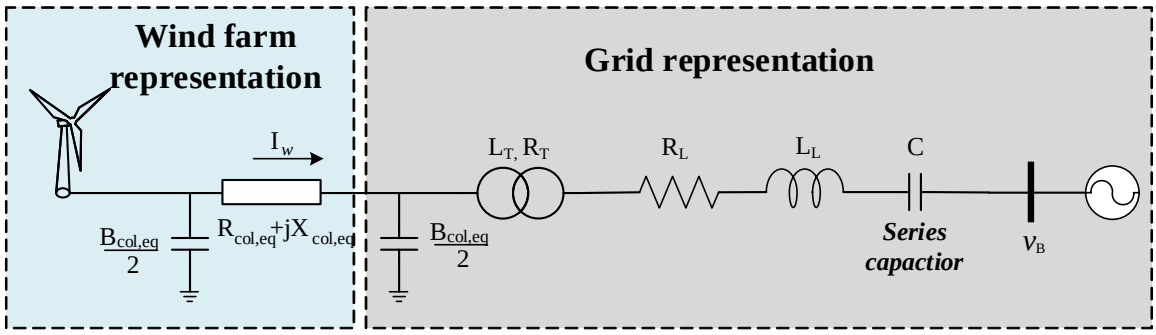

Fig. 5.1 Schematic of a wind farm connected to a series compensated transmission line through a collection system

If the frequency-dependent admittance model derived for the wind farm and the impedance given for the grid are considered, the system under consideration can be reduced to the equivalent circuit representation shown in Fig. 5.2. Variable Y'_{tot}, in Fig. 5.2, represents the admittance

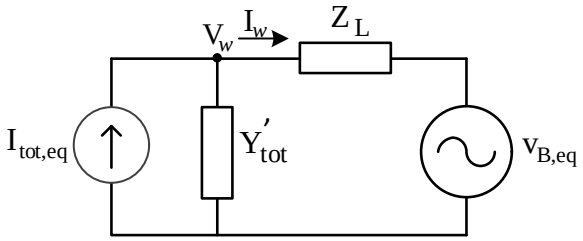

Fig. 5.2 Equivalent circuit of a wind farm connected to a series compensated transmission line through a collection system

representation for the wind farm, including a portion of the collection system, whereas Z_L represents the impedance model for the series compensated transmission line with the remaining section for the collection system. In the same figure, $I_{tot,eq}$ represents the Norton equivalent current source for the aggregated wind farm and $V_{B,eq}$ is the source voltage resulting from the Thevenin's equivalent for the transmission system. Based on the equivalent system, stability analysis for the interconnected system can be evaluated as described below [35].

Based on Fig. 5.2, the current I_w can be expressed as

$$I_w = I_{tot,eq} - Y_{tot}^{'} V_w \tag{5.1}$$

Using Kirchoff's voltage law, the expression for the voltage can be derived as

$$V_w = v_{B,eq} + Z_L I \tag{5.2}$$

Combining (5.1) and (5.2), the expression for the current I_w can be obtained as

$$I_w = \left[I_{tot,eq} - Y_{tot}^{'} v_{B,eq} \right] \left[\mathbf{I} + Y_{tot}^{'} Z_L \right]^{-1} \tag{5.3}$$

where $\mathbf{I}$ is a 2×2 identity matrix. From the expression in (5.3), it can be deduced that the closed-loop stability of the system depends on the poles of the expression $\left[\mathbf{I} + Y_{tot}^{'} Z_L\right]^{-1}$ or the transmission zeros of $\mathbf{I} + Y_{tot}^{'} Z_L$. The above assumption is true provided that $Y_{tot}^{'}$ is stable. Another approach would involve the use of the open-loop expression, $Y_{tot}^{'} Z_L$, and the analysis of its frequency characteristics. The later method, in this thesis, would involve the use of the generalized Nyquist criterion (GNC) as both the wind farm and the transmission system models are expressed using a MIMO model. The major advantage in evaluating the open-loop system lies in the fact that the individual subsystem characteristics can be initially analyzed individually. The obtained results can be used as a base to explain the reason behind possible interaction observed while evaluating the combined system (i.e. when observing $Y_{tot}^{'} Z_L$). Before proceeding to the analysis, a short background on the GNC is given in the following.

Generalized Nyquist Criterion

In accordance to [61], a system represented as part of the expression in (5.3), with the open-loop transfer function $G_{ol}\,(s)$ is stable if the Nyquist plot of the $eig(G_{ol})$, defined as the eigen-loci $\lambda_{ol1,2}$ satisfies the following conditions

- makes $n_{p,ol}$ number of anti-clockwise encirclement of -1 where $n_{p,ol}$ is the number of unstable open-loop poles of $G_{ol}(s)$.
- does not encircle the -1 point if $n_{p,ol}$ = 0.

The eigenvalue for the open-loop system can be obtained by solving $eig(G_{ol})$ as

$$\begin{aligned} \det\left[\lambda_{ol}\mathbf{I} - G_{ol}\right] &= 0 \\ \det\left\{\begin{bmatrix} \lambda_{ol} & 0 \\ 0 & \lambda_{ol} \end{bmatrix} - \begin{bmatrix} G_{ol,dd} & G_{ol,dq} \\ G_{ol,qd} & G_{ol,qq} \end{bmatrix}\right\} &= 0 \end{aligned} \tag{5.4}$$

Rearranging the above expression and solving for λ_{ol} results in (5.5).

$$\begin{aligned} (\lambda_{ol} - G_{ol,dd})(\lambda_{ol} - G_{ol,dd}) - G_{ol,qd}G_{ol,dq} &= 0 \\ \lambda_{ol1,2} = \frac{1}{2}\left[(G_{ol,dd} + G_{ol,qq}) \pm \sqrt{(G_{ol,dd} - G_{ol,qq}) + 4G_{ol,qd}G_{ol,dq}}\right] \end{aligned} \tag{5.5}$$

The expression in (5.5) gives the eigenvalue for the open-loop system G_{ol}, indicated by $\lambda_{ol,1}$ and $\lambda_{ol,2}$. For evaluating the stability, the frequency response of $\lambda_{ol,1}$ and $\lambda_{ol,2}$ (eigen-loci of $\lambda_{ol1,2}$), according to the conditions stated above, should not encircle the -1 point when $n_{p,ol}$ = 0.

5.2 Frequency-domain analysis for interconnected system

To evaluate the stability of the system shown in Fig. 5.1, the frequency domain admittance for the DFIG wind farm and the frequency domain impedance for the series compensated transmission line, derived in previous chapters, have been employed. The system is separated taking into consideration the individual system stability as described in Chapter 4 and shown in Fig. 5.1. The input admittance representation includes the admittance for the aggregated wind turbine, the collection system equivalent impedance and a single leg of the shunt capacitor admittance, shown in Fig.5.2 by the symbol Y'_{tot}. The input impedance for the grid includes the grid impedance together with the series capacitor and one shunt leg of the collection system is represented by the the symbol Z_L as in Fig. 5.2. The dashed box in Fig. 5.1 also indicates the point in the circuit where the systems is separated into the two individual subsystem. Inserting the description above in (5.3), the line current in dq components (i_{wd}, i_{wq}) can be expressed as

$$\begin{bmatrix} i_{w,d} \\ i_{w,q} \end{bmatrix} = \left[\mathbf{I} + Y'_{tot}Z_L\right]^{-1}\left(\begin{bmatrix} I_{tot,eqd} \\ I_{tot,eqq} \end{bmatrix} - Y'_{tot}\begin{bmatrix} v_{B,d} \\ v_{B,q} \end{bmatrix}\right) \tag{5.6}$$

Both Y'_{tot} and Z_L are MIMO representation. Hence the GNC described in Section. 5.1 can be applied to investigate any possible encirclement of -1 by the eigen-loci for $\lambda_{ol,1}$ and $\lambda_{ol,2}$.

In this section, the method described in Section. 5.1 has been applied to assess the stability of the overall wind farm system shown in Fig. 5.1. The structure follows a similar outline as in Section. 3.5 of Chapter 3, where the influence of different parameters has been considered. For this section assumptions and conclusion described in Section. 3.5 have been used to create a guideline for the analysis and an understanding of the obtained results.

5.2.1 Influence of controller parameters on overall system stability

In Section. 3.5, the impact of different controller parameter on the wind turbine's ability to dissipate power over a specific range of frequencies has been presented. In the analysis, a number of controller parameters has been considered to evaluate their impact on the input admittance of the generation system. In this section, the impact of these parameters on the overall system stability will be assessed. For this purpose, the impact of the RSC current controller closed-loop bandwidth ($\alpha_{cc,R}$) is considered first. It should be kept in mind that the RSC current controller is a proportional controller with gain $K_p = \alpha_{cc,R} L_R$. Initially a full aggregate model will be used in the evaluation. Figure. 5.3 shows the plot for SCL of 20% and a current controller bandwidth of $\alpha_{cc,R}$ = 1 pu.

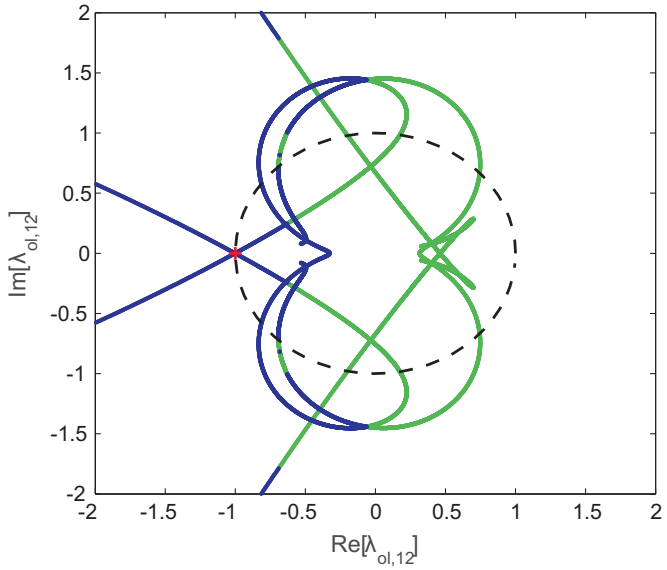

Fig. 5.3 Eigen-loci $Re[\lambda_{ol1,2}]$ vs $Im[\lambda_{ol,2}]$ for open-loop system G_{ol}. Output power of 1pu and $\alpha_{cc,R}$ = 1 pu at a SCL of 20%.

Fig. 5.3, shows $Re[\lambda_{ol1,2}]$ vs $Im[\lambda_{ol1,2}]$. However, it is difficult to evaluate net encirclement by just looking at Fig. 5.3. As a work around, the result available in Fig. 5.3, is replotted using $Re[\lambda_{ol1,2}]$ and $Im[\lambda_{ol1,2}]$ vs frequency as shown in Fig. 5.4. Using this approach, the zero crossing for the $Im[\lambda_{ol1,2}]$ and the corresponding frequency are visualized in a better manner. The reader should note that the plot is shifted in frequency to bring the resonance in the subsynchronous frequency to fall on positive values. For the result in Fig. 5.4, there exist two points where $Im[\lambda_{ol,12}]$ crosses zero. The first point falls at a low frequency of 2.5 Hz, correspond-

ing to poorly damped poles of the DFIG turbine. The second zero crossing occurs at 9.9 Hz. The corresponding $Re[\lambda_{ol1,2}]$ for the zero crossing frequencies of the $Im[\lambda_{ol,12}]$ is -39.74 and -1.028, respectively, thereby ensuring that the -1 point is not encircled.

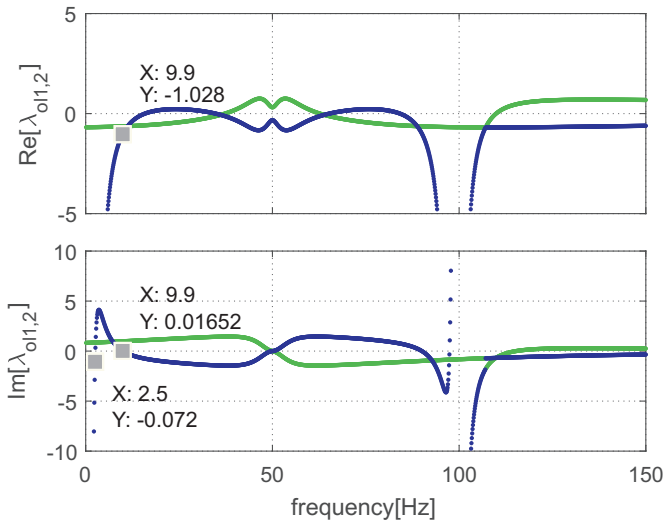

Fig. 5.4 Eigen-loci $\lambda_{ol,1}$ and $\lambda_{ol,2}$ vs frequency of G_{ol} for output power of 1 pu and $\alpha_{cc,R}$ = 1 pu at a SCL of 20%.

The resonance frequency for the transmission system as described earlier with SCL = 20%, can be calculated using $f_{res} = \sqrt{\frac{X_c}{X_{tot}}} f_s$, where X_{tot} would include the reactance of the grid transformer, the equivalent rotor and stator reactance for the IG and the transmission grid reactance. A rough calculation gives a resonance frequency of 9 Hz, which indicates that the open-loop resonance frequency closely corresponds to the subsynchronous resonance frequency. To further corroborate the conclusion above, the closed-loop system $(\mathbf{I} + Y'_{tot} Z_L)$ transmission zeros can be used to determine both the stability and the characteristic frequency of the oscillation. Figure. 5.5, shows the closed-loop pole-zeros map for the same conditions as in Fig. 5.4.

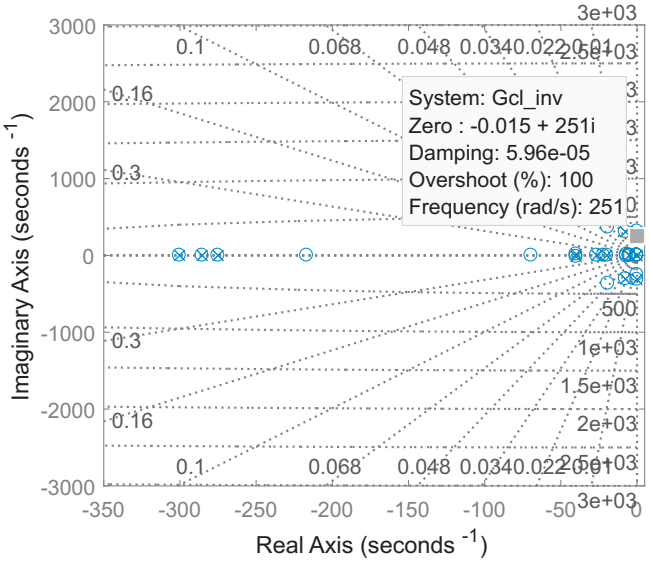

Fig. 5.5 Closed-loop pole-zero map for $\mathbf{I} + Y'_{tot} Z_L$. Output power of 1 pu and $\alpha_{cc,R}$ = 1 pu at a SCL of 20%.

As can be observed, the closed-loop system has a poorly damped zero around 251 rad/s that corresponds to 40.02 Hz that has a complementary frequency of ≈ 9.9 Hz for a 50 Hz system[1]. The system stability is also evaluated using time-domain simulations in PSCAD. The simulation model comprises a parallel line connected to the high-voltage side of the step-up transformer, in order to ensure stable operation during system start-up. The parallel line is then disconnected at $t = 4\ sec$ by operating the circuit breaker shown in the Fig. 5.6. Figure 5.7 shows the obtained simulation results under the assumption that the wind farm is producing 1 pu active power. As in the theoretical analysis, the reactive power from the wind farm is always controlled to Q_{out} = 0 pu. The current controller loop bandwidth is set to α_{cc} =1 pu. As expected from the theoretical analysis, stable operation is obtained for the considered control and system parameters. The lower plot shows the FFT on the total power indicating components around 40 Hz, thereby verifying the result obtained from the analytical analysis.

[1]Note that, the plots showing $Re[\lambda_{ol1,2}]$, $Im[\lambda_{ol1,2}]$ vs frequency is shifted in frequency for visualization purposes

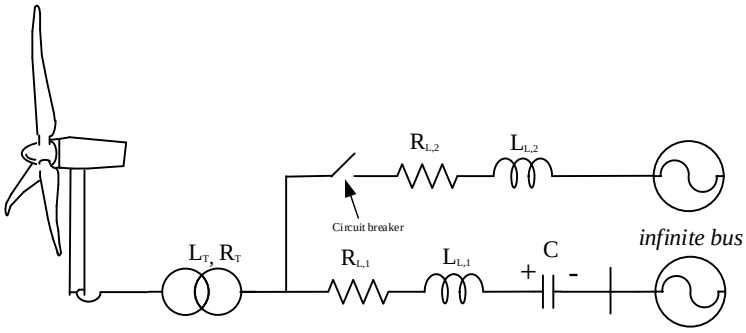

Fig. 5.6 Schematics of wind farm used for simulation

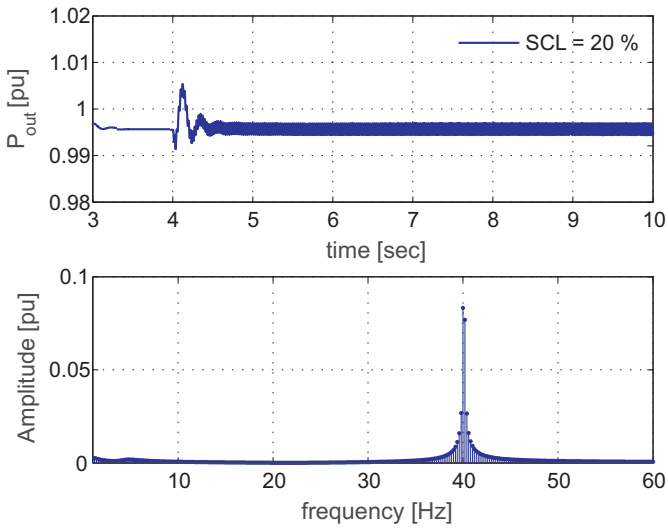

Fig. 5.7 Time domain simulation result for output power of 1 pu and $\alpha_{cc,R}$ = 1 pu at a SCL of 20%.

Returning to the impact of $\alpha_{cc,R}$, the stability of the system for increased value of $\alpha_{cc,R}$ = 2 pu and $\alpha_{cc,R}$ = 3 pu are shown in Fig 5.8 and Fig 5.9, respectively. As it can be observed in Fig. 5.8, when $\alpha_{cc,R}$ = 2 pu, there exist two zero crossing for the imaginary components one after the -1 point and one before the -1 point. This indicates the encirclement of the -1 point, thus unstable system. The result is also in direct agreement with the behavior of the wind turbine evaluated in Fig. 3.25 and subsequently in Fig. 3.26 that considered different current controller loop bandwidth. An increased gain of the current controller consequently results in higher negative real part of the input admittance matrix components presented in Fig. 3.25. Interpretation of the result in Fig. 3.25, using power dissipation capabilities of the DFIG shown in Fig. 3.26, led to the conclusion that when increasing the current controller loop-bandwidth, the ability of the turbine to dissipate power decreases. Instability is thereby expected when $\alpha_{cc,R}$ = 3 pu.

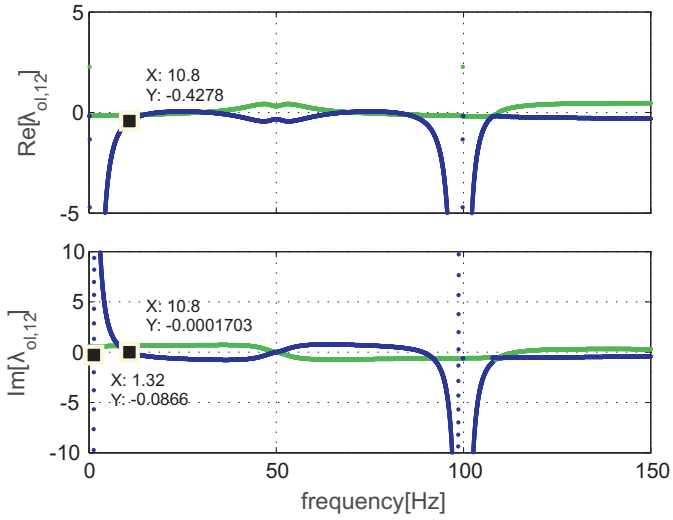

Fig. 5.8 Eigen-loci for $\lambda_{ol,1}$ and $\lambda_{ol,2}$ vs frequency for output power of 1pu and $\alpha_{cc,R}$ = 2 pu at a SCL of 20%.

The time-domain simulation when $\alpha_{cc,R}$ = 2 pu is depicted in Fig. 5.10. The obtained simulation result confirms the frequency-domain stability analysis with oscillatory frequency $\approx$ 40.89 Hz. Further the closed-loop transmission zeros for $\mathbf{I} + Y'_{tot}Z_L$ are used to verify the frequency of oscillation in the terminal power shown in Fig. 5.10. The pole-zero map is shown in Fig. 5.11.

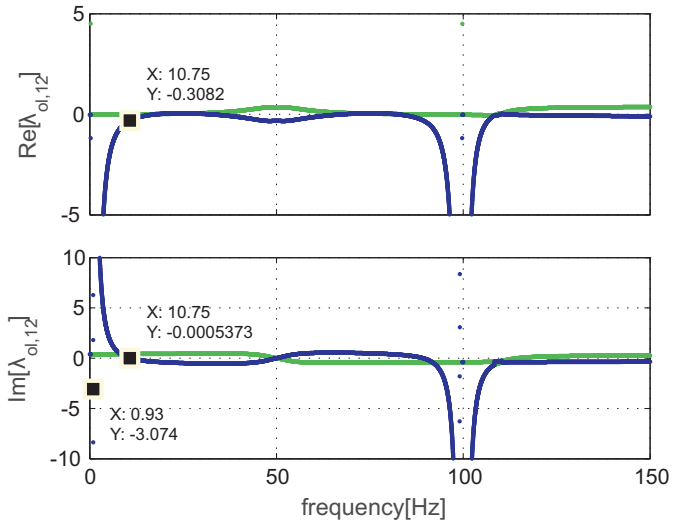

Fig. 5.9 Eigen-loci for $\lambda_{ol,1}$ and $\lambda_{ol,2}$ vs frequency for output power of 1 pu and $\alpha_{cc,R}$ = 3 pu at a SCL of 20%.

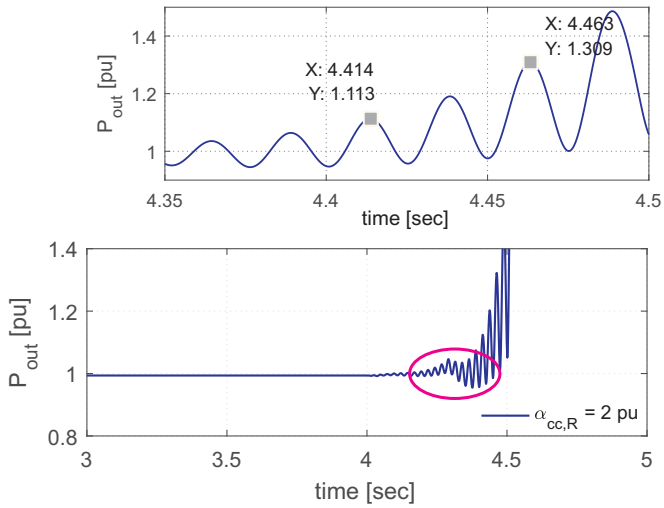

Fig. 5.10 Time domain simulation result for output power of 1 pu and $\alpha_{cc,R}$ = 2 pu at a SCL of 20%. Observed oscillatory frequency, $f_{osc} \approx 40.89$ Hz

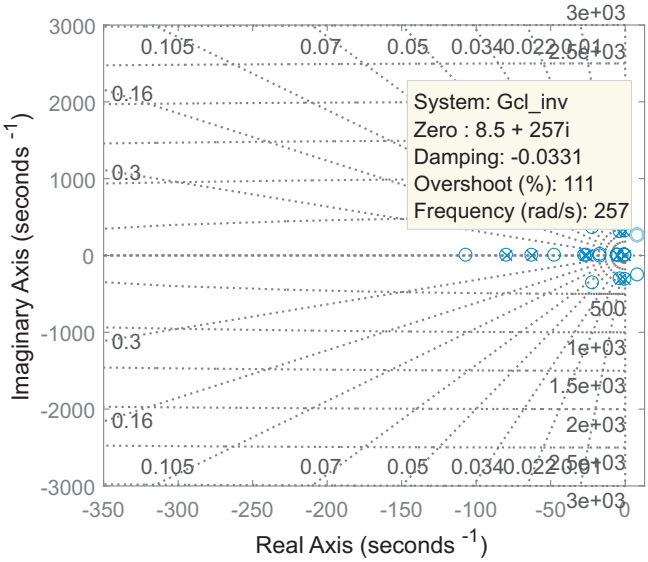

Fig. 5.11 Pole-zero map for $\mathbf{I} + Y'_{tot}Z_L$. Output power of 1 pu and $\alpha_{cc,R}$ = 2 pu at a SCL of 20%.

Similarly, time-domain verification for $\alpha_{cc,R}$ = 3 pu is shown in Fig. 5.12. Again, the result confirms the theoretical analysis. The trend where power dissipation capabilities are observed to decrease with increase in $\alpha_{cc,R}$ can be deduced from the time domain simulation of Fig. 5.7, Fig. 5.10 and Fig. 5.12, as the system damping at the resonance frequency (and thereby the time needed to reach instability) decreases when increasing $\alpha_{cc,R}$.

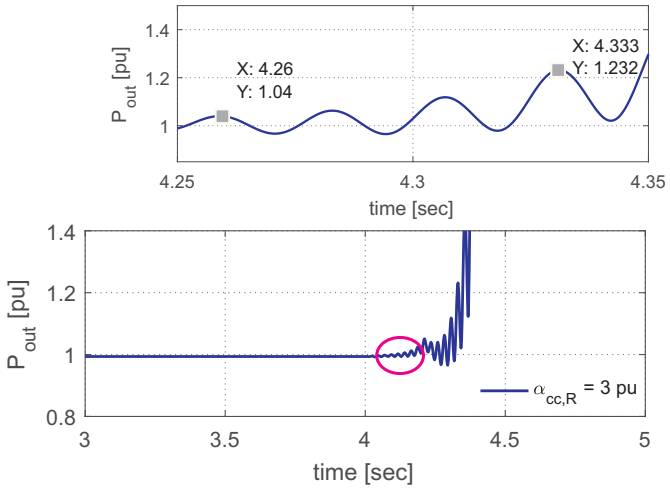

Fig. 5.12 Time domain simulation result for output power of 1 pu and $\alpha_{cc,R}$ = 3 pu at a SCL of 20%. Observed oscillatory frequency, $f_{osc} \approx 41.09$ Hz

The other RSC control parameter that has been evaluated in Section 3.5.2, is the outer-loop active (reactive) power controller integrator time constant ($T_{i,p}$). From the results presented in Fig. 3.27 and Fig. 3.28, the impact of varying $T_{i,p}$ is shown to have minimal effect both from the frequency response of the admittance matrix components and from the power dissipation behavior of the DFIG turbine itself. In this section, time constant $T_{i,p}$ is halved to 0.1 sec (standard condition $T_{i,p}$ = 0.2 sec) for the wind farm operating at marginal stability as in Fig. 5.4. The corresponding result is shown in Fig. 5.13. The GNC analysis leads to the same conclusions showing that the RSC outer-loop to have no impact on the system stability. The result is not far fetched as the DFIG turbine shows almost no variation in its frequency characteristics due to this parameter.

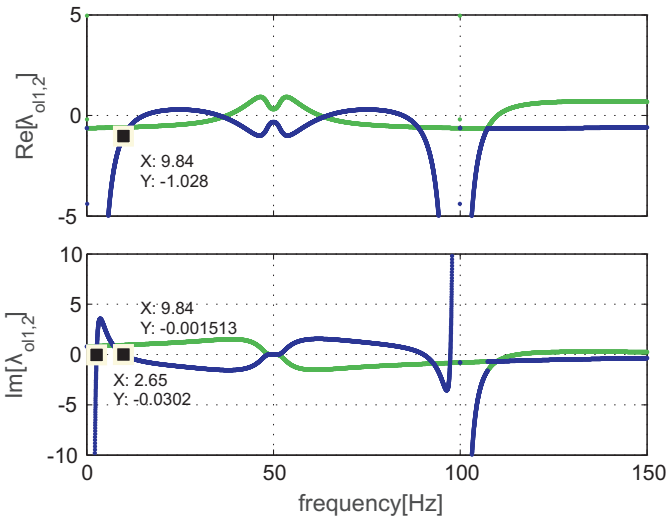

Fig. 5.13 Eigen-loci for $\lambda_{ol,1}$ and $\lambda_{ol,2}$ vs frequency for output power of 1 pu and $\alpha_{cc,R}$ = 1 pu at a SCL of 20%. Outer-loop power controller integrator time constant set to $T_{i,P}$ = 0.1 sec

Further evaluation dealing with the impact of the GSC controller has been presented in Section. 3.5.3. The impact of the GSC inner current controller-loop bandwidth, $\alpha_{cc,f}$, has been shown to be insignificant (Fig. 3.29 and Fig. 3.30) both on the frequency-domain input admittance matrix components and on the power dissipation behavior of DFIG generation unit. The impact of $\alpha_{cc,f}$ on the stability of the overall interconnected wind farm system when the GSC current controller loop bandwidth, $\alpha_{cc,f}$, is increased from 1 pu (base case) to 2 pu is here evaluated. An output power of P_{out} = 1 pu and Q_{out} = 0 pu is considered for the result shown in Fig. 5.14. As it can be observed, the system stability is not affected by an increase in the GSC current controller loop bandwidth.

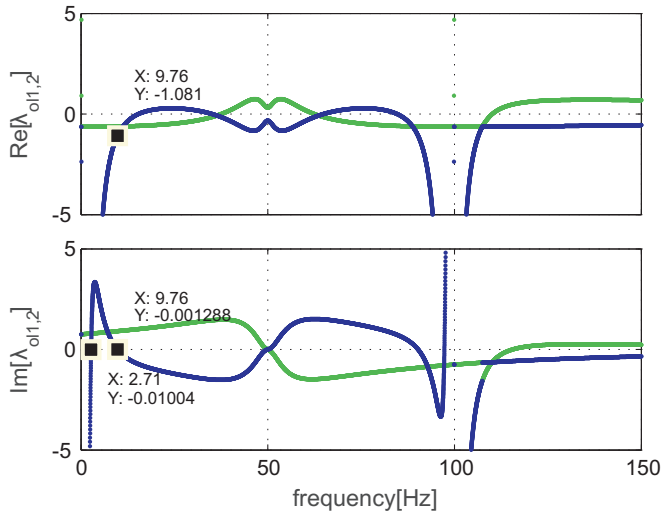

Fig. 5.14 Eigen-loci $\lambda_{ol,1}$ and $\lambda_{ol,2}$ vs frequency for output power of 1 pu and $\alpha_{cc,f}$ = 2 pu at a SCL of 20%.

The other GSC parameter used for evaluation is the dc-link voltage controller closed-loop bandwidth, α_{dc}. Based on the results shown in Fig. 3.31 and Fig. 3.32, it has been concluded that the impact of α_{dc} on the power dissipation of the DFIG generation system for operation in the supersynchronous speed range is insignificant. To asses its impact on the overall system, a marginally stable system operated at full power at compensation level of 20% has been considered. Figure. 5.15 shows the result for an increased dc-link voltage controller bandwidth from α_{dc} = 0.1 pu to α_{dc} = 0.2 pu. For an increased value of α_{dc}, the system stability falls in the stable region where both zero crossing frequency fall before the -1 point, thereby ensuring no encirclement of the -1 point.

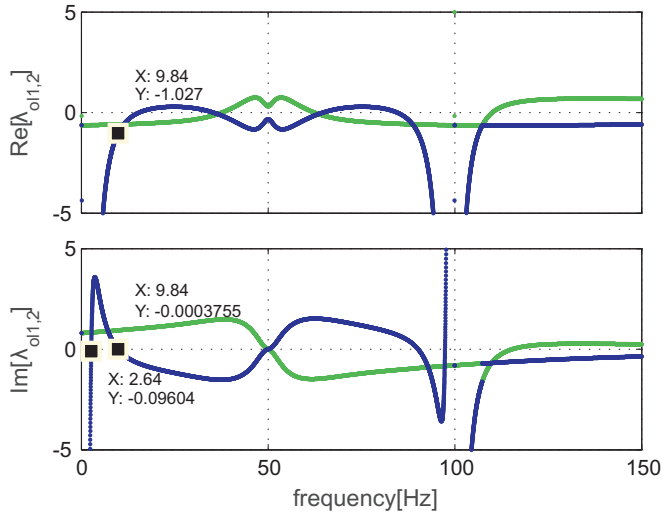

Fig. 5.15 Eigen-loci $\lambda_{ol,1}$ and $\lambda_{ol,2}$ vs frequency for output power of 1pu and α_{dc} = 0.2 pu at a SCL of 20%.

Time-domain result corroborating the above conclusion for increased value of $\alpha_{cc,f}$ and α_{dc} for operation in supersynchronous speed range is shown in Fig. 5.16

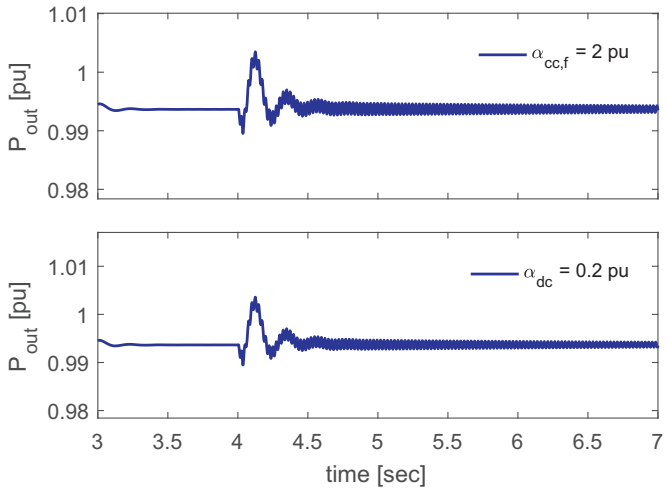

Fig. 5.16 Time domain simulation result for output power of 1 pu and $\alpha_{cc,f}$ = 2 pu (*upper plot*) and α_{dc} = 0.2 pu (*lower plot*) at a SCL of 20%.

5.2.2 Influence of operating condition on overall system stability

The influence of the operating condition includes both the level of active power output from the wind farm and the level of series compensation (SCL). The level of output power is directly dependent on the amount of wind speed incident on the wind turbine, which is variable in nature. When it comes to the level of series compensation, this is somewhat a fixed factor as there is a known amount of series compensation installed. However, the equivalent impedenace of the

grid, as seen from the wind farm, can change due to reconfiguration of the transmission system, thereby affecting the equivalent impedenace of the grid as viewed from the wind farm. As a result, varying SCL can be used to replicate the reconfiguration in the transmission system.

The investigation presented in Section. 3.5.4 has shown that the risk for instability is higher when the DFIG is operated in the subsynchronous speed range. Thus it is of interest to evaluate the overall system stability for low output power, where the generator is operated at subsynchronous speed range. For a SCL of 20%, the wind farm operated at full power, corresponds to a marginally stable system. The result using the GNC when the wind farm is operated at low wind speed of P_{out} = 0.25 pu (in the subsynchronous speed range) is shown in Fig. 5.17.

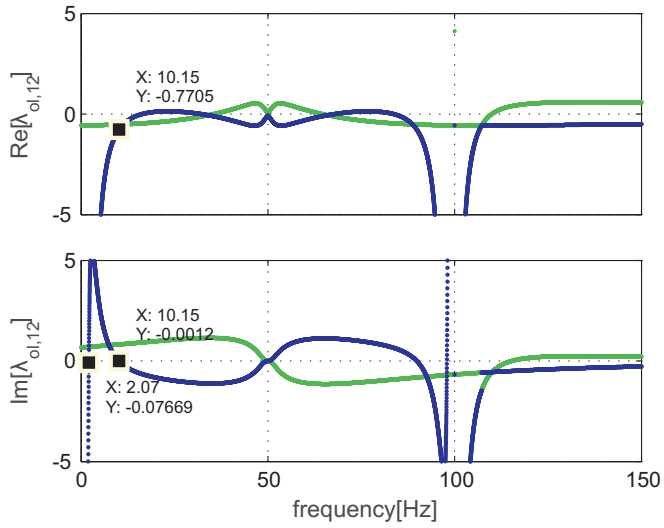

Fig. 5.17 Eigen-loci for $\lambda_{ol,1}$ and $\lambda_{ol,2}$ vs frequency for output power of 0.25 pu and $\alpha_{cc,R}$ = 1 pu at a SCL of 20%.

The result shown in the figure clearly indicates the encirclement of the -1 point around 10.1 Hz. The cycle of oscillation on the output power (for the wind farm system) is used to extract the frequency (shown in Fig. 5.18), indicating a resonance frequency of $\approx$ 40.5 Hz. This result is supported as the DFIG generator system, evaluated using Fig. 3.35, has been shown to present decreased power dissipation capabilities for operation in the subsynchronous speed range as compared to supersynchronous speed.

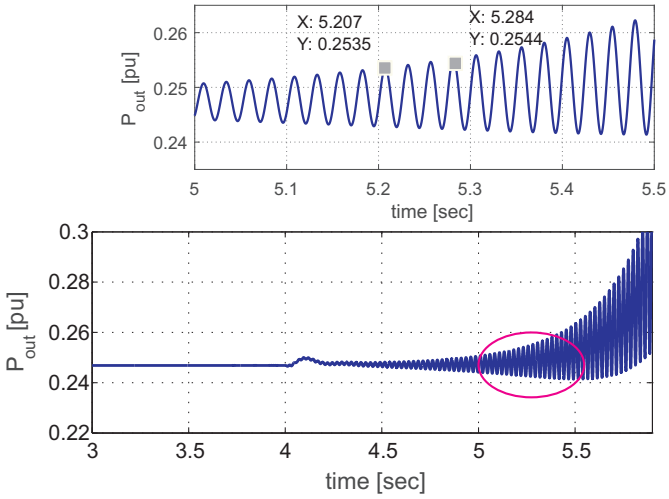

Fig. 5.18 Time domain simulation result for output power of 0.25 pu and $\alpha_{cc,R}$ = 1 pu at a SCL of 20%.

The stability of the interconnected system is restored when the SCL level is reduced down to 14% as depicted in Fig. 5.19

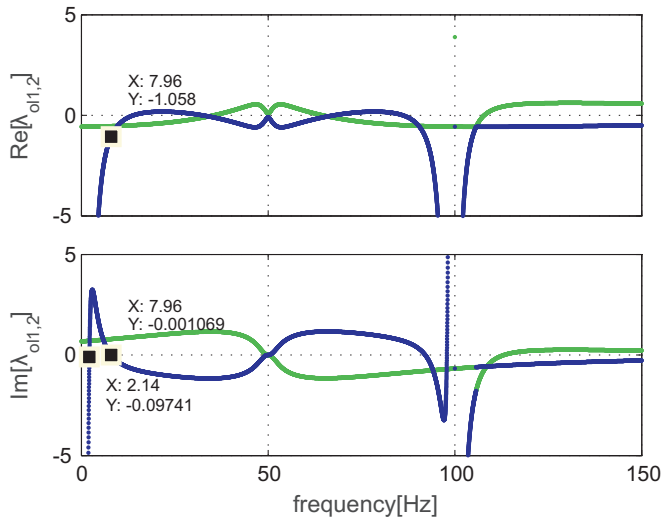

Fig. 5.19 Eigen-loci $\lambda_{ol,1}$ and $\lambda_{ol,2}$ vs frequency for output power of 0.25 pu and $\alpha_{cc,R}$ = 1 pu at a SCL of 14%.

Further analysis related to dc-link controller parameter for operation in subsynchronous speed range (see Fig. 3.36) is shown to have some impact on the $Y_{qd}(j\omega)$ component for the DFIG generator system input admittance matrix where a lower bandwidth of α_{dc} = 0.1 pu has a less negative real part as compared to α_{dc} = 0.2 pu. Power dissipation capabilities for the DFIG generator system also has been shown to slightly increase (at least for $\lambda_1(j\omega)$ component) for α_{dc} = 0.1 pu as compared to α_{dc} = 0.2 pu. Based on this, the impact of α_{dc} on the overall system stability for operation in the subsynchronous speed range (P_{out} = 0.25 pu) is evaluated. Figure. 5.20, shows the result where α_{dc} = 0.1 pu for a marginally stable system at compensation

level of 14.5%. In Fig. 5.21, the compensation level is maintained where as α_{dc} is increased to 0.2 pu. As can be observed, the lower bandwidth of 0.1 pu leads to a stable system whereas instability is predicated for α_{dc} = 0.2 pu.

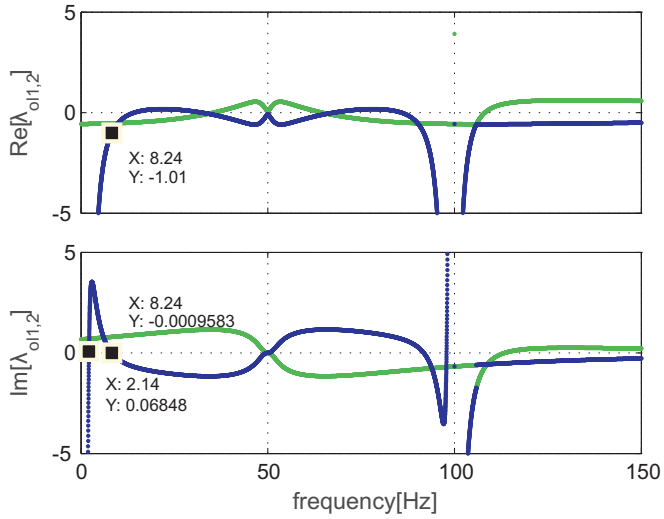

Fig. 5.20 Eigen-loci $\lambda_{ol,1}$ and $\lambda_{ol,2}$ vs frequency for output power of 0.25 pu and α_{dc} = 0.1 pu at a SCL of 14.5%.

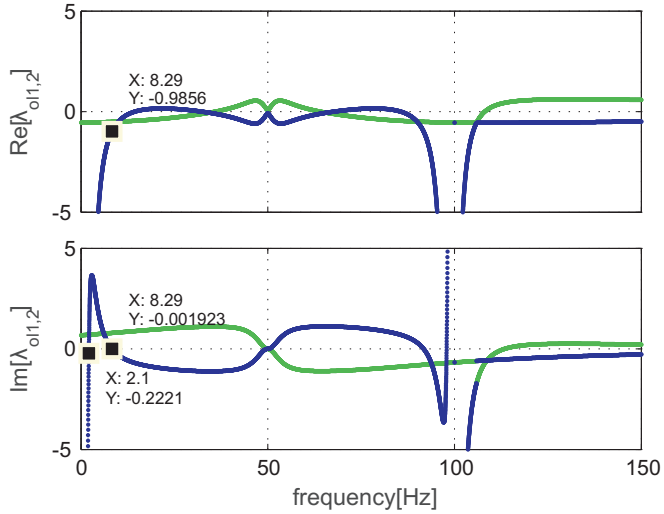

Fig. 5.21 Eigen-loci $\lambda_{ol,1}$ and $\lambda_{ol,2}$ vs frequency for output power of 0.25 pu and α_{dc} = 0.2 pu at a SCL of 14.5%.

The impact of α_{dc}, in comparison to other parameters, is still minimal even for operation in subsynchronous speed range. However, note should be taken on how this parameter affects the system stability. Depending on whether the wind turbine is operated in subsynchronous speed range, lowering α_{dc} leads to system stability whereas the same action may lead to instability when the wind turbine is operated in supersynchronous speed range. Time-domain simulation verification for the case are presented in Fig. 5.20 and Fig. 5.21 is shown in Fig. 5.22.

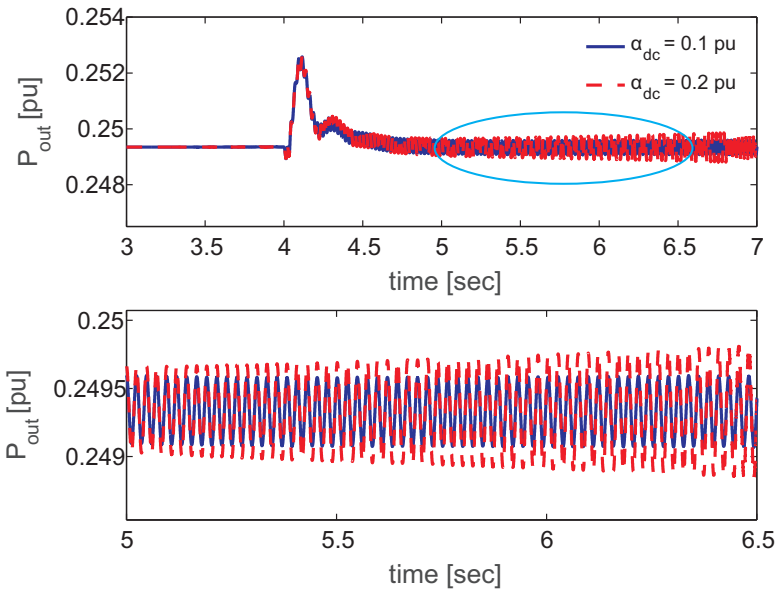

Fig. 5.22 Time domain simulation result for output power of 0.25 pu and $\alpha_{cc,R}$ = 1 pu at a SCL of 14.5%. α_{dc} = 0.1 pu *(blue curve)* and α_{dc} = 0.2 pu *(red dashed curve)*

As briefly mentioned in the beginning of this section, another aspect that influences the stability of the system is the SCL. From previous results, it has been observed that the variation of the SCL tends to move the resonance point of the transmission grid along the x-axis (frequency axis). Returning to the analysis using GNC, the wind farm is made to operate at full power (considering the best case scenario from a stability point of view), whereas the SCL is increased to SCL = 25% and SCL = 30% (from the marginally stable case, SCL = 20%). The obtained results are shown in Fig. 5.23 and Fig. 5.24. The GNC analysis predicts instability in both cases of SCL = 25% and 30%. From the grid impedance behavior for varied compensation level shown in Fig. 4.12, the zero crossing for the reactance tends to move to the right as the SCL is increased. On the other hand, looking at the dissipative property for the DFIG input admittance, for example shown in Fig. 3.26, the $\lambda_1(j\omega)$ tends to present a higher negative value for frequencies further to the right, i.e. in the range -50 Hz - 0 Hz [2]. As a result, higher compensation level can cause the resonance in the system to fall in the region where the dissipative behavior of the wind farm system is minimal.

[2]The negative frequency range appears due to results presented in dq frame where the subsynchronous frequency range 0- 50 Hz (in $\alpha\beta$) appear in the range -50 Hz - 0 Hz (in dq frame)

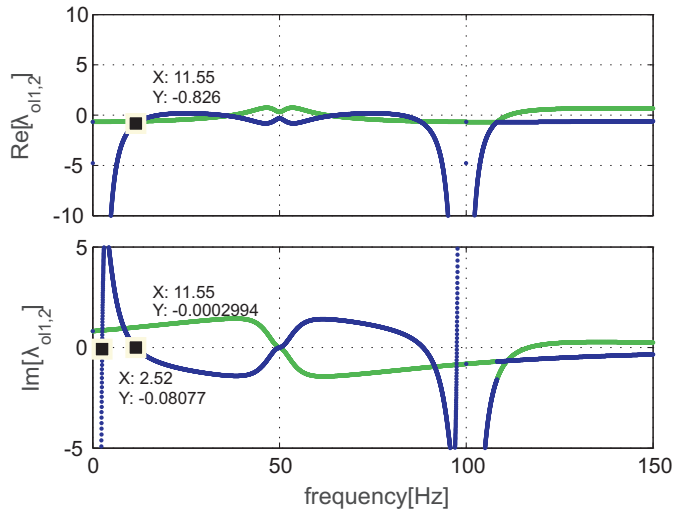

Fig. 5.23 Eigen-loci $\lambda_{ol,1}$ and $\lambda_{ol,2}$ vs frequency for SCL = 25%. Output power, P_{out} = 1 pu, Q_{out} = 0 pu and $\alpha_{cc,R}$ = 1 pu

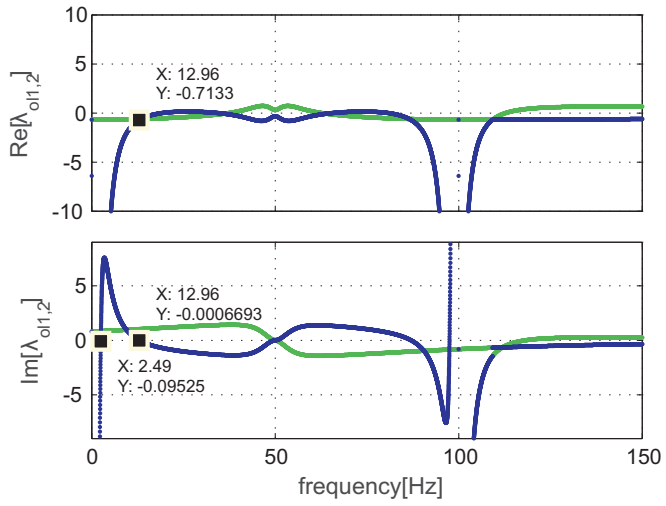

Fig. 5.24 Eigen-loci $\lambda_{ol,1}$ and $\lambda_{ol,2}$ vs frequency for SCL = 30%. Output power, P_{out} = 1 pu, Q_{out} = 0 pu and $\alpha_{cc,R}$ = 1 pu

Time-domain simulation results replicating the system configuration of P_{out} = 1 pu and SCL = 25% and SCL = 30% are depicted in Fig. 5.25 and Fig. 5.26, respectively. As can be viewed, in both cases the system experiences growing oscillation that results in instability. The cycle of oscillation is extracted from the time-domain simulation are 38.83 Hz and 37.38 Hz for SCL = 25 % and SCL = 30 %, respectively, that closely correspond to the analytical results presented before. It should be observed that the higher the SCL, the faster the system becomes unstable. This is due to the fact that the resonance point of the grid that tends to shift to the right would fall in the frequency range where the power dissipation capabilities of the DFIG generator system

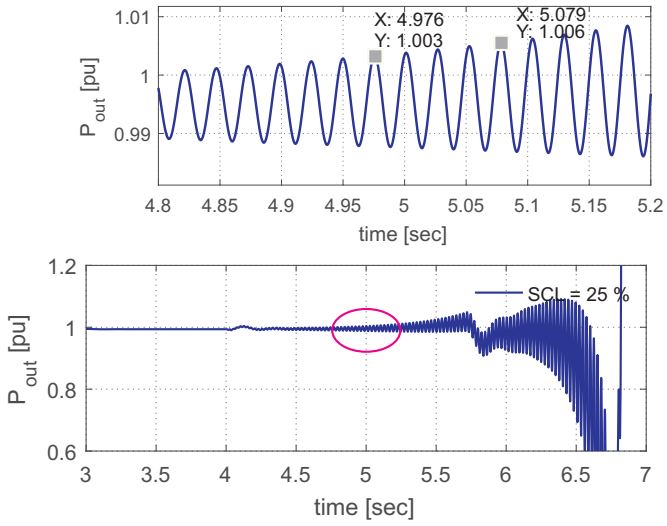

Fig. 5.25 Time domain simulation result for output power of 1 pu and $\alpha_{cc,R}$ = 1 pu at a SCL of 25%.

is minimal.

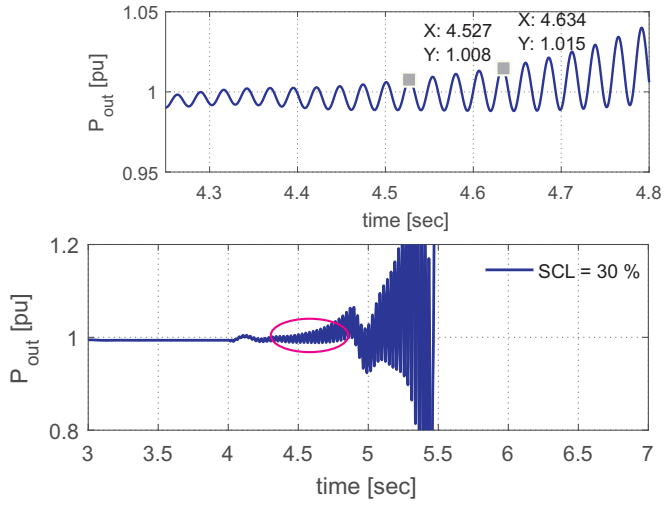

Fig. 5.26 Time domain simulation result for output power of 1 pu and $\alpha_{cc,R}$ = 1 pu at a SCL of 30%.

5.3 Frequency-domain analysis for interconnected system using MWT model

In Section 4.5.1, the impact of considering a single aggregate versus detailed MWT based aggregation has been presented. In this section, the GNC is used to evaluate system stability when using a MWT aggregate model for wind farm system representation. For the analysis, a five radial MWT model is considered where each radial has equal number of wind turbine (10 turbines rated at 2 MW). A case study that considers distributed power output within the wind farm and

a SCL that leads to a marginally stable system is initially evaluated using GNC. The obtained analytical result is compared with time-domain result for verification. Following this, the analytical results obtained using the five radial MWT representation are used as a base to evaluate the different wind farm aggregation methods (full aggregate, two radial MWT aggregate, e.t.c) discussed in Section. 4.3, from a total system stability point of view using GNC.

5.3.1 Influence of operating point on MWT overall stability

Initially, an unrealistic wind speed distribution has been considered for investigation and model verification. An output power of P_{radial} = 0.22 pu, 0.3 pu, 0.5 pu, 0.7 pu and 0.9 pu are used to evaluate the system stability using GNC. The result is shown in Fig. 5.27 is for an SCL = 18%. The result show that the system is stable with two zero crossing frequency at 2.4 Hz and 9.4 Hz.

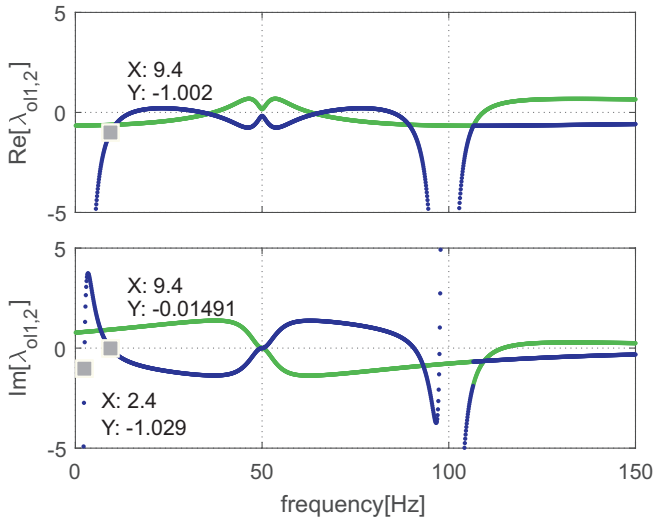

Fig. 5.27 Eigen-loci $\lambda_{ol,1}$ and $\lambda_{ol,2}$ vs frequency for output power of 0.22 pu, 0.3 pu, 0.5 pu, 0.7 pu and 0.9 pu and $\alpha_{cc,R}$ = 1 pu at a SCL of 18%.

Corresponding time-domain simulation, using a five aggregate wind farm model, is shown in Fig. 5.28. The upper plot shows the output power, while the lower plot shows the FFT performed on the active power at the PCC point. The oscillation frequency is around 41 Hz, which is in close proximity of the zero crossing frequency for $Im\left[\lambda_{ol1,2}\right]$ obtained using GNC.

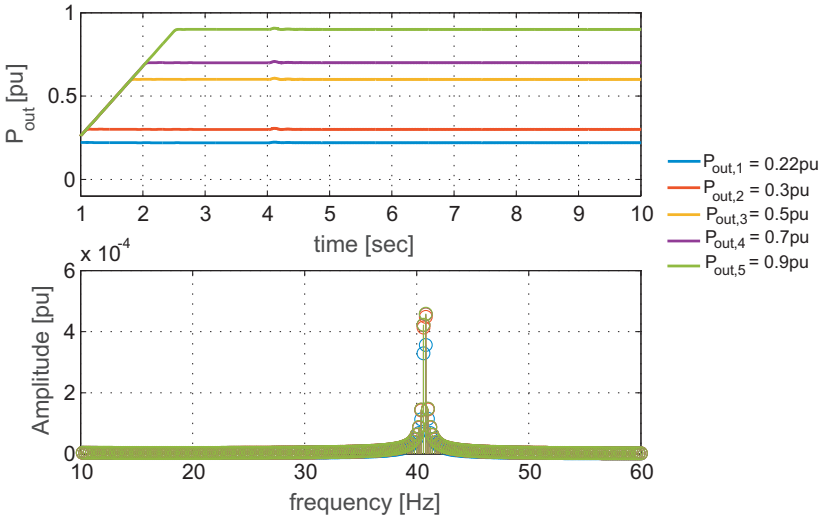

Fig. 5.28 Time domain simulation result for output power of P_{out} = 0.22 pu, 0.3 pu, 0.5 pu, 0.7 pu and 0.9 pu and $\alpha_{cc,R}$ = 1 pu at a SCL of 18% .

Next, to assess the need for a MWT, the same MWT wind farm model is considered for SCL = 19%, shown in Fig. 5.29, where the GNC analytical shows instability in the system. Further the same wind farm, based on the average power generated from it, is modeled using a single full aggregate model and the stability of the interconnected system is evaluated as depicted in Fig. 5.30. As can be viewed, the full-aggregated model predicts a stable system whereas MWT model predicated instability for the same level of series compensation.

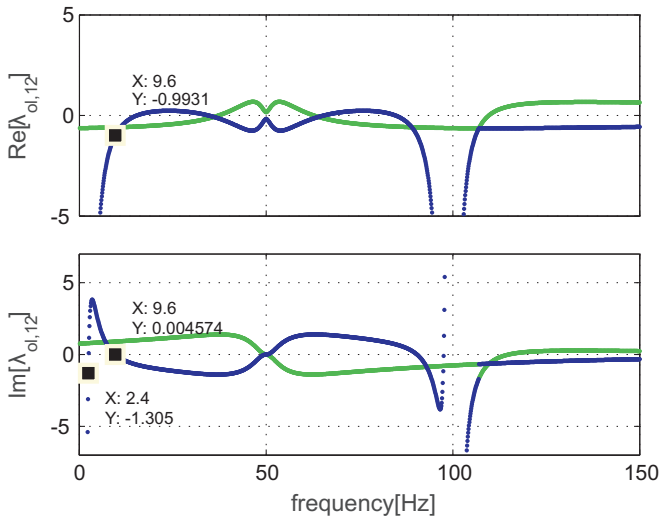

Fig. 5.29 Eigen-loci $\lambda_{ol,1}$ and $\lambda_{ol,2}$ vs frequency for output power of 0.22 pu, 0.3 pu, 0.5 pu, 0.7 pu and 0.9 pu and $\alpha_{cc,R}$ = 1 pu at a SCL of 19%.

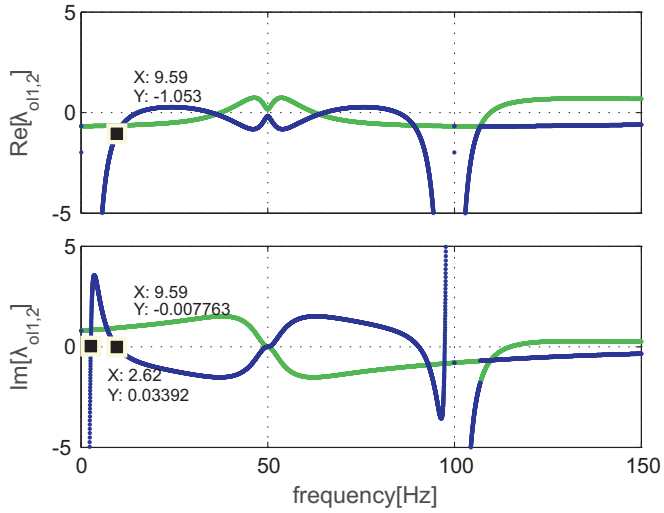

Fig. 5.30 Eigen-loci $\lambda_{ol,1}$ and $\lambda_{ol,2}$ vs frequency for output power of 0.526 pu and $\alpha_{cc,R}$ = 1 pu at a SCL of 19%.

Further, in Chapter 4, aggregation based on subsynchronous speed and supersynchronous speed turbine distribution has been evaluated to show a specific frequency domain property of the DFIG-based wind farm model. Stability analysis is here evaluated by using a multiple aggregate model having two aggregate (two radial MWT aggregate), one aggregate having P_{out} = 0.26 pu operating in subsynchronous speed and second aggregate with P_{out} = 0.68 pu operated at supersynchronus speed. Therefore, the total power output from the wind farm is unchanged. The analytical result using GNC is shown in Fig. 5.31. The result obtained using a two radial MWT aggregate model predicts instability, as in the detailed model of Fig. 5.29, having a zero crossing frequency around 9.7 Hz.

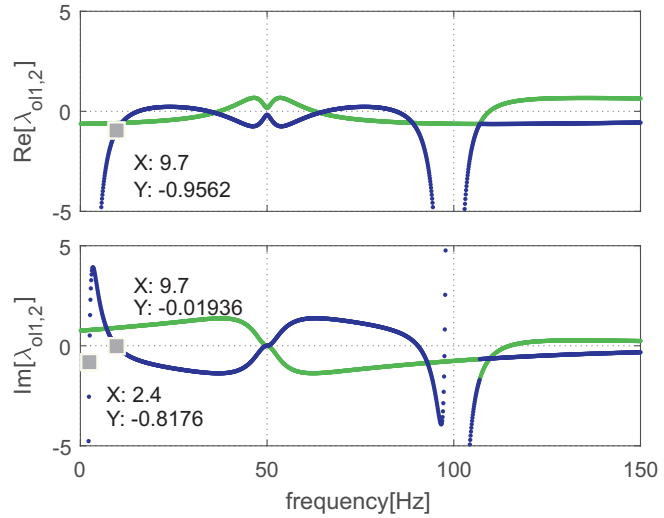

Fig. 5.31 Eigen-loci $\lambda_{ol,1}$ and $\lambda_{ol,2}$ vs frequency for output power of 0.26 pu and 0.68 pu and $\alpha_{cc,R}$ = 1 pu at a SCL of 19%.

Comparing the system stability analysis using a full aggregated wind farm model versus a two

radial MWT aggregate wind farm model shown in Fig 5.30 and Fig 5.31, respectively, the latter gives a correct prediction for system instability. From the results presented, it can be concluded that the detailed model gives the most accurate representation of the system. However, a good compromise can be achieved by using the two radial MWT aggregate wind farm representation that is capable to predicting system stability with good accuracy. A full aggregation , in some cases, might lead to erroneous results.

5.4 Conclusion

In this chapter, the risk of SSCI in a DFIG-based wind farm connected to a series compensated transmission line has been investigated using a impedance-based frequency-domain approach. The system has been modeled as a MIMO system, where two subsystems have been defined: an aggregate DFIG subsystem and a series compensated transmission line subsystem. The DFIG subsystem includes a portion of the collection grid and has been expressed in terms of its input admittance transfer function, $Y'_{tot}(s)$, whereas the transmission line is given in terms its impedance transmission function, $Z_L(s)$. Frequency-domain open-loop analysis of the systems have been investigated with respect to various parameters and system conditions. From the analysis, it can be concluded that the following conditions have a major influence on the stability of a DFIG wind generation system connected to a series compensated transmission line.

1. The closed-loop bandwidth of RSC current controller ($\alpha_{cc,R}$). The higher the RSC closed-loop current controller bandwidth, the higher the risk for SSCI. It has been concluded that, the higher the RSC current controller bandwidth, the higher the risk of SSCI, even at relatively low level of series compensation

2. The amount of active power generated by the DFIG. The more the power produced by the DFIG wind farm, the less the risk for SSCI. Similarly, it is shown that the amount of generated active power affects the level of series compensation acceptable for radial connection.

3. Level of series compensation (SCL). The higher the level of series compensation, the higher the risk for instability due to SSCI in case of radial connection

4. The closed-loop bandwidth of the dc-link voltage controller (α_{dc}). The impact of this parameter depends on whether the GSC is operated in rectifier mode or in inverter mode. In case of inverter operation mode, corresponding to supersynchronous speed range for the wind turbine, a higher α_{dc} is favorable (the overall impact is minimal). For rectifier operation, the opposite holds. The impact of this parameter is shown to be minimal as compared to $\alpha_{cc,R}$ and affects the system stability around marginal conditions only.

The overall system stability has been evaluated using an impedance-based GNC, where the open-loop system stability is used to asses the risk for SSCI. The obtained results are supported both by the closed-loop analysis and time-domain simulation using a detailed model representation of the DFIG implemented in PSCAD. Based on the above conclusions, the RSC controller

parameter, specifically $\alpha_{cc,R}$, plays a major role in shaping the DFIG impedance and thereby on the risk for SSCI.

The impact of aggregation method on SSCI analysis has been evaluated using case studies using a single full-aggregate wind farm representation versus a MWT aggregate wind farm representation. The MWT aggregate representation presents a clear advantage over the full aggregate wind farm representation with regards to system stability analysis. Further, analytical evaluation using the two radial MWT aggregate representation, as suggested in Chapter 4, has been shown to give a good balance (especially for SSCI analysis) between the single full aggregate wind farm representation and MWT aggregate wind farm representation involving multiple radials.

It should be noted that the stability analysis performed in this chapter has been focusing on a particular grid configuration and control structure. However, the method is not restricted to the configurations presented in this chapter and can be extended to include more complex grid configurations or alternative DFIG control structures.

Chapter 6

SSCI Mitigation using DFIG

6.1 Introduction

In an attempt to minimize the impact caused by SSCI, the development of mitigation strategies for this kind of interaction has become the focus of research in recent years. Some of the reported mitigation techniques involve the installation of static synchronous compensator (STATCOM) [62] [63], static var compensator (SVC) [64], thyristor controlled series capacitors (TCSC) [65] [66] and other more dedicated external devices like gate-controlled series capacitor (GCSC) [59]. Other cost effective SSCI mitigation techniques involve the modification of the DFIG controller, an example being the damping controller described in [67] that uses the measured rotor and stator currents to act on the RSC control loop. In this work, the damping controller parameters are determined by using a state observer based on a reduced order system state-space model of the turbine. Another type of damping controller, proposed in [60], involves a derivative current control loop, a second order low-pass filter and a lead-lag compensator, implemented on the RSC.

A different approach is proposed in [68], which involves the addition of a virtual impedance in series with the PI controller of the RSC current control loop. An impedance-based stability analysis is used to evaluate the impact of the proposed damping approach. However steps regarding the tuning of the proposed virtual impedance, in the design stage, is not explicitly presented in the paper. The author also proposes the addition of a parallel virtual impedance through the GSC. However, results that supports the use of GSC for damping are not reported in the paper.

The works presented in [69] [70] proposes the use of subsynchronous suppression filters in the DFIG controller. The approach involves the addition of a notch filter to the RSC current-control loop. The filter is utilized to attenuate the SSR mode, thereby eliminating the possible interaction that could occur and as a result stabilizing the SSCI. However, this method would require knowledge of the oscillatory frequency during system design and operation. In the work, the application of RLC circuit quantitatively derived for the specific system under consideration is used to determine this oscillatory frequency. This method lacks in the aspect that the system to be mitigated need to be first characterized before the design of the notch filter. Obtaining the equivalent RLC circuits would be problematic in case of new installations and/or in case of

network reconfiguration.

When it comes to mitigation techniques, which aim at improving the DFIG's or the network's behavior in order to make the system more passive at the frequencies of interest (passive techniques), the work presented in [71] suggests bypassing of the series capacitors in case of SSCI, while in [71–73] it is suggested to adjust the DFIG control parameters, especially the gain of the RSC current controller, in events of SSCI.

Other methods suggest the use of non-conventional control strategies for mitigating SSCI. The work presented in [74] proposes the use of a observer state-feedback approach for the implementation of a SSR damping controller. A quadratic optimal techinque is used to obtain the desired gain for the observer. As the considered radial system with a wind turbine and a transmission system results in a 22^{nd}-order model, the authors for practical purposes used a reduced order model for the state observer. However, placement for the SSR damping controller is chosen to be on the GSC converter, which is shown to have some disadvantages in other publications [11] [67] [68]. The work presented in [75] pinpoints the issue of SSCI due to RSC current controller and therefore proposes the use of direct-power controller in combination with direct-speed control (for MPPT) to control the rotor-side voltage, thereby avoiding the problematic inner current controller.

This chapter presents a possible SSCI mitigation techniques that can be employed to the DFIG wind turbine controller. The proposed approach aims at shaping the input admittance of the wind turbine within the desired frequency range in order to improve the system damping. Both frequency-domain analysis and time-domain simulation are used to evaluate the effectiveness of the proposed approach.

6.2 DFIG turbine modification for SSCI mitigation

In previous chapters, it has been established that the problem of SSCI in DFIG based wind farms is due to the energy interaction that occurs between the control system of the power electronic devices in the wind turbines within the wind farm system and the resonance conditions in the series compensated transmission grid. In this section, SSCI mitigation through variation of the DFIG system input admittance is investigated.

6.2.1 SSCI mitigation through control system modification

In-built controller modification based countermeasures have the advantage of begin costless, as they do not require the installation of expensive additional mitigation devices and can easily be implemented within the DFIG control system. For a DFIG based wind turbine, there exist two alternatives: one considering the GSC controller and the other considering the RSC controller. In [76], the author investigates the potential of the GSC controller for SSR mitigation using residual-based analysis and time-domain simulations in MATLAB. An auxiliary proportional damping controller implemented on the GSC utilizing the series capacitor voltage has been demonstrated to have effective damping effect. However, in [67], a comparison of the GSC and

RSC controller loops for SSCI mitigation by adding a supplementary damping controller utilizing multiple input signal has demonstrated that the supplementary controller utilizing the GSC provides good results around relatively low levels of series compensation, but failed for high levels. On the other hand, the RSC based supplementary controller showed good performance even for high level of series compensation. The work presented in [77], that evaluates the optimal location for a proportional based supplementary damping controller, also identifies various controller input signals for the damping controller, based on residual analysis and root-locus method. It has been concluded that the capacitor voltage is the ideal signal and the GSC is the ideal location. However in the author's recent work [11], it is clearly pointed out that the RSC inner-current controller loop is the best location for inserting the damping controller.

Returning to the analytical results presented in the previous chapters (see Section 3.5.3), the impact of the GSC controller on the power dissipation behavior of the DFIG has been demonstrated to be minimal, which hinders the use of this controller for mitigation purposes. On the other hand, it has been shown that the RSC controller (especially the RSC current control loop) has a significant impact on the frequency response of the DFIG in the subsynchronous frequency range. Hence, modification of RSC controller for SSCI damping has been considered here.

6.2.2 Proposed SSCI mitigation

The proposed mitigation technique for SSCI consists of two stages: an estimation stage and a damping controller stage. The estimation stage consists of an estimation algorithm used to extract the subsynchronous component from the measured signal. This signal serves as an input to the damping controller stage. The purpose of the damping controller stage is to enhance the damping of the system at the particular frequencies of interest. The proposed approach is implemented as part of the RSC current control loop as described below.

Estimation Method

The estimation algorithm (EA), as briefly stated, is used to estimate the subsynchronous component that would appears in the measured terminal power of the wind farm. In the event of a SSCI, the terminal voltage v_g, in addition to the fundamental component, will contain a subsynchronous component that would result in a subsynchronous current to flow in the network. As a results, the terminal power P_{out} will be constituted by an average component and an oscillatory component that can be expressed as

$$P_{out}(t) = P_{out,av}(t) + P^{a}_{out,osc}(t)\cos\left[\omega_{osc}t + \varphi(t)\right] \tag{6.1}$$

where $P_{out,av}$ represents the average component of the output power and the oscillatory part is expressed in term of its amplitude ($P^{a}_{out,osc}$), its frequency (ω_{osc}) and its phase (φ). The expression in (6.1) can be expressed, using the average value ($P_{out,av}$), a complex phasor for the

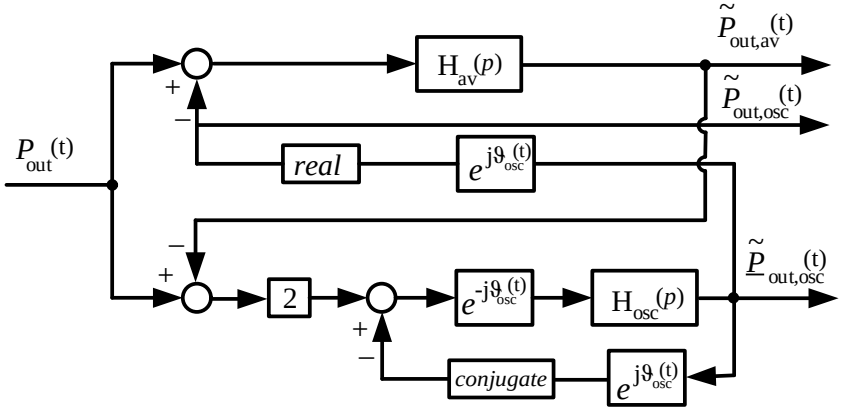

Fig. 6.1 Block diagram of LPF-based estimation algorithm

oscillatory component($\underline{P}_{out,osc} = P^{a}_{out,osc} e^{j\varphi(t)}$) and the oscillation angle ($\theta_{osc}(t) = \omega_{osc} t$), as

$$P_{out}(t) = P_{out,av}(t) + \frac{1}{2}\underline{P}_{out,osc}(t)\, e^{j\theta_{osc}(t)} + \frac{1}{2}\underline{P}^{*}_{out,osc}(t)\, e^{-j\theta_{osc}(t)} \tag{6.2}$$

From the above expression, it can be deduced that the terminal power is partitioned into three frequency components having frequencies at 0, ω_{osc} and $-\omega_{osc}$. As described in [78], by rearranging (6.2) and by applying low-pass filtering, the different terms can be isolated and estimated from the input signal, as

$$\begin{aligned}
\tilde{P}_{out,av}(t) &= H_{av}\left[P_{out}(t) - \tilde{P}_{out,osc}(t)\right] \\
\underline{\tilde{P}}_{out,osc}(t) &= H_{osc}\left[\left\{2P_{out}(t) - 2\tilde{P}_{out,av}(t) - \underline{\tilde{P}}^{*}_{out,osc} e^{-j\theta_{osc}(t)}\right\} e^{-j\theta_{osc}(t)}\right] \\
\tilde{P}_{out,osc}(t) &= \frac{1}{2}\underline{\tilde{P}}_{out,osc}(t)\, e^{j\theta_{osc}(t)} + \frac{1}{2}\underline{\tilde{P}}^{*}_{out,osc}(t)\, e^{-j\theta_{osc}(t)}
\end{aligned} \tag{6.3}$$

where terms with superscript as $\tilde{P}_{out,av}$ are estimated variables. In (6.3), H_{av} and H_{osc} are the transfer function of the low-pass filters for the average and the oscillatory component, respectively. Here, a first order low-pass filter having cutoff frequency of α_{LPF} as expressed in (6.4) has been considered for the filters

$$H_{av}(s) = H_{osc}(s) = \frac{\alpha_{LPF}}{s + \alpha_{LPF}} \tag{6.4}$$

Figure 6.1 shows the block-diagram representation of the implemented estimation algorithm. In state-space form, the dynamics for the LPF based estimator, can be written as [78] [79]

$$\frac{d}{dt}\begin{bmatrix} \tilde{P}_{out,av} \\ \tilde{P}_{out,osc} \\ \tilde{P}_{out,B} \end{bmatrix} = \begin{bmatrix} -\alpha_{LPF} & -\alpha_{LPF} & 0 \\ -2\alpha_{LPF} & -2\alpha_{LPF} & -\omega_{osc} \\ 0 & \omega_{osc} & 0 \end{bmatrix} \begin{bmatrix} \tilde{P}_{out,av} \\ \tilde{P}_{out,osc} \\ \tilde{P}_{out,B} \end{bmatrix} + \begin{bmatrix} \alpha_{LPF} \\ 2\alpha_{LPF} \\ 0 \end{bmatrix} P_{out}(t) \tag{6.5}$$

Using state-space form, the frequency response for the Low-Pass Filter based Estimation Algorithm (LPF-EA) can be evaluated. The response of the system from the input $P_{out}\,(t)$ to the oscillator component $\tilde{P}_{out,osc}$ and to the average components $\tilde{P}_{out,av}$ are presented in Fig. 6.2. The measured signal is assumed to contain a 35 Hz oscillatory frequency and hence the notch filter is centered around this frequency in the estimation of the average component. The cut-off frequency α_{LPF} is here set to 6.28 rad/sec

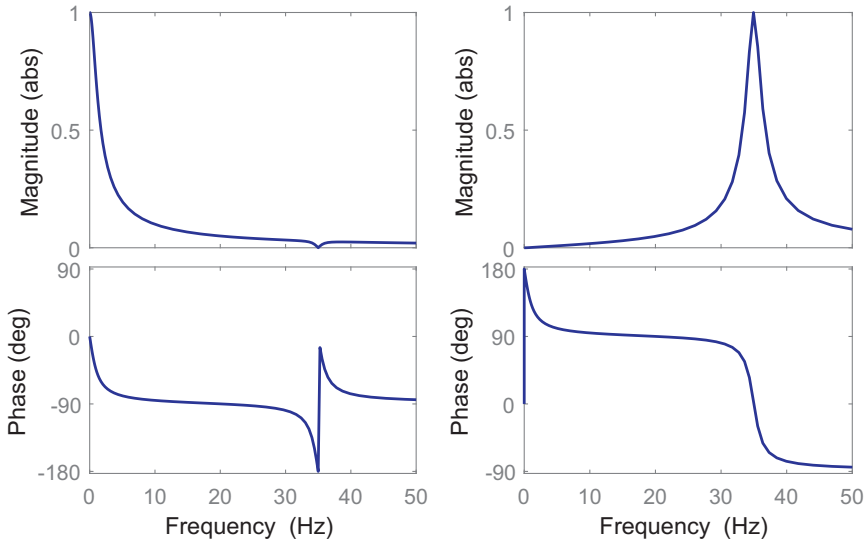

Fig. 6.2 Frequency response of low-pass filter based estimation algorithm from $P_{out}\,(t)$ to $\tilde{P}_{out,av}$ (*left figure*) and $\tilde{P}_{out,osc}$ (*right figure*). A cut-off frequency of 6.28 rad/sec is considered for first order filter

From Fig. 6.2, it can be observed that the LPF-EA has the property of a resonant filter having a center frequency at ω_{osc}. As it can be noted, the algorithm presents a 1 pu gain and 0^o phase shift at the oscillatory frequency ω_{osc} (see Fig. 6.2, right plot). Although not visible, it also presents a notch at 0 Hz. To extract the average power, the algorithm for the average component presents a 1 pu and 0^o phase shift at 0 Hz and a notch at the oscillatory frequency of ω_{osc} (see Fig. 6.2, left plot). According to the analysis performed in [32], the selection of the loop bandwidth for the estimator is a trade-off between the speed of response and the damping of the system. It is recommended in [79] to set the cut-off frequency of the filter at least one fifth of the minimum frequency span between the two estimates.

Subsynchronous damping controller

The subsynchronous damping controller links the estimated subsynchronous component to the RSC current controller. The proposed control algorithm utilizes the estimated subsynchronous power component as an input. For the controller at hand, the following assumptions have been considered

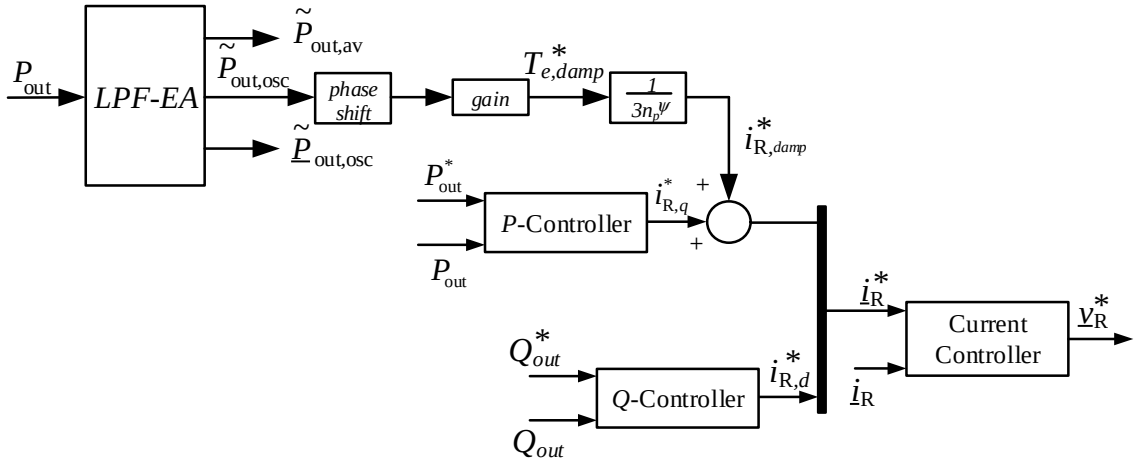

Fig. 6.3 Block diagram representation of subsyncrhornous damping controller implemented on RSC current controller.

- The network, in the supersynchronous range, is assumed to have enough positive damping to counteract possible negative damping that arises from the wind farm system (in the supersynchronous range) [31]. Therefore, supersynchronous components are not here considered.
- The subsynchronous oscillatory frequency is known with good accuracy. This is not a valid assumption in case of SSCI, as the oscillatory frequency varies depending on the controller parameters and operating condition. However, this particular issue is addressed further in Section 6.4

As previously mentioned, the estimated oscillatory component of the output power, $\tilde{P}_{out,osc}$, obtained from the EA serves as an input for the damping controller. To obtain a damping torque reference, a phase shift of 90^0 is introduced in the estimated subsynchronous power component. Here, extra care should be taken as phase shift other than 90^0 would result in the introduction of an active torque that could compromise the effectiveness of the damping controller. The generated reference value is then multiplied by a gain in order to obtain the required damping torque reference for the RSC controller. Figure 6.3 shows the block-diagram representation of the implemented damping controller. To generate the damping torque reference current ($i^*_{R,damp}$), the torque equation given in (6.6) has been used.

$$T_e = 3n_p\psi_{s,d}i_{R,q} \tag{6.6}$$

As it is done in the previous chapters, the impact of the implemented damping controller on the input admittance for the DFIG is evaluated. A steady-state representation of the estimation algorithm with a proportional damping controller has been included in the derived mathematical model presented in Section 3.4. The frequency response of the input admittance obtained using this mathematical model is presented in Fig. 6.4. An operating condition corresponding to P_{out} = 1 pu, Q_{out} = 0 pu and control loop parameters α_{cc} = 1 pu and α_{dc} = 0.1 pu have been used.

The cut-off frequency for the low-pass filters is set to α_{LPF} = 0.2 pu and the subsynchronous frequency is assumed equal to 35 Hz. The solid line indicates the frequency characteristic of the DFIG when the damping controller is implemented where as the dashed line show the result for a system without damping controller.

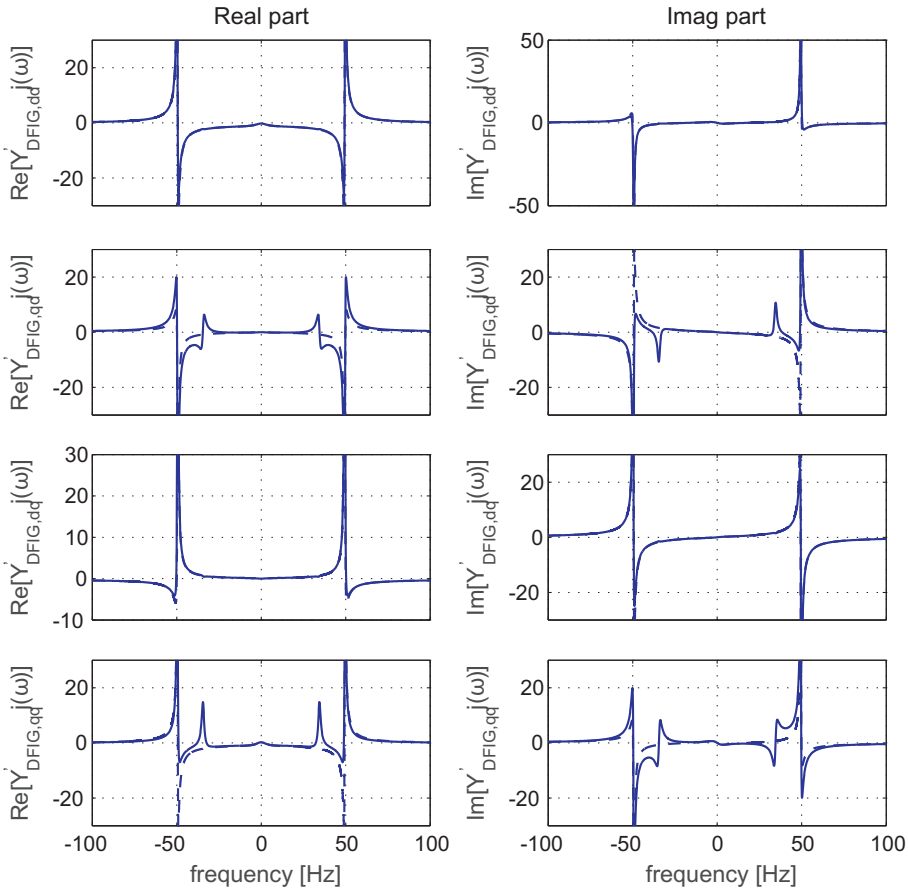

Fig. 6.4 Input admittance for a DFIG with a proportional damping controller (*solid line*), (gain = 0.4) versus DFIG with no damping controller (*dashed line*).

As it can be seen from the plot, the inclusion of the damping controller results in a positive real part, around the frequency of interest, both on the $Y_{DFIG,qd}$ and $Y_{DFIG,qq}$ components. This is not surprizing, as the the damping controller only affects the q component (torque component) of the reference rotor current,$i^*_{R,q}$. The impact of including a SSCI damping controller functionality to the RSC current controller is evaluated from the power dissipation capabilities for the DFIG system. For this purpose, a system with no damping controller versus a system having a damping controller centered around 35 Hz having bandwidth of α_{LPF} = 0.2 pu is shown in Fig. 6.5. As can be viewed from the result, the power dissipative behavior of the turbine is drastically improved at the desired frequency.

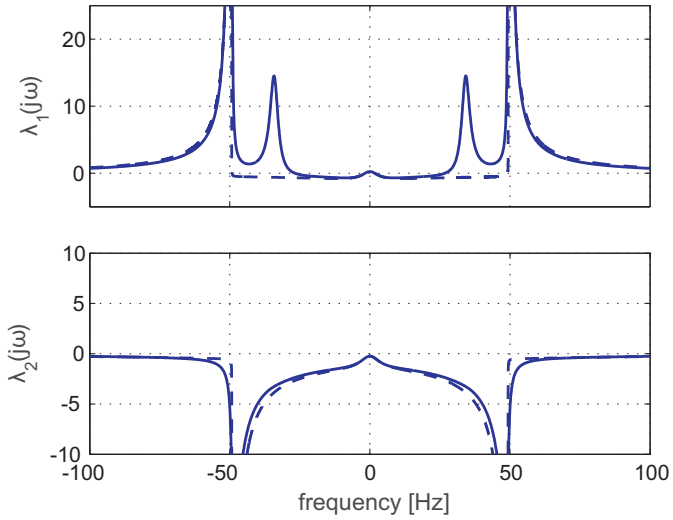

Fig. 6.5 Input admittance for a DFIG with a proportional damping controller (*solid line*), (gain = 0.4) versus DFIG with no damping controller (*dashed line*).

Figure 6.6 shows the pole-zero mapping for the DFIG turbine as the gain of the damping controller, k_{damp} is increased from 0.1 to 0.5 with a step of 0.05. As it can be observed, there is an upper limit on k_{damp}, as the stability of the DFIG turbine is affected at higher gain.

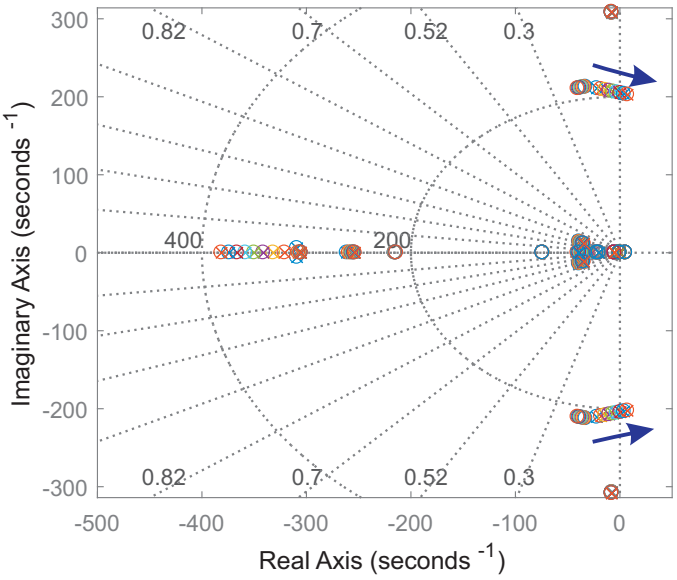

Fig. 6.6 Pole-zero movement of DFIG turbine for varied value of proportional gain. k_{damp} varied from 0.1 to 0.5 with a step of 0.05. Estimator bandwidth α_{LPF}= 0.2 pu

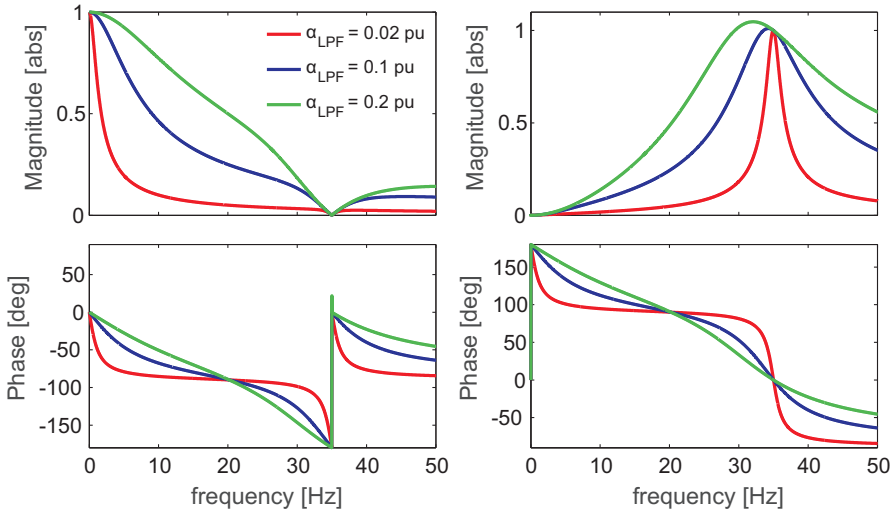

Fig. 6.7 Frequency response of low-pass filter based estimation algorithm from $P_{out}\,(t)$ to $\tilde{P}_{out,av}$ (*left figure*)and $\tilde{P}_{out,osc}$ (*right figure*) for a varied low-pass filter bandwidth

The other aspect to be evaluated is the loop bandwidth for the LPF-EA. Figure. 6.7, shows the frequency response of the LPF-EA for different values of α_{LPF}. As shown, increasing the loop bandwidth widens the bandpass region (*right plot*), thereby affecting the algorithm's selectivity. On the other hand, the higher the bandwidth, the faster the estimation speed. SSCI is a fast phenomenon; as a result, the speed of estimation plays a significant role during damping. In addition, there is typically only one mode that the damping controller needs to damp and this mode in relation to the average power will set the speed of response of the estimator.

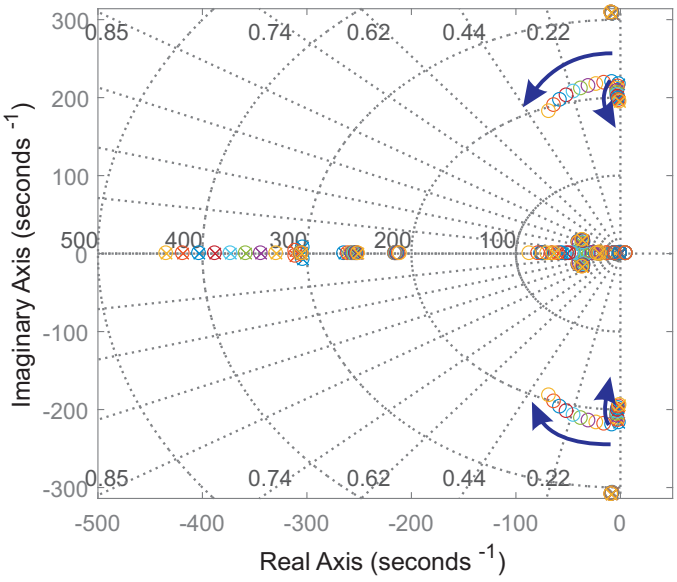

Fig. 6.8 Pole-zero movement of DFIG turbine for varied value of estimator closed-loop bandwidth. α_{LPF} varied from 0.02 pu to 0.2 pu with a step of 0.02. Proportional gain k_{damp} = 0.35

The effect of increasing the loop bandwidth for the LPF-EA on the overall dynamics of the

DFIG is demonstrated in Fig. 6.8 using pole-zero map. As it can be observed, higher bandwidth has the tendency of moving the zeros towards the left. The poles show a tendency of improvement in damping at the same time their corresponding frequency is observed to change as indicated by the arrow. This can be due to the widening of the bandpass frequency in the LPF-EA that indirectly affect the characteristic frequency of the corresponding poles of the DFIG turbine with a damping controller.

6.3 Frequency-domain stability analysis

In Chapter 5, frequency-domain analysis has been used to evaluate the impact of various controller parameters and operating conditions on the behavior of the DFIG turbine. An impedance based GNC has also been introduced in Section 5.1 to measure the risk of instability. In this section, a similar approach will be applied to inspect the effectiveness of the proposed SSCI mitigation technique. Initially accurate knowledge of system parameter and SSR oscillatory frequency ω_{osc} is assumed. Using the GNC, Fig. 6.9 shows the characteristics for the eigen-loci, $\lambda_{ol1,2}$, for P_{out} = 1 pu at a compensation level of 20% and a damping controller gain of k_{damp} = 0.3.

As observed during the power dissipation evaluation for the wind farm, higher RSC closed-loop current controller bandwidth ($\alpha_{cc,R}$) leads to a drastic reduction in the power dissipation capabilities of the wind farm. From the time-domain simulation presented in Fig. 5.10, $\alpha_{cc,R}$ of 2 pu leads to a very fast subsynchronous oscillation to build up even at 20% compensation that eventually leads to instability within a 1 sec time frame. As a result, a cut-off frequency of α_{LPF} = 0.3 pu (to match the build-up speed) is considered on the LPF-EA in this case.

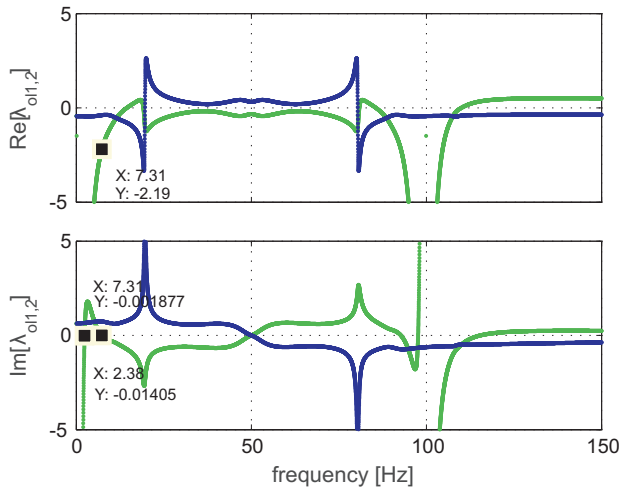

Fig. 6.9 Eigen-loci $\lambda_{ol1,2}$. $Re\,[\lambda_{ol1,2}]$ vs frequency (*upper plot*). $Im\,[\lambda_{ol1,2}]$ vs frequency (*lower plot*). P_{out} = 1 pu, α_{cc} = 2 pu, α_{LPF} = 0.3 pu, k_{damp} = 0.3 at 20% compensation level.

As it can be observed from the plot in Fig. 6.9, the GNC indicates a stable system with two zero crossing of $Im[\lambda_{ol1,2}]$, and the corresponding points for $Re[\lambda_{ol1,2}]$ occur before the -1

point (shown with markers). The operating point for the grid is altered by increasing the SCL to estimate the limitation of the damping controller. The GNC for a SCL = 35% is shown in Fig. 6.10. Still, thanks to the presence of the damping controller, stable operation has been obtained

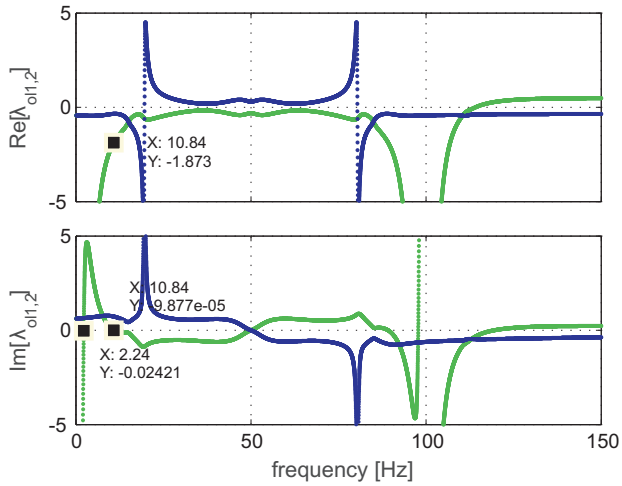

Fig. 6.10 Eigen-loci $\lambda_{ol1,2}$. $Re\,[\lambda_{ol1,2}]$ vs frequency (*upper plot*). $Im\,[\lambda_{ol1,2}]$ vs frequency (*lower plot*). P_{out} = 1 pu, α_{cc} = 2 pu, α_{LPF} = 0.3 pu, k_{damp} = 0.3 at 35% compensation level.

In Fig. 6.11, time-domain simulations when the wind farm is operated at $\alpha_{cc,R}$ = 2 pu for the two SCL values are shown. Similar to the single-line diagram representation shown in Fig. 5.6, a parallel line is connected at the PCC to ensure stable operation, especially during system start-up. At t = 4 sec, the circuit breaker is opened to simulate a radial connection. The result shows a satisfactory damping capabilities for up to compensation level of 35%.

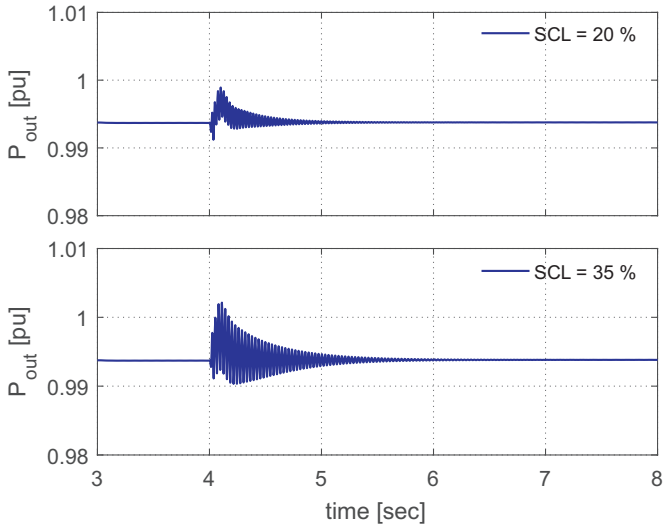

Fig. 6.11 Time domain simulation result for output power P_{out} = 1 pu, $\alpha_{cc,R}$ = 2 pu and α_{LPF} = 0.3 pu. SCL = 20% (*upper plot*) and SCL = 35% (*lower plot*).

The impact of k_{damp} discussed in Section 6.2.2 with regards to the DFIG wind turbine has been evaluated from the SSCI damping capabilities of the investigated system (wind farm + transmission line with series compensation). The gain for the damping controller is increased from k_{damp} = 0.3 to k_{damp} = 0.5 for a SCL = 20% as in Fig. 6.9. GNC based result is shown in Fig. 6.12. As it can be observed, the frequency-domain analysis predicts the risk for instability, as there are two zero crossing for the two curves ($Im[\lambda_{ol,1}]$- blue curve and $Im[\lambda_{ol,2}]$ and green curve). Focusing on the $Im[\lambda_{ol,2}]$ (green curve) the zero crossing occurs on the right side of the -1 point indicating encirclement of the -1 point.

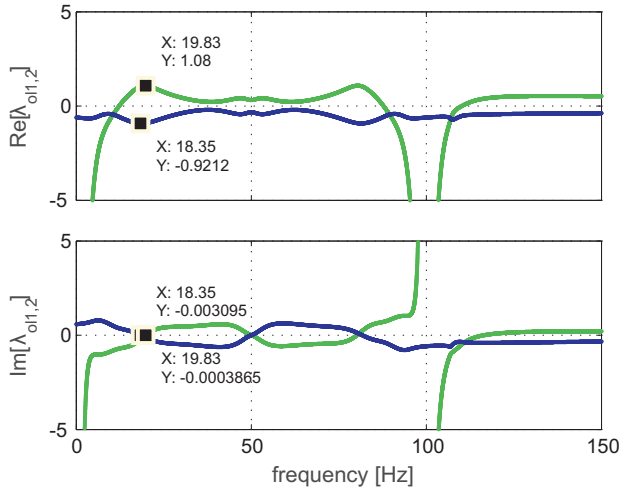

Fig. 6.12 Eigen-loci $\lambda_{ol1,2}$ for P_{out} = 1 pu, α_{cc} = 2 pu, α_{LPF} = 0.2 pu, k_{damp} = 0.5 at 20% compensation level. $Re\,[\lambda_{ol1,2}]$ vs frequency (*upper plot*). $Im\,[\lambda_{ol1,2}]$ vs frequency (*lower plot*).

The time-domain simulation result, for an increased k_{damp} = 0.5, depicted in Fig. 6.13 supports the analytical result from Fig. 6.12.

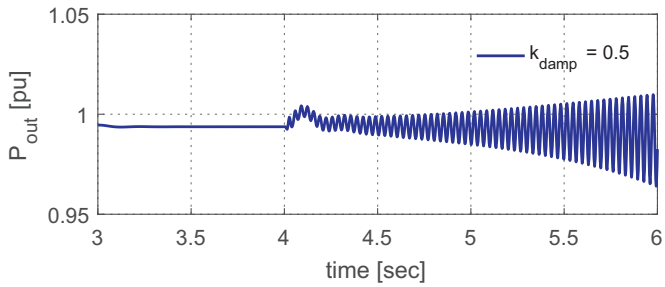

Fig. 6.13 Time domain simulation result. Output power P_{out} = 1 pu, $\alpha_{cc,R}$ = 2 pu and α_{LPF} = 0.3 pu at SCL = 20 %. Damping controller gain k_{damp} = 0.5.

From the analysis with regards to operating points discussed in Section 5.2.2, it has been concluded that operation of the wind turbines in the subsynchronous speed range leads to a higher

risk of instability due to SSCI. Consequently, it is interesting to evaluate the effectiveness of the damping controller for this operating condition. Figure. 6.14 shows the eigen-loci $\lambda_{ol1,2}$ for output power of P_{out} = 0.25 pu, α_{LPF} = 0.2 pu, k_{damp} = 0.3 at 25% compensation level. It can be observed in the figure that the - 1 point thereby ensuring that the -1 point is not encircled.

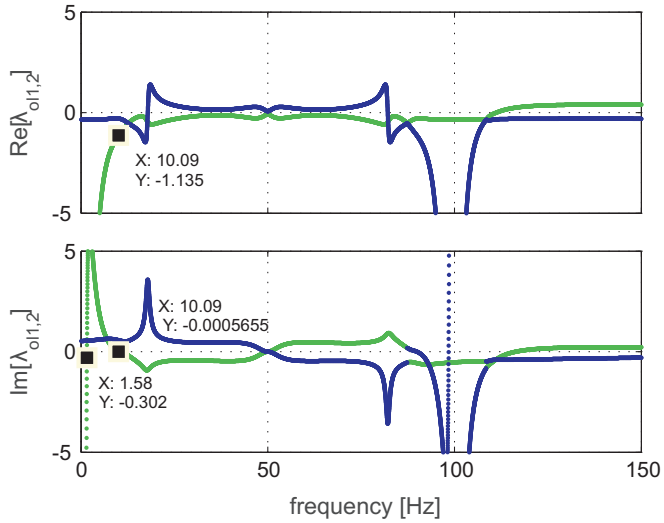

Fig. 6.14 Eigen-loci $\lambda_{ol1,2}$ for P_{out} = 0.25 pu, $\alpha_{cc,R}$ = 2 pu, α_{LPF} = 0.2 pu, k_{damp} = 0.3 at 25% compensation level. $Re\left[\lambda_{ol1,2}\right]$ vs frequency (*upper plot*). $Im\left[\lambda_{ol1,2}\right]$ vs frequency (*lower plot*).

From the result presented in Fig. 6.10 and Fig. 6.14, it is shown that improvement to system damping at higher SCL is achievable. It should be noted that depending on the operating condition (amount of wind available) the improvement can be limited to SCL = 25%. This is due to the fact that wind turbines operated under low-speed have lower power dissipation capabilities (as shown in Fig. 3.34) and consequently limited damping capabilities from the wind farm.

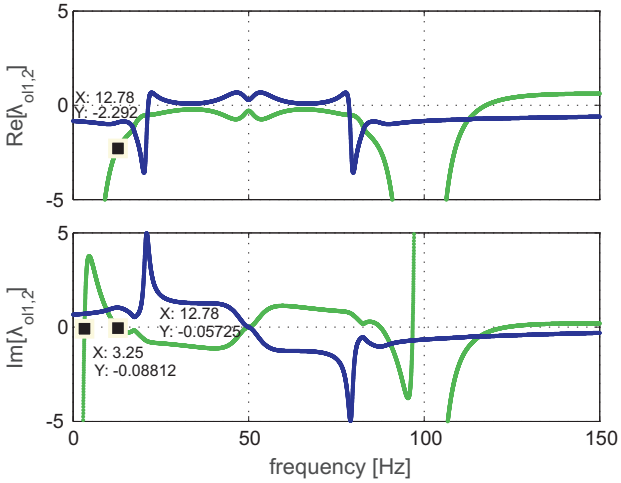

Fig. 6.15 Eigen-loci $\lambda_{ol1,2}$. $Re\left[\lambda_{ol1,2}\right]$ vs frequency (*upper plot*). $Im\left[\lambda_{ol1,2}\right]$ vs frequency (*lower plot*). P_{out} = 1 pu, α_{cc} = 1 pu, α_{LPF} = 0.2 pu, k_{damp} = 0.3 at 50% compensation level.

Note that the use of the damping controller in combinations with a reduction of $\alpha_{cc,R}$ from 2 pu to 1 pu allows to further extend the range of allowed SCL, as shown in Fig. 6.15, where a SCL of 50% is considered.

Corresponding time-domain simulation is shown in Fig. 6.16.

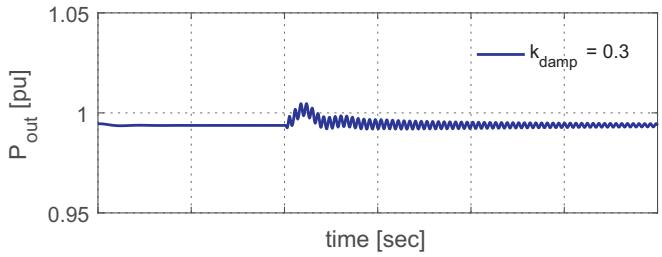

Fig. 6.16 Time domain simulation result. Output power P_{out} = 1 pu at SCL = 50%. Damping controller gain k_{damp} = 0.3 and α_{LPF} = 0.2 pu

The limit of the damping controller when the turbine us operated in the subsynchronous speed range with $\alpha_{cc,R}$ = 1 pu is considered. Figure. 6.17 shows the GNC of the interconnected system for output power of P_{out} = 0.25 pu, α_{LPF} = 0.2 pu, k_{damp} = 0.3 at 50% compensation level. The zero-crossing frequency corresponding real value falls both after the - 1 point thereby ensuring that the -1 point is not encircled.

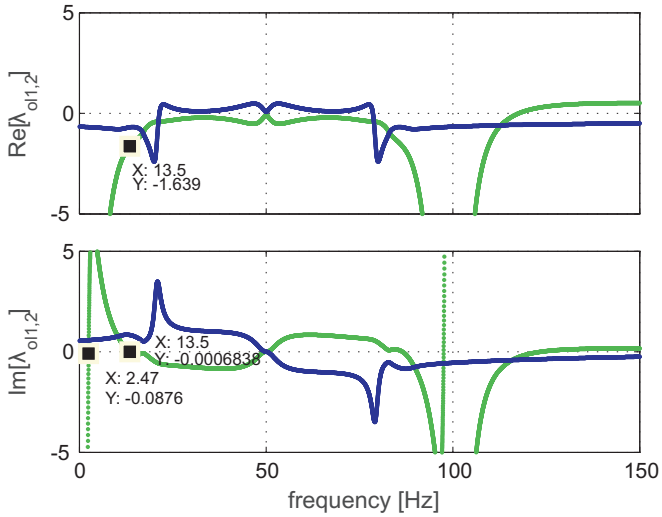

Fig. 6.17 Eigen-loci $\lambda_{ol1,2}$. $Re\,[\lambda_{ol1,2}]$ vs frequency (*upper plot*). $Im\,[\lambda_{ol1,2}]$ vs frequency (*lower plot*). P_{out} = 1 pu, α_{cc} = 0.25 pu, α_{LPF} = 0.2 pu, k_{damp} = 0.3 at 50% compensation level.

From the result presented in this section, the proposed damping controller has been shown to improve the SCL level. For example stating a specific case where low-wind speed condition is assumed, the SCL has been shown to improve by a factor that is approximately equal to 1.78. In addition higher level is achievable by reducing the speed of response of the RSC current control loop.

6.4 Improved estimation method

In the above analysis, the oscillatory frequency of the subsynchronous component is assumed to be known with good accuracy. However, when dealing with SSCI this assumption is not valid as the oscillatory frequency is dependent both on the operating conditions and the considered controller structure. As shown in Fig. 6.7, an error in the assumed frequency in the EA will result in both a phase and an amplitude error in the estimates. This evidently would result in an error in the damping controller that might negatively affect the system stability.

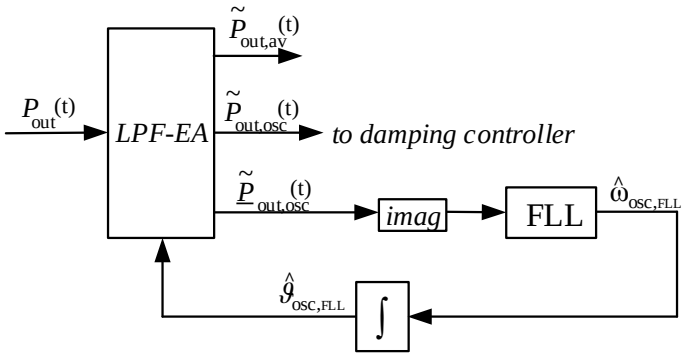

Fig. 6.18 Block diagram representation of estimation algorithm with frequency adaptation features

To overcome this problem, Fig. 6.18 shows the block diagram of the improved estimation algorithm. The output of the estimation algorithm is further passed as an input to a frequency-locked loop (FLL), used to estimate the frequency of the subsynchronous component. As a result, the estimation algorithm is equipped with a frequency adaptation algorithm. The equation governing the FLL is expressed here as

$$\hat{\omega}_{osc,PLL} = k_1 \varepsilon(t) \tag{6.7}$$

where $\varepsilon(t)$ is the error signal given by $\mathrm{Im}\left[\underline{\hat{P}}_{out,osc}(t)\right]$ where as k_1 is set to α_{PLL}^2 in accordance to the recommendation in [80].

6.5 Time-domain based simulation

In Section. 6.3, the effectiveness of the proposed damping controller for SSCI has been shown through impedance based frequency analysis and the results have been supported using time-domain simulation. During the analysis, an initial assumption, where ω_{osc} is known with accuracy has been considered. In this section, time-domain based simulation results for the improved damping controller are presented.

6.5.1 Mitigation based on full aggregate wind farm representation

For this first set of simulation results, the operating points corresponding to P_{out} = 0.25 pu and Q_{out} = 0 pu and controller parameters α_{cc} = 2 pu, α_{dc} = 0.2 pu and α_{LPF} = 0.3 pu have been considered. The result for this operating point with frequency adaptation (α_{FLL} = 0.02 pu) is shown in Fig. 6.19 using the blue curve. The upper plot shows the terminal output power. In the same figure, result where the frequency adaptation is turned off is also included using dashed red curve. As can be seen, the result with FLL is able to track and damp out the SSCI whereas the system with no FLL, with a 3% error in the oscillatory frequency (ω_{osc}), is unable to prevent the instability.

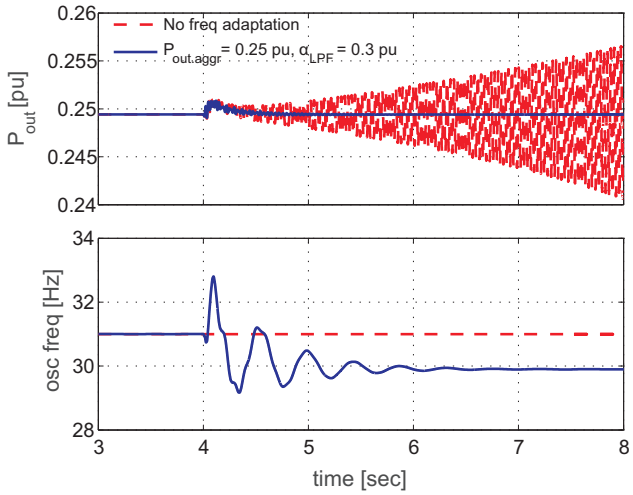

Fig. 6.19 Time domain simulation result. Output power P_{out} = 0.25 pu at SCL = 25%. **upper plot**: terminal output power for system having frequency adaptation (*blue curve)* and system with frequency adaptation turned off having error in ω_{osc} (*red dashed curve*). **lower plot**: estimated frequency using FLL (*blue curve*) and ω_{osc} for LPF-EA in the damping controller (*red dashed curve*).

From Fig. 6.19, it is evident that frequency adaptation is a crucial part of the damping controller. Further evaluation of the estimation algorithm with frequency adaptation at a reduced $\alpha_{cc,R}$ = 1 pu, for two different operating point of P_{out} = 1 pu and P_{out} = 0.25 pu are considered. The level of series compensation is here increased to SCL = 50%. The result for full power output is shown in Fig. 6.20. As it can be observed, the damping controller is able to control the oscillation that builds up at 4 sec after the opening of the parallel line. The lower plot, shows the estimated frequency output from the FLL. Having an initial error of $\approx$ 2 Hz, the FLL is able to track the correct oscillatory frequency.

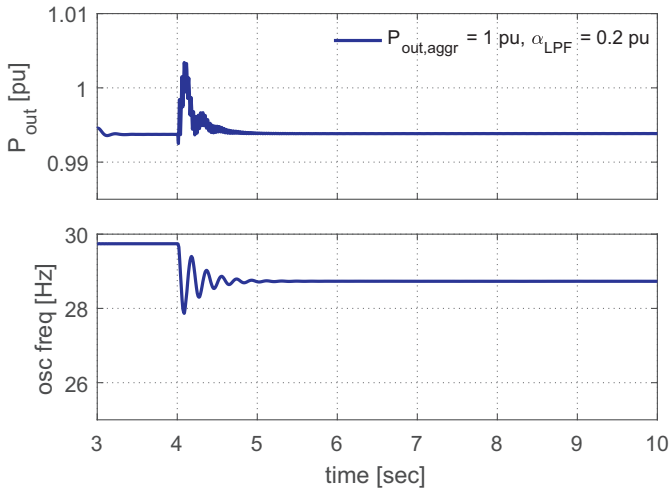

Fig. 6.20 Time domain simulation result. Output power P_{out} = 1 pu (*upper plot*) at SCL = 50%. Estimated frequency using frequency adaptation (*lower plot*).

The result shown in Fig. 6.21 corresponds to operation at a low power output from the wind farm. The output of the FLL is shown in the lower plots; again, the damping controller works properly and the FLL is capable of tracking the oscillatory frequency.

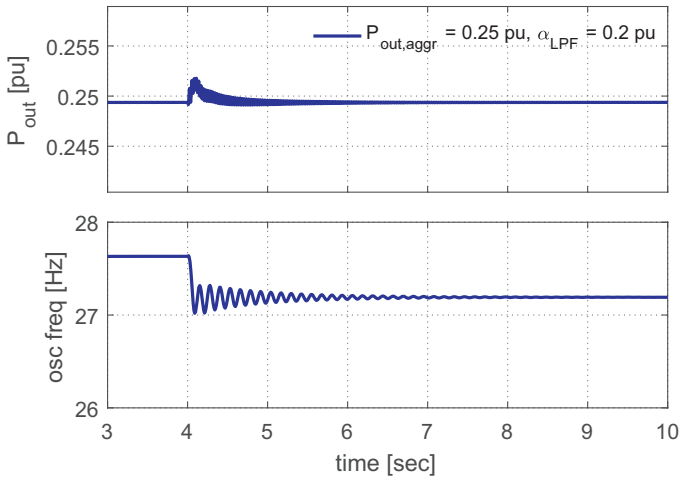

Fig. 6.21 Time domain simulation result. Output power P_{out} = 0.25 pu (*upper plot*) at SCL = 50%. Estimated freq using frequency adaptation (*lower plot*). α_{LPF} = 0.2 pu and α_{FLL} = 0.02 pu

In some cases, a requirement from the wind turbine operator can be to activate the damping controller functionality only upon the detection of a SSCI. Some case studies are presented here where the damping controller is activated after that the estimated level of subsynchronous component reaches a threshold level of 0.1 pu. The result for a transmission line operated at SCL = 50% is evaluated in Fig. 6.22. The lower plot indicates the instant when the damping controller is activated according to the setting. In this particular case, the damping controller is activated at t = 4.2 sec. A closed-loop bandwidth of α_{LPF} = 0.2 pu has been considered. From the result, it is evident that the damping controller is able to control the SSCI in this situation.

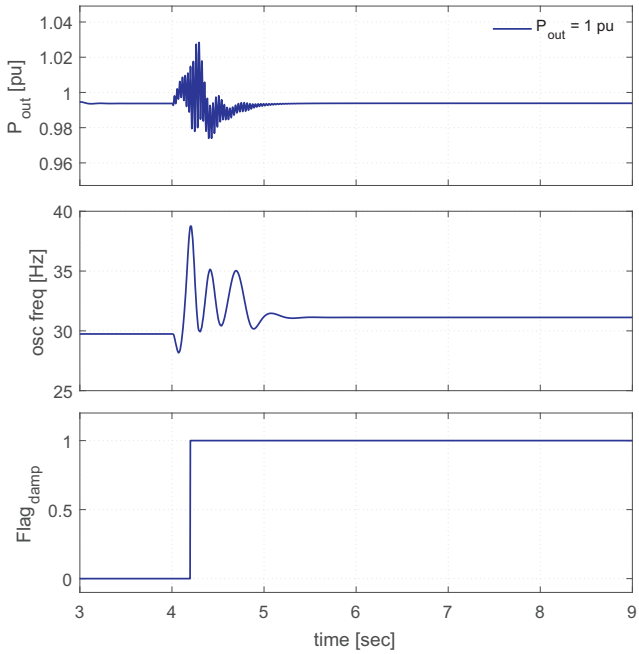

Fig. 6.22 Time domain simulation for output power of P_{out} = 1 pu, Q_{out} = 0 pu, α_{cc} = 1 pu and SCL = 50%. P_{out} of wind farm having damping controller with FLL (*Upper plot*). Estimated oscillatory frequency from FLL (*middle plot*). Flag for activation of damping controller(*Lower plot*).

Testing the limits of the damping controller, once SSCI is detected, a case study with $\alpha_{cc,R}$ = 2 pu and P_{out} = 0.25 pu (subsynchronous speed operation) is shown in Fig. 6.23. From the result, it is shown that the algorithm fails to control SSCI even though the damping controller is activated 0.1 sec after the trigger of the SSCI. From the middle plot, it is evident that the FLL is unable to track the oscillatory frequency. It is should be noted that for the same system condition (see Fig. 6.19), where the damping controller is active all the time, the SSCI is damped. As a recommendation, the capability for damping SSCI once the oscillation has started is best achieved at a lower $\alpha_{cc,R}$ of 1 pu.

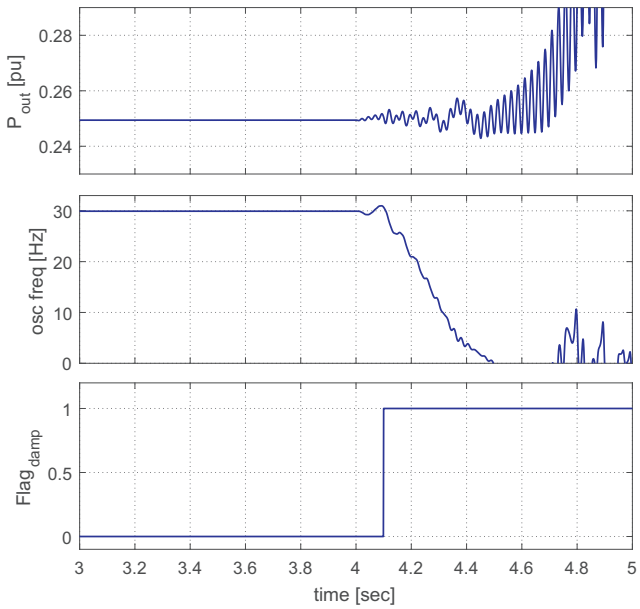

Fig. 6.23 Output power of a DFIG wind farm connected to a series compensated transmission line. *Upper plot*: Operation with damping controller. *middle plot*: Estimated oscillatory frequency from FLL. *Lower plot*: Flag for activation of damping controller. $Pout$ = 0.25 pu, Q_{out} = 0 pu, α_{cc} = 2 pu and 25% compensation level

6.5.2 Mitigation based on multiple wind turbine aggregate representation

In the result presented so far, a single aggregate representation for the wind farm has been considered to evaluate the effectiveness of the proposed damping controller. In this section, a multiple wind turbine aggregate model for the wind farm that is based on three radials is adopted. The purpose is to evaluate the performance of the damping controller under the condition that not all wind turbines within the wind farm are equipped with damping capabilities. As a start, a case study where two radials are equipped with damping controller and the third radial has no damping capabilities is evaluated. The result for full power production at SCL = 50% is shown in Fig. 6.24.

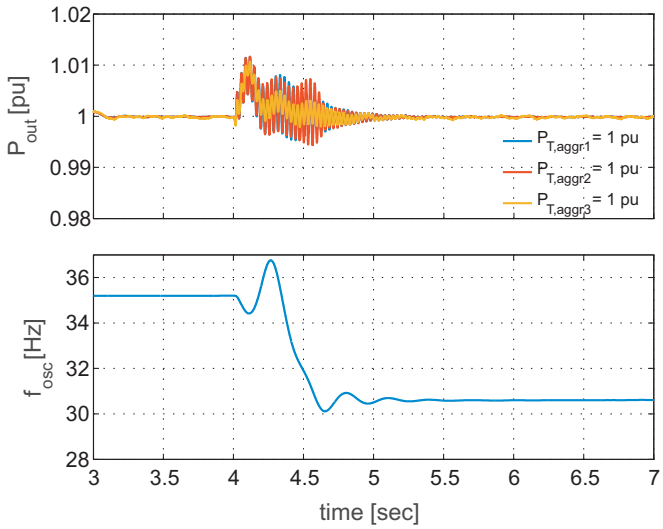

Fig. 6.24 Time domain simulation result. Output power P_{out} = 1 pu (*upper plot*) for three radial system operated at α_{cc} = 1 pu and SCL = 50%. Estimated frequency using FLL (*lower plot*). Damping controller parameters of α_{LPF} = 0.2 pu and α_{FLL} = 0.02 pu

A second case study, where all three radials (thus all wind turbines) are operated at subsynchronous speed with damping controller activated for the first and second radial (65% of the wind turbines), is considered in Fig. 6.25 for the same level of series compensation. The results presented in Fig. 6.24 and Fig. 6.25 indicate that it is sufficient to have 65% of the wind turbines within the wind farm to be equipped with damping controller capabilities, even at low wind speed condition.

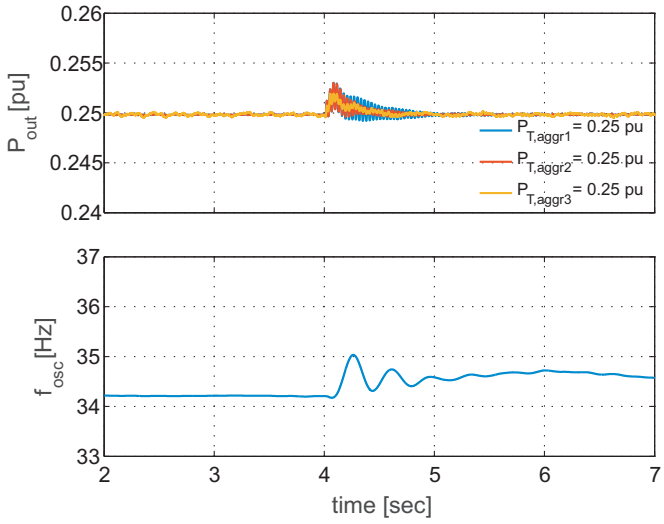

Fig. 6.25 Time domain simulation result. Output power P_{out} = 0.25 pu (*upper plot*) for three radial system at SCL = 50%. Estimated freq using frequency adaptation (*lower plot*). α_{LPF} = 0.2 pu and α_{FLL} = 0.02 pu

The third case study considered involves operation of the wind farm under the condition that

only one radial, having a generation capacity of 30 MW (30% of the wind turbines), is equipped with a damping capabilities. In Fig. 6.26, full power output for a compensation level of 35% is shown. As it can be observed from the result, output power from radial one, which is equipped with the damping controller, is observed to exhibit a higher portion of the oscillation. This is justified as these are the turbines that actively generate the damping torque needed to damp out the oscillation. However, it should be noted that the level of compensation plotted here is 35%; higher SCL would result in an unstable system.

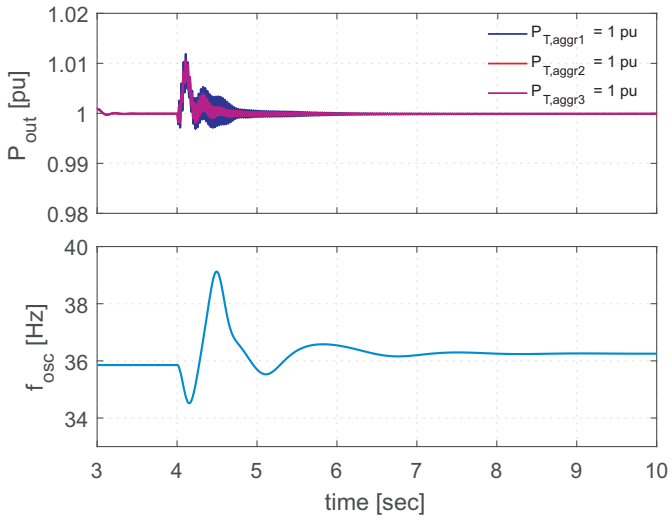

Fig. 6.26 Time domain simulation result. Output power P_{out} = 1 pu (*upper plot*) for three radial system at SCL = 35%. Estimated freq using frequency adaptation (*lower plot*). α_{LPF} = 0.2 pu and α_{FLL} = 0.02 pu

To summarize the finding of this section, the damping controller is effective in tracking and damping the oscillatory component due to SSCI even at high level of series compensation. However a majority of the wind turbines should be equipped with the damping capabilities in order to achieve high level of compensation at low wind-speed conditions.

6.6 Conclusion

This chapter has dealt with mitigation techniques for SSCI in DFIG based wind farms. A mitigation technique employing an estimation algorithm and a proportional damping controller has been used to shape the input admittance of the DFIG. The impact of the mitigation method on the DFIG input admittance has been investigated and it has been shown that with the proposed approach it is possible to increase the power-dissipation properties of the wind turbine in the frequency range of interest. To further improve the mitigation technique, a frequency adaptation has been introduced to the estimation algorithms, in order to accurately estimate the subsynchronous oscillatory frequency.

The effectiveness of the proposed method has been evaluated using impedance-based GNC. The results have been further supported through time-domain simulation using PSCAD. Thanks to

the proposed approach, effective mitigation of SSCI has been achieved, also when drastically increasing the level of series compensation in the transmission line.

Chapter 7

Conclusions and future work

7.1 Conclusions

This thesis has dealt with the investigation of the risk for subsynchronous controller interaction (SSCI) in wind farms connected to a series-compensated transmission line. In particular, the focus of this work has been on the risk for SSCI in DFIG-based wind farms. System modeling, frequency-domain stability studies as well as impedance-shaping schemes to improve the system damping at the frequencies of interest have been covered.

After a description of different kinds of SSR phenomena that can be encountered in the power system provided in Chapter 2, the thesis has focused on SSCI in wind-based generating plants, particularly in DFIG-based wind farms. In Chapter 3 , an overview of the main components that constitute a DFIG wind turbine together with a detailed description of the control structure has been provided. Aiming at understanding the frequency characteristic of the DFIG in order to be able to identify and analyze the key factors that can influence the risks for SSCI, a linearized model of the wind turbine system has been derived. Using an averaging technique, the linearized mathematical model of the DFIG has been verified against a full-switching model implemented in PSCAD. The adopted system modeling is based on a modular approach, consisting of building subsystem blocks that are properly interconnected to obtain the analytical representation of the investigated system. This modeling approach gives the possibility to identify how the individual components of the system can impact the frequency characteristic of the overall wind-turbine model.

It is shown that the impact of the electrical machine on the system stability is highly associated to its negative slip (as the machine is operated as a generator) and thereby on the operating condition of the system. In addition, analytical analysis shows that the loop bandwidth of the current controller implemented on the rotor-side converter (RSC) directly impacts the negative real part of the DFIG input admittance, leading to an increased risk of instability when increasing the speed of response of this control loop.

The inclusion of the outer-control loops (i.e., active- and reactive-power controllers and dc-link voltage controller), leads to an unsymmetrical frequency-dependent admittance matrix for

the DFIG. Therefore, the classical frequency-based analytical methods, such as passivity and net-damping criterion, can be difficult to be applied to assess the stability of the system. To overcome this and gain insights on the impact of different control parameters and system operating conditions on the risk for SSCI, a method based on the power-dissipation properties of the DFIG transfer-function matrix (to be considered as an extension of the passivity approach for multiple-input/multiple-output systems) has been adopted. Based on this approach, it is confirmed that the main control parameter that affects the power-dissipation properties (and thereby the risk for SSCI) is the closed-loop bandwidth of the RSC current controller. On the other hand, it has been shown that the speed of response of the current controller implemented in the grid-side converter (GSC) as well as the different outer-control loops have a minimal influence on the power-dissipation capability of the DFIG. However, it has been highlighted that the impact of the dc-voltage controller might be noticeable under specific operating conditions, particularly depending if the GSC is operated as an inverter or as a rectifier. In addition, it has been shown that the level active power output from the wind farm (thus, the amount of available wind speed - ω_r) also significantly affects the DFIG ability to dissipate power in case of resonant conditions in the subsynchronous-frequency range. This condition is particularly evident depending if the wind turbine operates at low-power production (corresponding to operation of the machine in the subsynchronous-speed range) or at high-power production (operations in the supersynchronous-speed range).

The linearized model of the DFIG in combination with the model representation of the collection system has been derived to obtain the linearized mathematical model of the overall wind farm. In Chapter 4, it has been highlighted that the choice of the aggregation criteria needs special attention. Using power-dissipation theory, it has been shown that only wind turbines experiencing similar wind distribution should be aggregated together, in order to guarantee proper system representation and thereby avoid erroneous conclusions. In particular, it has been shown that, for the specific focus of this work, the wind farm can be represented using a two-aggregated wind turbines model, where one of the aggregates is used to represent those wind turbines that are operated at subsynchronous speed (i.e., wind turbines facing low-wind speed), while the second represents turbines operated at the supersynchronous speed. Analytical analysis as well as time-domain simulations have shown that this aggregation approach provides a more accurate system representation as compared with the full aggregation, typically adopted in the literature, while preserving a relative simplicity of the model.

In Chapter 5, the impedance-based generalized Nyquist criterion (GNC) has been adopted to evaluate the risk of instability for the investigated system. The system under study comprises a DFIG-based wind farm radially connected to a series-compensated transmission system. Using the GNC approach, factors affecting the risk of instability due to SSCI have been identified. The results obtained through the theoretical analysis have been verified using a detailed time-domain simulation model.

To mitigate the risk of SSCI in DFIG-based wind turbines, a damping controller implemented within the DFIG turbine control system has been proposed. The suggested approach involves the modification of the RSC control system of the DFIG, with the goal of enhancing the system damping at the specific frequency of interest. The damping controller proposed in Chapter 6 is composed by an estimation stage, based on a combination of low-pass filters utilized to isolate

the subsynchronous component in the measured active-output power, and a proportional damping controller stage for generating the desired reference damping signal. The later serves as an additional input to the current control loop of the RSC. Theoretical analysis has clearly shown that the use of the damping controller effectively modifies the frequency characteristic of the DFIG and enhances the power-dissipation properties at the selected frequency. One difficulty in the implementation of the damping controller is that, as mentioned earlier, unlike other kind of classical SSRs that can be encountered in the power systems (such as SSR due to torque interaction, TI), in case of SSCI the resonance frequency is typically dependent on a number of factors. To overcome this issue, a frequency-locked loop (FLL) has been added in the estimation stage, thus providing the damping controller frequency-adaptation capabilities. Time-domain simulation results representing different case studies have been presented to verify the effectiveness of the proposed adaptive-damping controller. Furthermore, it has been shown that the use of the proposed damping controller allows to drastically increase the stability margin of the system, or for a given stability margin to increase the maximum level of series-compensation in the transmission system.

7.2 Future work

The investigation of resonant conditions in systems with high penetration of power-electronic devices is a complex task. The focus of this thesis has been on DFIG-based wind farms employing conventional control strategies. Investigation relating to the risk of SSCI in full-power converter type wind turbines has not been here addressed. Although there exists no reported incidents related to control interaction in this type of wind turbines, investigation on the risk of SSCI for this turbine topology is of high interest.

As shown in this thesis, the use of the proposed damping controller allows to reduce the risk for SSCI. It will definitely be of interest to evaluate the impact of this additional control loop on the ratings of the back-to-back converter of the DFIG. Due to hardware limitations as well as unfavorable system conditions or in case of more realistic wind farm representations (especially in case of multivendor systems), this solution might be insufficient. In such cases, external power-electronic based devices, such as STATCOMs or other kind of FACTS controllers connected to the point of common coupling with the grid, might be necessary to mitigate unstable conditions. However, due to the variable nature of the frequency characteristic of the wind turbines, the control of such devices is not trivial and needs a deep investigation.

References

[1] “Statistics.” [Online]. Available: www.svenskenergi.se/Elfakta/Elproduktion

[2] “Statistics and forecast.” [Online]. Available: http://svenskvindenergi.org/statistik/2017-3

[3] *IVA Fem vägval för Sveriges utveckling - syntesrapport från Vägval el*.

[4] Global Wind Energy Council (GWEC), *Global wind statistics 2017*.

[5] Wind European, *Wind in Power 2017* . Available online, 2018.

[6] A. J. Roscoe, M. Yu, R. Ierna, J. Zhu, A. Dysko, H. Urdal, and C. Booth, “A VSM (virtual synchronous machine) convertor control model suitable for RMS studies for resolving system operator/owner challenges,” in *Proc. Of 15th Wind Integration Workshop*, Nov. 2016.

[7] H. Urdal, R. Ierna, J. Zhu, C. Ivanov, A. Dahresobh, and D. Rostom, “System strength considerations in a converter dominated power system,” *IET Renewable Power Generation*, vol. 9, no. 1, pp. 10–17, 2015.

[8] National Grid (UK), *The Grid Code*, 2016.

[9] C. Buchhagen, C. Rauscher, A. Menze, and J. Jung, “BorWin1 - First Experiences with harmonic interactions in converter dominated grids,” in *Proceedings of International ETG Congress 2015; Die Energiewende - Blueprints for the new energy age*, Nov 2015, pp. 1–7.

[10] M. Bongiorno, A. Peterson, and E. Agneholm, “The Impact of Wind Farm on Subsynchronous Resonance in Power Systems,” Elforsk, Stockholm, Sweden, Elforsk Report 11:29, May, 2011.

[11] H. A. Mohammadpour and E. Santi, “Analysis of Subsynchronous Control Interactions in DFIG-based Wind Farms: ERCOT case study,” in *2015 IEEE Energy Conversion Congress and Exposition (ECCE)*, Sept 2015, pp. 500–505.

[12] R. K. Varma, S. Auddy, and Y. Semsedini, “Mitigation of Subsynchronous Resonance in a Series-Compensated Wind Farm using FACTS Controllers,” *IEEE Trans. Power Del.*, vol. 23, no. 3, pp. 1645–1654, July 2008.

[13] P. Pourbeik, R. Koessler, D. Dickmander, and W. Wong, "Integration of Large Wind Farms into Utility Grids (Part 2-Performance Issues)," in *Power Engineering Society General Meeting, 2003, IEEE*, vol. 3. IEEE, 2003.

[14] H. Xie, B. Li, C. Heyman, M. de Oliveira, and M. Monge, "Subsynchronous Resonance Characteristics in Presence of Doubly-Fed Induction Generator and Series Compensation and Mitigation of Subsynchronous Resonance by Proper Control of Series Capacitor," *Renewable Power Generation, IET*, vol. 8, no. 4, pp. 411–421, May 2014.

[15] L. Fan, R. Kavasseri, Z. L. Miao, and C. Zhu, "Modeling of DFIG-based Wind Farms for SSR Analysis," *IEEE Trans. Power Del.*, vol. 25, no. 4, pp. 2073–2082, Oct 2010.

[16] A. Ostadi, A. Yazdani, and R. K. Varma, "Modeling and Stability Analysis of a DFIG-based Wind-Power Generator Interfaced With a Series-Compensated Line," *IEEE Trans. Power Del.*, vol. 24, no. 3, pp. 1504–1514, July 2009.

[17] C. Zhu, M. Hu, and Z. Wu, "Parameters impact on the performance of a double-fed induction generator-based wind turbine for subsynchronous resonance control," *IET Renewable Power Generation*, vol. 6, no. 2, pp. 92–98, March 2012.

[18] L. Wang, X. Xie, Q. Jiang, H. Liu, Y. Li, and H. Liu, "Investigation of SSR in Practical DFIG-based Wind Farms Connected to a Series-Compensated Power System," *IEEE Trans. on Power Syst.*, vol. 30, no. 5, pp. 2772–2779, Sept 2015.

[19] A. Tabesh and R. Iravani, "Small-Signal Model and Dynamic Analysis of Variable Speed Induction Machine Wind Farms," *Renewable Power Generation, IET*, vol. 2, no. 4, pp. 215–227, December 2008.

[20] L. Fan and Z. Miao, "Nyquist-Stability-Criterion-based SSR Explanation for Type-3 Wind Generators," *IEEE Trans. Energy Convers.*, vol. 27, no. 3, pp. 807–809, Sept 2012.

[21] Z. Miao, "Impedance-Model based SSR Analysis for Type 3 Wind Generator and Series-Compensated Network," *IEEE Trans. Energy Convers.*, vol. 27, no. 4, pp. 984–991, Dec 2012.

[22] M. Hall and D. Hodges, "Experience with 500-kv Subsynchronous Resonance and Resulting Turbine Generator Shaft Damage at Mohave Generating Station," *IEEE PES Special Publication, Analysis and Control of Subsynchronous Resonance, IEEE Publication*, vol. 76, pp. 22–29, 1976.

[23] P. Anderson and R. Farmer, *Series Compensation of Power Systems*. United States of America: PBLSH, 1991.

[24] IEEE SSR Working Group, "Terms, Definitions and Symbols for Subsynchonous Oscillations," *IEEE Transaction*, vol. PAS-104, June 1985.

[25] R. Farmer, A. Schwalb, and E. Katz, "Navajo Project Report on Subsynchronous Resonance Analysis and Solutions," *IEEE Trans. Power App. Syst.*, vol. 96, no. 4, pp. 1226–1232, July 1977.

[26] L. C. Gross, "Sub-synchronous Grid Conditions: New event new problem and new solutions," in *37th Annual Western Protective Relay Conference, Spokane, Washington*, 2010.

[27] C. Wagner, "Self-Excitation of Induction Motors with Series Capacitors," *Electrical Engineering*, vol. 60, no. 12, pp. 1241–1247, 1941.

[28] T. Ackermann and R. Kuwahata, "Lesson Learned from International Wind Integration Studies," Australian Energy Market Operator, Melbourne, Australia, Tech. Rep., 2011.

[29] R. K. Varma, S. Auddy, and Y. Semsedini, "Mitigation of Subsynchronous Resonance in a Series-Compensated Wind Farm using FACTS Controllers," *IEEE Trans. Power Del.*, vol. 23, no. 3, pp. 1645–1654, 2008.

[30] P. Anderson, B. Agrawal, and J. V. Ness, *Subsynchronous Resonance in Power Systems*. New York, United States of America: IEEE Press, 1989.

[31] K. Padiyar, *Analysis of Subsynchronous Resonance in Power Systems*. United States of America: Kluwer Academic Publishers, 1999.

[32] M. Bongiorno, J. Svensson, and L. Angquist, "Online Estimation of Subsynchronous Voltage Components in Power Systems," *IEEE Trans. Power Del.*, vol. 23, no. 1, pp. 410–418, 2008.

[33] M. Bongiorno, "On Control of Grid-connected Voltage Source Converter," Chalmers University of Technology, Gothenburg, Sweden, PhD Thesis, 2007.

[34] L. Harnefors, M. Bongiorno, and S. Lundberg, "Input-Amittance Calculation and Shaping for Controlled Voltage-Source Converters," *IEEE Trans. Ind. Electron.*, vol. 54, no. 6, pp. 3323–3334, Dec 2007.

[35] J. Sun, "Impedance-based Stability Criterion for Grid-Connected Inverters," *IEEE Trans. Power Electron.*, vol. 26, no. 11, pp. 3075–3078, Nov 2011.

[36] A. Bayo-Salas, J. Beerten, J. Rimez, and D. Van Hertem, "Impedance-based Stability Assessment of Parallel VSC HVDC Grid Connections," in *11th IET International Conference on AC and DC Power Transmission*, Feb 2015, pp. 1–9.

[37] J. E. Slotine and W. Li, *Applied Nonlinear Control*. New Yersey:Prentice-hall Englewood Cliffs, 1991, vol. 199, no. 1.

[38] L. H. Hansen, L. Helle, F. Blaabjerg, E. Ritchie, S. Munk-Nielsen, H. W. Bindner, P. E. Sørensen, and B. Bak-Jensen, *Conceptual Survey of Generators and Power Electronics for Wind Turbines*. Technical University of Denmark, 2002.

[39] T. Ackermann, *Wind Power in Power Systems*. John Wiley & Sons, 2005.

[40] L. Harnefors, "Modeling of Three-Phase Dynamic Systems using Complex Transfer Functions and Transfer Matrices," *IEEE Trans. Ind. Electron.*, vol. 54, no. 4, pp. 2239–2248, 2007.

References

[41] F. Fateh, W. Warren.N., and D. Gruenbacher, "Mitigation of Torsional Vibration in the Drivetrain of DFIG based Grid-Connected Wind Turbine," in *Seventh Annual IEEE Energy Conversion Congress and Exposition*, September 2015.

[42] A. Petersson, "Analysis, Modeling and Control of Doubly-Fed Induction Generators for Wind Turbines," Ph.D. dissertation, Chalmers University of Technology, 2005.

[43] H. Mohammadpour, Y. J. Shin, and E. Santi, "SSR analysis of a DFIG-based Wind Farm Interfaced with a Gate-Controlled Series Capacitor," in *Twenty-Ninth Annual IEEE Applied Power Electronics Conference and Exposition (APEC), 2014*, March 2014, pp. 3110–3117.

[44] G. Slemon, *IEEE Trans. Ind. Appl. title=Modelling of Induction machines for Electric Drives, year=1989, volume=25, number=6, pages=1126-1131, doi=10.1109/28.44251, ISSN=0093-9994, month=Nov,*.

[45] A. Petersson, "Analysis, Modeling and Control of Doubly-Fed Induction Generators for Wind Turbines," Chalmers University of Technology, Gothenburg, Sweden, Licentiate Thesis, 2003.

[46] R. Datta and V. Ranganathan, "Decoupled Control of Active and Reactive Power for a Grid-Connected Doubly-Fed Wound Rotor Induction Machine without Position Sensors," in *Thirty-Fourth IAS Annual Industry Applications Conference, 1999. . Conference Record of the 1999 IEEE*, vol. 4, 1999, pp. 2623–2630 vol.4.

[47] R. Ottersten, "On Control of Back-to-Back Connected and Sensorless Induction Machine Drives," Chalmers University of Technology, Gothenburg, Sweden, PhD Thesis, 2003.

[48] L. Harnefors and H.-P. Nee, "Model-based Current Control of AC Machines using the Internal Model Control Method," *IEEE Trans. Ind. Appl.*, vol. 34, no. 1, pp. 133–141, 1998.

[49] M. Bongiorno and T. Thiringer, "A Generic DFIG Model for Voltage Dip Ride-Through Analysis," *IEEE Trans. Energy Convers.*, vol. 28, no. 1, pp. 76–85, March 2013.

[50] L. Harnefors, *Control of Power Electronic Converter and Variable-Speed Drives*. Västerås, Sweden: Applied Signal Processing and Control, Dept. of Electronics, Mälardalen University, 2002.

[51] O. Wallmark, L. Harnefors, and O. Carlson, "An Improved Speed and Position Estimator for Salient Permanent-Magnet Synchronous Motors," *IEEE Trans. Ind. Electron.*, vol. 52, no. 1, pp. 255–262, 2005.

[52] R. Nath and C. Grande-Moran, "Study of Sub-Synchronous Control Interaction due to the Interconnection of Wind Farms to a Series Compensated Transmission System," in *Transmission and Distribution Conference and Exposition (T D), 2012 IEEE PES*, May 2012, pp. 1–6.

[53] D. Xiaoliang and X. Xiaorong, "Influence of DFIG Controller Parameter on SSR Under all Operation Areas," in *Power System Technology (POWERCON), 2014 International Conference on*, Oct 2014, pp. 2618–2622.

[54] H. Ghasemi, G. Gharehpetian, S. A. Nabavi-Niaki, and J. Aghaei, "Overview of Subsynchronous Resonance Analysis and Control in Wind Turbines," *Renewable and Sustainable Energy Reviews*, vol. 27, pp. 234 – 243, 2013.

[55] J. C. Willems, "Dissipative Dynamical Systems Part i: General Theory," *Archive for Rational Mechanics and Analysis*, vol. 45, no. 5, pp. 321–351, Jan 1972. [Online]. Available: https://doi.org/10.1007/BF00276493

[56] A. M. S. Al-bayati, F. Mancilla-David, and J. L. Dominguez-Garcia, "Aggregated models of wind farms: Current methods and future trends," in *2016 North American Power Symposium (NAPS)*, Sept 2016, pp. 1–6.

[57] L. M. Fernandez, F. Jurado, and J. R. Saenz, "Aggregated Dynamic Model for Wind Farms with Doubly Fed Induction Generator Wind Turbines," *Renewable energy*, vol. 33, no. 1, pp. 129–140, 2008.

[58] E. Muljadi, C. Butterfield, A. Ellis, J. Mechenbier, J. Hochheimer, R. Young, N. Miller, R. Delmerico, R. Zavadil, and J. Smith, "Equivalencing the Collector System of a Large Wind Power Plant," in *Power Engineering Society General Meeting, 2006. IEEE*. IEEE, 2006, pp. 9–pp.

[59] H. A. Mohammadpour and E. Santi, "Modeling and Control of Gate-Controlled Series Capacitor Interfaced with a DFIG-based Wind Farm," *IEEE Trans. on Ind. Electron.*, vol. 62, no. 2, pp. 1022–1033, Feb 2015.

[60] P. H. Huang, M. S. E. Moursi, W. Xiao, and J. L. Kirtley, "Subsynchronous Resonance Mitigation for Series-Compensated DFIG-based Wind Farm by using Two-Degree-of-Freedom Control Strategy," *IEEE Trans. Power Syst.*, vol. 30, no. 3, pp. 1442–1454, May 2015.

[61] S. Skogestad and I. Postlethwaite, *Multivariable feedback control: analysis and design*. Wiley New York, 2007, vol. 2.

[62] M. S. El-Moursi, B. Bak-Jensen, and M. H. Abdel-Rahman, "Novel STATCOM Controller for Mitigating SSR and Damping Power System Oscillations in a Series Compensated Wind Park," *IEEE Trans. Power Electron.*, vol. 25, no. 2, pp. 429–441, Feb 2010.

[63] S. Golshannavaz, M. Mokhtari, and D. Nazarpour, "SSR Suppression via STATCOM in Series Compensated Wind Farm Integrations," in *19th Iranian Conference on Electrical Engineering, 2011*, May 2011, pp. 1–6.

[64] H. Xie and M. M. de Oliveira, "Mitigation of SSR in presence of Wind Power and Series Compensation by SVC," in *International Conference on Power System Technology (POWERCON), 2014*, Oct 2014, pp. 2819–2826.

[65] H. A. Mohammadpour, J. Siegers, and E. Santi, "Controller Design for TCSC using Observed-State Feedback Method to Damp SSR in DFIG-based Wind Farms," in *IEEE Applied Power Electronics Conference and Exposition (APEC), 2015*, March 2015, pp. 2993–2998.

[66] H. A. Mohammadpour and E. Santi, "Sub-synchronous Resonance Analysis in DFIG-based Wind Farms: Mitigation Methods; TCSC, GCSC, and dfig controllers - Part II," in *IEEE Energy Conversion Congress and Exposition (ECCE), 2014*, Sept 2014, pp. 1550–1557.

[67] A. E. Leon and J. A. Solsona, "Sub-synchronous Interaction Damping Control for DFIG Wind Turbines," *IEEE Trans. Power Syst.*, vol. 30, no. 1, pp. 419–428, Jan 2015.

[68] I. Vieto and J. Sun, "Damping of Subsynchronous Resonance involving Type-III Wind Turbines," in *IEEE 16th Workshop on Control and Modeling for Power Electronics (COMPEL), 2015*, July 2015, pp. 1–8.

[69] H. Liu, X. Xie, Y. Li, H. Liu, and Y. Li, "Damping DFIG-Associated SSR with Subsynchronous Suppression Filters: A Case Study on a Practical Wind Farm System," in *International Conference on Renewable Power Generation (RPG 2015)*, Oct 2015, pp. 1–6.

[70] H. Liu, X. Xie, Y. Li, H. Liu, and Y. Hu, "Damping Subsynchronous Resonance in Series-Compensated Wind Farms by adding Notch Filters to DFIG Controllers," in *IEEE Innovative Smart Grid Technologies - Asia (ISGT ASIA), 2015*, Nov 2015, pp. 1–5.

[71] X. Xie, L. Wang, H. Liu, H. Liu, and Y. Li, "A Mechanism Study of SSR for Multiple DFIG Wind Generators Connected to a Series-Compensated Power System," in *International Conference on Power System Technology (POWERCON), 2014*, Oct 2014, pp. 2769–2774.

[72] G. D. Irwin, A. K. Jindal, and A. L. Isaacs, "Sub-synchronous Control Interactions between Type-3 Wind Turbines and Series Compensated AC Transmission Systems," in *2011 IEEE Power and Energy Society General Meeting*, July 2011, pp. 1–6.

[73] D. Xiaoliang and X. Xiaorong, "Influence of DFIG Controller Parameter on SSR under all Operation Areas," in *International Conference on Power System Technology (POWERCON), 2014*, Oct 2014, pp. 2618–2622.

[74] H. A. Mohammadpour, A. Ghaderi, H. Mohammadpour, and E. Santi, "SSR Damping in Wind Farms using Observed-state Feedback Control of DFIG Converters," *Electric Power Systems Research*, vol. 123, pp. 57–66, 2015.

[75] L. Wang, J. Peng, Y. You, and H. Ma, "SSCI Performance of DFIG with Direct Controller," *IET Generation, Transmission & Distribution*, 2017.

[76] L. Fan and Z. Miao, "Mitigating SSR Using DFIG-Based Wind Generation," *IEEE Trans. Sustain. Energy*, vol. 3, no. 3, pp. 349–358, July 2012.

[77] H. A. Mohammadpour and E. Santi, "SSR Damping Controller Design and Optimal Placement in Rotor-Side and Grid-Side Converters of Series-Compensated DFIG-based Wind Farm," *IEEE Trans. Sustain. Energy*, vol. 6, no. 2, pp. 388–399, April 2015.

[78] L. Angquist and C. Gama, "Damping Algorithm based on Phasor Estimation," in *Power Engineering Society Winter Meeting, 2001. IEEE*, vol. 3, 2001, pp. 1160–1165 vol.3.

[79] M. Beza, *Power System Stability Enhancement Using Shunt-Connected Power Electronic Devices with Active Power Injection Capability*. Departement of Energy and Environment, Electrical Power Engineering, Chalmers University of Technology, 2015, 168.

[80] L. Angquist and M. Bongiorno, "Auto-normalizing Phase-Locked Loop for Grid-connected Converters," in *IEEE Energy Conversion Congress and Exposition, 2009. ECCE 2009.*, Sept 2009, pp. 2957–2964.

[81] IEEE SSR Task Force, "First Benchmark Model for Computer Simulation of Subsynchronous Resonance," *IEEE Trans. Power Syst. Appl.*, vol. PAS-9618, no. 5, pp. 1565–1571, Sept./Oct. 1977.

References

Appendix A

Benchmark Model for SSR Studies

A.1 Introduction

In this appendix, the two IEEE benchmark model used for SSR studies are introduced. The first IEEE benchmark model deals with SSR as a result of radial resonance while the second benchmark model deals with parallel resonance in the power system

A.1.1 IEEE First Benchmark Model (IEEE FBM)

The IEEE First Benchmark Model (IEEE FBM) shown in Fig. A.1 is based on a radial connection of a 892.4 MVA synchronous generator connected to a series compensated transmission network [30] [81]. The system has a rated voltage of 539 kV and a rated frequency of 60 Hz. The parameters for the synchronous generator and for the transmission line can be found in Table A.1 and Table A.2, respectively. The generator shaft model parameters are reported in Table A.3.

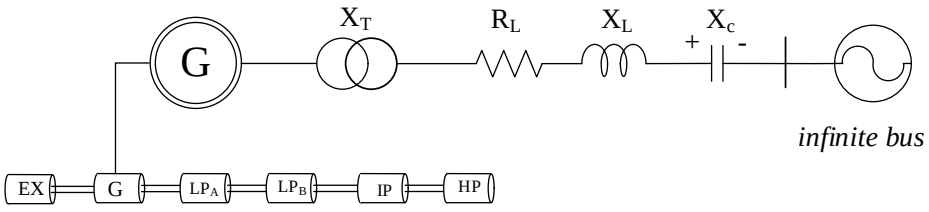

Fig. A.1 Single-line diagram of IEEE first benchmark model

TABLE A.1: IEEE FBM Synchronous Generator Parameters

Reactance	Values [pu]	Time constants	Value [sec]
$X_{a\sigma}$	0.13	$T_{d0}^{'}$	4.3
X_d	1.79	$T_{d0}^{''}$	0.032
$X_d^{'}$	0.169	$T_{q0}^{'}$	0.85
$X_d^{''}$	0.135	$T_{q0}^{''}$	0.05
$X_q^{'}$	0.228		
$X_q^{''}$	0.2		

TABLE A.2: IEEE FBM Network Parameters

Network resistance	R_L	0.02 pu
Transformer reactance	X_T	0.14 pu
Transformer ratio		26/539 kV
Line reactance	X_L	0.5 pu

TABLE A.3: IEEE FBM Shaft Parameters

Mass	Inertia H [s^{-1}]	Shaft section	Spring constant K [pu T/rad]
	H [s^{-1}]		K [pu T/rad]
HP turbine	0.092897	HP-IP	19.303
IP turbine	0.155589	IP-LPA	34.929
LPA turbine	0.858670	LPA-LPB	52.038
LPB turbine	0.884215	LPB-GEN	70.858
Generator	0.868495	GEN-EX	2.82
Exciter	0.0342165		

The IEEE FBM has been modified to accommodate an aggregate DFIG based wind farm, the parameter of which are presented in Table A.4. The Network parameter for the modified IEEE FBM is given in Table A.6

TABLE A.4: DFIG Aggregate Model parameter

Rated power	100 MW
Rated voltage	33 kV
X_{ls}	0.158367 pu
X_m	3.8271871 pu
X_{lr}	0.065986 pu
R_s	0.0092417 pu
R_r	0.0075614 pu
X_f	1.055 pu
R_f	0.1055 pu
C_{dc}	2.54 pu

TABLE A.5: Induction Generator Parameters

Rated power	100 MW
Rated voltage	26 KV
X_{ls}	0.08168 pu
X_{lr}	0.14870 pu
X_m	4.289 pu
R_s	0.004820 pu
R_r	0.006313 pu

TABLE A.6: Network Parameters for DFIG Farm

Network resistance	R_L	0.02 pu
Transformer reactance	X_T	0.14 pu
Transformer resistance	R_{TL}	0.0146 pu
Transformer ratio		33/161 kV
Line reactance	X_L	0.1 pu
Line resistance	R_L	0.02 pu
Series compensation	X_c	% of X_L
Line reactance (line 2)	X_{L2}	0.1 pu
Line resistance (line 2)	R_{L2}	0.002 pu

Appendix B

Transformation for three-phase system

B.1 Introduction

In this appendix, the transformation used to extract the complex vector from three-phase quantities and vice verse is presented.

B.1.1 Transformation of three-phase quantities into vectors

A three-phase system composed of three quantities, $s_a(t)$, $s_b(t)$ and $s_c(t)$ can be transformed into a vector having two components in a stationary complex reference frame, referred to as xy by applying the transformation stated by

$$\underline{s}^{xy}(t) = s_x + js_y = K\left[s_a(t) + s_b(t)\, e^{j\frac{2}{3}\pi} + s_c(t)\, e^{j\frac{4}{3}\pi}\right] \tag{B.1}$$

The transformation constant K can be chosen between 1, $\sqrt{1/2}$ or $\sqrt{2/3}$ to obtain amplitude invariant, rms invariant or power invariant transformation, respectively. The expression of (B.1) is expressed in matrix form as (B.2)

$$\begin{bmatrix} s_x(t) \\ s_y(t) \end{bmatrix} = \mathbf{T}_{32} \begin{bmatrix} s_a(t) \\ s_b(t) \\ s_c(t) \end{bmatrix} \tag{B.2}$$

where the matrix $\mathbf{T}_{32}$ is expressed as

$$\mathbf{T}_{32} = K \begin{bmatrix} 1 & -\frac{1}{2} & -\frac{1}{2} \\ 0 & \frac{\sqrt{3}}{2} & -\frac{\sqrt{3}}{2} \end{bmatrix}$$

Assuming there is no zero sequence, the inverse transformation is given by

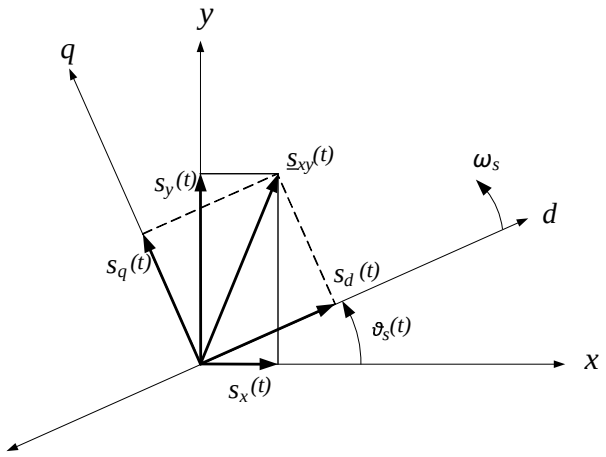

Figure B.1: Relation between xy-frame and dq-frame

$$\begin{bmatrix} s_a(t) \\ s_b(t) \\ s_c(t) \end{bmatrix} = \mathbf{T}_{23} \begin{bmatrix} s_x(t) \\ s_y(t) \end{bmatrix} \tag{B.3}$$

where the matrix $\mathbf{T}_{23}$ is given by

$$\mathbf{T}_{32} = \frac{1}{K} \begin{bmatrix} \frac{2}{3} & 0 \\ -\frac{1}{3} & \frac{1}{\sqrt{3}} \\ -\frac{1}{3} & -\frac{1}{\sqrt{3}} \end{bmatrix}$$

B.1.2 Transformation from fixed to rotating reference frame

For a vector expressed as $\underline{s}_{xy}$ in the xy-frame having an angular frequency $\omega_s(t)$ in the counter-clockwise direction, a rotating dq-frame that rotates with the same angular frequency $\omega_s(t)$ can be defined. In this rotating reference frame, the vector $\underline{s}_{xy}$ appears as a fixed vector. By projecting the vector $\underline{s}_{xy}$ in the d-axis and q-axis of the dq-frame, the components of the vector in the dq frame can be obtained as illustrated in Fig. B.1

The transformation can be expressed using vector notations as

$$\underline{s}_{dq}(t) = s_d(t) + j s_q(t) = \underline{s}_{xy}(t) e^{-j\vartheta_s(t)} \tag{B.4}$$

where $\vartheta_s(t)$ is expressed as

$$\vartheta_s(t) = \vartheta_s^0(t) + \int \omega_s(t) dt$$

The inverse transformation from the rotating dq-frame is expressed as

$$\underline{s}_{xy}(t) = \underline{s}_{dq}(t)e^{j\vartheta_s(t)} \tag{B.5}$$